Innovative Strategies for Observations in the Arctic Atmospheric Boundary Layer

Stephan T. Kral

UNIVERSITY OF BERGEN

Innovative Strategies for Observations in the Arctic Atmospheric Boundary Layer

Stephan T. Kral

Thesis for the degree of Philosophiae Doctor (PhD)
at the University of Bergen

Date of defense: 20.11.2020

Year: 2020

Title: Innovative Strategies for Observations in the Arctic Atmospheric Boundary Layer

Name: Stephan T. Kral

Print: Skipnes Kommunikasjon / University of Bergen

Scientific environment

The work for this study was carried out at the Geophysical Institute (GFI), University of Bergen (UiB), Norway. I was a member of the POLAR research group on polar climate and Research Group 5 on atmosphere, cryosphere and ocean processes at the Bjerknes Centre for Climate Research. The PhD position was funded by the Norwegian Research Council's FRINATEK program through the Innovative Strategies for Observations in the Arctic Atmospheric Boundary Layer (ISOBAR) project (251042/F20). As a PhD student, I was enrolled in the Research School on Changing Climates in the Coupled Earth System (CHESS), which provided a number of relevant courses for my education. My participation in the annual meeting of the International Society for Atmospheric Research using Remotely piloted Aircraft (ISARRA), 2018 in Boulder, Colorado, and the LAPSE-RATE campaign, 2018 in the San Luis valley, Colorado, were both supported by the US National Science Foundation (AGS 1807199), and the US Department of Energy (DE-SC0018985), in the form of travel support for early-career scientists. Acting as the leader for two of the ISOBAR work packages linked me to a number of international institutions and leading scientists. In the field of boundary-layer research I collaborated with scientists from the Universities of Wageningen and Marquette, the Finnish Meteorological Institute and the University Centre in Svalbard, the latter two also via my co-supervisors Timo Vihma and Marius Jonassen. Together with the University of Applied Sciences Ostwestfalen-Lippe, University of Tübingen and University of Oklahoma, I worked on the application of unmanned aircraft systems for atmospheric research.

Acknowledgements

Abstract

In this thesis, consisting of five scientific papers, I investigate the potential of unmanned aircraft systems (UAS) in stable boundary layer (SBL) research, by developing and applying a new innovative observation strategy. In this strategy we supplement ground-based micrometeorological observations from masts and remote-sensing systems with a number of different UAS. To achieve good agreement between the different systems employed in this approach, I further investigate the quality and intercomparability of UAS-based observations of atmospheric temperature, humidity, pressure and wind, and develop and apply common, best-practice data processing methods.

In Paper I we give a brief introduction to the ISOBAR project and provide an overview over the first SBL campaign at Hailuoto and the prevailing synoptic, sea-ice and micrometeorological conditions. We demonstrate the quality of our measurement approach by combining UAS profile data with observations from the wind and temperature sensing systems. Repeated UAS temperature profiles give detailed insight into the temporal evolution of the SBL, which we find was often subject to rapid temperature changes affecting the entire depth of the SBL. We further highlight the potential of the sampled data by detailed investigations of a case study, featuring rapid shifts in turbulent regimes and strong elevated thermal instabilities, which were likely to result from the instability of an elevated internal gravity wave.

In Paper II we assess the quality and intercomparability of UAS-based atmospheric observations from the most extensive intercomparison experiment to date. We evaluate the precision and bias of temperature, humidity, pressure, wind speed and direction observations from 38 individual UAS with 23 unique sensor configurations based on observations next to a 18-m mast equipped with reference instruments. In addition, we investigate the influence of sensor response on the quality of temperature and humidity profiles. By grouping the different sensor–platform combinations with respect to the type of aircraft, sensor type and sensor integration (i.e., measures for aspiration and radiation shielding), we attempt to draw general conclusions from the intercomparison results. Overall, we find most observation systems in good agreement with the reference observations, however, some systems showed fairly large biases. In general, hovering multicopters showed less variability than fixed-wing systems and we attribute this finding to the difference in sampling strategies. The most consistent observations of the mean wind were achieved by multicopter-mounted sonic anemometers. Sensor response errors were smaller for fine-bed thermistors compared to temperature sensors of integrated-circuit type, and sensor aspiration proofed to be substantially relevant. We conclude, that sensor integration considerations, like radiation shielding and aspiration, are likely to be as important as the choice of the sensor type, and give a couple of recommendations for future perspectives on UAS-based atmospheric measurements.

Paper III presents the ISOBAR project to a broader scientific audience, including a description of the two measurement campaigns, ISOBAR17 and ISOBAR18 and the contrasting meteorological and sea ice conditions. We further provide an overview on the micrometeorological conditions during the 13 intensive observational periods (IOPs), which resulted in detailed data sets on the SBL in unprecedented spatiotemporal resolution. Numerous cases with very-stable stratification under clear-sky and

weak-wind conditions were observed, featuring a variety of different SBL processes. These processes resulted in rapid changes in the SBL's vertical structure. Based on selected in-depth case studies, we investigate the interactions of turbulence in the very stable boundary layer (VSBL) with different processes, i.e., a shear instability, associated with a low-level jet; a rapid and strong cooling event, observed a couple of meters above the ground; and a wave-breaking event, caused by the enhancement of wind shear. In a first qualitative model validation experiment we use data from one IOP to assess the performance of three different types of numerical models. Only the turbulence resolving large-eddy simulation model is found capable of reproducing a VSBL structure similar to the one observed during the IOP. The other models, i.e., an operational weather prediction and a single-column model, substantially overestimated the depth of the SBL.

Paper IV introduces a new fixed-wing UAS for turbulence observations and first results from validation experiments carried out during ISOBAR18. Airborne observations of mechanical turbulence from straight horizontal flight paths are compared to corresponding eddy-covariance measurements mounted on a 10-m mast during weakly stable conditions with moderate wind speeds. Different average and spectral turbulence quantities, as well as mean wind speed and direction were computed for both systems and compared to each other. The UAS observations of mean wind and turbulence are in good agreement with the reference observations and the turbulence spectra agree qualitatively in the onset of the inertial subrange and the turbulence production range. Minor differences are likely to be caused by a slightly elevated UAS flight level and additional small altitude variations in the presence of relatively strong vertical gradients. In a second comparison, vertical profiles of mean wind and turbulence variables, determined from straight horizontal UAS flights at several different levels are compared qualitatively to profile observations from the 10-m mast and a phased-array sodar system providing 10-min averaged wind and vertical velocity variance profiles above 35 m. Qualitatively, the results agree well for the first two out of three profiles. During the third profile, the UAS data indicate the existence of a low-level jet but not an upside-down boundary layer structure, which would be expected due to the elevated source of turbulence. This observation is, however, not supported by the other measurement systems. Instead, the sodar data indicate a strong decrease in wind speed during the time of this profile. The fact that the lower part of the UAS profile was sampled before the start of the strongest transition, resulted in a seemingly wrong shape of the vertical profiles. This finding highlights the relevance of non-stationarity and the importance of additional reference systems for the correct interpretation of UAS sampled turbulence profiles.

Paper V explores the potential of a new method to estimate profiles of turbulence variables in the SBL. In this method we apply a gradient-based scaling scheme for SBL turbulence to multicopter profiles of temperature and wind, sampled during ISOBAR18. We first validate this method by scaling turbulence observations from three levels on a 10-m mast with the corresponding scaling parameters, and comparing the resulting non- dimensional parameters to the semi-empirical stability functions proposed for this scheme. The scaled data from the three levels largely collapse to the predicted curves, however, minor differences between the three levels are evident. We attribute this discrepancy to the non-ideal observation heights for the determination of vertical gradients at the upper turbulence observation level. After the successful val-

idation we apply this method to UAS profiles, by computing profiles of the gradient Richardson number to which we then apply the stability functions to derive turbulence variables. We demonstrate this approach based on three case studies covering a broad range of SBL conditions and boundary layer heights. Since the application of this scaling scheme is only valid within the SBL, we estimate the boundary layer height from the sodar and two different methods based on UAS data. Comparisons at the lowest levels against turbulence variables from the 10-m mast and at higher levels against a Doppler wind lidar, which also provides estimates of some turbulence variables, indicate broad agreement and physical meaningful results of this method.

Supplementing the findings from the five scientific papers, this thesis also provides the detailed description on the methodology and data processing procedures, I applied for the synthesis of observations from UAS, micrometeorological masts and boundary-layer remote-sensing systems. Furthermore, I present results on the validation of the different wind observation methods, using lidar wind observations as the common reference. Finally, I provide an outlook on future perspectives of SBL and UAS-based boundary-layer research, and how further developments in SBL observation strategies may benefit from recent and future developments.

Scientific contributions

The present thesis consists of this synthesis and the following papers, which will be referred to by their Roman numerals.

- **Paper I:**
  Kral, S. T., J. Reuder, T. Vihma, I. Suomi, E. O'Connor, R. Kouznetsov, B. Wrenger, A. Rautenberg, G. Urbancic, M. O. Jonassen, L. Båserud, B. Maronga, S. Mayer, T. Lorenz, A. A. M. Holtslag, G.-J. Steeneveld, A. Seidl, M. Müller, C. Lindenberg, C. Langohr, H. Voss, J. Bange, M. Hundhausen, P. Hilsheimer and M. Schygulla, 2018: Innovative Strategies for Observations in the Arctic Atmospheric Boundary Layer (ISOBAR) —The Hailuoto 2017 Campaign. *Atmosphere*, 9 (7), 268, doi:10.3390/atmos9070268.

- **Paper II:**
  Barbieri, L., S. T. Kral, S. C. C. Bailey, A. E. Frazier, J. D. Jacob, J. Reuder, D. Brus, P. B. Chilson, C. Crick, C. Detweiler, A. Doddi, J. Elston, H. Foroutan, J. González-Rocha, B. R. Greene, M. I. Guzman, A. L. Houston, A. Islam, O. Kemppinen, D. Lawrence, E. A. Pillar-Little, S. D. Ross, M. P. Sama, D. G. Schmale, T. J. Schuyler, A. Shankar, S. W. Smith, S. Waugh, C. Dixon, S. Borenstein and G. de Boer, 2019: Intercomparison of Small Unmanned Aircraft System (sUAS) Measurements for Atmospheric Science during the LAPSE-RATE Campaign. *Sensors*, 19 (9), 2179, doi:10.3390/s19092179.

- **Paper III:**
  Kral, S. T., J. Reuder, T. Vihma, I. Suomi, K. Flacké Haualand, G. H. Urbancic, B. R. Greene, G.-J. Steeneveld, T. Lorenz, B. Maronga, M. O. Jonassen, H. Ajosenpää, L. Båserud, P. B. Chilson, A. A. M. Holtslag, A. D. Jenkins, R. Kouznetsov, S. Mayer, E. A. Pillar-Little, A. Rautenberg, J. Schwenkel, A. Seidl and B. Wrenger, 2020: The Innovative Strategies for Observations in the Arctic Atmospheric Boundary Layer Project (ISOBAR) — Unique fine-scale observations under stable and very stable conditions. *Bull. Amer. Meteor. Soc.*, doi:10.1175/BAMS-D-19-0212.1.

- **Paper IV:**
  Rautenberg, A., M. Schön, K. zum Berge, M. Mauz, P. Manz, A. Platis, B. van Kesteren, I. Suomi, S. T. Kral, and J. Bange, 2019: The Multi-Purpose Airborne Sensor Carrier MASC-3 for Wind and Turbulence Measurements in the Atmospheric Boundary Layer. *Sensors*, 19 (10), 2292, doi:10.3390/s19102292.

- **Paper V:**
  Greene, B. R., S. T. Kral, P. B. Chilson and J. Reuder, 2020: Gradient-based turbulence estimates from multicopter profiles of the stable boundary layer during ISOBAR18. In preparation for *Bound.-Layer Meteor.*.

The experimental data presented in Paper I and Paper III were collected during the two ISOBAR measurement campaigns on Hailuoto (ISOBAR17 and ISOBAR18) for

which I had the main responsibility for the planning, execution and coordination of all data sampling. My specific focus during the planning of these campaigns was dedicated to the identification of existing shortcomings in previous observational studies, and the attempt to overcome those by combining fixed- and rotary-wing UAS measurements with classical ground-based in-situ and remote-sensing technology. For these papers I had the main responsibility for the bulk of the data analysis, the writing and the general layout. To Paper II the first author Lindsay Barbieri and I contributed equally, with me leading the data analysis but also contributing substantially to the writing and Lindsay being in charge of coordinating the writing of the manuscript and the correspondence with the editors of the journal. The data sampling for this paper was carried out by the collaborators and was coordinated and supervised by Lindsay and me. My contribution to Paper IV was the sampling of the ground-based reference data during ISOBAR18, as well as the analysis and interpretation of this data, in particular with respect to non-stationarity and its implications on the corresponding UAS profiles of mean wind and turbulence quantities. The concept for Paper V is based on ideas I originally developed together with Zbigniew Sorbjan and Joachim Reuder, and then further evolved during the ISOBAR18 campaign and the following meetings with Brian Greene and Phil Chilson. The bulk of the analysis and the writing of the manuscript has been done by Brian Greene. In addition to my leading role in the ISOBAR18 campaign, I contributed to methodology, analysis, and interpretation of the presented data and results, in particular with respect to the SBL depth as a limiting factor for the applicability of this method. Furthermore, I contributed general structure and the writing of several sections of the manuscript.

Additional papers

In addition to the manuscripts listed above to be evaluated for my PhD thesis, I have (co-)authored several other peer-reviewed publications on related topics:

- de Boer, G., C. Diehl, J. Jacob, A. Houston, S. W. Smith, P. Chilson, D. G. Schmale, J. Intrieri, J. Pinto, J. Elston, D. Brus, O. Kemppinen, A. Clark, D. Lawrence, S. C. C. Bailey, M. P. Sama, A. Frazier, C. Crick, V. Natalie, E. Pillar-Little, P. Klein, S. Waugh, J. K. Lundquist, L. Barbieri, **S. T. Kral**, A. A. Jensen, C. Dixon, S. Borenstein, D. Hesselius, K. Human, P. Hall, B. Argrow, T. Thornberry, R. Wright, and J. T. Kelly, 2019: Development of community, capabilities and understanding through unmanned aircraft-based atmospheric research: The LAPSE-RATE campaign. *Bull. Amer. Meteor. Soc.*, doi:10.1175/bams-d-19-0050.1.

- Hackerott, J. A., M. Bakhoday Paskyabi, J. Reuder, A. P. de Oliveira, **S. T. Kral**, E. P. Marques Filho, M. dos Santos Mesquita, and R. de Camargo, 2017: A Surface-Layer Study of the Transport and Dissipation of Turbulent Kinetic Energy and the Variances of Temperature, Humidity and CO_2. *Bound.-Layer Meteor.*, 165, 211-231, doi:10.1007/s10546-017-0271-0.

- Båserud, L., J. Reuder, M. O. Jonassen, **S. T. Kral**, M. Bakhoday Paskyabi, and M. Lothon, 2016: Proof of concept for turbulence measurements with the RPAS

SUMO during the BLLAST campaign. *Atmos. Meas. Tech.*, 9, 4901–4913, doi:10.5194/amt-9-4901-2016.

- Reuder, J., L. Båserud, M. O. Jonassen, **S. T. Kral**, and M. Müller, 2016: Exploring the potential of the RPA system SUMO for multipurpose boundary-layer missions during the BLLAST campaign. *Atmos. Meas. Tech.*, 9, 2675–2688, doi:10.5194/amt-9-2675-2016.

- Reuder, J., L. Båserud, **S. Kral**, V. Kumer, J. W. Wagenaar, and A. Knauer, 2016: Proof of Concept for Wind Turbine Wake Investigations with the RPAS SUMO. *Energy Procedia*, 94, 452–461, http://doi.org/10.1016/j.egypro.2016.09. 215.

- **Kral, S. T.**, A. Sjöblom, and T. Nygård, 2014: Observations of summer turbulent surface fluxes in a High Arctic fjord. *Quart. J. Roy. Meteor. Soc.*, 140, 666–675, doi:10.1002/qj.2167.

Contents

1 Introduction

The atmospheric boundary layer (ABL) has been studied intensely for more then half a century. Yet, the progress of understanding the stable boundary layer (SBL) is lacking far behind its unstable counterpart, the convective boundary layer (Fernando and Weil, 2010). This lack of understanding manifests itself in the rather limited ability to predict SBL conditions by numerical weather prediction (NWP) or climate models (Holtslag et al., 2013). For NWP, this is demonstrated by large errors under clear-sky and weak-wind nighttime conditions, where surface temperature biases in the order of $10\,\mathrm{K}$ are common, even in short-term (24-h) NWP products (e.g., Atlaskin and Vihma, 2012). Apart from the surface temperature, other key variables, such as the boundary-layer depth and wind speed are also subject to biases in NWP, as well as in climate models.

The SBL is of high relevance for a wide range of practical applications with direct impact on our society. Accurate near-surface frost forecasts are, for example, important for road de-icing (Karsisto et al., 2017) or in agriculture for plant and yield protection. Also, the forecast of fog and haze (Román-Cascón et al., 2019) or air quality (Fernando and Weil, 2010) critically depends on reliable estimates of stratification, wind speed, turbulence intensity and boundary-layer depth. The wind energy sector requires reliable forecasts, for the estimation of the energy production (e.g., Martin et al., 2017) and turbine loads (e.g., Sathe et al., 2012). The SBL poses substantial challenges here, as it is often characterized by strong wind shear and turbine wakes that propagate over long distances (Dörenkämper et al., 2015).

A better understanding of the governing physical processes within the SBL is also crucial with respect to the role of polar regions in a changing climate. The observed temperature increase during the last decades is most pronounced at night and in polar regions (e.g., Vose et al., 2005; McNider et al., 2010). Esau et al. (2012) showed that the strongest warming occurs in areas with shallow boundary layers and hypothesize that the observed polar amplification may be partly attributed to the limited effective heat capacity of the SBL, resulting from its low boundary-layer depth and strong stable stratification. In addition, the vertical resolution of numerical models is often too coarse for an appropriate representation of very shallow SBLs (Byrkjedal et al., 2007).

The relatively poor performance of NWP and climate models under SBL conditions is highly related to the parameterization schemes applied to represent processes on scales that can not be resolved. The SBL is characterized by numerous physical processes on a variety of scales, such as turbulence, radiation, surface coupling and heterogeneity, internal gravity waves, and other non-turbulent motions. With increasing stability the turbulence becomes very weak and the other processes gain relative importance. Their physical nature and their interactions are, however, often not clear. Overall, this indicates a general need for a better understanding of turbulence in the SBL and its interaction with other physical processes (Mahrt, 2014). Furthermore, the multiplicity of relevant processes and scales, and their complex interactions makes it difficult to develop robust SBL parametrizations for weather and climate models (Steeneveld, 2014). For decades, large-scale NWP and climate models have applied a so-called "enhanced mixing" approach (Louis, 1979), i.e., ABL parametrizations, which produce much higher turbulence dissipation than can be justified from observations. This

is done to improve the large-scale performance of the model, by improving the ability to predict the lifetime of synoptic scale weather systems. However, this approach comes at the cost of the model's performance under SBL conditions. In climate models, this may result in a positive surface temperature bias (Holtslag et al., 2013), which increases the upwelling longwave radiation (temperature feedback) and decreases the reflected shortwave radiation through enhanced snow and ice melt (albedo feedback).

Although a number of field campaigns have been dedicated to study the SBL, the observation strategies and observational capabilities were not sufficient to provide comprehensive data sets to study all relevant SBL processes. In particular data from SBL field campaigns in the Arctic and over sea-ice are sparse. Continuous observations are typically limited in the vertical by the height of meteorological masts, whereas higher vertical profiles from radio- or tethersondes only give snapshots with limited time resolution. In addition, the vertical resolution and quality of radiosdonde data is insufficient for process studies within the often very shallow SBL.

The growing availability of unmanned aircraft systems (UAS[1]) offers promising new observational strategies in the field of ABL research. The application of meteorological UAS dates back to the late 1960s (Konrad et al., 1970). During the past two decades, fixed-wing UAS have become increasingly popular for atmospheric research (Elston et al., 2015), as a direct result of the substantial progress in micro-electronics and component miniaturization. Rather recently, rotary-wing systems, mainly multicopters, gained popularity in particular for data sampling in the ABL. UAS, equipped with in-situ sensors for atmospheric measurements, are able to overcome at least parts of the shortcomings associated with the traditional ABL observation strategies. They can be operated in a flexible way, e.g., in terms of location and climb rate; can provide direct in-situ observations; can be operated in a broad range of atmospheric conditions without taking high risks; and they are recoverable. However, as UAS-based observations are still a fairly new observation technique, standard procedures and best practices for, e.g., sensor integration, sampling strategies, calibration and data post-processing procedures, have not been fully established yet.

The aim of this thesis is to apply UAS in combination with well-established observation techniques, to lay the foundation for an improved understanding of the SBL, which still poses observational and modelling challenges (e.g., Fernando and Weil, 2010; Holtslag et al., 2013; Mahrt, 2014). This requires the development of new, innovative observation strategies with the goal to supplement ground-based observations from meteorological masts and remote-sensing systems in the best possible way and to probe the SBL at high spatial and temporal resolution. Furthermore, the synthesis of observational data from different platforms needs special attention. In particular, the quality of UAS observation and their inter-comparability have not yet been assessed systematically, and there is a lack for best-practices in terms of data processing and sensor integration. This thesis has the objective to address such issues in order to provide high-quality UAS observations, to supplement traditional observation methods and to lay the foundation for future advancements in SBL research. Applying this innovative observation strategy during two field campaigns, targeting the SBL over sea ice, resulted in a data set of unprecedented spatiotemporal resolution. Based on these data, I

---

[1]In this study I exclusively focus on the class of unmanned aircraft systems with a weight limit of 25 kg and any use of the abbreviation "UAS" refers to this class of systems.

aim to demonstrate the potential of this observation strategy by investigating a number of selected case studies. In particular, I investigate the temporal evolution of the SBL structure, the formation and variability of LLJs and their interaction with surface turbulence, and the role of wave-turbulent interaction and intermittency. In addition, a first validation of a new turbulence resolving fixed-wing UAS, which has been used for the first time during ISOBAR18, is carried out. Furthermore, we apply an alternative scaling scheme for the description of turbulence in the SBL based on UAS profiles. The overall goal of the ISOBAR project in which this thesis forms the major part of the observational work packages is to contribute to better SBL parametrization schemes in NWP and climate models in the future.

2 Background

2.1 The stable atmospheric boundary layer

The atmospheric boundary layer (ABL), is clearly the part of the atmosphere, which is most important for the Earth's ecosystem, since it is in direct contact with the surface. This is where almost all exchange of heat, mass and momentum between the surface and the free atmosphere takes place. The properties of the ABL vary on time scales of about an hour or less in response to changes in the surface forcing, such as, surface roughness, transfer of moisture (through evaporation and transpiration), transfer of heat and the emission of trace gases and aerosols (Stull, 1988). Over land and at lower latitudes, the structure of the ABL is thus following a diurnal cycle resulting from differential radiative heating and cooling through the course of the day. Its thickness is typically in the order of some hundred meters, but may reach up to a few kilometers as a result of strong convection, or become as shallow as a few tens of meters under very-stable conditions. The key physical processes taking place within the ABL are the turbulent transfer of energy, momentum, and mass, which influence a broad variety of processes in the entire atmosphere. Thus, this layer cannot be regarded as an entity, isolated from the rest of the atmosphere. Some obvious examples for these physical processes are the slowing of cyclones when entering land from the ocean, or the rapid modification of maritime air masses moving over Arctic areas.

A stable atmospheric boundary layer (SBL) commonly forms under clear-sky conditions in absence of incoming (downwelling) solar radiation, as a result from a negative radiation balance dominated by the upwelling long-wave radiation (e.g., Mahrt, 2014). Such conditions are typically found during night time at lower latitudes and during winter in polar regions. However, the formation of an SBL may also result from synoptic situations with warm air advection over a colder surface, as frequently observed over ocean and sea surfaces. Both clear-sky radiative cooling and warm air advection, lead to the formation of a stable stratification, i.e., a positive vertical potential temperature gradient, which suppresses turbulence and vertical exchange processes. Whereas stable stratification is a common feature of the nocturnal boundary layer at lower latitudes, the wintertime SBL in polar regions often prevails for several days or even weeks. Such a long-lived SBL is, in contrast to the nocturnal SBL, not topped by a neutrally stratified residual layer remaining from day time convective mixing. Instead it is directly linked to the free atmosphere above.

2.2 Relevant SBL processes

The flow in the ABL is generally turbulent, consisting of three-dimensional chaotic motions on time scales spanning over several orders of magnitude, from fractions of seconds up to an hour and corresponding length scales from millimeters to the height of the boundary layer (kilometers) (Holtslag et al., 2013). Turbulence is generally strongest in the ABL, but significant turbulence may also be present higher up in the atmosphere, e.g., as a result of strong convection, wind shear or atmospheric instabilities. The tur-

bulent diffusion of heat, momentum and matter is several orders of magnitude more efficient than molecular diffusion. Turbulence in the unstable or convective boundary layer is generally be generated through convection, i.e., solar surface heating creates thermal instability, and through wind shear due to friction. In contrast, in the SBL the stable stratification suppresses vertical motions and turbulence is only produced mechanically. In addition to viscous dissipation of the smallest turbulent scales the effects of buoyancy also contribute to the destruction of turbulence. As a result, the turbulent state of the SBL is very sensitive to changes in the mean profiles of wind and temperature.

Any layer of the atmosphere absorbs and emits long-wave radiation depending on its temperature and the concentration of absorbing gases (e.g., water vapor). With strong vertical temperature, and even more important, humidity gradients, this may result in significant radiation divergence. E.g., Hoch et al. (2007) and Steeneveld et al. (2010) observed heating rates of several $\mathrm{K\,h^{-1}}$ in the SBL. Under such condition radiation divergence may become very important for the thermodynamic evolution of the SBL.

A low-level jet (LLJ), a local wind maximum in the lowermost few hundred meters of the atmosphere, is a common feature of the SBL and may act as an elevated source of turbulence, in addition to wind shear caused by surface friction. It typically occurs in a thin layer at the top of the SBL and can be generated by various mechanisms, including inertial oscillations, related to spatial or temporal variation in surface friction (Andreas et al., 2000); baroclinicity, due to inhomogeneities in the horizontal temperature field (Guest et al., 2018); drainage and katabatic flows (Renfrew and Anderson, 2006), often detaching from the surface when reaching a certain altitude (Vihma et al., 2011); directional shear; or barrier flows (Petersen et al., 2009).

Due to its stable stratification the SBL allows for the propagation of internal gravity waves (Nappo, 2012). Gravity waves may be generated by various processes such as the flow over topography, sudden changes in surface roughness and convection. They are often of stationary behavior (standing wave). In general, linear gravity waves are able to transport momentum but not heat. However, when becoming unstable they may cause significant turbulence contributing to both the momentum and heat flux (Nappo et al., 2014; Sun et al., 2015).

Strong surface cooling may trigger the formation of radiation fog when saturation is reached. In addition to the latent heat release associated with condensation, this implies also a modification of the radiative properties of the SBL. Long-wave radiative cooling becomes most relevant at the top of the fog layer and thus starting a mixing process below, shifting the vertical temperature profile towards a moist adiabatic lapse rate. In polar regions, fog may also occur as sea smoke in the vicinity of open water.

If the SBL is reaching a very-stable state, typically associated with clear-sky conditions, weak winds and turbulence, other types of motion, so-called submeso motions, with horizontal length scales of less than a few kilometers (Belušić and Mahrt, 2008; Mahrt, 2009) may become important. In contrast to turbulence, which is fully three dimensional, including vortex stretching and diffusion, submeso motions are of two-dimensional character and only contribute to diffusion indirectly by generation of turbulence. Such motions include, e.g., microfronts (Lang et al., 2018; Mahrt, 2019), wave-like phenomena (Fritts et al., 2003), solitary modes (Rees et al., 1998; Anderson, 2003; Mahrt, 2010), and meandering motions (Cava et al., 2019a). Microfronts can be observed as a result of different air masses being advected. They are typically charac-

terized by sharp changes in temperature and shifting wind directions. Even small heterogeneities in the surface properties, topography or scattered cloud cover may result in the formation of shallow air masses with very different properties (internal boundary layers). Wave-like motions in the very-stable boundary layer (VSBL) typically occur with only a few periods, whereas they are more persistent at higher levels. Although solitary modes can commonly be observed in the VSBL, typically as wave events with a single or two cycles, their origin remains unclear (Rees et al., 1998; Mahrt, 2014).

One of the most challenging features of the VSBL is the intermittency of the turbulent flow. Intermittency refers to highly variable turbulence, which is typically characterized by periods with very-weak turbulence (often below the detection limit of meteorological instruments) and episodic events with enhanced turbulence (e.g., Sun et al., 2012; Mahrt, 2014). This typically corresponds to large areas with very weak and small patches with stronger turbulence. Its importance is highlighted by the fact that the main fraction of the total turbulent fluxes over a certain time period may be caused by few short events of enhanced turbulence (Yagüe et al., 2006). Turbulent quantities, such as turbulent kinetic energy or dissipation, typically vary by orders of magnitude, which implies rapid changes of the meteorological properties of the VSBL.

As identified by previous studies, intermittency may result from a number of different physical processes frequently occurring in the SBL. These processes include downward bursting of turbulence (Nappo, 1991); shear instabilities, often associated with the variability of a LLJ (Mahrt and Vickers, 2002); pressure gradient-based turbulence (Holdsworth and Monahan, 2019); drainage flows; and downward propagating wave instabilities (Blumen et al., 2001; Sun et al., 2012). In addition, intermittency is often produced by submeso motions whose timescale is not large compared to the turbulent adjustment timescale. This means that the properties of the mean flow, such as the vertical wind shear, may change before they are in balance with the turbulence they generate. As a consequence the turbulence cannot maintain equilibrium with such motions and may become intermittent (Conangla et al., 2008; Mahrt, 2009; Mahrt et al., 2012; Sun et al., 2012; Mahrt, 2014; Zhou and Chow, 2014; Sun et al., 2015).

2.3 Theory and classification

Monin and Obukhov (1954) developed a theory for atmospheric turbulence within the ABL, which links the turbulent fluxes of, e.g., momentum and sensible heat to the vertical gradients of their respective meteorological parameters, e.g., wind speed and temperature, as a function of the height above the surface, z and the Obukhov Length, L, (Obukhov, 1946, 1971). The non-dimensional vertical gradients of mean wind speed, U, and potential temperature, θ, are expressed as:

$$\phi_m\left(\frac{z}{L}\right) = \frac{\kappa z}{u_*}\frac{\partial \mathbf{U}}{\partial z}, \tag{2.1a}$$

$$\phi_h\left(\frac{z}{L}\right) = \frac{\kappa z}{\theta_*}\frac{\partial \theta}{\partial z}, \tag{2.1b}$$

with

$$u_* = \left(\overline{u'w'}^2 + \overline{v'w'}^2 \right)^{1/4}, \tag{2.2a}$$

$$\theta_* = \frac{\overline{w'\theta_v'}}{u_*}, \tag{2.2b}$$

$$L = -\frac{u_*^3 \theta_v}{g \kappa \overline{w'\theta_v'}}, \tag{2.2c}$$

$$\frac{z}{L} = -\frac{zg \kappa \overline{w'\theta_v'}}{u_*^3 \theta_v}, \tag{2.2d}$$

$$\kappa = 0.40. \tag{2.2e}$$

In this traditional formulation of the so-called Monin–Obukhov Similarity Theory (MOST, a.k.a. surface-scaling theory) the scaling parameters, i.e., u_*, θ_* and L, are determined at the surface (i.e., the lowest measurement level). Gradients and (co)variances can be determined from tower and eddy-covariance (EC) measurements, respectively.

The MOST may still be considered as the foundation of our current understanding of the ABL. However, its validity is limited to the Surface Layer (SL), roughly the lowermost 10 % of the ABL, where turbulent fluxes can be considered as constant with height, and to homogeneous surface conditions (see, e.g., Foken, 2006). According to Grachev et al. (2005), the constant-flux assumption underlying the original MOST, is reasonably accurate for stable conditions only in the range $0 < z/L < 0.1$.

The universal functions describing the relationship between the vertical gradients and the corresponding fluxes have to be determined experimentally and numerous functions have been proposed during the years. At present, the most commonly used similarity functions are the Businger–Dyer relationship (Businger et al., 1971), which are based on the Kansas-experiment in 1968. Their current form is based on a re-evaluation by Högström (1988), who considered some important sensor issues and applied an updated value of the von-Kármán constant of $\kappa = 0.40$ to a number of common similarity formulations. For the SBL the Businger–Dyer formulations are only defined in the stability range $0 \leq \frac{z}{L} \leq 0.5$ as

$$\phi_m = 1 + 6\frac{z}{L}, \tag{2.3a}$$

$$\phi_h = 0.95 + 7.8\frac{z}{L}. \tag{2.3b}$$

However, there is still debate about the exact shape of the universal functions and scaling relationships diverge between proposed formulations with increasing stability (Foken, 2006).

Several studies have proposed definitions for different regimes in order to classify the turbulent characteristics of the SBL. Basically all of them distinguish between a "weakly-stable" boundary layer (WSBL) and a "very-stable" boundary layer (VSBL) regime, but they show differences in terms of the parameters and thresholds used for their definition, or may include additional (sub-)regimes.

In general, the WSBL regime is characterized by well-established turbulence. The local scaling scheme, a modification of the surface scaling similarity theory (i.e.,

MOST) in which the local turbulent fluxes are related to the local gradients (Nieuw-stadt, 1984; Holtslag and Nieuwstadt, 1986; Sorbjan, 1989), can be applied. In this scaling scheme the local stability parameter

$$\Lambda(z) = -\left.\frac{u_*^3 \theta_v}{g \kappa \overline{w' \theta_v'}}\right|_z \tag{2.4}$$

is used instead of the Obukhov Length, L (2.2c).

In the VSBL regime, turbulence is generally very weak or intermittent (e.g., Maurit-sen and Svensson, 2007) and a satisfactory scaling relating the thermodynamic profiles and the turbulent fluxes is lacking. Under such conditions, processes of often non-local nature, such as, drainage flows; internal gravity waves (Sun et al., 2015); the Coriolis force (Grachev et al., 2005); low-level jets (Banta et al., 2003, 2006; Banta, 2008; Cava et al., 2019b); radiation divergence (Hoch et al., 2007; Steeneveld et al., 2010); sub-meso motions (Acevedo et al., 2014), including microfronts (Lang et al., 2018; Mahrt, 2019) may become important. Some authors define an additional transition regime in which the magnitude of the sensible heat flux is decreasing with increasing stabil-ity (Mahrt, 1998). Grachev et al. (2005) define the transition regime as where local scaling outperforms traditional MOST. They also propose an additional Ekman scaling regime in which the near-surface turbulence is significantly influenced by the Corio-lis force. The VSBL regime may be subdivided into an intermittent and a radiation (extremely-stable) regime in which the turbulent heat flux is so weak that the surface energy balance is dominated by the balance between the upwelling long-wave radiation and the ground heat flux (van de Wiel et al., 2003). Recently, Pfister et al. (2019) pro-posed a classification scheme for the nocturnal boundary layer based on static stability, wind regime and radiative forcing.

Most published similarity functions have in common that they are not well-defined beyond the WSBL regime (Foken, 2008). In the VSBL regime, i.e., for $z/\Lambda > 1$, verti-cal motions are inhibited by the strong stratification and the turbulence is no longer sig-nificantly influenced by the surface (e.g., Monin and Yaglom, 1971). Under such con-ditions, MOST predicts that turbulence quantities become independent of z (Obukhov, 1946; Monin and Obukhov, 1954), which implies that the similarity functions, ϕ, have to approach a constant value for $z/\Lambda \gg 1$ (Foken, 2008). Zilitinkevich and Calanca (2000) propose an extension of MOST for the SBL, with the free-flow static stability, i.e., the Brunt–Väisälä frequency, N, as an additional scaling parameter. This theory has been extended by including the effects of the Coriolis force (Zilitinkevich and Esau, 2005), which can reach the same order of magnitude as the surface stress in the very-stable regime (Grachev et al., 2005). Two of the major shortcomings of MOST (or its local scaling formulation) in the SBL are related to self-correlation in the formulation of the non-dimensional momentum flux (Baas et al., 2006), and the fact that turbulent fluxes are generally very weak and therefore hard to measure.

Sorbjan (2010) presents alternative gradient-based scaling schemes, which are for-mally equivalent to MOST, employing the Richardson number,

$$\mathrm{Ri} = \frac{g}{T_0} \frac{\partial \theta / \partial z}{(\partial / \partial z)^2}, \tag{2.5}$$

as stability parameter to overcome the two above mentioned shortcomings of MOST.

Their so-called gradient-based master scaling relies on the three scaling parameters

$$U_s = \kappa \, z \, N, \tag{2.6a}$$

$$T_s = \kappa \, z \, \Gamma, \tag{2.6b}$$

$$L_s = \kappa \, z, \tag{2.6c}$$

with the Brunt–Väisälä frequency $N = \sqrt{\beta \Gamma}$, the buoyancy parameter $\beta = g/T_0$ and the vertical potential temperature gradient Γ. Applying the above scaling results in the non-dimensional functions

$$G_m(\text{Ri}) = \frac{u_*^2}{U_s^2}, \tag{2.7a}$$

$$G_h(\text{Ri}) = -\frac{\overline{w'\theta'}}{U_s \, T_s} \tag{2.7b}$$

$$G_w(\text{Ri}) = \frac{\sigma_w}{U_s}, \tag{2.7c}$$

$$G_\theta(\text{Ri}) = \frac{\sigma_\theta}{T_s}, \tag{2.7d}$$

similar to (2.3) and with σ_w and σ_θ denoting the standard deviation of the vertical wind and potential temperature, respectively. The shape of these functions can be directly converted from classical universal MOST functions or vice versa. Based on SHEBA and CASES-99 data, Sorbjan and Grachev (2010) and Sorbjan (2010) propose the following definitions:

$$G_m = \frac{1}{\text{Ri}(1 + 300\text{Ri}^2)^{3/2}}, \tag{2.8a}$$

$$G_h = \frac{1}{0.9\text{Ri}^{1/2}(1 + 250\text{Ri}^2)^{3/2}}, \tag{2.8b}$$

$$G_w = \frac{1}{0.85\text{Ri}^{1/2}(1 + 450\text{Ri}^2)^{1/2}}, \tag{2.8c}$$

$$G_\theta = \frac{5}{(1 + 2500\text{Ri}^2)^{1/2}}. \tag{2.8d}$$

Once the empirical formulations (2.8) are known, it is possible to determine the turbulence variables in (2.7) from the corresponding scaling parameters, $\{z, \Gamma, \beta\}$, and the Richardson number, Ri All these variable can be determined from vertical profile measurements. Since these equations involve the scaling parameter z, it is, however, important that the application of this method is limited to the depth of the SBL, where there is a direct coupling between the atmosphere and the underlying surface.

2.4 SBL campaigns and observation strategies

A number of field experiments dedicated to the SBL have been carried out during the last decades, providing a wealth of observational data. Most of them do, however, target the nocturnal SBL at mid-latitudes over rather flat grasslands (e.g., CASES-99, Poulos

et al., 2002), in hilly terrain (e.g., SABLES 98, Cuxart et al., 2000), or in the vicinity of mountains (e.g., MATERHORN, Fernando et al., 2015). Data on the polar SBL, in particular over sea-ice covered regions, origins only from a handful of campaigns of which the "Surface Heat Budget of the Arctic Ocean (SHEBA)" experiment (Persson et al., 2002; Uttal et al., 2002; Grachev et al., 2008) can be regarded as the most important one. In the context of major field campaigns in the Arctic Ocean one should also mention the Soviet and Russian "North-Pole" drift stations with overall 40 drifts between 1937 and 2013. Unfortunately the data from these campaigns has not yet been made publicly available. Other major campaigns with focus on the SBL over sea ice include the Tara drift station in the central Arctic during spring and summer 2007 (Vihma et al., 2008), the N-ICE2015 drifting station north of Svalbard in the winter and spring 2015 (Cohen et al., 2017), and the Weddell ice station in the Austral autumn and winter 1992 (Andreas and Claffey, 1995; Andreas et al., 2005). Observations over the Antarctic ice shelf also form valuable data bases for SBL studies (e.g., Anderson, 2003, 2009; Vignon et al., 2017, 2018; Cava et al., 2019a).

Traditionally, observation strategies for ABL studies rely on a variety of observations systems. In-situ observations of the basic meteorological and turbulence parameters are typically observed continuously from weather masts, or at certain time intervals from tethersondes or radiosonde ascents. In addition, the basic meteorological parameters can also be sensed remotely by, e.g., light detection and ranging (lidar), sonic detection and ranging (sodar) or passive microwave radiometer systems. Such methods typically provide continuous time series of wind, temperature and humidity profiles. All these measurement methods and devices have certain shortcomings, e.g., weather masts are limited in height, tethersondes require considerable infrastructure and their operation is often limited by the wind speed (Palo et al., 2017). Radiosondes only provide snapshots of vertical SBL profiles in relatively poor temporal resolution and the sensor packages are typically lost. Doppler lidars and sodars provide wind information with a vertical resolution in the order of $5\,m$ to $20\,m$, typically in the lowest few hundred meters above the ground. However, their performance largely depends on the atmospheric properties, i.e., the backscattering of electromagnetic waves by aerosols, and of sound waves by density inhomogeneities caused by turbulence or temperature inversions, respectively. Furthermore, the lowest measurement level of such systems is often in the order of $40\,m$. Microwave radiometers measure atmospheric brightness temperatures at certain wavelengths, e.g., in the range of the absorption band of O_2 and H_2O from which atmospheric temperature and humidity profiles can be retrieved. However, the applied retrievals are not trivial and the resulting profiles may be rather smooth. Overall, traditional methods for profiling the lower atmosphere beyond the vertical range of meteorological masts are not sufficient to give a satisfactory picture on the state of the SBL and its evolution, limiting the insight in the governing processes.

2.5 UAS in atmospheric research

During the past two decades, a number of ABL campaigns made use of UAS for the sampling of kinematic and thermodynamic atmospheric data (e.g., van den Kroonenberg et al., 2008; Houston et al., 2012; Reuder et al., 2012b; Bonin et al., 2013; Lothon et al., 2014; Reuder et al., 2016a). Several UAS models have also been operated in po-

lar regions, providing data that have been used for process studies (Curry et al., 2004; Cassano et al., 2010; Cassano, 2013; Knuth and Cassano, 2014; Jonassen et al., 2015), meso-scale model validation (Mayer et al., 2012b,c) and the evaluation of the benefit of UAS data assimilation (Jonassen et al., 2012). The above mentioned studies made use of fixed-wing UAS, whose specifications, such as, takeoff weight, sensor payload an flight capabilities, cover a broad range. Rather recently, rotary-wing (mostly multi-copter) UAS have gained increasing popularity (e.g., Neumann and Bartholmai, 2015; Palomaki et al., 2017; Wrenger and Cuxart, 2017).

In general, there is a large variety of different sensor–platform integration solutions used by the UAS-based atmospheric research community. Larger systems allow for the integration of sensor packages designed for high-quality meteorological observations, as typically used on meteorological masts or radiosondes. The payload limitations of smaller systems, however, require more light-weight solutions, which are often custom-built. In both cases, the integration into a moving measurement platform and the underlying sampling strategy may affect the quality of the observations made. So far, only simple validation experiments have been carried out, typically comparing one individual UAS against reference systems, such as meteorological masts (e.g., van den Kroonenberg et al., 2008; Wildmann et al., 2014a; Neumann and Bartholmai, 2015; Palomaki et al., 2017), tethersondes (e.g., Mayer et al., 2012b), radiosondes (e.g., Reuder et al., 2009; Jonassen et al., 2015) or remote-sensing systems (e.g., Spiess et al., 2007; van den Kroonenberg et al., 2008; Wildmann et al., 2014a).

UAS sampling strategies differ considerable depending on the UAS capabilities and the atmospheric phenomena of interest. While multicopter systems can hover and ascend or descend vertically over a fixed location, fixed-wing systems have to operate within a certain airspeed range to stay airborne. Fixed-wing UAS are therefore typically operated along straight horizontal flight paths for turbulence sampling (e.g., Wildmann et al., 2014a, 2015; Reuder et al., 2016a,b; Båserud et al., 2016) or helical flight paths for vertical profiling (e.g., Reuder et al., 2016a; Båserud et al., 2019). Vertical profiles are often also realized by horizontal straight or circular flights at various altitude levels (e.g., Wildmann et al., 2015). Multicopter UAS typically perform flight maneuvers, such as hovering at a fixed altitude or vertical profiling, while in both cases maintaining a horizontally fixed location. Moreover, they can also be operated on flight paths similar to the ones typical for fixed-wing systems. The repetition rate of UAS flights crucially depends on the flight preparation time and the reliability of the system. Smaller UAS of limited complexity, such as the SUMO (Reuder et al., 2012a), can thus be operated with very short down-time in a semi-continuous manner.

A high fraction of the studies involving UAS for atmospheric data sampling have focused on the demonstration of the systems and their validation. Only during a few campaigns UAS have been operated as an integral component of a broader observation strategy (e.g., Lothon et al., 2014). Furthermore, the issues of (inter)comparability and UAS data quality have only been addressed superficially.

3 Main objectives and research questions

The SBL is subject to a myriad of different physical processes and their complex interactions, which are not well understood (Section 2.2). It is commonly accepted that this lack of understanding is reflected by shortcomings in current parameterizations of the SBL in NWP and climate models. Since numerous meteorological applications are negatively affected by this issue, there is an urging need for advances in this field of research. Traditional ABL observation methods have specific limitations, hampering a better understanding of the SBL, which is often highly non-stationary and subject to inhomogeneities. Micrometeorological masts are, once deployed, rather inflexible with respect to siting, and often too low to capture the entire ABL depth and the layers above that may interact with the ABL. Boundary layer remote-sensing methods are typically limited in their spatial resolution, as the derived quantities are volume averages, their derivation is often based on certain assumptions, and the quality of the observation depends on physical properties of the atmosphere. Radiosondes can only provide a snapshot of the atmospheric state and a sufficiently high repetition rate of ascents is not feasible. Typical ascent rates in the order of $5\,\mathrm{m\,s}^{-1}$ result also in very few data points within a shallow SBL, which might in addition be compromised by handling induced sensor biases during the first seconds after release.

The recent availability of UAS, equipped with meteorological sensors, offers a new promising tool for substantial advancements in the field of SBL research. For example, turbulence resolving fixed-wing UAS, can sample turbulence spatially, which is thought to be superior to fixed-point time series observations, since it is less prone to non-stationarity of the flow. Vertical ascending and descending multicopters can provide in-situ profiles of the entire ABL and beyond, and close the observational gap between the highest mast and lowest remote-sensing or radiosonde levels. Frequently repeated UAS profiles also enhance the temporal resolution of these boundary layer profiles. Fixed-wing UAS can reach much higher altitudes than multicopters and can thus also provide tropospheric profiles, similar to radiosondes, but with superior vertical resolution and higher repetition rates. Although this new observation technique offers a great potential, its application requires some careful considerations to make the best possible use of it. To assure a high data quality, I therefore consider the characterisation of the sensor–platform systems, in terms of accuracy, precision and sensor response, as essential. Before the start of this PhD project, and in particular the ISOBAR and LAPSE-RATE campaigns, UAS in atmospheric research have been used rather stand-alone and not as one component in a broader observation strategy. Furthermore, only very limited efforts have been made to characterize sensor–platform integration solutions and asses the quality of UAS based meteorological observations. In ABL research, UAS sampled data are most valuable when supplementing other micrometeorological measurement systems. Thus, new observation strategies have to be developed for micrometeorological experiments, making use of a variety of different observation systems. Such observations strategies, of course, have to be adapted with respect to the specific research questions to be addressed, but also additional factors as the availability of systems and manpower, the existing regulations, as well as safety and logistical considerations.

Based on the above mentioned shortcomings of traditional observation methods and the potential of UAS in the field of ABL research, I formulate the main hypothesis for this thesis:

> An appropriate characterization of the SBL is hampered by the lack of observations at a sufficient spatiotemporal resolution, which cannot be achieved by classical state-of-the-art instrumentation alone. High quality UAS data, sampled horizontally and vertically with high repetition rates, has the potential to close this observational gap.

Thus, the aim of this PhD thesis is to explore the potential of UAS within the field of SBL research by generating best-practices to assure the quality and (inter)-comparability of UAS sampled data, by developing observation strategies to best supplement ground-based in-situ and remote-sensing boundary layer observation techniques, and finally to demonstrate the value of this approach by investigating different SBL phenomena. In order to illuminate on the knowledge needs identified above, I formulate the following research questions, which guide the scientific work addressed in the five manuscripts of this thesis:

RQ-1 How can ground-based SBL observations from micrometeorological masts and remote-sensing systems be best supplemented by vertical UAS profiles?

    (a) What are the optimal UAS observation strategies?
    (b) What data procedures are required to achieve a high data quality?

RQ-2 What is the quality of observations on the basic meteorological parameters based on small UAS?

    (a) What is the accuracy, precision and inter-comparability of UAS observations on air temperature, humidity, pressure and wind?
    (b) How does the sensor response affect the observed temperature and humidity profiles?
    (c) What flight patterns and data processing methods are required to enable robust comparison results?
    (d) How are differences in the performance related to the UAS design, the sensor type or sensor integration measures?
    (e) Can general conclusions in terms of recommendations and best-practices be drawn?

RQ-3 How does the structure and evolution of the SBL depend on the synoptic conditions and how do various processes interact?

    (a) How, do vertical profiles of the SBL evolve under conditions with strong surface cooling?
    (b) Is there observational evidence for fine-scale instabilities within the otherwise VSBL with strong temperature inversions?
    (c) How do non-turbulent motions like LLJ and wave-like motions trigger enhanced turbulence near the surface in the SBL?
    (d) Can vertical profiles of Ri give further insight in the development of wave instabilities?

RQ-4 Can wind speed, direction and mechanical turbulence be observed reliably from a current state-of-the-art fixed-wing UAS in the SBL?

    (a) How do turbulence and mean wind observations from UAS observations sampled along straight horizontal trajectories and fixed-point EC observations at the same observation height compare against each other?

    (b) Which factors limit the comparability of spatial UAS-based and temporal fixed-point turbulence observations?

    (c) How well do horizontal profiles of wind speed, sampled along straight horizontal trajectories at several different heights compare to corresponding mean sodar wind profiles under WSBL conditions with moderate winds?

    (d) How does non-stationarity affect UAS profiles of the mean wind and turbulence variables?

RQ-5 Can gradient-based similarity formulations for the SBL be applied to UAS profiles of wind and temperature in order to estimate turbulence profiles beyond the height of micrometeorological masts?

    (a) Do the ISOBAR18 observations from the 10-m mast collapse to common functions of Ri?

    (b) Does the application of these formulations to UAS data yield reasonable flux and turbulence profiles under different SBL conditions?

    (c) What considerations are necessary for a reliable application of this approach?

The research questions above are addressed by the five papers in the following way. Paper I: RQ-1 and RQ-3; Paper II: RQ-2; Paper III: RQ-1 and RQ-3; Paper IV: RQ-4; Paper V: RQ-5.

4 Field campaigns

As an integral part of this PhD thesis I participated in four field campaigns between November 2016 and July 2018. For the three campaigns directly linked to the ISOBAR project, I had the main responsibility for the scientific planning, organization and execution.

4.1 Test and Validation Campaign, Andøya 2016

The first ISOBAR campaign was carried out from 30 Nov to 14 Dec 2016 on Andøya, Norway. Our project team, consisting of 10 scientists from 3 different institutes, was hosted and supported by the Andøya Space Center (ASC) in Andenes. The main purpose of this campaign was the test and validation of different sampling strategies for our partially new UAS systems and their sensors under challenging conditions, such as low temperatures and darkness. Secondary goals were the training of partially rather inexperienced UAS operators, i.e., remote-control (RC) pilots and ground control station (GCS) operators. Flight operations took place over the coastal area at the ASC and over land at a small hobby airfield about 10 km south of ASC (Figure 4.1). One important added bonus for the success of the following campaigns ISOBAR17 and ISOBAR18 was also that the key members of the different research groups had

Figure 4.1: Satellite image of the northern part of Andøya with the two operation areas marked by circles. The bottom right inlay map shows Andøya and the Lofoten islands, the top left northern Europe, both with markers for the corresponding areas of the other maps.

the chance to get to know each other much better. Unfortunately, the weather conditions during our stay were unfavorable for UAS flights, with strong winds and heavy snow-showers, during several days. Although this limited the number of flights that could be performed during the campaign, we still managed to develop safe and efficient sampling strategies and gain experience and confidence in our systems and operation skills. Furthermore, we learned important lessons on the pitfalls of UAS operations in darkness and low temperatures, which significantly improved our performance during the two following scientific campaigns. In the preparation phase of this campaign, I contributed to the organisation, logistics and general concept. During the campaign, I was mainly in charge of the preparation and operation of our different UAS and the planning of the individual field days.
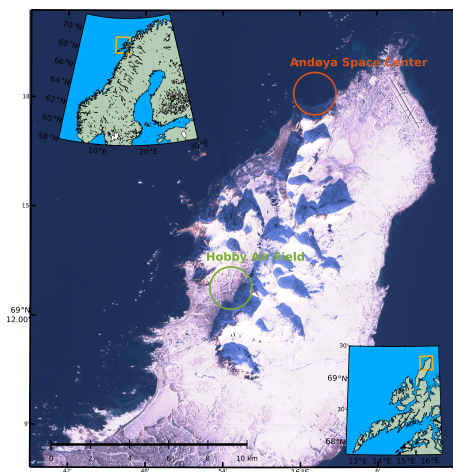
4.2 SBL campaigns over sea ice — ISOBAR17 and ISOBAR18

The two following ISOBAR campaigns, referred to as ISOBAR17 and ISOBAR18, were both carried out in the vicinity of the Finnish island of Hailuoto over the sea ice of the Bothnian Bay (Figure 4.2). This field site was chosen because of its typically good and homogeneous sea ice conditions (Uotila et al., 2015), the easy accessibility compared to the Arctic Ocean, and the comparable liberal Finnish air traffic and safety regulations with respect to UAS operations. In contrast to the Arctic Ocean, ISOBAR17 and ISOBAR18 could be realized with a fraction of the budget and significantly less logistical effort. Hailuoto (Swedish Karlö) is a $200\,\mathrm{km}^2$ large island located about 20 km to the west from the city of Oulu on the Finnish mainland. Its landscape is mostly covered by boreal forest and heath, with its highest point reaching up to 20 m asl. During the past decades, the Bothnian Bay, i.e., the northernmost part of the Baltic Sea, was typically entirely frozen every winter (Uotila et al., 2015) with up to 0.8 m thick land-fast ice near the coast of Hailuoto. The 2014/2015 winter season was the first exception in the sea ice

Figure 4.2: Satellite image of the ISOBAR field site with markers for the locations of instrumentation employed during the two campaigns in 2017 and 2018 and shaded areas indicating the typical operation areas for the different UAS. The two inlay maps at the top show Northern Europe (left) and the island of Hailuoto (right) with markers for the corresponding areas of the other maps.

climatology and a number of the following years did not show a complete sea ice cover either.

For both ISOBAR campaigns, I acted as the campaign leader. Conceptual aspects related to this role are the general campaign layout, the main goals of the campaigns, the general sampling strategy, the coordination of IOPs and UAS flights, the SUMO and Bebop2Met sampling strategy, as well as the remote-sensing scanning patterns. Organizational aspects included the UAS operation permissions and communication routines for coordination with air traffic from and to Oulu airport; logistics related to instrumentation, spare parts, tools and shipping; board, lodging and field facilities, coordination of field installation and maintenance. In terms of operational aspects I carried out most of the maintenance and repairs for the meteorological masts and the SUMO and Bebop2met UAS, and served as an RC pilot and pilot in command for the Bebop2Met and SUMO.
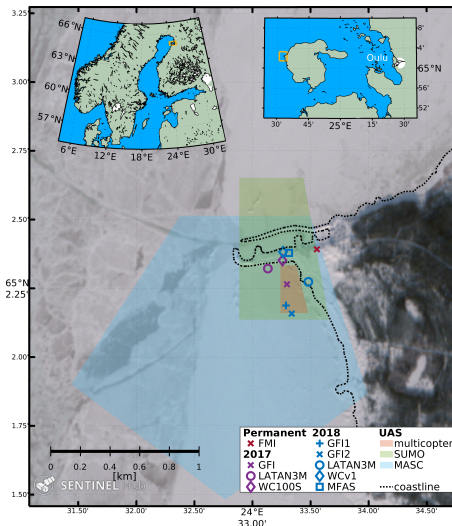
4.2.1 ISOBAR17

The first campaign on Hailuoto was car-
ried out from 11 to 27 Feb 2017 with
in total 16 participants from five dif-
ferent research institutes, i.e., the Geo-
physical Institute at the University of
Bergen (GFI), the Finnish Meteorologi-
cal Institute (FMI), the University Cen-
tre in Svalbard (UNIS), the University of
Applied Sciences and Arts Ostwestfalen-
Lippe (UOWL) and the University of
Tübingen (UT). Our field site was located
at 65.0384 °N and 24.5549 °E and con-
sisted of one 4-m mast for surface layer
observations over the sea ice. This mast
was equipped with an eddy-covariance
system; a net-radiation sensor system;
three levels with slow-response sensors
for wind speed, direction, temperature
and relative humidity; four component
net-radiation sensors; and the ground heat
flux in snow and ice.

   A WINDCUBE 100S scanning wind
lidar was operated in two different plan
position indicator (PPI) modes, one at the
lowest possible elevation angle of 1°, in
order to get an information on horizon-
tal structures of the wind field in the sur-
face layer, and a second PPI scan at a
more conventional elevation angle of 75°,

Figure 4.3: The 4-m mast during ISOBAR17.
Photo taken by S. Kral.

to provide detailed information on the vertical wind profile in addition to some infor-
mation on the horizontal structures at elevated levels. For vertical wind and attenuated
backscatter profiles of the ABL we installed a vertical-pointing sodar system (LATAN-
3M, Kouznetsov, 2009) on the sea ice close to the shore. This sodar has a very good
spatiotemporal resolution resulting in observations every 3 s from 10 m to 340 m with
10 m vertical resolution.

   In addition to these stationary and ground-based systems, our measurement strategy
largely relied on a suite of UAS for atmospheric profile measurements of temperature,
humidity, pressure, wind speed and direction, and turbulence observations along hori-
zontal, straight paths at fixed altitudes.

   The first week of the field campaign was mainly dedicated to the installation of the
ground-based measurement systems and the preparation of the UAS systems. The lat-
ter included test flights in order to tune the flight controls and calibration flights for
the meteorological sensors in the vicinity of the ground-based systems. The meteo-
rological conditions during this period were, apart from the very beginning, not very
favourable for the formation of a VSBL. During the remaining field period we con-

ducted six intensive observation periods (IOPs, see Table 4.1), although not all of them were targeting the VSBL, due to the unusual climatological conditions in Feb 2017. The most interesting IOP from this campaign is IOP 6 from the night of Feb 26 to 27, which was characterized by partially very-stable stratification and subject to a series of rapid large-amplitude temperature changes.

Table 4.1: List of IOPs during ISOBAR17, including a short description of the most important characteristics and the maximum temperature difference between the 4.0-m and 1.0-m levels, ΔT_{4m-1m}, and the corresponding lapse rate, Λ.

IOP No.	Start date time UTC	End date time UTC	Short description	No. UAS flights
1	14 Feb 2017 15:00	15 Feb 2017 06:30	near-neutral to very-stable; light to calm winds; $\Delta T_{4m-1m} = 3.8\,\mathrm{K}$ ($\Lambda = 1.3\,\mathrm{K\,m^{-1}}$)	15
2	20 Feb 2017 23:00	21 Feb 2017 06:00	near-neutral; moderate winds; $\Delta T_{4m-1m} = 0.8\,\mathrm{K}$ ($\Lambda = 0.3\,\mathrm{K\,m^{-1}}$)	13
3	21 Feb 2017 17:00	21 Feb 2017 23:00	partially very-stable; calm to light winds; $\Delta T_{4m-1m} = 6.4\,\mathrm{K}$ ($\Lambda = 2.1\,\mathrm{K\,m^{-1}}$)	9
4	25 Feb 2017 04:00	25 Feb 2017 11:00	near-neutral; moderate winds; $\Delta T_{4m-1m} = 0.5\,\mathrm{K}$ ($\Lambda = 0.2\,\mathrm{K\,m^{-1}}$)	24
5	26 Feb 2017 02:00	26 Feb 2017 07:30	near-neutral to weakly-stable; moderate winds; rapid cooling ($\sim 10\,\mathrm{K}$ in $3\,\mathrm{h}$); $\Delta T_{4m-1m} = 0.3\,\mathrm{K}$ ($\Lambda = 0.1\,\mathrm{K\,m^{-1}}$)	23
6	26 Feb 2017 14:00	27 Feb 2017 02:00	near-neutral to very-stable; light to calm winds; wave breaking (Kelvin-Helmholtz inst.); $\Delta T_{4m-1m} = 6.2\,\mathrm{K}$ ($\Lambda = 2.1\,\mathrm{K\,m^{-1}}$)	32

4.2.2 ISOBAR18

ISOBAR18 took place from 5 to 26 Feb in 2018 at the same location as ISOBAR17, but with an improved set of instrumentation and increased manpower. With an additional group from the University of Oklahoma (OU) joining our field team, the total number of participants increased to 26 with at most 19 on the field site at the same time. The most important change in instrumentation was the installation of a 10-m mast (Figure 4.4) on the sea-ice, which replaced the 4-m mast used during ISOBAR17. For the installation of in total three sonic anemometers, I reconfigured the data logger and wrote a new, updated logger program, which also provides data storage for the slow-response instrumentation at a sampling rate of 1 Hz. Apart from the two additional sonic anemometers, the instrumentation on this main mast was identical to the one used in 2017. A second smaller mast with an EC system at 2 m agl. and a net radiation sensor was installed about 65 m to the north-northwest of the 10-m mast. Instead of the scanning wind lidar, a WINDCUBE v1 profiling wind lidar was installed, which is a simpler and less powerful system designed for mea-

Figure 4.4: The 10-m mast during ISOBAR18. Photo taken by K. Flacké Haualand.

suring profiles of the horizontal wind speed up to 250 m. In addition to the vertically pointing LATAN-3M sodar we made use of a Scintec MFAS sodar providing wind profiles up to approximately 500 m. The CopterSonde (CS, Segales et al., 2020) from the OU group added another multicopter system for boundary layer profiling to our fleet of UAS. Furthermore, MASC-2 was replaced by its successor MASC-3 (Rautenberg et al., 2019). The miniTalon was not used during this campaign, but various new systems at an experimental stage were operated during the campaign for testing and development purposes.

During ISOBAR18 the meteorological and sea ice conditions were much more favourable for the formation of a VSBL. In total we carried out eight IOPs during this campaign as described in Table 4.2.

Table 4.2: List of IOPs during ISOBAR18 in 2018, including a short description of the most important characteristics and the maximum temperature difference between the 6.9-m and 0.6-m levels, $\Delta T_{6.9m-0.6m}$, and the corresponding lapse rate, Λ.

IOP No.	Start date time UTC	End date time UTC	Short description	No. UAS flights
7	10 Feb 2018 11:30	11 Feb 2018 01:00	near-neutral to weakly-stable; moderate winds; $\Delta T_{6.9m-0.6m} = 3.2\,\mathrm{K}$ ($\Lambda = 0.5\,\mathrm{K\,m^{-1}}$)	13
8	16 Feb 2018 05:00	17 Feb 2018 04:00	weakly-stable; elevated inversion$> 50\,\mathrm{m}$; LLJ; $\Delta T_{6.9m-0.6m} = 1.5\,\mathrm{K}$ ($\Lambda = 0.2\,\mathrm{K\,m^{-1}}$)	28
9	17 Feb 2018 14:00	18 Feb 2018 02:30	weakly to very-stable; light to calm winds; $\Delta T_{6.9m-0.6m} = 5.6\,\mathrm{K}$ ($\Lambda = 0.9\,\mathrm{K\,m^{-1}}$)	38
10	18 Feb 2018 13:30	19 Feb 2018 02:30	weakly to very-stable; very light to calm winds; LLJ (upside-down mixing); wave breaking; $\Delta T_{6.9m-0.6m} = 5.1\,\mathrm{K}$ ($\Lambda = 0.8\,\mathrm{K\,m^{-1}}$)	45
11	19 Feb 2018 15:00	19 Feb 2018 22:00	weakly-stable; moderate winds; LLJ; $\Delta T_{6.9m-0.6m} = 3.5\,\mathrm{K}$ ($\Lambda = 0.6\,\mathrm{K\,m^{-1}}$)	14
12	20 Feb 2018 11:00	21 Feb 2018 06:00	near-neutral to very-stable; light winds; elevated inversion $100\,\mathrm{m}$ to $180\,\mathrm{m}$; $\Delta T_{6.9m-0.6m} = 5.4\,\mathrm{K}$ ($\Lambda = 0.9\,\mathrm{K\,m^{-1}}$)	51
13	22 Feb 2018 05:00	22 Feb 2018 18:00	near-neutral to weakly stable; light winds $\Delta T_{6.9m-0.6m} = 2.1\,\mathrm{K}$ ($\Lambda = 0.3\,\mathrm{K\,m^{-1}}$)	9
14	23 Feb 2018 13:00	24 Feb 2018 06:00	weakly to very-stable; light winds; LLJ; waves; $\Delta T_{6.9m-0.6m} = 4.3\,\mathrm{K}$ ($\Lambda = 0.7\,\mathrm{K\,m^{-1}}$)	44

4.3 LAPSE-RATE campaign, San Luis Valley 2018

The "Lower Atmospheric Profiling Studies At Elevation — A Remotely Piloted Aircraft Team Experiment (LAPSE-RATE)" was initiated by representatives of the University of Colorado, the National Center for Atmospheric Research, and the National Oceanic and Atmospheric Administration, the hosts of the sixth annual meeting of the "International Society for Atmospheric Research using Remotely Piloted Aircraft (IS-ARRA)" in Boulder, 2018. The week-long campaign took place in the San Luis Valley, Colorado, from 14 to 21 July, 2018 (de Boer et al., 2019). In addition to targeting

Figure 4.5: The mobile weather mast during LAPSE-RATE 2018 with seven UAS systems hovering next to it. Photo taken by J. Reuder.

scientific themes, such as the morning boundary layer transition, deep convection initiation, aerosol properties, valley drainage flows and atmospheric turbulence profiling, the campaign also offered the opportunity to conduct the most extensive intercomparison study on UAS atmospheric measurements to date.

For the intercomparison experiment a total of 38 individual UAS performed, as far as possible, standardized flight patterns, i.e., hovering or circling next to a 18 m tall meteorological reference tower and profiling the lowermost 120 m of the atmosphere, to assess the performance of UAS-based temperature, humidity, pressure, wind speed and wind direction measurements. For this experiment I, together with Lindsay Barbieri, Gijs de Boer and Joachim Reuder, worked out the overall design of the experiment, including the definition of flight patterns, definition of a standard data format and data processing requirements. The documentation of the various sensor–platform configurations, the scheduling and coordination of flights and instructing the RC and GCS pilots was also an important part of this.

5 Methods

In this section I will outline the data sampling and processing methods employed for this thesis and the included Papers. In the first subsection I will give and overview over the instruments and observations systems we used, briefly introduce the measurement principles and discuss some of the considerations relevant for the further data processing and final interpretation of the data. The second subsection is meant to describe the data processing steps we employed to achieve a good data quality in general, and a high agreement of the different systems relative to each other.

5.1 Observation systems

5.1.1 Ground-based in-situ instrumentation

The backbone of modern micrometeorological measurement campaigns are eddy-covariance (EC) systems, i.e., fast-response sensors capable of resolving fluctuations of wind, temperature and trace gases, such as water vapor (H_2O), carbon dioxide (CO_2), and methane (CH_4), at sampling frequencies of $10\,Hz$ to $100\,Hz$, thus allowing for direct flux measurements (e.g., Lee et al., 2004; Foken, 2008). EC systems usually consist of a sonic anemometer, measuring the 3D wind vector and the sonic temperature, and additional sensors, such as, fine-wire thermocouples for temperature and optical open or closed-path gas analysers for the detection of trace gas concentrations (see Figure 5.1). 3D-sonic anemometers have three pairs of transducers, separated by a distance in the order of $10\,cm$ along
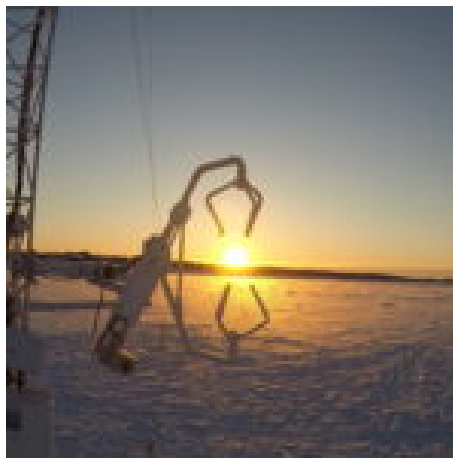
Figure 5.1: EC system consisting of a CSAT-3 and LI-7500 during ISOBAR18. Photo taken by K. Flaké Haualand.

which ultrasonic pulses are sent in alternating direction. The difference in time-of-flight along one path in opposing directions is directly related to the velocity of the air along this path. The mean time-of-flight averaged over both directions is related to the speed of sound and the so-called sonic temperature, which is very close to the virtual temperature. Coordinate transformation of the measurements from the three, often non-orthogonal, paths yields the wind vector in a Cartesian, instrument-fixed, coordinate system. Open-path infra-red gas analysers (IRGA) make use of radiative properties of specific trace gases. They typically operate with two specific wavelengths in the infra-red spectra, one strongly and one weakly affected by the trace gas of interest. By relating the absorption of these two wavelengths to each other, one can compute the concentration of the trace gas along the measurement path, which also has

a length in the order of 10 cm. The high sampling frequencies are necessary to capture a large fraction of the relevant time scales characterizing turbulent flows. During the two ISOBAR campaigns on Hailuoto (Section 4.2.1 and 4.2.2), we relied on Campbell Scientific CSAT-3[1] sonic anemometers, one of the highest quality research-grade systems available, and LI-COR LI-7500[2] open path CO_2/H_2O gas analyzers as seen in Figure 5.1.

Near-surface vertical gradients of standard meteorological parameters, such as temperature, humidity, wind speed and direction, are directly linked to the corresponding fluxes and may become very strong in the VSBL. Thus vertically dense observations at several levels are desirable. Temperature differences can be measured with very high precision based on (E-type) thermocouples, when they are all connected to the same cold junction. State of the art data loggers provide accurate, temperature controlled, cold junctions with high thermal stability. Since thermocouples can be designed as fine-wire sensors with low thermal inertia, they can even resolve turbulent fluctuations. For vertical gradients of the wind speed and direction, standard cup or propeller anemometers and wind vanes can be used, but especially in the VSBL, which is often subject to calm or very weak winds, sensor calibration and response are important. Furthermore, mechanical anemometers require a minimum wind speed and are subject to mechanical inertia resulting in overspeeding. Therefore, the use of high quality 2D or 3D sonic anemometers is of advantage. For all wind sensors flow distortion by supporting structures may be of importance. Standard humidity measurements are most commonly based on a capacitive sensors and combined with resistors to compensate for temperature dependence of the conductor. This makes it especially important to have humidity sensors well calibrated to be able to measure accurate gradients. Especially under cold conditions these sensors should be well ventilated since the measurement principle relies on diffusion of humidity, which is slower with colder temperatures. For our gradient measurements during the ISOBAR17 and ISOBAR18 campaigns we used: aspirated Campbell ASPTC[3] thermocouples with additional PT100 temperature sensors and Rotronic HC2S[4] humidity sensors, all installed in the same fan-aspirated radiation shield; Vector A100LK[5] cup anemometers and Vector W200P[6] wind vanes. The net radiation, i.e., the budget of up- and downwelling long- and short-wave components, contribute substantially to the surface energy balance and can be sampled with four-component net-radiation sensors. During polar winter, the long-wave components are of course of higher importance. As explained in Section 2.2, radiation divergence may become significant in the SBL and therefore radiation observations should be taken at several levels, at least for the upwelling long-wave component. Here, sensor calibration issues are very relevant again (Steeneveld et al., 2010). The ground or soil heat flux also contributes substantially to the surface energy balance and can be measured with special ground heatflux plates, which use thermopiles to measure temperature gradients across the sensor plate. The systems we used were the Kipp & Zonen CNR1[7]

---

[1]https://www.campbellsci.com/csat3

[2]https://www.licor.com/env/support/LI-7500/home.html

[3]https://www.campbellsci.com/asptc

[4]https://www.campbellsci.com/hc2s3

[5]https://www.campbellsci.com/a100lk

[6]https://www.windspeed.co.uk/ws/index.php?option=displaypage&op=page&Itemid=61

[7]https://www.campbellsci.com/cnr1

net radiometer, and the Hukseflux HFP01[8] ground heat flux plates.

In addition to data from the above mentioned systems we also made use of the WMO weather station Hailuoto Marjaniemi[9,10] operated by FMI, which is located at our field site. This station provides wind speed observations at 46 m asl., temperature, humidity, pressure at 2 m agl., and automatic weather, visibility, cloud and precipitation observations.

5.1.2 ABL remote-sensing systems

Sodar (sonic detection and ranging) systems can be used to remotely sense a number of parameters in the Boundary Layer, such as the 3D wind vector and variances of its components and the temperature structure parameter (Weill et al., 1980). The measurement principle makes use of the scattering of sound waves by small-scale density inhomogeneities, e.g., resulting from temperature variances generated by turbulence. By emitting pulsed sound waves that meet the Bragg condition, i.e., waves with a wave length matching the size of the density inhomogeneities (Bradley, 2008), and listening to the returned signal, radial wind speeds

Figure 5.2: LATAN-3M 1D sodar during ISOBAR18. Photo taken by J. Reuder.

can be computed from the Doppler shift of the returned sound wave. Spectral broadening of the returned signal may be related to velocity variances, whereas the strength of the returned signal is related to the temperature structure parameter. If the emitter (i.e., speaker) also serves as a receiver (i.e., microphone), then the system is described as monostatic and if emitter and receiver are separated as bistatic. Special geometries (e.g., parabolic reflectors) help to steer the signal in the desired direction and by using arrays of microphones and phasing them (triggering the signal emission with a time shift between the microphones) the signal can even be sent in different directions. This makes it possible to convert the radial velocities to 3D wind vectors.

The time between signal emission and reception can be related to the height of backscatter. By splitting the time series of the returned signal into shorter periods and taking the geometry of the sound path into account, height ranging can be achieved. The spatial resolution and maximum range depend a lot on the strength of the signal and in turn affect the sampling frequency, since the sensing process can not be repeated before the signal has been returned from the highest level to be sensed. Modern sodars are typically multi-frequency systems, operating in the audible range of roughly 1 kHz to 6 kHz, which improve the data quality, since the signal may interact with disturbances on a variety of scales. One of the major drawbacks of sodars is that the

---

[8]https://www.campbellsci.com/hfp01

[9]https://en.ilmatieteenlaitos.fi/observations-in-finland?station=101784

[10]https://oscar.wmo.int/surface/index.html#/search/station/stationReportDetails/0-20000-0-02873

Figure 5.3: MFAS 3D sodar during ISOBAR18. Photo taken by A. Seidl.

quality and intensity of the back-scattered signal depend on the atmospheric conditions. The signal is often weak at the top of a LLJ, when co-located with the top of an inversion layer. Due to signal attenuation in the inversion layer, the backscatter from the area above the LLJ may be too weak for a proper characterization (Bradley, 2008). In strong wind condition the ABL is often neutrally stratified and thus the atmosphere may lack strong enough density gradients to provide sufficient backscatter (e.g., Kallistratova and Kouznetsov, 2011). These drawbacks induce statistical observation biases and make it difficult to build wind climatologies based on sodar observations. During the two ISOBAR campaigns (Section 4.2.1 and 4.2.2), we measured profiles of vertical velocity and backscatter based on the 1D monostatic and multi-frequency sodar LATAN-3M (Figure 5.2 Kouznetsov, 2009). In the following year we had an additional 3D monostatic multi-frequency MFAS[11] sodar produced by Scintec (Figure 5.3).

Doppler wind lidar (light detection and ranging) systems may also be used to sense vertical profiles of the 3D wind vector or radial wind speeds along certain directions. Most common systems use pulsed light signals (Huffaker and Hardesty, 1996) but also continuous wave lidars exist. In contrast to sodars, pulsed wind lidars emit light signals and the relevant backscattering process is Rayleigh scattering at aerosols (Garnier and Chanin, 1992). Due to significant differences in the speed of sound and light, and signal processing limitations, the spatial resolution is typically limited to about 20 m (for pulsed lidars), whereas sodars may resolve scales on the range of meters (Petenko et al., 2019). However, higher sampling rates may be achieved with pulsed lidar systems, independent of the maximum range of the system, which depends on the signal strength and optical properties of the atmosphere. Continues wave lidars, focus their beam on a certain height to sense this level and thus have higher resolution closer to the ground and about 10 m in a distance of 100 m (Slinger and Harris, 2012). Turbulence parameters may be computed based on the spectral broadening of the returned signal, and at larger time scales, simply because of the relatively high sampling rate. Simpler lidar types may only direct their beam in four horizontally perpendicular directions

Figure 5.4: WINDCUBE v1 lidar during ISOBAR18. Photo taken by J. Reuder.

---

[11]http://scintec.com/english/web/Scintec/Details/A032000.aspx

at fixed elevation angles and potentially a fifth vertical beam. Such systems are typically operated in the DBS (Doppler beam swinging) mode from which the 3D wind vectors may be computed. More sophisticated scanning lidars may in addition to simple staring modes or the DBS mode perform a VAD (velocity azimuth display, i.e., scanning a number of fixed azimuth angles with constant elevation), or PPI (plan position indicator, i.e., continuous azimuth cycling with constant elevation) or RHI (range height indicator, i.e continuous elevation sector cycling with constant azimuth). Other more complex scanning modes, often a combination of the just described ones or adaptive modes, can also be realized. Scanning wind lidars may give detailed insight into processes such as the evolution of atmospheric waves and their interaction with turbulence, coherent structures, wakes (e.g., wind turbine or terrain induced), or wind shear to name a few. However, the performance of Doppler wind lidars largely depends on the presence and concentration of aerosol particles in the atmosphere, which may be problematic in polar regions with long-lived SBLs. The carrier-to-noise ratio (CNR), which is closely linked to the optical properties of the atmosphere related to aerosols, is used as a quality parameter for lidar measurements. We used a WINDCUBE 100S[12] (Leosphere) scanning Doppler wind lidar on Hailuoto in 2017 and a WINDCUBE v1 (Leosphere), a pulsed profiling Doppler wind lidar in 2018 (Figure 5.4).

5.1.3 Unmanned aircraft systems

Thanks to recent developments in micro-electronics and component miniaturization, small unmanned aircraft systems (UAS), a.k.a. unmanned aerial vehicles (UAV) or remotely piloted aircraft systems (RPAS), have gained increasing popularity in several fields of atmospheric research (Elston et al., 2015). As the term "system" suggests, a UAS does not only consist of an aircraft but also components such as sensor payloads; navigation units (inertia measurement unit, IMU, and global navigation satellite systems, GNSS); data acquisition systems; ground control station (GCS); remote control (RC); and, strictly speaking, also the safety pilot and GCS operator. Data acquisition is often done by transmission to the GCS and/or through a data logger built into the aircraft. Some sensor packages are designed for self-sufficient operation with integrated data acquisition system and often no possibility for direct integration to the other UAS components. Navigation of the aircraft can be based on manual controls via RC or on predefined flight plans uploaded to the aircraft's autopilot. Most systems also offer the possibility to send new commands and updated flight plans from the GCS during flight. In this section, the focus will be on battery-powered aircraft and their application for in-situ observations within the ABL and the lower troposphere. I distinguish between fixed-wing and rotary-wing multicopter systems.

Fixed-wing systems are most commonly based on electrically powered propeller airplanes. Thanks to their aerodynamics and airfoil wing design they generate their own updraft, and thrust is only required to accelerate and to compensate for frictional drag. This makes them very efficient and increases the operation safety, e.g., it is still possible to land safely with very little battery left. Based on their purpose, different designs are preferred. Endurance and payload requirements typically scale with the dimensions of the aircraft.

---

[12]https://www.environmental-expert.com/products/windcube-model-100s-200s-400s-3d-wind-doppler-lidar-399367

Our main workhorse during the cam-
paigns on Andøya 2016 (Section 4.1) and
Hailuoto 2017 and 2018 (Section 4.2.1
and 4.2.2) was the Small Unmanned
Meteorological Observer SUMO (Reuder
et al., 2009, 2012a, Figure 5.5), designed
for efficient profiling of the boundary
layer and troposphere up to levels of
about 5000 m (aviation authorities did not
permit flights above 1900 m agl. dur-
ing the Hailuoto campaigns). SUMO is
equipped with meteorological sensors for
temperature, humidity and pressure and
can also sense the wind speed by apply-

Figure 5.5: SUMO. Photo taken by J. Reuder.

ing a so-called now-flow sensor algorithm, which is based on the variations of the
GNSS measured ground speed along a circular flight pattern performed with constant
air speed (Mayer et al., 2012a). SUMO does not require any special launching equip-
ment, such as a winch or bungee, since it can be hand-launched and it is designed
for belly-landing. It does not require long pre-flight preparations, which makes it ex-
tremely efficient for high repetition rates. Furthermore, due to its EPP airframe, its
interior electronics are well insulated and work reliably even under harsh polar con-
ditions. The version of SUMO used during ISOBAR was basically identical to the
one described by (Reuder et al., 2012a), with only two major changes. The flight en-
durance could be enhanced due to improved batteries with much higher capacity at the
same weight. To aid better and faster decision making, I programmed an add-on for the
GCS to stream real-time data to a second laptop, where continuously updated profiles
of the most important variables can be monitored.

The second fixed-wing system we used during the above-mentioned three cam-
paigns is the Multi-purpose Airborne Sensor Carrier (MASC), designed for turbu-
lence observations along horizontal transects. Two different versions of MASC were
used: MASC-2 in 2016 and 2017 (Wildmann et al., 2014a); MASC-3 in 2018
(Rautenberg et al., 2019, Figure 5.6). This aircraft is equipped with a custom-built

multi-hole probe for wind and turbu-
lence observations, based on differen-
tial pressure measurements (Wildmann
et al., 2014b), and a fast-response fine-
wire temperature sensor to capture turbu-
lent temperature fluctuations (Wildmann
et al., 2013) in addition to slow-response
sensors for temperature and humidity ob-
servations.

Most rotary-wing UAS used in atmo-
spheric research are multicopters with at
least four propellers (quadcopters), which
have become increasingly popular dur-
ing the last 5 years (e.g., Jonassen et al.,
2015; Palomaki et al., 2017; Wrenger and

Figure 5.6: MASC-3. Photo taken by A. Raut-
enberg.

Cuxart, 2017; Lee et al., 2018; González-Rocha et al., 2019; Segales et al., 2020). They offer a cost-efficient and flexible way of probing the lower few hundred meters of the atmosphere, although also much higher altitudes can be reached. Their main advantage over fixed-wing aircraft is their ability to hover at a constant altitude and horizontal position or ascent and descent above the same location, which makes the data very similar to mast observations. Furthermore, they are generally easier to operate. However, this may have the drawback that they are also attractive to inexperienced operators, which may result in poor quality of the sampled data or even accidents.

During the first two ISOBAR campaigns we operated two different multicopter systems, i.e., Bebop2Met and AMOR Q13 (Wrenger and Cuxart, 2017), whereas one additional multicopter UAS (CopterSonde, Segales et al., 2020) was used during the last campaign.

The Bebop2Met (Figure 5.7) has been developed during the planning and early phase of ISOBAR and is based on the off-the-shelf Bebop2[13] by Parrot quad-copter, which is modified by replacing the on-board autopilot firmware with the the Paparazzi[14] autopilot and adding a small custom-built payload with a humidity and temperature sensor to it. To this development I actively contributed to the sensor integration, in particular with considerations on ventilation and propeller down-wash, and the implementation of data and communication as well as RC solutions. The sensor is placed a few cm above one of the propellers (right rear propeller in Figure 5.7) to assure sufficient ventilation. The backward-trajectory of the propeller in-

Figure 5.7: Bebop2Met. Photo taken by J. Reuder.

duced airflow at this position is largely horizontal, thus the sampled air has not been displaced significantly in the vertical direction before reaching the sensor, which is especially important when taking observations within an inversion layer. For wind speed estimations, following the approach by Palomaki et al. (2017), the autopilot was running an additional control loop to turn the nose of the copter into the wind direction (see Section 5.2.3). This featurewas, however, only available during the campaign in 2018 and not all of our three, in principal, identical Bebop2Met systems could be calibrated and tuned well enough to make use of the wind estimation data.

The Advanced Mission and Operation Research (AMOR) Q13 UAS (Figure 5.8) is a custom-built multicopter, which can be equipped with a number of different instruments. For our purposes, the sensor packages for the different versions of this UAS consisted of a slow-response humidity and temperature sensor, a fast-response thermo-couple temperature, and a hot-wire wind sensor (the latter two only available on one of the two versions operated during ISOBAR18). All sensors are positioned on a roughly 1 m long horizontal boom to minimize flow contamination caused by the propellers.

---

[13]https://www.parrot.com/us/drones/parrot-bebop-2
[14]https://wiki.paparazziuav.org/wiki

Figure 5.8: AMOR Q13. Photo taken by B. Wrenger.

Furthermore, these wind observations were at an experimental stage and the sensor broke after a few scientific flights due to the harsh environmental conditions.

The CopterSonde (Figure 5.9) is based on a model quadcopter airframe and a custom-built shell, housing the electronics. Two iterations of the CopterSonde were used, the older one with humidity and temperature sensors mounted under the front propellers (Greene et al., 2019a) and the newest version with three sets of identical sensors being integrated into the nose of the shell and aspirated by a ducted fan (Segales et al., 2020). The CopterSonde employed one type of combined temperature and humidity sensor and an additional, slightly faster responding, temperature sensor. Estimates of the horizontal wind speed are based on a very similar approach to the one described for the Bebop2Met (see also Segales et al., 2020).

During the LAPSE-RATE campaign in July 2018 (Section 4.3) ten teams deployed 34 UAS of different types (de Boer et al., 2019). The intercomparison experiment conducted during the first days of the campaign encompassed a total of 38 UAS systems with 23 unique sensor and platform configurations. The only system also used during the ISOBAR campaigns was the CopterSonde.

Figure 5.9: CopterSonde. Photo taken by W. Doyle.

5.2 Possibilities and limitations of observation methods

In this section, I intend to outline the different methods underlying the three above mentioned categories of observation systems. In order to combine the different systems it is essential to evaluate and contrast their possibilities and limitations.

5.2.1 Ground-based in-situ methods

The great advantage of the EC technique is the ability to directly measure turbulent fluctuations and fluxes, without the need for making assumptions on the eddy diffusivity. Therefore, EC systems often serve as a reference for the validation of other indirect methods. The determination of turbulence variables at high quality, however, is not possible without some fundamental assumptions. These assumptions include the

homogeneity and stationarity of the flow, which are a direct consequence of Taylor's hypothesis of "frozen" turbulence (Taylor, 1938), i.e., turbulence is transported with the mean flow and its statistical properties do not change. In particular under conditions with strong dynamic stability, Taylor's hypothesis can be questioned, as the mean-flow is often highly variable. EC-based computation of turbulence variables implies data averaging over a certain time period, but the choice of an appropriate averaging scale is not trivial. On one hand, the interval should be sufficiently long to capture a fair number of the largest-scale turbulent eddies to minimize the random error of the turbulence estimates. On the other hand, it should be short enough to avoid flux contamination by non-stationarity, i.e., atmospheric motions, which do not contribute to turbulence. In particular in the VSBL, where various types of submeso motions may act on similar time scales as the turbulence adjustment time scale, the separation of scales and the choice of an appropriate averaging scale becomes ambiguous. Nevertheless, science-grade EC systems, such as the CSAT-3 sonic anemometers used in this study, outperform most other types of wind sensors, in terms of precision, accuracy, response and sampling frequency and are thus extremely valuable for micrometeorological observations.

The determination of vertical gradients at a micrometeorological mast typically requires more than one instrument of the same type and may be biased by individual instrument offsets. This error source can be minimized by performing careful side-by-side calibrations of the respective instruments. Furthermore, the discrete vertical resolution and chosen method to compute the vertical gradients may be a considerable source of uncertainty. For the determination of vertical temperature gradients from discrete levels, the use of thermocouples is of advantage, since they measure temperature differences and it is possible to connect all sensors to the same cold-junction, which serves as a common temperature reference. Such a setup basically eliminates the offset error in the vertical temperature gradients. For the measurement of vertical wind speed gradients, factory calibrated sonic anemometers typically outperform cup or propeller anemometers, since they do not include any moving parts (World Meteorological Organization, 2008), so that they respond much faster to variations in the wind speed and are not subject to overspeeding. Moreover, to reduce radiation errors in the temperature and humidity measurements, proper radiation shielding and sensor ventilation are essential.

Apart from technical challenges with resolving turbulent fluxes and vertical gradients and their implications for the application of flux–gradient relationships (as in MOST), additional problems may arise in the VSBL. In the very-stable regime, time-averaged fluxes may not be in balance with the local gradients, as turbulence may be produced elsewhere and advected to the observation site by the often weak background flow. Turbulence may result from strong but vertically limited local gradients, which can not be adequately resolved by the incrementally spaced instruments on a micrometeorological mast. Furthermore, the majority of the total flux observed at a fixed location may be caused by short events of intermittent turbulence, however, the spatial extent of such turbulent patches may remain unclear, unless a dense network of micrometeorological masts can be installed.

For all fixed-point measurement it is critical to assure that the observations are representative for the prevailing conditions that shall be studied. As mentioned above, time-averaged turbulence variables but also vertical gradients may be altered by non-

stationarity and heterogeneity of the flow.

5.2.2 ABL remote-sensing methods

remote-sensing methods, such as Doppler wind lidar and sodar, can provide time series of vertical profiles of the 3D wind vector at a time resolution in the order of seconds. For sodar-based 3D-wind observations, the time resolution may also increase to several minutes, depending on the maximum altitude that shall be sensed and the sequence for the different beam directions. However, the spatial resolution of these systems is still rather coarse with range gates in the order of 10 m. Since the 3D wind vector typically has to be computed from radial velocity measurements along different beam directions, the resulting wind profiles have the characteristics of volume averages, with the horizontal cross-section increasing with height. This implies that non-stationarity within the averaging period and inhomogeneity on the scale of this cross-section have a negative influence on the quality of the computed wind vector. The strength of the observed signal, and thus the quality of the measurements, depend on the acoustic or optical scattering properties of the lower atmosphere, which may be problematic in the SBL. Moreover, the lowest measurement level that can be resolved is typically in the range of 20 m to 50 m. Scanning wind lidars have the capability for observations at low elevation angles. This observation strategy offers the possibility of spatial observations, however, the rather coarse spatial resolution (e.g., the WC100S has 50-m range gates) and the fact that only radial velocities may be observed directly, exhibit some limitations of this technique. Furthermore, an adaptive scanning software is needed, e.g., to enable the instrument to scan along the prevailing wind direction, and the implication of such software is often hampered by the instruments firmware.

5.2.3 UAS observation methods

UAS observations from in-situ sensors have the characteristics of time series along 3D trajectories, i.e., one specific point in space can be observed at any certain time step. This implies that UAS observations typically provide quasi-instantaneous snapshots of the atmospheric state over the period of a certain flight segment such as a vertical profile. The fact that the entire trajectory is typically probed with the same sensors eliminates the problem of sensor bias, e.g., when determining vertical gradients. However, UAS observations are subject to errors resulting from the sensor response time, i.e., temporal changes are smoothed. In the case of vertical profiles, this may result in a distorted shape of vertical gradients, the underestimation of local extrema (e.g., maximum temperature of an inversion) or a deeper/shallower inversion layer observed during ascent/descent. This error can, however, be reduced by using faster sensors and by decreasing the vertical speed of the UAS. Additional errors in the vertical profiles may result from the limited accuracy and precision of altitude measurements. GNSS altitude data may vary substantially in the order of several meters over typical UAS flight times of 15 min to 90 min. Pressure-based altitude data is more stable over shorter periods, but many sensors, typically integrated in UAS autopilots, are subject to considerable drift, likely caused by a not constant autopilot temperature. Furthermore, changes in the atmospheric state within the period of a flight may add to the uncertainty. In cold environments, the assumption of a standard atmosphere temperature and

lapse rate, applied in the conversion from pressure to height based on the hypsometric equation, is far from valid and causes large positive altitude errors, which increase with height. Additional potential sources of errors for observations of thermodynamic variables, e.g., temperature and humidity, may be caused by solar and infrared heating of the sensors. This can be mitigated by considerations on the sensor placement, ventilation and radiation shielding.

For UAS wind observations, there are basically two different approaches, i.e., the direct instrument-based measurement, and the indirect estimation based on aircraft motion and orientation. For the direct measurement, different types of sensors can be used. On fixed-wing aircraft, the 3D wind vector relative to the aircraft is typically measured with a multihole pressure probe, but also the use of sonic anemometers is possible. The conversion to a Cartesian earth-bound coordinate system requires a number of conversions (Lenschow and Spyers-Duran, 1989) and measurements on the orientation and speed of the aircraft, from reference systems (IMU, GNSS). Accurate turbulence measurements from moving platforms are thus extremely challenging, because the turbulent quantities have to be computed from direct observations of the air velocity relative to the aircraft, and the velocity and attitude of the aircraft relative to the Earth. In addition, geometrical aspects play an important role, such as in-flight sensor orientation and flow distortion. Especially in atmospheric layers with weak turbulence, these issues increase, since the input parameters for the motion correction may be several orders of magnitude larger than the turbulent fluctuations to be resolved. To give an illustrative example: in weak wind conditions of $1\,\mathrm{m\,s^{-1}}$ vertical velocity fluctuations may be of the order of $10\,\mathrm{mm\,s^{-1}}$, whereas the aircraft may move at a ground speed of, e.g., $20\,\mathrm{m\,s^{-1}}$ and therefore sense air speeds in the same order of magnitude. Thus, it is extremely important to have good knowledge of the input errors and reduce them as far as possible by relying on the most sophisticated sensors available.

During the past years, attempts have been made to equip multicopter UAS with sonic or hot-wire anemometers. These systems work over a much wider airspeed range, thus, they can also provide observations when the multicopter is not or only slowly moving relative to the air. Especially for turbulence measurements, but also for observations on the mean wind, flow induced by the propellers may cause considerable errors. To reduce or avoid this problem the sensors have to be mounted in a fair horizontal or vertical distance from propellers, which in turn may pose flight control challenges.

In indirect wind sensing methods, information on the aircraft movement relative to the ground and/or its orientation (attitude angles) is used to estimate the horizontal wind speed and direction. For fixed-wing systems the fact is used, that in an earth-bound coordinate system an aircraft with a constant airspeed moves slower against the wind than with the wind. Assuming stationary conditions, one can compute the wind speed from any kind of 2D horizontal flight pattern, preferably a circle (Mayer et al., 2012a). To assure constant airspeed on the SUMO, which typically does not carry a Pitot tube for its measurement, the autopilot maintains constant throttle and climb angle settings. Since this setting makes it challenging to maintain flight stability at a fixed altitude it is only used during vertical profile mode on a helical flight track. Since the wind estimation typically uses data over a full circle, the estimated wind speed and direction resemble a spatial average over the height range corresponding to one helical circle, but can still be computed at the same sampling rate as the input data.

This constellation resembles a running window average, and correspondingly results in some smoothing of the data, which also has to be taken into consideration for a correct height attribution. To get the corresponding height for each wind estimate, I compute the mean height of the helical circle the input data origins from. Although this method has been developed by Mayer et al. (2012a), I managed to improve the quality of the resulting wind estimates by defining rigid airspeed and climb rate settings for the profiling patterns, and by applying a height correction, as well as filtering out all data that did not fulfill the constant airspeed assumption over a full helical circle.

To estimate the horizontal wind speed and direction from multicopter UAS, one can make use of the relationship between the multicopter tilt angle and the horizontal wind speed during operation at a fixed horizontal position. Obviously, the higher the wind speed, the more the multicopter has to tilt to maintain its position. However, this approach requires additional assumptions and the calibration of each individual or type off UAS. For the Bebop2Met and the CopterSonde, we follow the approach developed by (Palomaki et al., 2017), which assumes that the aerodynamic drag coefficient, air density and exposed cross section of the multicopter, can be approximated by one single constant. Based on this simplification, the wind speed for a multicopter kept at a fixed position can be approximated by

$$U^2 = c \tan\alpha, \tag{5.1}$$

where c is the above mentioned constant, U the horizontal wind speed and α the total tilt angle of the copter, with

$$\alpha = \arccos(\cos\theta \, \cos\phi), \tag{5.2}$$

where ϕ and θ are the pitch and roll angle, respectively. The constant c has to be determined empirically through side-by-side calibration next to wind anemometers on a meteorological mast or other reference observation systems, such as sodar or lidar. Due to considerable differences in the front, rear and side shape and the corresponding cross sections of the Bebop2Met and CopterSonde, a directional influence of the constant c is very plausible and likely a source of uncertainty in this method. During the test campaign on Andøya and ISOBAR17, I developed the idea for an autopilot control loop for turning the Bebop2Met's nose into the wind to reduce this uncertainty and the calibration effort substantially. This could be realized by changing the aircraft's yaw angle (turning the UAS around its vertical axis) just as much that the aircraft's roll angle is kept close to zero and the pitch angle negative (nose down and into the wind). In this state, the aircraft is not affected by a side-wind component, apart from small-scale turbulent motions, whose contribution to the mean wind can be neglected, and the wind direction is directly given by the yaw angle. This feature was, however, only available during the ISOBAR18 and not all of our three, in principal, identical Bebop2Met systems could be calibrated and tuned well enough to make use of the wind estimation data. A similar autopilot algorithm was implemented in the CopterSonde after the ISOBAR18 campaign and was available during LAPSE-RATE. During the ISOBAR18 campaign the Bebop2Met flight plans typically included a calibration phase during which the UAS was hovering next to the 10-m mast to sample, temperature, humidity and wind reference data for calibration, before and after performing vertical profiles. The Bebop2met wind speed estimation could therefore be calibrated against

mast and lidar data (Section 5.3.2). As this method is based on some simplifications and there is still room for an improved implementation, the resulting wind estimates are not always optimal. The resulting estimates should not be interpreted without a comparison to the corresponding lidar or sodar data, but if the wind speed profiles agree in general, the UAS profiles are valuable due to their higher spatial resolution and sharper gradients.

Compared to fixed-point observations of time series, horizontal sampling, e.g. from turbulence resolving fixed-wing UAS, has a number of advantages. Taylor's hypothesis of frozen turbulence (Taylor, 1938) states that turbulence is advected horizontally with the mean flow while its average characteristics do not change. Based on this, it is assumed that turbulence, which is defined as a spatial statistical property of an air mass, can be derived from time averaged observations from a meteorological mast equipped with corresponding turbulence resolving instruments, e.g., EC systems. In the VSBL, often characterized by very weak or calm winds, high non-stationarity and non-homogeneity, the validity of Taylor's hypothesis is questionable. Through horizontal sampling, turbulence could, however, be derived from spatial averages taken during a much shorter time period. Such quasi-instantaneous snapshots are much less subject to non-stationarity and thus can provide a more representative measure of turbulence. By comparing such observations to corresponding mast observations, the validity and limitations of Taylor's hypothesis could be tested for different stability regimes. However, the precise measurement of turbulent fluctuations from a moving platform is much more challenging than observations from a fixed location. With current UAS and sensor technology the error propagation from wind sensors, GNSS and IMU systems on the derived turbulent fluctuation is likely to cause high uncertainties, when very weak fluctuations shall be resolved. In addition, rather small variations in flight altitude may induce a wrong signal when there are strong vertical gradients of turbulence variables.

As most current UAS are still non-autonomous and can therefore not be operated unattended, they typically require at least two person, one RC or safety pilot and one GCS operator. During field campaigns with limited manpower this may imply that UAS operations cannot be carried out permanently. The endurance and reliability of the UAS, experience of the operators and the preparation time may, however, decrease the downtime between flights and increase the total data sampling time. For example, the relative old but very reliable UAS SUMO (Reuder et al., 2012a), can apart from takeoff and landing or low-level flights, be operated without visual contact, so that the operators don't have to be exposed to a harsh environmental conditions for the entire flight. Other limiting factors for UAS operations are linked to the capabilities of the UAS, the operational regulations and restrictions, environmental conditions, availability of UAS batteries and charging capabilities, field facilities etc. Overall, this typically result in UAS data sets with irregular sampling times and intervals.

5.3 Data processing

The observational approach of the ISOBAR project, and in particular the data sets from the two scientific measurement campaigns on Hailuoto, pose the challenge of fusing observations from different observation systems. The three categories of instrumentation described in Section 5.1 are very different in their characteristics. Surface-based

in-situ observations provide time series of point measurements at a fixed location. Data from ground-based remote-sensing systems represent volume-averages in the form of time series profiles. UAS in-situ observations are typically time series of point measurements along a 1D, 2D or 3D trajectory. In addition to this, all sensors employed on the systems in use are subject to different sources of errors and uncertainties, resulting from different calibration references, ventilation, radiation shielding, response times and sampling rates, etc. When combining such different data sets, it is therefore essential to perform a number of measures to assure the robustness of the results. In this section, I will outline the quality assurance measures and checks we carried out to achieve this for the two Hailuoto data sets. Amongst the presented data processing steps I developed the presented methods for UAS altitude correction, improved the UAS sensor response time correction, and adjusted and improved the multicopter and SUMO wind estimation method for our purposes (see Section 5.2.3). In addition, I carried out an extensive wind estimation validation for the sodar and the three UAS, SUMO, Bebop2Met and CopterSonde, against the common lidar reference, based on the ISOBAR18 data set (see Section 5.3.2). Furthermore, I carried out all of the data processing for the EC, slow-response meteorology, WINDCUBE v1 lidar, MFAS sodar, SUMO and Bebop2Met data; determined sensor offsets for Bebop2Met, SUMO, CopterSonde, and Q13 temperature and humidity data; and synthesised the multi-platform-based vertical profile data.

5.3.1 General data processing, quality assurance and control

All of our recorded data underwent thorough automatic and visual inspection to assure the quality of the resulting data sets. For the slow response mast data this mainly included automatic algorithms to check the physical range; detect spikes; and "frozen" values (constant reading over longer periods), which sometimes occurred after changing the memory card on the data logger. All suspicious data detected in these checks were removed. In addition, we checked the slow-response wind data for flow distortion problems, which turned out to be an issue on the 10-m mast used during ISOBAR18, due to the diameter of the mast. Wind speed data with a direction from the mast was therefore flagged for suspicious data. All the instrumentation on our meteorological masts were thoroughly checked in the lab before the field deployment. Small offsets in the wind directions due to mounting errors were corrected by comparing the wind direction data during events with strong winds and near-neutral stratification. This was also done for the sonic anemometers and the sodar and lidar systems, with the permanent wind measurements at 46 m serving as the common reference. At the beginning or end of our field campaigns we carried out intercomparison experiments for all of our temperature and radiation sensors. For this we mounted them at the same level in close proximity to each other and operated them for a period of several hours. The resulting data sets were used for post-field calibration against a common reference.

Computing turbulence properties from the eddy-covariance systems requires a number of more sophisticated quality checks (e.g., Lee et al., 2004; Foken, 2008). We therefore made use of the TK3 software package, which includes physical range checks; despiking; stationarity test; planar-fit coordinate transformation; integral test on developed turbulence; Moore, Schotanus and WPL density corrections (for a full documentation on the software package see, Mauder and Foken, 2015). Based on the applied

quality checks, the TK3 software package outputs a number of quality flags for the different turbulence parameters. Our standard averaging period was set to 10 min as a result of ogive test, following Foken et al. (2006) and applying their flux convergence classification scheme. In addition, we also converted the information from the flux classification into additional quality flags for the different turbulence parameters. Furthermore, we computed turbulent properties applying different averaging periods ranging from 1 min to 30 min.

Data processing for the remote-sensing systems MFAS and WINDCUBE v1 largely relied on the quality checks implemented in the manufacturer's firmware for these systems. After inspection of the output data and minor adjustments to the quality thresholds applied in the firmware, the data was reprocessed with the highest possible time resolution. During post-processing we only adjusted for small altitude offsets due to the slightly elevated installation height and wind direction offsets as described above. Time averaged data for longer averaging intervals, e.g., 1 min, 10 min and 30 min were, if the original sampling period allowed for, computed from the highest resolution data and applying rigid thresholds for the data availability. The WINDCUBE 100S data was, in addition to the standard signal quality checks implemented in the firmware, checked for clutter by hard targets at low elevation angles. By applying the VAD technique (Päschke et al., 2015), we computed averaged wind profiles from the different PPI scans, assuming horizontal homogeneity. Furthermore, we derived turbulent statistics of the flow by analysing deviations from the mean state over one entire scan. The LATAN-3M sodar data with low signal-to-noise ratio was removed, before computing time-averaged profiles of vertical velocity and its variance. The attenuated backscatter signal, measured directly by the sodar, was used to visually estimate the ABL height, which is characterized by a sharp decrease of the echo intensity.

5.3.2 Novel UAS specific data processing methods

One of the main shortcomings with atmospheric UAS observations is the lack of best-practice procedures to assure the quality and intercomparability of sampled data (Wyngaard et al., 2019). However, there is a growing awareness for this problem in the scientific community applying UAS for atmospheric research. Experience from previous measurement campaigns already showed that fusing UAS-based data from different systems to other rather well-established measurement systems is challenging. During the first two campaigns related to the ISOBAR project and this thesis, our project group identified a number of challenges to consider when performing UAS measurements. The most important challenges for the synthesis of UAS data from different platforms we identified are related to inaccuracies in vertical positioning, sensor bias, and sensor response time. With this in mind, my participation in the LAPSE-RATE campaign motivated me, together with Lindsay Barbieri and other campaign participants, to carry out the intercomparison study presented in Paper II. Already during the intercomparison experiment it became evident that different altitude measurement methods resulted in substantial actual altitude biases, as could be observed from a camera mounted on the reference mast. In Paper II, we therefore recommend altitude post-processing based on pressure and ambient temperature data if high-precision altitude measurements are not possible. The findings of this study, together with our experiences in the field, encouraged us in our efforts to develop solid methods in order to minimize the uncertainties

when merging data from different UAS platforms and other observation systems.

UAS altitude correction

Basically all UAS employed during the ISOBAR campaigns used either simple GNSS or pressure sensors, or fused both of them through extended Kalman filters, to determine the flight and observation altitude. This was also the case for most platforms operated during the LAPSE-RATE campaign 2018, with some exceptions for the most sophisticated UAS. Those were either equipped with additional lidar sensors to determine the height above ground, or relied on differential GPS (DGPS) or real-time kinematic (RTK) positioning, which may increase the position accuracy to the order of cm. The vertical accuracy of standard GNSS systems is in the order of 5 m, and GNSS measured altitudes tend to vary substantially on time scales of several seconds to minutes, which is related to the changing positions of the navigation satellites. Pressure-based altitude measurements are typically less variable but are mostly assuming a standard atmosphere and are subject to rather linear changes on longer time scales. Natural large-scale variation in the surface pressure may become important, but we attribute this problem mainly to sensor drifts, potentially caused by limited performance of the temperature stabilization in cold environments. Figure 5.10 shows an example of an altitude time series as observed during ISOBAR18 from the pressure and GNSS systems on one of the Bebop2Met UAS, together with the corrected altitude. As seen from this example, the GNSS altitude indicates a start and landing point at about 20 m asl., which is quite remarkable, considering that the actual start and landing took place on the sea ice. Apart from some variability in the beginning of this flight (05:35–05:36) there is no notable difference in the "smoothness" compared to the pressure-based altitude. The pressure-based altitude is set to zero during the startup process, as it is done by most UAS autopilots. Although the GNSS altitude at the time of takeoff has a bias of about 20 m, pressure- and GNSS-based readings equal at an altitude of about 150 m, whereas the maximum values reach 250 m (pressure) and 242 m (GNSS), respectively. The landing altitude (the UAS landed at its starting position) from the GNSS has roughly the same bias as at the start, whereas the pressure-based altitude is about 3.5 m higher than at the start. We attribute the faster increase in pressure-based altitude to the assumption of a standard atmosphere profile, which is commonly used for the conversion from pressure to altitude. Obviously, the assumption of a temperature of 15 °C (at 0 m asl.) and a vertical lapse rate of $-6.5\,\mathrm{K\,km^{-1}}$ does not hold in the polar stable boundary layer, which is typically much colder close to the surface and is often characterized by strong inversions with positive lapse rates.
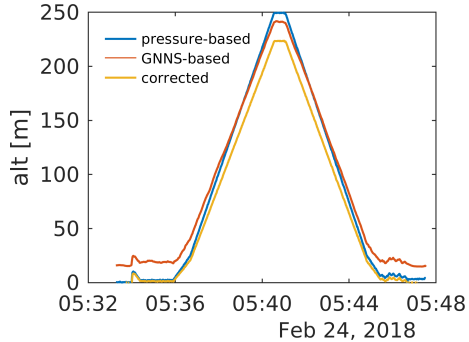

Figure 5.10: Example time series of UAS altitude-based on GNSS and pressure data in addition to a corrected altitude (based on detrended pressure and ambient temperature profile).

To achieve a high quality and comparability of our UAS altitude reference, we post-processed all flight data following the same routine based on measured pressure and temperature. In a first step, we isolate short periods in the time series just before the start and after the landing during which the UAS was clearly standing on the ground (sea ice) with the motors being switched off to avoid contamination of the pressure measurements. The mean pressure of these two periods is then used to linear detrend the pressure time series so that start and landing at the same altitude are associated with the same pressure. In a second step, we compute the altitude thickness, Δz_i, for layers, i, with pressure increments of $\Delta p = 0.25$ hPa, based on the density computed with the mean observed temperature $\overline{T_i}$ within this thin layer

$$\Delta z_i = \frac{\Delta p \, R \, \overline{T_i}}{g \, p_i}, \tag{5.3}$$

with the specific gas constant for dry air $R = 287.0583 \, \mathrm{J \, kg^{-1} \, K^{-1}}$ and gravity $g = 9.81 \, \mathrm{m \, s^{-1}}$. The corrected altitude is then the sum of all layer depths Δz_i. In order to apply this method, one first has to interpolate the time series of pressure and temperature to a regular pressure grid corresponding to Δz and after the conversion to the corrected altitude one has to interpolate to the original time series. In our algorithm we take the mean temperature from both ascent and descent data, which is consistent with the pressure detrending. The resulting corrected altitude, yellow line in Figure 5.10, is qualitatively following the GNSS altitude, but with less fluctuations and correct takeoff and landing altitudes. At the highest level seen in this example, the difference between purely pressure-based and the corrected altitude is more than 26 m, corresponding to a relative error of 12 %. Applying this algorithm to all of our UAS profiles improved the comparability substantially, especially in relatively thin layers with strong gradients, e.g., temperature inversions and LLJ.

Sensor response time correction

Almost all of our temperature and humidity sensors were of different kinds - some of them factory calibrated and others calibrated in the lab. Moreover, very different solutions for radiation shielding and ventilation of these sensors existed. One of the important outcomes of the intercomparison study (Paper II) is that differences in sensor type and integration may result in remarkable discrepancy in temperature and humidity observations. To reduce the bias of our temperature measurements, we spent some of our flight time (multicopters only) hovering in the vicinity of our meteorological masts at the level of one of the higher temperature sensors. In addition, we conducted a number of intercomparison flights during which all of our UAS were profiling vertically at roughly the same time and in short distance to one another. Based on direct comparison to the mast data and the intercomparison between the UAS at levels with near-neutral stratification, we determined a mean bias for each of our UAS temperature sensors and corrected for it to match the mast observations. A similar correction was also performed to the UAS humidity data, however, these sensors suffered from significant response time issues, which limits the availability of reliable calibration data drastically. Apart from the fast-response fine-wire and thermocouples, all UAS temperature sensors have a notable response time in the order of seconds. This results in

hysteresis effects also depending on the vertical ascent or descent rate applied for profiling the atmosphere and the prevailing vertical temperature gradients (Foken, 2006). We therefore apply a sensor response correction (largely inspired by the work of Jonassen, 2008), assuming that the response of a temperature sensor to an instantaneous step change in the ambient temperature would follow the exponential solution

$$T(t) = T_\infty \left(1 - e^{-\frac{t}{\tau}}\right),\tag{5.4}$$

where T_∞ is the temperature after the step change and τ the time constant, i.e., the time it takes to adjust to a temperature value corresponding to 63 % of the absolute temperature difference. When τ is known, the following correction algorithm can be applied.

$$T_j^c = \frac{T_j - \left(T_{j-1}\, e^{-\frac{\Delta t}{\tau}}\right)}{1 - e^{-\frac{\Delta t}{\tau}}},\tag{5.5}$$

with the corrected temperature, T^c, the time index j and the time step Δt. The time constant can be estimated by two different methods. The first is through comparing the consecutive ascent and descent profiles. Without correction, these profiles typically reveal differences, e.g., in estimates of the inversion depth. This may, however, be problematic since the characteristics of inversions may change on relatively short time scales due to a number of atmospheric phenomena, such as internal gravity waves, subsidence or turbulent bursts. A second method is to expose the sensor to a quasi-step-change. This can be realized by heating the sensor and turning the heating off instantaneously, by ascending rapidly through an inversion layer and then keeping a fixed altitude until the sensor has fully adjusted to the ambient conditions, or by exposing the sensor to different temperatures by moving it quickly from a warm room to the outside or vice versa. Due to the lack of sensor heating capabilities, we could only realize the latter of the two approaches during ISOBAR18. The correction method presented above is, however, very sensitive to sensor noise, which is artificially amplified. To overcome this issue, we apply a second order Savitzky-Golay (Schafer, 2011) filter with a window size of 15 s to smooth the input data before applying the correction. The Savitzky-Golay filter has the advantage that it does not show an impact on the response time, which is applied in the actual correction. The determination of the response time is not without uncertainties and the values estimated from different suitable UAS flights and other experiments were subject to substantial scatter. We therefore decided a rather conservative approach, selecting response times in the lower range, which were also rather close to the values stated by the sensor manufacturers. Too long response times may result in over-correction with unrealistic temperature gradients. To minimize the sensor response problem, we were operating with relatively slow vertical climb rates of about $1\,\mathrm{m\,s^{-1}}$ for the multicopters and roughly $3\,\mathrm{m\,s^{-1}}$ for the SUMO.

Attempts to apply the same correction method also to the relative humidity data did not show the same success as for the temperature. The sensor response of capacitive humidity sensors is more complex than the one for e.g. thermistors. Humidity sensors respond differently to an increase or decrease of humidity with much longer response times for the latter case. Furthermore, temperature has a major effect on the response time resulting in much slower response under cold conditions. This non-linear dependence complicates the characterisation of the sensor. Moreover, our correction attempts

indicated that there is a clear dependency on the sign of the temperature tendency, i.e., the sensor shows different behaviour when ascending or descending through an inversion layer. In addition, sensor aging may also play a role.

UAS wind estimation

Indirect UAS wind measurements (as described in Section 5.1.3) also require some additional considerations. Multicopter calibration data from flight periods next to the mast had to be performed within the lowermost 10 m of the atmosphere, which at times was characterized by relatively strong gradients and temporal variability. In addition, the flight altitude could not be matched the exact heights of the instruments, which was partially related to uncertainties in the raw altitude readings. We therefore had to compute mean wind speeds for UAS hovering periods, to be used as calibration data set. In addition, we made use of the lidar data for this calibration to account for the influence of the vertical climb rate and include calibration data at higher wind speeds. For this we bin averaged the relevant UAS data matching the corresponding lidar range gates. Since the autopilot control loops induce variation in the attitude angles, we smoothed the Bebop2Met data by applying a Hanning filter with 7-s window length. Only flight periods with enabled yaw-control loop (turning the multicopter nose into the wind) and additional small horizontal and vertical motions were selected for the calibration. The same restrictions were used when applying the wind estimation algorithm to the entire profiles, however, by limiting the vertical climb rate to $\pm1.5\,\mathrm{m\,s^{-1}}$. One of our Bebop2Met multicopters could not be calibrated in a wide enough range of wind speeds and can therefore not be used for wind estimation.

The SUMO wind estimate is arguably more robust since it does not require any calibration. However, the no-flow sensor algorithm (Mayer et al., 2012a) works only under the assumption of constant air speed. Since the SUMO does not carry any air speed sensor (e.g., Pitot tube), the autopilot is set to maintain a constant throttle and pitch angle during ascent and descent. Since the wind estimation is based on input GNSS ground speed and heading data over a full 360-deg turn, we neglected all data for which the pitch and throttle settings were not meeting this condition for an entire circular flight track. During some flights, when the SUMO experienced strong winds at certain levels, the settings for the climb angle and throttle had to be changed during ascent or descent, which then resulted in a gap in the wind speed data. The fact that the wind speed estimate is based on data from a longer time period during which the altitude changes makes it necessary to compute a mean altitude corresponding to this time period. In addition, this also has implications for the interpretation of the wind data, which thus resemble volume averages.

To validate our UAS wind sensing methods, we compared wind measurements taken during vertical profile flights and sodar 10-min time series against lidar observations. Figure 5.11 shows a scatter plot for wind speed (first row) and direction (second row) from the MFAS sodar, SUMO, Bebop2Met and CopterSonde (from left to right). Both sodar and SUMO show a very good agreement with relatively small root-mean-square errors of less than $0.5\,\mathrm{m\,s^{-1}}$. Note that the sodar validation had to be based on 10-min averages, (corresponding to sampling rate of the sodar), whereas all other comparisons utilize data with 1-s time resolution. Both of the multicopters presented in this comparison show a notable weaker agreement with the lidar wind speed observations This
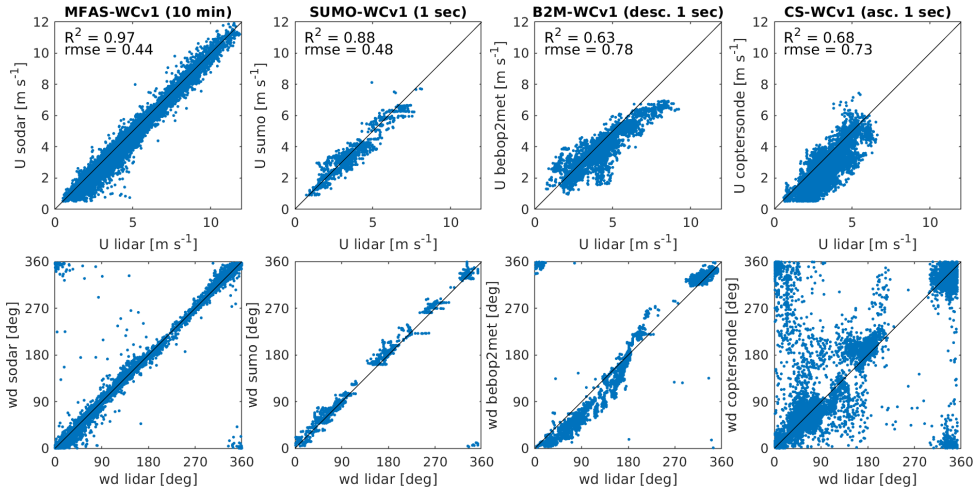
Figure 5.11: Scatter plot of wind speed and direction measurements compared to the WIND-CUBE v1 lidar observations for (from left to right) the MFAS sodar, SUMO, Bebop2Met and CopterSonde. MFAS data is compared to 10 min means from the lidar to match the time resolution of the sodar. All other comparisons are based on 1-s time resolution data. Only data from altitudes falling in one of the 20-m lidar range gates is taken into account. B2M data origins from the descent profiles, CS data from the ascent and sumo data from both. Coefficient of determination, R^2 and root-mean-square error, *rmse* for the wind speed are written to each of corresponding panels.

is most likely due to non-ideal calibration conditions and the shape of the conversion function (Palomaki et al., 2017), which may be too simple. E.g., the underestimation of higher wind speeds by Bebop2Met may be related to aerodynamic effects of a changing drag coefficient and increased area exposed to the wind with higher pitch angles. The wind direction estimates for both SUMO and Bebop2Met show satisfying agreement with the lidar direction. For the majority of the CopterSonde wind direction estimates this is also the case, but there is also a fair number of data points with large deviations. Additional analysis (not shown) focusing on the influence of the profiling direction showed that the quality of the SUMO wind estimates did not depend on the profiling direction, whereas the agreement for the CopterSonde was better during ascent and for the Bebop2Met during descent. The reason for this different behavior of the two multicopter systems remains, however, unclear. Considering this relatively new approach for multicopter wind sensing and the not ideal calibration conditions, we regard this first validation as encouraging. However, for the interpretation of wind profiles we do not rely on multicopter data without comparing the relevant profiles against sodar or lidar observations from the same time period.

5.3.3 Synthesis of multi-platform observations

The novelty of the ISOBAR observational approach lies in the idea to profile the SBL with high spatiotemporal resolution based on UAS and remote-sensing systems, in order to extend the vertical range of meteorological masts. To achieve a high quality

level, the above-mentioned data processing steps are essential for this approach. Figure 5.12 shows an example from an 80 min long period during ISOBAR18, when all four profiling UAS were operated and all ground-based in-situ and remote-sensing systems provided data. The temperature profiles from the three multicopter UAS align very well to the 10-m mast data and the observations taken at 46 m (Figure 5.12, left panel). The lower portion of the SUMO temperature profile also matches the upper parts of the multicopter profiles. Small difference in the shape of temperature profiles in the inversion layer are, however, evident, but it cannot be validated clearly whether they are caused by atmospheric phenomena, such as internal gravity waves. In any case their magnitude in the order of less than 1 K is fairly small.

The synthesis of wind speed observations from ground-based in-situ, remote-sensing systems, and UAS also resulted in an overall good agreement (Figure 5.12, right panel). Especially in the lower few hundred meters, the wind field was typically fairly variable in time (compare standard deviations, indicated by the shaded areas in Figure 5.12). At around 100 m, the Doppler wind lidar shows a relatively persistent lo-
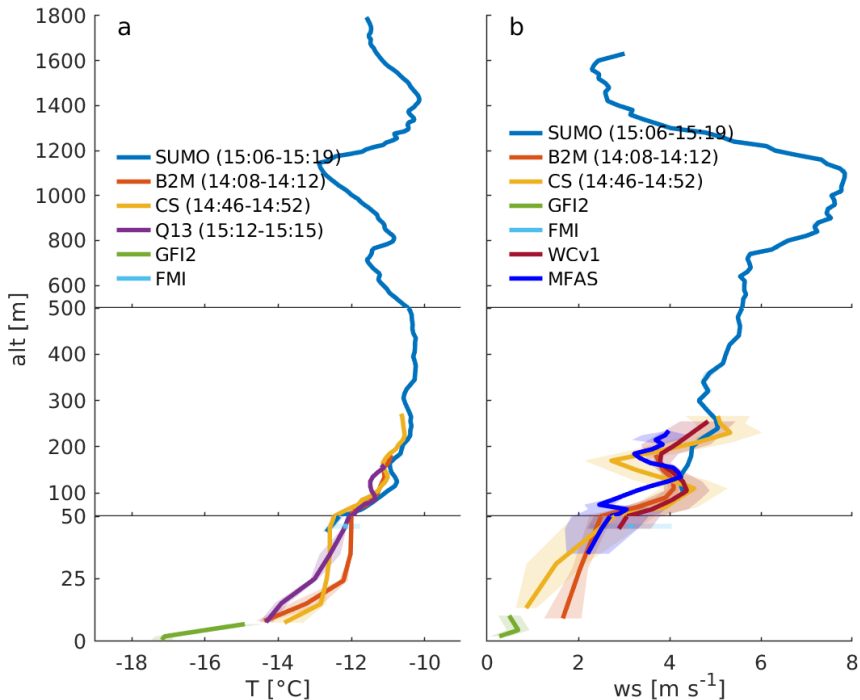
Figure 5.12: Temperature and wind speed profiles observed on 2018-02-18 between 14:00 and 15:20 UTC. Data from the ground-based systems GFI2 (10-m mast), FMI (46-m mast), WCv1 (lidar) and MFAS (sodar) correspond to to time-averaged mean (solid lines) and standard deviation (shadings) for the entire 80-min period. UAS data is height-averaged, using 10-m bins. The UAS flight times for the ascents is given in the legends for the four systems, SUMO, Bebop2Met (B2M), CopterSonde (CS) and AMOR Q13. The height axes are split in three intervals with resolution decreasing upwards.

cal wind maxima, which is also reproduced by the Bebop2Met and CopterSonde. The shape of this feature looks a bit different in the MFAS sodar data, which is in this case due to varying data availability above the 65-m level for the averaging period shown here. The SUMO wind speed profile does not fully reproduce this LLJ-like feature. This is because the wind speed data corresponds to a mean over a full flight circle, which in this case corresponds to roughly 50 m altitude difference.

A high temporal resolution of boundary-layer and lower-troposphere profiles was realized by repeated UAS missions with short downtimes during the, in total, 14 IOPs (Table 4.1 and 4.2) of the two Hailuoto campaigns. During the IOPs our goal was to perform multicopter UAS profiles up to 200 m to 300 m roughly every 30 min and SUMO profiles up to 1800 m every 3 h to 4 h. This resulted in extensive data sets of temperature and wind profiles for numerous IOPs from which the evolution of the SBL and various other relevant processes can be studied. Figure 5.13 presents the evolution of temperature and wind speed profiles obtained using the various profiling platforms deployed during ISOBAR18 between 2018-02-17 14:00 and 2018-02-18 03:00 UTC. This time series features a total number of 37 UAS flights, which are highly consistent in both wind and temperature observations and highlight the spatiotemporal data resolution resulting from our observation strategy.
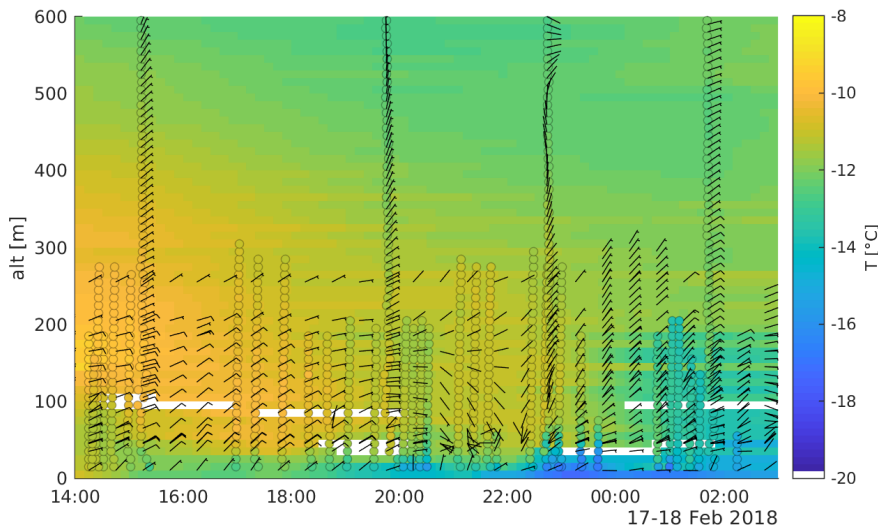
Figure 5.13: Time series of temperature and wind profiles in the lowermost 600 m of the atmosphere from 17-18 Feb 2018 between 14:00 and 03:00 UTC. Colored contours displaying the multi-platform-based interpolated temperature with 10 m bin-averaged UAS observations (circles) and wind barbs from the highest 10-m mast level, lidar, sodar and SUMO observations on top.

6 Summary and main findings of the papers

In this thesis I apply a new observational approach to lay the foundation for a new paradigm of SBL studies in Arctic regions . The novelty in the observation strategy is the combination of well-established micrometeorological in-situ instrumentation and boundary-layer remote-sensing systems with the extensive use of different UAS, tailored towards the sampling of the structure of the SBL and its temporal evolution with unprecedented spatiotemporal resolution. The potential of this approach has been demonstrated and improved during two major field campaigns and is presented in the two resulting papers (Paper I and Paper III). A third field campaign offered the possibility for the most extensive intercomparison study on UAS systems and sensors for atmospheric research to date (Paper II). This study provided invaluable insight and guidance for the quality control and subsequent analysis of the UAS-based meteorological data sets of the two main SBL campaigns. Furthermore, data from various observation systems sampling during the ISOBAR campaigns were analyzed in a number of detailed case studies with respect to the evolution of the VSBL and the role of different phenomena for its dynamics (Paper I and Paper III). One additional study I contributed to (Paper IV) presents a new highly sophisticated UAS for direct observations of turbulence in the ABL and demonstrates its potential and limitations for observations in the SBL. The last study (Paper V) investigates the applicability of traditional and alternative SBL scaling schemes to the ISOBAR18 mast data and presents a new method for the estimation of turbulence profiles based on vertically sampled UAS data.

In **Paper I** we introduce the ISOBAR project with its observational and modelling components. We give an overview over the first field campaign, ISOBAR17, carried out over the sea ice of the northern Baltic Sea at the Finnish island Hailuoto during three weeks in February 2017. In contrast to our expectations and the climatology of the study region, we experienced quite unusual conditions for this time of the year, with relatively mild temperatures, and fractional sea ice cover or open water in large parts of the Bothnian Bay. Nevertheless, a fair amount of VSBL could be sampled in situations characterized by clear sky and weak to calm winds. Under such conditions, the boundary-layer depth, as indicated by the sodar, reached values as low as 20 m. The main objectives of this manuscript is to address research questions RQ-1 and parts of RQ-3.

Addressing research question RQ-1, we demonstrate the potential of our observation strategy by the compilation of composite profiles of temperature and wind. These profiles were based on the complementary data sets, sampled by the meteorological masts, multicopter and fixed-wing UAS, and a scanning Doppler wind lidar. This resulted in high-resolution vertical temperature profiles, ranging from 0 m to 1800 m, with good agreement between the different systems. The wind speed profiles still reveal a sampling gap between the height of the micrometeorological mast and the lowest SUMO level from which wind speed estimates are available (typically 40 m). This gap might, however, be filled in the near future by the development of an improved wind determination algorithm for the Bebop2Met multicopter system (Section 5.3). We also found the SUMO wind speed estimates to be in good agreement with the Doppler wind lidar at the levels where the CNR was above its detection threshold, which was un-

fortunately often not the case for all atmospheric levels, due to generally low aerosol concentrations.

Through intensive multicopter sampling during one IOP, we achieved detailed insight into the thermodynamic evolution of the SBL over a period of 8 h, which illuminates on research question RQ-3a. The SBL was stably stratified resulting in a surface-based inversion of about 50 m depth, with a temperature difference of 5 K to 7 K and very little temporal variability during the first 6.5 h. The UAS profile, taken about 15 min after this rather stationary period, indicated a rapid cooling of more than 4 K near the surface and of about 1 K at the original top of the inversion, in addition to a deepening of the inversion layer. The following profiles showed that both the cooling and the deepening continued, however, at a slower rate close to the surface. The temperatures above the inversion layer remained rather constant and did not show any sign of large-scale advection.

From the micrometeorological measurements over the see ice, we found that the observed SBL evolution coincided with a series of strong rapid temperature changes near the surface. A closer look revealed quite different characteristics of the individual temperature jumps. The initial cooling event was associated with a sharp temperature drop at all levels, calming of the wind and vanishing of turbulence. This was followed by an evenly sharp warming event about 30 min later and a similar cooling event with the same periodicity. The subsequent rapid and strong temperature changes were mostly seen at the highest mast level (4 m), and the frequency of occurrence of these events increased. During this period, one of the multicopter profiles sampled a strong instability, manifested by a temperature decrease of 5 K over an altitude increase of 10 m. This instability was located just below a layer, subject to strong vertical oscillations, as indicated by the sodar echogram. This observation lead us to the conclusion that both the elevated instability and the observed rapid changes in near-surface temperatures were likely to be caused by a Kelvin–Helmholtz instability. This case gives some insight into the complexity of wave–turbulence interactions (RQ-3c).

The work presented in this manuscript describes one of the most extensive ABL campaigns involving UAS-based data sampling and most likely the first of its kind in polar regions. Apart from planning this experiment and organizing the logistics related to this campaign, I carried out all data processing for the ground-based in-situ systems, SUMO and Bebop2Met and the analysis and interpretation presented in this manuscript. Novel aspects of this work and my contribution are: the combination of different measurements systems to substantially reduce the observational gap in vertical profiles of the SBL; the rapid UAS profiling, providing detailed insight in the evolution of the SBL; and the study of a wave-breaking event based on mast, UAS and remote-sensing data.

In **Paper II** we present results from an intercomparison experiment for atmospheric measurements based on UAS, addressing research questions RQ-2. The experiment was carried out as part of the LAPSE-RATE campaign in the San Luis Valley, Colorado, USA, which took place from 14-19 July, 2018. Performing standardized flight patterns, we evaluated 38 individual UAS with 23 unique sensor configurations. These flight patterns included a fixed-altitude flight period followed by two vertical profiles (ascent and descent). In order to assure a high level of comparability, the UAS were either hovering (multicopters) or circling (fixed-wings) at the height of an 18-m meteorological mast, to evaluate precision and bias of the UAS measurements. In addition,

we assessed the sensor response time for the temperature and relative humidity measurements, by comparing consecutive profiles up to 120 m, sampled during the ascents and descents. These comparisons took mainly place during convective and well-mixed boundary-layer conditions with low cloud cover. All groups involved in the experiment delivered the corresponding UAS data in a standardized format, without performing any corrections. The only conversions applied were conversions to physical units and the coordinate transformation to an earth-bound coordinate system. We applied a unified data processing procedure, including a novel and robust pressure to altitude conversion, for the following analysis. Accuracy and precision of the UAS observations were assessed by computing mean and standard deviation for the fixed-altitude periods and comparing these to the corresponding values from the mast data. We computed the absolute-mean-deviation (*amd*) between the two profiles as a metric for the sensor response. The mean-absolute-deviation (*mad*) of the mast data is used as a proxy for the instationarity during the period of the two profiles, in order to distinguish between the sensor response and the variability of the atmospheric state during the profile flights. All of these measures were applied to address research question RQ-2c.

The comparison of UAS temperature observations with the reference observations indicated broad agreement (RQ-2a), with 11 out of 42 UAS sensors showing biases within ±0.25 K and 27 within ±1 K. The sensor configurations with considerable disagreement in the range of several Kelvin, showed in general a positive bias, and were mostly of the integrated-circuit type. Furthermore, investigation of the type of configuration revealed that unaspirated sensors had significantly higher bias than aspirated ones, whereas multicopter sensors showed in general higher variability than fixed-wing sensors (RQ-2d). The comparison of relative humidity measurements against the mast indicated a lower level of agreement than was observed for temperature and no clear sensor type dependency. The majority of UAS measurements showed a negative bias between 5 % to 10 % (RQ-2a). Sensors without aspiration were frequently subject to a high negative humidity bias exceeding 10 %. The variability of multicopter-based measurements was again higher than those observed by fixed-wings (RQ-2d). The majority of pressure observations showed good agreement to the reference observations, with only 3 sensors showing biases exceeding ±1.5 hPa (RQ-2a). No clear patterns with respect to aircraft type or sensor configuration could be found, except that all of the sensors with poor agreement were mounted below the main multicopter body and thus likely to be affected by rotor induced pressure enhancement (RQ-2d). UAS-based wind speed and direction observations showed in general good agreement with the reference measurements, with the majority of wind speed biases within ±0.5 m s^{-1} (RQ-2a). Fixed-wing UAS reported higher variability in their wind speed measurements compared to multicopters and showed a tendency for positive biases. The most consistent wind observations were achieved by multicopter-mounted sonic anemometers, whereas the lowest agreement was found for wind estimates based on aircraft dynamics for both multicopter and fixed-wing systems (RQ-2d).

The assessment of the sensor response times for relative humidity and temperature showed clear hysteresis effects for some of the sensors (RQ-2b). It appeared that the fine-bead thermistors responded slightly faster than the integrated-circuit temperature sensors, which is in general agreement with the response times stated by the manufacturers. In terms of sensor integration, the most striking difference was found for relative humidity and temperature sensors, with aspirated integrations clearly outperforming the

unaspirated ones. Other than that, we did not find evidence for clear patterns related to the UAS or sensor type and the integration solutions (RQ-2d).

Based on our experiences during the intercomparison campaign with respect to altitude deviations between the different systems and the potential consequences for profile observations, we strongly recommend high-precision altitude measurements or at least pressure- and temperature-based post-processing for all kinds of atmospheric UAS-based observations (RQ-2c and (RQ-2e)). We conclude that UAS are broadly providing accurate atmospheric measurements, but that sensor integration considerations, especially with respect to aspiration and solar radiation shielding, are likely more important than the choice of sensor type and platform (RQ-2e).

This UAS intercomparison experiment is unique for a number of reasons. For the first time, a high number of different UAS and a large variety of sensors were compared systematically against a common reference. Furthermore, the collection of metadata on the different UAS and sensor types, characteristics and its sensor–platform integration, allowed for the detailed analysis of the data quality and its interpretation as a function of different sensor integration solutions, measurement methods and UAS type. Other novel aspects of this intercomparison experiment are the standardized flight patterns performed by all UAS (as far as possible) and the uniform data post-processing procedures I developed, in particular an altitude correction algorithm based on the the hydrostatic equation (see Section 5.3), to achieve the highest possible level of intercomparability between the different UAS platforms. In order to quantify the sensor response from UAS profiles and the contribution of non-stationarity I defined the metrics *amd* and *mad*.

In **Paper III** we provide a general overview of the ISOBAR project and the two campaigns on Hailuoto during February 2017 (ISOBAR17) and 2018 (ISOBAR18). We further describe contrasts between these campaigns, demonstrate the quality of our observation strategy and highlight a number of scientific results, including a first validation of three different numerical models. Over the two campaigns we carried out a total of 14 IOPs, mostly targeting the VSBL and associated atmospheric phenomena and turbulence interaction processes. The findings of this paper are largely related to research questions RQ-1 and RQ-3.

The meteorological and sea ice conditions during 2018 were much closer to the climatological mean conditions for February in contrast to the exceptionally mild conditions with little sea ice in 2017. While the synoptic conditions were quite variable during February that year, the weather in 2018 was dominated by a blocking situation with high pressure and generally weak geostrophic flow. This situation was only interrupted for about one week, in the middle of February 2018, by the passage of a low pressure system, resulting in southerly flow with milder temperatures and a small reduction in the sea ice cover. Overall, the synoptic situation and sea ice conditions were more favorable for the VSBL formation during ISOBAR18.

We demonstrated the quality of our multi-platform atmospheric profile observations of wind and temperature, which could be further improved compared to the ISOBAR17 campaign and Paper I (RQ-1a). Improvements could be achieved through upgrades and extensions in our instrumentation and advanced data post-processing procedures. The most important changes in the instrumentation were the installation of a 10-m mast with two additional sonic anemometers up to 10 m, a better data availability from the Doppler wind lidar, and one additional multicopter system. A uniform UAS altitude

post-processing algorithm, in combination with sensor offset corrections, increased the agreement between the different temperature sensing systems. Preliminary wind estimates based on the multicopter attitude information, showed promising results, indicating high potential to close the gap between the highest mast and lowest sodar, lidar or SUMO levels (RQ-1). This relatively new approach is, however, still under development and thus subject to considerable uncertainties. Moreover, the improved data availability from the Doppler wind lidar, and the additional 3D sodar, contributed substantially to the quality and data density of wind profiles compared to ISOBAR17.

We study the evolution of the SBL based on frequent UAS profiles and permanent mast observations during a period of 4.5 h in which we conducted 14 individual profile flights. The high repetition rate, in combination with a spatial temperature resolution in the order of 1 m, allowed for detailed insight into the thermodynamic structure of the SBL. The observations showed an overall cooling of the ABL, which was seen in an increase in inversion strength and depth (RQ-3a). Investigations of the fine-scale temperature structure revealed thin layers of thermal instabilities below 70 m agl., consistently resembled in a number of consecutive profiles (RQ-3b). The near-surface temperature observations on the 10-m mast showed a series of rapid temperature changes and shifts in wind direction, indicating the passage of cold microfronts originating from a clean sea ice fetch. We hypothesise that the thermal instabilities observed by the UAS were related to such microfronts, which may appear rather irregular in their shape.

Based on our different observation systems we attempt to disentangle the complexity of the VSBL during one IOP and shed some light on a variety of different relevant processes, to address research question RQ-3c. We therefore present three detailed case studies for shorter periods within this IOP, which were dominated by different processes.

The first case was initiated by a rapid temperature drop, which was followed by a calming of the near-surface winds leading to the formation of a VSBL, with weak turbulence of intermittent character. At elevated layers of about 100 m, the flow accelerated and formed a weak LLJ. The time series of wind profiles from the Doppler lidar showed an intensification of the LLJ and a lowering of its core. This results in enhancement of the wind shear below the LLJ core, which eventually resulted in an instability. The observed from the three EC systems on the 10-m mast showed that this event was triggering strong turbulent mixing and an acceleration of the near-surface flow. The collapse of the LLJ initiated a transition from the very-stable regime back to the weakly-stable regime (RQ-3c).

The start of our second case study was characterized by a sharp surface-based inversion, with $\Delta T_{10m-0.6m} \approx 4.5\,\text{K}$, and weak winds, meandering from south-southwest to north-northeast. The turbulence observed by the three EC systems on the 10-m mast was again weak and of intermittent character, whereas the remote-sensing wind observations indicated some wave activity below 100 m. Most remarkable about this event is a series of amplifying temperature oscillations, most pronounced at the 4.5 m, 6.9 m and 10.3 m levels, resulting in a 4 K cooling event observed at the 10.3-m level. This event is accompanied by a gradual shift of the near surface wind direction to a northerly direction starting at the surface and propagating upward. The resulting local directional wind shear causes the wave to grow in amplitude and modulate the static stability in the lowermost 10 m, which increases non-linearity and eventually causes the wave to collapse, resulting in enhanced near-surface turbulence (RQ-3c). Due to the short du-

ration of this event of about 10 min, vertical UAS profiles could not provide further insight, since the nearest multicopter profile was sampled about 10 min after the end of the event.

The third case study was again characterized by a VSBL with a strong surface-based inversion and weak near-surface winds. The vertically pointing sodar and Doppler wind lidar indicated an internal gravity wave with a period of 4 min below 200 m. When the wave was eventually breaking it caused enhanced turbulence in the before weakly turbulent near-surface layers. Combining UAS temperature profiles from the preceding period with the lidar wind speed profiles corresponding to the flight times, we computed profiles of the gradient Richardson number. These profiles indicated a layer of weaker stability, associated with the shear above the core of a forming LLJ, which subsided to lower levels over the course of the UAS profiles (RQ-3d). For the same period, the time series of lidar wind speed indicated a downward transfer of momentum, consistent with the evolution of the LLJ. Due to the weaker stability and its high amplitude, the wave eventually became unstable, resulting in a strong turbulent burst in the layer below 75 m. Wavelet estimates from the 10-m vertical velocity showed how this wave-breaking event triggered a turbulence cascade to smaller scales (RQ-3c).

Finally, we used our observational data from the 10-m and 46-m masts, and the SUMO for a first qualitative model validation study, comparing three different types of models, i.e., an operational NWP model, a single-column model (SCM) and a large-eddy simulation (LES) model. This validation confirms that the structure of the VSBL was inadequately represented by the NWP and SCM, whereas the LES was able to resolve the very shallow SBL observed during the validation period. We attribute this behaviour to the turbulence parameterization schemes employed in the SCM and NWP model that lead to excessive turbulent mixing in the SBL, and differences in the model initialization.

This manuscript presents the ISOBAR project and its two main field campaigns. In particular ISOBAR18 can be considered as a very extensive SBL campaign, which is unique in the way UAS are used to supplement ground-based in-situ and remote-sensing systems at a unprecedented high temporal resolution. Our innovative observation strategy and the novel UAS data processing methods, I developed (Section 5.3.2), resulted in a unique, high-resolution data set on the SBL of high quality. In a number of case studies for which I present my analysis and interpretation, I demonstrate the potential of this observation approach and data set to gain new insight on the SBL evolution and different interaction processes.

In **Paper IV** we present MASC-3, a highly sophisticated UAS, designed for direct observations of turbulence in the ABL. The article provides detailed information on technical aspects of the UAS, including the airframe design, autopilot and payload components, software systems, operation modes and data processing procedures. Furthermore, we validate the UAS wind and mechanical turbulence observation system based on data sampled during ISOBAR18 to address research questions RQ-4. One measurement flight, when MASC-3 was operated approximately at the level of the highest EC system, was used to compare observations of various key turbulence variables from the two different systems to one another. A second UAS flight, consisting of three individual vertical profiles, is used to demonstrate the capabilities of MASC-3 to sample vertical profiles of basic meteorological and turbulent variables, which are also compared to mast and sodar profiles.

The meteorological conditions during the two validation flights, which were carried out during the afternoon and evening of the same day, were characterized by a relatively strong but weakening pressure gradient resulting in moderate wind speeds of approximately $10\,\mathrm{m\,s^{-1}}$ and $6\,\mathrm{m\,s^{-1}}$ at the 10-m level, respectively. During both cases a shallow surface-based inversion was present. With maximum near surface lapse rates of $0.05\,\mathrm{K\,m^{-1}}$ and $0.10\,\mathrm{K\,m^{-1}}$, respectively, these inversions were relatively weak compared to the most extreme conditions sampled during ISOBAR18. The state of the ABL can thus be categorized as weakly-stable.

For the validation against the stationary EC system, MASC-3 performed two horizontal, straight legs at an altitude (mean and standard deviation) of $(11.7 \pm 0.2)\,\mathrm{m}$ and $(11.4 \pm 0.3)\,\mathrm{m}$, respectively, so slightly above the EC observation height of $10.3\,\mathrm{m}$. The flight legs were both oriented to the south, corresponding to head-wind conditions. The direction of the legs was chosen based on the mean wind direction at the 100-m level, which was from the south. Note that the 10-m wind direction was SSE. From the northern turning point, located near the 10-m mast, the legs extended approximately 1100 m southward. Considering the UAS airspeed of $19.7\,\mathrm{m\,s^{-1}}$ and the mean horizontal wind speed of $9.25\,\mathrm{m\,s^{-1}}$, the mean sampling period for each leg of 80 s corresponds to a time period of 170 s. According to Taylor's hypothesis (Taylor, 1938), the air mass with its mean turbulence properties, as sampled by the UAS along a straight leg, is advected past the stationary mast over a period of 170 s. For each UAS leg and the corresponding EC time series the mean wind speed and direction, variance of the horizontal and vertical wind, turbulent kinetic energy, kinematic momentum flux, and integral length scales of the horizontal and vertical wind, are computed and compared. In addition turbulent power spectra and structure function of the horizontal and vertical wind are validated.

We find MASC-3 observations of mean wind and variables of mechanical turbulence in good agreement with point observations from the mast. The inertial subrange and production range can clearly be identified at very similar wave numbers in the turbulence power spectra and structure function for both observation systems. Existing minor differences are likely to be related to substantial vertical gradients in turbulence properties and the slight offset in observation height. Mean wind and turbulence quantities, averaged along horizontal flight legs (quasi-spatial averaging), show also good agreement to the corresponding time-averaged EC data, with smaller differences being present mainly in the quantities related to the horizontal wind (RQ-4a). The vertical gradients evident in the data from the three EC levels ($2.0\,\mathrm{m}$, $4.5\,\mathrm{m}$ and $10.3\,\mathrm{m}$) support the interpretation that the noted differences are partially caused by the offset in observation altitude. Other factors potentially contributing to discrepancies between the EC and MASC-3 observations are: the questionable assumption of Taylor's hypothesis with respect to surface heterogeneities affecting larger scales of turbulent motions, random turbulence sampling errors, temporal variations of the MASC-3 observation height and air speed, uncertainties related to the calibration and alignment of the five-hole probe and the accuracy of the individual sensors required for the transformation to turbulent fluctuations in an earth-bound coordinate system (RQ-4b).

The second UAS flight is used to demonstrate the capabilities of MASC-3 to determine vertical profiles of mean and turbulent quantities. The flight consisted of three individual profiles (two ascents and one descent), during which two horizontal flight legs (only considering head-wind conditions) per observation level were performed.

The observation levels ranged from approximately 15 m to 145 m and were vertically separated by increments of 20 m to 25 m and the flight legs had the same length and orientation as in the previous flight mentioned above. For a qualitative assessment of the UAS profiles the corresponding variables determined from the three EC systems are used to check the consistency of the UAS observations at the lower flight levels. In addition, profiles of mean wind speed and direction are compared to the corresponding sodar observations with a 10-min time resolution. Each UAS profile took between 16 min and 30 min.

The profiles of mean wind, direction and potential temperature agree very well to the corresponding observations from the mast (near the surface) and the sodar (wind speed and direction above the lowest resolved level at 35 m) for the first ascent and descent profiles (RQ-4c). The profile taken during the second ascent over a period of 26 min shows higher discrepancy to the reference observation and reveals a feature resembling a LLJ, which cannot be detected in any of the sodar profiles. However, the corresponding sodar profiles clearly indicate a strong decrease in wind speed at all observation levels during the time period of this last profile. The fact that the lower part of the last MASC-3 profile was sampled before this transition started explains the jet-like shape of the wind speed profile (RQ-4c). The UAS profiles of turbulence variables (i.e., variance of horizontal and vertical wind; turbulent kinetic energy; and the kinematic momentum flux) are in overall good agreement to the mast observations (RQ-4c) but also show clear signs of being strongly influenced by temporal changes of the prevailing conditions. In addition to the above-mentioned decrease in wind speed, the surface heat fluxes strongly responded to a substantial decrease in cloud cover. Especially at the elevated levels, turbulence does not seem to be in balance with the surface conditions as a result of this non-stationarity (RQ-4d).

Novel aspects of this work are the validation of direct turbulence observations based on UAS against an EC system in a WSBL, and the interpretation of UAS profiles of mean and turbulence variables supported by ground-based remote-sensing systems. In the presented case it becomes evident that the information contained in the UAS profiles may be misinterpreted without the additional knowledge on the temporal evolution of the ABL, as obtained from the sodar observations. To this article I contributed by analysing the sodar, radiation and cloud observation reference data, which led to detection of substantial temporal changes of the atmospheric forcing conditions. This finding was essential for the correct interpretation of the corresponding UAS profiles, which were largely affected by non-stationarity.

In **Paper V** we apply the local scaling scheme (Nieuwstadt, 1984), an extension of traditional MOST, and an alternative gradient-based scaling scheme to the ISOBAR18 data from the 10-m mast, and validate corresponding definitions of similarity functions (Dyer, 1974; Sorbjan and Grachev, 2010; Sorbjan, 2010). Furthermore, we invert the application of the gradient-based scaling scheme to determine profiles of turbulence variables from vertical UAS profile data and evaluate the quality of this novel approach and its limitation. In this manuscript we attempt to address research questions RQ-5.

The flux–gradient relationships, in the form of the local scaling scheme after Nieuwstadt (1984) (Equations 2.1 and 2.4), applied to the 10-min averaged turbulent fluxes and vertical gradients observed on the 10-m mast, collapse to universal functions of the local Obukhov stability parameter, for onshore flow. However, we note slightly better agreement for data sampled at the 4.5-m level compared to the observation levels

at 2.0 m and 10.3 m. The determination of the vertical gradients (see Equation 2.1) is based on a second-order polynomial fit as a function of the logarithmic measurement height, and thus ideally requires several observation levels above and below the EC level to which the flux–gradient relationship is applied. This condition is best fulfilled at the 4.5-m level, whereas the temperature profile for the 10.3-m level has to be extrapolated. Furthermore, the analysis also shows clear signs of self-correlation. The application of Sorbjan's (2010) so-called master scaling shows good agreement to the similarity functions, as defined by Sorbjan and Grachev (2010); Sorbjan (2010), and appears to overcome the issue of self-correlation, but similar differences between the three observation levels, as found for the flux–gradient relationship, are evident (RQ-5a).

After this general evaluation of universal scaling laws for the ISOBAR18 mast data, we investigate the potential of estimating profiles of turbulence statistics based on temperature and wind profile observations from the CopterSonde UAS. For an accurate height allocation of the UAS data the observation altitude is post-processed as described in Section 5.3. Since the wind estimation method of the CopterSonde (see Section 5.1.3) is likely to be subject to higher uncertainties than the directly measured temperature data, we make use of additional sodar wind profiles to validate the quality of the estimates. Temperature data are low-pass filtered, offset and response-time corrected (see Section 5.3). The issue of the scaling scheme being designed for time-averaged EC and gradient data, whereas UAS provide profile observations of quasi-instantaneous character, is addressed by averaging two to three consecutive UAS profiles, typically covering a time period of about one hour. In a first step we compute profiles of the gradient Richardson number from temperature and wind data, both re-gridded in the vertical with a 5-m resolution, applying first-order centered finite differencing to determine vertical gradients of temperature and horizontal velocity components. Turbulence variables are then calculated by solving the set of equations (2.6–2.8). We provide several different estimates of the boundary-layer depth based on (a) vertical UAS profiles of wind speed, direction, temperature; (b) profiles of Ri determined from UAS data; (c) sodar attenuated backscatter profiles, to evaluate the vertical limit for this scaling approach. Since these estimates do not always provide consistent results and due to the fact that the boundary layer height if often poorly defined under very-stable conditions, we provide turbulence estimates for the entire vertical observation range and put the resulting profiles in perspective to our estimates of SBL depth. We present three case studies, each consisting of two to three individual UAS profiles (ascent) sampled during 1 h, to demonstrate this gradient-based flux and turbulence estimation method. These three cases cover a wide range of SBL conditions, with varying characteristics of the vertical temperature and wind profiles, and presence of internal gravity waves.

The first case, from IOP-8 (see Table 4.2 for a summary of the conditions), is characterized by an elevated inversion and a LLJ with a core velocity of $5 \, \mathrm{m \, s^{-1}}$ at 70 m. The estimates of SBL depth vary considerable between the three methods in use and suggest a range between 55 m to 125 m, with the lowest and highest value corresponding to the sodar and Ri estimates, respectively. The resulting profiles of Ri and turbulence variables u_*, $\overline{w'\theta'}$, σ_w, σ_θ, indicate a dynamically near-neutral layer with weak fluxes and turbulence, topped by a weakly-stable layer, associated with the elevated inversion and the wind shear caused by the LLJ. The profiles of turbulence variables match the ob-

servations from the three mast levels very well and display a physical plausible shape. Above a height of about 100 m, the profiles of u_* and $\overline{w'\theta'}$ approach zero. Also σ_w and σ_θ show reduced values above this height, but mostly considerably larger than zero and with substantial scatter, in particular for σ_w. The layer above 125 m, potentially even lower, is clearly outside the SBL and the application of the scaling parameter z (2.6), i.e., the height above ground, becomes very doubtful. The WINDCUBE v1 lidar (see Section 5.1) also provides profile time series of mean wind speed and vertical velocity standard deviation, which we use for an additional validation of the corresponding UAS profiles. Despite the much coarser vertical resolution of the lidar (20 m), the horizontal wind speed and also the standard deviation of the vertical wind agree in shape and roughly in their mean values. However, the UAS profile reveal a higher scatter and stronger gradients, which can be explained by spatial and temporal sampling differences.

The second case origins from IOP-10 (Table 4.2) and was characterized by a slightly elevated inversion with the strongest temperature gradients between 90 m and 100 m. The winds in the lowermost 10 m were calm, but increased above this level reaching a local maximum at about 200 m. The computed profile of Ri, indicates very-stable conditions in the atmospheric column from 10 m to 120 m and a tendency to rather neutral conditions above, with some scatter indicating shallow layers of both unstable and very-stable conditions. The sodar echogram indicates a double layer structure with a surface-based turbulent layer extending to a mean altitude of 35 m and an elevated layer, which is subject to wave like motions of roughly 2-min period, between 75 m and 200 m. Based on the temperature and wind speed profiles and Ri profiles we estimated the SBL depth to 80 m and 60 m, respectively.

The resulting turbulence profiles agree well to the EC observations, displaying very weak fluxes below 120 m. They only deviate from zero at about 70 m, where Ri indicates a shallow weakly-stable layer, coinciding with the top of the SBL. Above 120 m, more layers display positive and negative deviations from zero for u_* and $\overline{w'\theta'}$, respectively, which is likely to be related to internal gravity waves at these altitudes. The profiles of the standard deviations, σ_w and σ_θ, are subject to larger scatter with increasing height, but agree to the EC observations near the surface. UAS estimates of σ_w are qualitatively similar to the lidar observations, however, the variability appears much larger.

During the third case, also sampled during IOP-10 (Table 4.2), a strong surface-based inversion was present, while the wind in the lowermost 50 m was relatively weak but subject to considerable directional shear. These conditions are reflected in the UAS-based Ri profile, by high stability values, with Ri > 0.5 and up to Ri = 5.5, in the lowermost 120 m. Above this layer, the dynamic stability indicates an average shift to more neutral stability with higher variability and two shallow layers of strong instability centered at about 170 m and 200 m. From the sodar echogram we can identify a very shallow surface-based turbulent layer with a depth of only 20 m and a second turbulent layer from on average 60 m to 120 m, which is most likely the result from turbulence induced by elevated shear. UAS profiles of the basic meteorological parameters and profiles of Ri suggest an SBL depth of 80 m and 20 m, respectively. The resulting profiles of turbulence variables are all close to zero near the surface, which is in agreement with the surface-based observations. All show a major peak centered at about 70 m (with negative kinematic heat flux), which is associated with the strong wind shear at

this level. At higher levels, turbulence parameters are in general closer to zero again, with some scatter at levels of near-neutral stability. However, these levels are clearly outside of the SBL and the applied scaling with the height above surface is thus doubtful. The lidar-estimated σ_w profile is very smooth compared to the UAS profile, which shows substantial scatter. Apart from the uncertainty of turbulence estimates at levels above the SBL, this could also be explained by the differences in spatiotemporal sampling between the systems.

In this paper we introduce a novel approach for estimating turbulent fluxes beyond the highest observation level of a micrometeorological mast and in the entire SBL. In this method we first apply a gradient-based turbulence scaling scheme to the micrometeorological mast data, and after this validation to UAS profile observations within and above the SBL. To this work I contributed to the development of the general concept and methodology of this approach, and processed the EC data from the 10-m mast, the lidar and sodar. Furthermore, I contributed to several different data processing steps, in particular for the estimation of vertical gradients from the mast and UAS data and the sensor calibration, altitude and response time correction of the UAS data. I also carried out the analysis of the different profile data to estimate the depth of the SBL and provided the interpretation for the different layers, seen in the sodar echogram, as well as a critical evaluation of the vertical validity of the gradient-based turbulence estimates.

7 Conclusions and outlook

This thesis targets the SBL over Arctic sea ice, by employing a new observational approach based on the extensive use of UAS to supplement ground-based observations from meteorological masts and remote-sensing systems. Furthermore, a part of this thesis is dedicated to considerations related to the quality of UAS observations for ABL research in general. In particular, the comparability of different UAS to one another and other ABL observation systems, and corresponding data post-processing procedures. Three major field campaigns were carried out. Two of them targeting the SBL over the ice-covered Bothnian Bay at the Finnish island Hailuoto during February 2017 and 2018 (ISOBAR17 and ISOBAR18), and one in the San Luis Valley in Colorado in July 2018 (LAPSE-RATE), during which we conducted the most extensive UAS intercomparison study to date. An additional test and validation field campaign was conducted as part of ISOBAR during two weeks in November and December 2016. Data from the three major field campaigns formed the basis for the three papers presented in this thesis.

The SBL observations from ISOBAR17 and ISOBAR18 showed overall good agreement between the different observation systems employed. Detailed insight into the evolution of the SBL could be gained from frequent multicopter boundary-layer profiles, at high vertical resolution. We found the SBL being subject to rapid changes in both, the surface meteorological parameters and the vertical structure. Various VSBL processes, such as shear and wave instabilities and their interactions with turbulence, could be investigate in detail based on a number of case studies using complementary data from the different observation systems.

ISOBAR17 and ISOBAR18 also provided the opportunity for the first application of a number of new UAS, e.g., Bebop2Met, CopterSonde and MASC-3. We also adapted and applied a new method to estimate wind speed and direction profiles based on multicopter attitude data and applied this method to the Bebop2Met and CopterSonde UAS. During ISOBAR18, MASC-3, a fixed-wind UAS designed for direct observations of turbulence within the ABL, was validated against ground-based reference systems under WSBL conditions. Near-surface observations on mean and turbulence variables were in good agreement with stationary mast observations, but due to strongly non-stationary conditions vertical profiles of turbulence and mean parameters were hard to interpret without additional reference measurements from remote-sensing profiling systems. However, some issues remain related to the accuracy and precision of all relevant subsystems required for high-quality turbulence observations, in particular in the VSBL. Furthermore the complexity of such UAS currently still requires intensive and time consuming flight preparation procedures, which limits the capability of the system for semi-continuous observations and resulted in a relatively low number of successful scientific flights during ISOBAR18.

Based on the ISOBAR18 data set we utilize a new method to retrieve profiles of turbulent fluxes from UAS observations, by inverting a gradient-based SBL scaling scheme proposed by Sorbjan (2010). We first validate this method by scaling turbulence variables from the EC systems on the micrometeorological mast with their corresponding scaling variables and comparing them to the semi-empirical similarity func-

tions proposed by (Sorbjan and Grachev, 2010; Sorbjan, 2010). After this successful validation we apply this method to UAS profiles for three case studies, characterized by different stability, SBL depth and structure of the SBL and the layers above. Furthermore, we estimate the depth of the SBL based on sodar and UAS profiles of wind and temperature, and the derived Ri profiles. These SBL depth estimates are used for a critical evaluation of the limitations of this turbulence estimation method, in terms of the vertical applicability. We find the derived profiles of turbulence variables within the SBL in good agreement with the corresponding variables derived near the surface from the 10-m mast and lidar observations at levels above 45 m.

Overall, the findings from ISOBAR17 and ISOBAR18 have shown the potential to contributed to an improved understanding of the governing processes in the SBL and VSBL. The full analysis of the collected data set is, however, far beyond the volume of one single doctoral project and might engage boundary layer scientists during the coming decade(s). In this context, we are in the process of documenting and publishing the ISOBAR data sets following traceable data archiving standards, to enable other researchers to work with our data. Yet, I would also like to give an overview of my vision on the many ways to expand on the ISOBAR data sets. So far the investigations on the different SBL processes were based on a few selected case studies, whereas the data sets from the 14 IOPs include a fair number of additional interesting cases for in-depth analyses. Further insight may be achieved by a more general approach, e.g., by computing composite time series and vertical profiles of the relevant parameters for different processes similar to a study on microfronts by Mahrt (2019). So far, we broadly distinguish only between the weakly-stable and very-stable regime. A more sophisticated categorization, following common definitions or potentially applying new regime definitions, will also be of high relevance for investigations on the validity and limitation of similarity theory and attempts to find more sophisticated formulations also valid in the VSBL. Future studies, as the ones suggested here, would also highly benefit from the inclusion of other relevant SBL data sets, such as SHEBA or CASES-99.

The ISOBAR project also included a work package on numerical modeling experiments based on our observations. A first validation experiment of rather qualitative character has already been carried out and is shortly presented in Paper III. At present, our project partners are working on process studies based on state-of-the-art mesoscale and single-column models. In addition, they plan to perform LES studies to evaluate gradient-based similarity relationships. Ideally this will enable us to develop new SBL parametrization schemes. Those will be implemented in NWP and single-column models and validated against observational data from the IOPs.

The UAS intercomparison study, conducted during the LAPSE-RATE field campaign, gave important insight into the quality of airborne in-situ observations with respect to sensor types and integration solutions. The study closes with a number of recommendations, amongst others on best practices for altitude post-processing procedures, which should be applied to systems not capable of high-precision position measurements. These procedures have already been applied for the synthesis of UAS data from the ISOBAR18 campaign. In the field of UAS-based atmospheric research there is still a general need for community standards and best practices, in terms of sensor requirements, sampling strategies, calibration and data processing procedures.

A number of issues, however, need further attention in the near future to improve the quality of UAS atmospheric data. Uncertainties in the altitude measurements, which are

very critical in the SBL with its typically strong vertical gradients, can be avoided by making use of high-precision differential or real-time kinematic (RTK) GNSS. In addition to a better height allocation of the observations, this also opens new perspectives on low-level UAS observations from fixed-wing aircraft, in particular for turbulence observations at atmospheric levels with prevailing strong vertical gradients. The issue of sensor response times, which is especially problematic for humidity measurements in cold environments, should receive higher attention, in terms of: the development and implementation of faster sensors, e.g., miniaturized dew-point mirrors; a better characterization of the sensor time constants, including its dependency on other parameters, as in particular temperature; and the development of standardized response-time correction procedures. A number of groups in the field of UAS research are currently working on different approaches for multicopter-based wind observations and promising results have been reported (Neumann and Bartholmai, 2015; Palomaki et al., 2017; Wang et al., 2018; González-Rocha et al., 2020; Segales et al., 2020). However, the validation of these methods is often based on relatively small data sets in limited ranges of wind speeds. One issue that has not yet attracted a lot of attention is the potential of induced mixing by rotary-wing UAS. Especially for larger systems this may be problematic, since the rotor downwash may induce substantial vertical motions, masking other much weaker processes in the SBL. This may contaminate the UAS measurements itself or observations by other systems, located nearby or even in larger distances. This may also cause a seemingly constant bias for rotor-aspirated thermodynamic sensors, when sampling in strong inversions (Greene et al., 2019b).

One of the strengths of UAS, the possibility of frequently repeated flights, at the moment still comes at the cost of the required manpower for its operation. Especially operations during polar night are demanding, and although the sampling frequency of vertical profiles in particular during ISOBAR18 was very high, even denser temporal sampling would be beneficial, to also sample vertical profiles during phenomena lasting only a couple of minutes. Sampling turbulence spatially has a number of advantages over the traditional method of fixed-point EC observations. Fixed-wing UAS equipped with turbulence resolving sensors can sample a specific air mass in a much shorter time period compared to fixed-point observations, and thus reduce the problem of non-stationarity, considerably. This offers a great potential to advance in the field of SBL research, in particular in VSBL conditions. However, obtaining representative turbulence observations from these platforms also involves systemic challenges due to measured parameters (e.g., air speed, UAS speed, and attitude angles) being an order of magnitude larger than the turbulent fluctuations, so that these parameters have to be measured with extremely high precision and accuracy to resolve the very weak turbulent fluctuations typical for the VSBL. Strong vertical gradients, also characteristic for the VSBL, cause another challenge, as even small variations in flight altitude may alter the observations substantially. A much better altitude control for UAS autopilots can be achieved by the implementation of the latest generations of GNSSs with RTK capabilities.

The still rapid development in UAS technology, small and lightweight sensors and analysis tools opens new paths for UAS-based atmospheric research. During ISOBAR17 and ISOBAR18 we adjusted our flight plans and strategies with the help of real-time data visualization tools for the different observation systems, e.g., to focus on layers with strong vertical gradients. I recommend to push this approach even further

to autonomous intelligent flight strategies, e.g., by automatically using information like strong vertical oscillations detected by a Doppler lidar or sodar system for guiding a UAS to the relevant layer. Thermography based on infra-red cameras, photogrametry or small geo-lidar systems, offer new perspectives for the investigation of the role of heterogeneities in terms of variability in the surface temperature (Cuxart et al., 2016) and surface roughness. UAS-based observations of radiation flux divergence are expected to be less prone to uncertainties related to sensor biases than mast-based observations. For the investigation of gravity waves in the SBL, which are often stationary, fixed-point observations are only of limited value. Here, the integration of microbarograph sensors into fixed-wing UAS could offer an exciting opportunity.

Future SBL campaigns would in general benefit a lot from further improved observation strategies, also including new technological developments. Such strategies should include swarm operations by multiple UAS, simultaneously probing the SBL at different locations. One example is the horizontal sampling from multiple fixed-wing UAS at low altitudes, combined with co-located multicopters performing vertical profiles. This would further increase the resolution in the spacial domain, which is expected to give deeper insight into a number of still poorly understood SBL processes (Mahrt, 2014). In addition, such strategies should also make use of other new and exciting observation techniques, such as, multicopter-mounted wind lidars (Vasiljević et al., 2020) and turbulence resolving sonic anemometers, or distributed wind and temperature sensing methods from three-dimensional arrays of fibre optics (Thomas et al., 2012; Sayde et al., 2015; Lapo et al., 2020) and adaptive networks of scanning wind lidars (Floors et al., 2016; Cheynet et al., 2017; Valldecabres et al., 2018). Distributed wind and temperature sensing could even be combined with UAS, e.g., two or more coordinated multicopters spanning an array of fibres and by that extending the vertical range of such installations.

Bibliography

Acevedo, O. C., F. D. Costa, P. E. S. Oliveira, F. S. Puhales, G. A. Degrazia, and D. R. Roberti, 2014: The influence of submeso processes on stable boundary layer similarity relationships. *J. Atmos. Sci.*, **71 (1)**, 207–225, doi:10.1175/jas-d-13-0131. 1. 9

Anderson, P. S., 2003: Fine-scale structure observed in a stable atmospheric boundary layer by sodar and kite-borne tethersonde. *Bound.-Layer Meteor.*, **107 (2)**, 323–351, doi:10.1023/A:1022171009297. 6, 11

Anderson, P. S., 2009: Measurement of Prandtl number as a function of richardson number avoiding self-correlation. *Bound.-Layer Meteor.*, **131 (3)**, 345–362, doi:10.1007/s10546-009-9376-4. 11

Andreas, E. L., and K. J. Claffey, 1995: Air-ice drag coefficients in the western Weddell Sea: 1. Values deduced from profile measurements. *J. Geophys. Res.*, **100 (C3)**, 4821, doi:10.1029/94jc02015. 11

Andreas, E. L., K. J. Claffy, and A. P. Makshtas, 2000: Low-level atmospheric jets and inversions over the western Weddell Sea. *Bound.-Layer Meteor.*, **97 (3)**, 459–486, doi:10.1023/A:1002793831076. 6

Andreas, E. L., R. E. Jordan, and A. P. Makshtas, 2005: Parameterizing turbulent exchange over sea ice: The Ice Station Weddell results. *Bound.-Layer Meteor.*, **114 (2)**, 439–460, doi:10.1007/s10546-004-1414-7. 11

Atlaskin, E., and T. Vihma, 2012: Evaluation of NWP results for wintertime nocturnal boundary-layer temperatures over Europe and Finland. *Quart. J. Roy. Meteor. Soc.*, **138 (667)**, 1440–1451, doi:10.1002/qj.1885. 1

Baas, P., G. J. Steeneveld, B. J. H. van de Wiel, and A. A. M. Holtslag, 2006: Exploring self-correlation in flux-gradient relationships for stably stratified conditions. *J. Atmos. Sci.*, **63 (11)**, 3045–3054, doi:10.1175/JAS3778.1. 9

Banta, R., 2008: Stable-boundary-layer regimes from the perspective of the low-level jet. *Acta Geophys.*, **56 (1)**, 58–87, doi:10.2478/s11600-007-0049-8. 9

Banta, R. M., Y. L. Pichugina, and W. A. Brewer, 2006: Turbulent velocity-variance profiles in the stable boundary layer generated by a nocturnal low-level jet. *J. Atmos. Sci.*, **63 (11)**, 2700–2719, doi:10.1175/jas3776.1. 9

Banta, R. M., Y. L. Pichugina, and R. K. Newsom, 2003: Relationship between low-level jet properties and turbulence kinetic energy in the nocturnal stable boundary layer. *J. Atmos. Sci.*, **60 (20)**, 2549–2555, doi:10.1175/1520-0469(2003)060<2549:rbljpa>2.0.co;2. 9

Båserud, L., J. Reuder, M. O. Jonassen, T. A. Bonin, P. B. Chilson, M. A. Jiménez, and P. Durand, 2019: Potential and limitations in estimating sensible-heat-flux profiles from consecutive temperature profiles using remotely-piloted aircraft systems. *Bound.-Layer Meteor.*, **174 (1)**, 145–177, doi:10.1007/s10546-019-00478-9. 12

Båserud, L., J. Reuder, M. O. Jonassen, S. T. Kral, M. B. Paskyabi, and M. Lothon, 2016: Proof of concept for turbulence measurements with the RPAS SUMO during the BLLAST campaign. *Atmos. Meas. Tech.*, **9 (10)**, 4901–4913, doi:10.5194/amt-9-4901-2016. 12

Belušić, D., and L. Mahrt, 2008: Estimation of length scales from mesoscale networks. *TELLUS A*, **60 (4)**, 706–715, doi:10.1111/j.1600-0870.2008.00328.x. 6

Blumen, W., R. Banta, S. P. Burns, D. C. Fritts, R. Newsom, G. S. Poulos, and J. Sun, 2001: Turbulence statistics of a Kelvin–Helmholtz billow event observed in the night-time boundary layer during the Cooperative Atmosphere–Surface Exchange Study field program. *Dyn. Atmos. Oceans*, **34 (2-4)**, 189–204, doi:10.1016/s0377-0265(01)00067-7. 7

Bonin, T., P. Chilson, B. Zielke, and E. Fedorovich, 2013: Observations of the early evening boundary-layer transition using a small unmanned aerial system. *Bound.-Layer Meteor.*, **146 (1)**, 119–132, doi:10.1007/s10546-012-9760-3. 11

Bradley, S., 2008: *Atmospheric acoustic remote sensing*. CRC Press, Boca Raton. 27, 28

Businger, J. A., J. C. Wyngaard, Y. Izumi, and E. F. Bradley, 1971: Flux-profile relationships in the atmospheric surface layer. *J. Atmos. Sci.*, **28 (2)**, 181–189, doi:10.1175/1520-0469(1971)028<0181:FPRITA>2.0.CO;2. 8

Byrkjedal, Ø., I. Esau, and N. G. Kvamstø, 2007: Sensitivity of simulated wintertime Arctic atmosphere to vertical resolution in the ARPEGE/IFS model. *Climate Dyn.*, **30 (7-8)**, 687–701, doi:10.1007/s00382-007-0316-z. 1

Cassano, J. J., 2013: Observations of atmospheric boundary layer temperature profiles with a small unmanned aerial vehicle. *Antarct. Sci.*, **26 (02)**, 205–213, doi:10.1017/s0954102013000539. 12

Cassano, J. J., J. A. Maslanik, C. J. Zappa, A. L. Gordon, R. I. Cullather, and S. L. Knuth, 2010: Observations of antarctic polynya with unmanned aircraft systems. *EOS, Trans., Am. Geophys. Union*, **91 (28)**, 245, doi:10.1029/2010eo280001. 12

Cava, D., L. Mortarini, D. Anfossi, and U. Giostra, 2019a: Interaction of submeso motions in the Antarctic stable boundary layer. *Bound.-Layer Meteor.*, **171 (2)**, 151–173, doi:10.1007/s10546-019-00426-7. 6, 11

Cava, D., L. Mortarini, U. Giostra, O. Acevedo, and G. Katul, 2019b: Submeso motions and intermittent turbulence across a nocturnal low-level jet: A self-organized criticality analogy. *Bound.-Layer Meteor.*, doi:10.1007/s10546-019-00441-8. 9

Cheynet, E., J. Jakobsen, J. Snæbjörnsson, J. Mann, M. Courtney, G. Lea, and B. Svardal, 2017: Measurements of surface-layer turbulence in a wide Norwegian fjord using synchronized long-range Doppler wind lidars. *Remote Sensing*, **9 (10)**, 977, doi:10.3390/rs9100977. 62

Cohen, L., S. R. Hudson, V. P. Walden, R. M. Graham, and M. A. Granskog, 2017: Meteorological conditions in a thinner Arctic sea ice regime from winter through summer during the Norwegian Young Sea Ice expedition (N-ICE2015). *J. Geophys. Res.: Atmos.*, **122 (14)**, 7235–7259, doi:10.1002/2016jd026034, URL http://dx.doi.org/10.1002/2016JD026034, 2016JD026034. 11

Conangla, L., J. Cuxart, and M. R. Soler, 2008: Characterisation of the nocturnal boundary layer at a site in northern Spain. *Bound.-Layer Meteor.*, **128 (2)**, 255–276, doi:10.1007/s10546-008-9280-3. 7

Curry, J. A., J. Maslanik, G. Holland, and J. Pinto, 2004: Applications of aerosondes in the arctic. *Bull. Amer. Meteor. Soc.*, **85 (12)**, 1855–1862, doi:10.1175/bams-85-12-1855. 12

Cuxart, J., C. Yagüe, G. Morales, E. Terradellas, J. Orbe, J. Calvo, A. Fernández, M. R. Soler, C. Infante, P. Buenestado, A. Espinalt, H. E. Joergensen, J. M. Rees, J. Vilá, J. M. Redondo, I. R. Cantalapiedra, and L. Conangla, 2000: Stable atmospheric boundary-layer experiment in Spain (SABLES 98): A report. *Bound.-Layer Meteor.*, **96 (3)**, 337–370, doi:10.1023/a:1002609509707. 11

Cuxart, J., B. Wrenger, D. Martínez-Villagrasa, J. Reuder, M. O. Jonassen, M. A. Jiménez, M. Lothon, F. Lohou, O. Hartogensis, J. Dünnermann, L. Conangla, and A. Garai, 2016: Estimation of the advection effects induced by surface heterogeneities in the surface energy budget. *Atmos. Chem. Phys.*, **16 (14)**, 9489–9504, doi:10.5194/acp-16-9489-2016. 62

de Boer, G., C. Diehl, J. Jacob, A. Houston, S. W. Smith, P. Chilson, D. G. Schmale, J. Intrieri, J. Pinto, J. Elston, D. Brus, O. Kemppinen, A. Clark, D. Lawrence, S. C. C. Bailey, M. P. Sama, A. Frazier, C. Crick, V. Natalie, E. Pillar-Little, P. Klein, S. Waugh, J. K. Lundquist, L. Barbieri, S. T. Kral, A. A. Jensen, C. Dixon, S. Borenstein, D. Hesselius, K. Human, P. Hall, B. Argrow, T. Thornberry, R. Wright, and J. T. Kelly, 2019: Development of community, capabilities and understanding through unmanned aircraft-based atmospheric research: The LAPSE-RATE campaign. *Bull. Amer. Meteor. Soc.*, doi:10.1175/bams-d-19-0050.1. 22, 32

Dörenkämper, M., B. Witha, G. Steinfeld, D. Heinemann, and M. Kühn, 2015: The impact of stable atmospheric boundary layers on wind-turbine wakes within offshore wind farms. *J. Wind Eng. Ind. Aerodyn.*, **144**, 146–153, doi:10.1016/j.jweia.2014.12.011. 1

Dyer, A. J., 1974: A review of flux-profile relationships. *Bound.-Layer Meteor.*, **7 (3)**, 363–372, doi:10.1007/bf00240838. 54

Elston, J., B. Argrow, M. Stachura, D. Weibel, D. Lawrence, and D. Pope, 2015: Overview of small fixed-wing unmanned aircraft for meteorological sampling. *J. Atmos. Oceanic Technol.*, **32 (1)**, 97–115, doi:10.1175/jtech-d-13-00236.1. 2, 29

Esau, I., R. Davy, and S. Outten, 2012: Complementary explanation of temperature response in the lower atmosphere. *Environ. Res. Lett.*, **7 (4)**, 044 026, doi:10.1088/1748-9326/7/4/044026. 1

Fernando, H. J. S., and J. C. Weil, 2010: Whither the stable boundary layer? *Bull. Amer. Meteor. Soc.*, **91 (11)**, 1475–1484, doi:10.1175/2010BAMS2770.1, https://doi.org/10.1175/2010BAMS2770.1. 1, 2

Fernando, H. J. S., E. R. Pardyjak, S. Di Sabatino, F. K. Chow, S. F. J. De Wekker, S. W. Hoch, J. Hacker, J. C. Pace, T. Pratt, Z. Pu, W. J. Steenburgh, C. D. Whiteman, Y. Wang, D. Zajic, B. Balsley, R. Dimitrova, G. D. Emmitt, C. W. Higgins, J. C. R. Hunt, J. C. Knievel, D. Lawrence, Y. Liu, D. F. Nadeau, E. Kit, B. W. Blomquist, P. Conry, R. S. Coppersmith, E. Creegan, M. Felton, A. Grachev, N. Gunawardena, C. Hang, C. M. Hocut, G. Huynh, M. E. Jeglum, D. Jensen, V. Kulandaivelu, M. Lehner, L. S. Leo, D. Liberzon, J. D. Massey, K. McEnerney, S. Pal, T. Price, M. Sghiatti, Z. Silver, M. Thompson, H. Zhang, and T. Zsedrovits, 2015: The MATERHORN: Unraveling the intricacies of mountain weather. *Bull. Amer. Meteor. Soc.*, **96 (11)**, 1945–1967, doi:10.1175/BAMS-D-13-00131.1. 11

Floors, R., A. Peña, G. Lea, N. Vasiljević, E. Simon, and M. Courtney, 2016: The RUNE experiment—a database of remote-sensing observations of near-shore winds. *Remote Sensing*, **8 (11)**, 884, doi:10.3390/rs8110884. 62

Foken, T., 2006: 50 Years of the Monin–Obukhov Similarity Theory. *Bound.-Layer Meteor.*, **119**, 431–447, doi:10.1007/s10546-006-9048-6. 8, 42

Foken, T., 2008: *Micrometeorology*. Springer Berlin Heidelberg, doi:10.1007/978-3-540-74666-9. 9, 25, 38

Foken, T., F. Wimmer, M. Mauder, C. Thomas, and C. Liebethal, 2006: Some aspects of the energy balance closure problem. *Atmos. Chem. Phys.*, **6 (2)**, 3381–3402, doi:10.5194/acpd-6-3381-2006. 39

Fritts, D. C., C. Nappo, D. M. Riggin, B. B. Balsley, W. E. Eichinger, and R. K. Newsom, 2003: Analysis of ducted motions in the stable nocturnal boundary layer during CASES-99. *J. Atmos. Sci.*, **60 (20)**, 2450–2472, doi:10.1175/1520-0469(2003)060<2450:aodmit>2.0.co;2. 6

Garnier, A., and M. L. Chanin, 1992: Description of a Doppler Rayleigh LIDAR for measuring winds in the middle atmosphere. *Appl. Phys. B: Photophys. Laser Chem.*, **55 (1)**, 35–40, doi:10.1007/bf00348610. 28

González-Rocha, J., S. F. J. D. Wekker, S. D. Ross, and C. A. Woolsey, 2020: Wind profiling in the lower atmosphere from wind-induced perturbations to multirotor UAS. *Sensors*, **20 (5)**, 1341, doi:10.3390/s20051341. 61

González-Rocha, J., C. A. Woolsey, C. Sultan, and S. F. J. D. Wekker, 2019: Sensing wind from quadrotor motion. *J. Guid. Control Dynam.*, **42 (4)**, 836–852, doi:10.2514/1.g003542. 31

Grachev, A. A., E. L. Andreas, C. W. Fairall, P. S. Guest, and P. O. G. Persson, 2008: Turbulent measurements in the stable atmospheric boundary layer during SHEBA: ten years after. *Acta Geophys.*, **56 (1)**, 142–166, doi:10.2478/s11600-007-0048-9. 11

Grachev, A. A., C. W. Fairall, P. O. G. Persson, E. L. Andreas, and P. S. Guest, 2005: Stable boundary-layer scaling regimes: The SHEBA data. *Bound.-Layer Meteor.*, **116 (2)**, 201–235, doi:10.1007/s10546-004-2729-0. 8, 9

Greene, B., A. Segales, T. Bell, E. Pillar-Little, and P. Chilson, 2019a: Environmental and sensor integration influences on temperature measurements by rotary-wing unmanned aircraft systems. *Sensors*, **19 (6)**, 1470, doi:10.3390/s19061470. 32

Greene, B. R., S. T. Kral, L. Båserud, P. B. Chilson, E. A. Pillar-Little, J. Reuder, A. R. Segales, A. Seidl, and B. Wrenger, 2019b: Synthesis and validation of meteorological parameters from different RPAS during the ISOBAR campaigns at Hailuoto. International Society for Atmospheric Research using Remotely piloted Aircraft (ISARRA) Meeting 2019, URL http://www.isarra.org/wp-content/uploads/2019/08/ISARRA_2019_Tue_Greene.pdf. 61

Guest, P., P. O. G. Persson, S. Wang, M. Jordan, Y. Jin, B. Blomquist, and C. Fairall, 2018: Low-level baroclinic jets over the New Arctic Ocean. *J. Geophys. Res. Oceans*, **123 (6)**, 4074–4091, doi:10.1002/2018jc013778. 6

Hoch, S. W., P. Calanca, R. Philipona, and A. Ohmura, 2007: Year-round observation of longwave radiative flux divergence in Greenland. *J. Appl. Meteorl. Clim.*, **46 (9)**, 1469–1479, doi:10.1175/jam2542.1. 6, 9

Högström, U., 1988: Non-dimensional wind and temperature profiles in the atmospheric surface-layer – A re-evaluation. *Bound.-Layer Meteor.*, **42 (1-2)**, 55–78, doi:10.1007/BF00119875. 8

Holdsworth, A. M., and A. H. Monahan, 2019: Turbulent collapse and recovery in the stable boundary layer using an idealized model of pressure-driven flow with a surface energy budget. *J. Atmos. Sci.*, doi:10.1175/jas-d-18-0312.1. 7

Holtslag, A. A. M., and F. T. M. Nieuwstadt, 1986: Scaling the atmospheric boundary layer. *Bound.-Layer Meteor.*, **36 (1-2)**, 201–209, doi:10.1007/bf00117468. 9

Holtslag, A. A. M., G. Svensson, P. Baas, S. Basu, B. Beare, A. C. M. Beljaars, F. C. Bosveld, J. Cuxart, J. Lindvall, G. J. Steeneveld, M. Tjernström, and B. J. H. Van De Wiel, 2013: Stable atmospheric boundary layers and diurnal cycles – Challenges for weather and climate models. *Bull. Amer. Meteor. Soc.*, **94 (11)**, 1691–1706, doi:10.1175/BAMS-D-11-00187.1. 1, 2, 5

Houston, A. L., B. Argrow, J. Elston, J. Lahowetz, E. W. Frew, and P. C. Kennedy, 2012: The collaborative colorado–nebraska unmanned aircraft system experiment. *Bull. Amer. Meteor. Soc.*, **93 (1)**, 39–54, doi:10.1175/2011bams3073.1. 11

Huffaker, R. M., and R. M. Hardesty, 1996: Remote sensing of atmospheric wind velocities using solid-state and CO_2 coherent laser systems. *Proc. IEEE*, **84 (2)**, 181–204, doi:10.1109/5.482228. 28

Jonassen, M., P. Tisler, B. Altstädter, A. Scholtz, T. Vihma, A. Lampert, G. König-Langlo, and C. Lüpkes, 2015: Application of remotely piloted aircraft systems in observing the atmospheric boundary layer over Antarctic sea ice in winter. *Polar Res.*, **34 (0)**, doi:10.3402/polar.v34.25651. 12, 30

Jonassen, M. O., 2008: The Small Unmanned Meteorological Observer (SUMO) – Characterization and test of a new measurement system for atmospheric boundary layer research. mathesis, Geophysical Institute, University of Bergen, URL http://www.uib.no/filearchive/master_jonassen.pdf. 42

Jonassen, M. O., H. Ólafsson, H. Ágústsson, O. Rögnvaldsson, and J. Reuder, 2012: Improving high-resolution numerical weather simulations by assimilating data from an unmanned aerial system. *Mon. Weather Rev.*, **140 (11)**, 3734–3756, doi:10.1175/MWR-D-11-00344.1. 12

Kallistratova, M. A., and R. D. Kouznetsov, 2011: Low-level jets in the Moscow region in summer and winter observed with a sodar network. *Bound.-Layer Meteor.*, **143 (1)**, 159–175, doi:10.1007/s10546-011-9639-8. 28

Karsisto, V., S. Tijm, and P. Nurmi, 2017: Comparing the performance of two road weather models in the Netherlands. *Wea. Forecasting*, **32 (3)**, 991–1006, doi:10.1175/waf-d-16-0158.1. 1

Knuth, S. L., and J. J. Cassano, 2014: Estimating Sensible and Latent Heat Fluxes Using the Integral Method from in situ Aircraft Measurements. *J. Atmos. Oceanic Technol.*, **31 (9)**, 1964–1981, doi:10.1175/JTECH-D-14-00008.1, http://dx.doi.org/10.1175/JTECH-D-14-00008.1. 12

Konrad, T. G., M. L. Hill, J. R. Rowland, and J. H. Meyer, 1970: A small, radio-controlled aircraft as a platform for meteorological sensor. *APL Tech. Dig.*, **10**, 11–19, 19710054637. 2

Kouznetsov, R. D., 2009: The multi-frequency sodar with high temporal resolution. *Meteorol. Z.*, **18 (2)**, 169–173, doi:10.1127/0941-2948/2009/0373. 19, 28

Lang, F., D. Belušić, and S. Siems, 2018: Observations of wind-direction variability in the nocturnal boundary layer. *Bound.-Layer Meteor.*, **166 (1)**, 51–68, doi:10.1007/s10546-017-0296-4. 6, 9

Lapo, K., A. Freundorfer, L. Pfister, J. Schneider, J. Selker, and C. Thomas, 2020: Distributed observations of wind direction using microstructures attached to actively heated fiber-optic cables. *Atmos. Meas. Tech.*, **13 (3)**, 1563–1573, doi:10.5194/amt-13-1563-2020. 62

Lee, T., M. Buban, E. Dumas, and C. Baker, 2018: On the use of rotary-wing aircraft to sample near-surface thermodynamic fields: Results from recent field campaigns. *Sensors*, **19 (1)**, 10, doi:10.3390/s19010010. 31

Lee, X., W. J. Massman, and B. E. Law, 2004: *Handbook of micrometeorology: a guide for surface flux measurement and analysis*. Atmospheric and oceanographic sciences library, KLUWER ACADEMIC PUBLISHERS, doi:10.1007/1-4020-2265-4. 25, 38

Lenschow, D. H., and P. Spyers-Duran, 1989: Measurement Techniques: Air Motion Sensing. *National Center for Atmospheric Research, Bulletin No. 23*, doi: https://www.eol.ucar.edu/raf/Bulletins/bulletin23.html. 35

Lothon, M., F. Lohou, D. Pino, F. Couvreux, E. R. Pardyjak, J. Reuder, J. Vilà-Guerau de Arellano, P. Durand, O. Hartogensis, D. Legain, P. Augustin, B. Gioli, D. H. Lenschow, I. Faloona, C. Yagüe, D. C. Alexander, W. M. Angevine, E. Bargain, J. Barrié, E. Bazile, Y. Bezombes, E. Blay-Carreras, A. van de Boer, J. L. Boichard, A. Bourdon, A. Butet, B. Campistron, O. de Coster, J. Cuxart, A. Dabas, C. Darbieu, K. Deboudt, H. Delbarre, S. Derrien, P. Flament, M. Fourmentin, A. Garai, F. Gibert, A. Graf, J. Groebner, F. Guichard, M. A. Jiménez, M. Jonassen, A. van den Kroonenberg, V. Magliulo, S. Martin, D. Martinez, L. Mastrorillo, A. F. Moene, F. Molinos, E. Moulin, H. P. Pietersen, B. Piguet, E. Pique, C. Román-Cascón, C. Rufin-Soler, F. Saïd, M. Sastre-Marugán, Y. Seity, G. J. Steeneveld, P. Toscano, O. Traullé, D. Tzanos, S. Wacker, N. Wildmann, and A. Zaldei, 2014: The bllast field experiment: Boundary-layer late afternoon and sunset turbulence. *Atmos. Chem. Phys.*, **14 (20)**, 10 931–10 960, doi:10.5194/acp-14-10931-2014. 11, 12

Louis, J.-F., 1979: A parametric model of vertical eddy fluxes in the atmosphere. *Bound.-Layer Meteor.*, **17 (2)**, 187–202, doi:10.1007/bf00117978. 1

Mahrt, L., 1998: Nocturnal boundary-layer regimes. *Bound.-Layer Meteor.*, **88 (2)**, 255–278, doi:10.1023/A:1001171313493. 9

Mahrt, L., 2009: Variability and maintenance of turbulence in the very stable boundary layer. *Bound.-Layer Meteor.*, **135 (1)**, 1–18, doi:10.1007/s10546-009-9463-6. 6, 7

Mahrt, L., 2010: Common microfronts and other solitary events in the nocturnal boundary layer. *Quart. J. Roy. Meteor. Soc.*, **136 (652)**, 1712–1722, doi:10.1002/qj.694. 6

Mahrt, L., 2014: Stably stratified atmospheric boundary layers. *Annu. Rev. Fluid Mech.*, **46**, 23–45, doi:10.1146/annurev-fluid-010313-141354. 1, 2, 5, 7, 62

Mahrt, L., 2019: Microfronts in the nocturnal boundary layer. *Quart. J. Roy. Meteor. Soc.*, **145 (719)**, 546–562, doi:10.1002/qj.3451. 6, 9, 60

Mahrt, L., S. Richardson, N. Seaman, and D. Stauffer, 2012: Turbulence in the nocturnal boundary layer with light and variable winds. *Quart. J. Roy. Meteor. Soc.*, **138 (667)**, 1430–1439, doi:10.1002/qj.1884. 7

Mahrt, L., and D. Vickers, 2002: Contrasting vertical structures of nocturnal boundary layers. *Bound.-Layer Meteor.*, **105**, 351–363, doi:10.1023/A:1019964720989. 7

Martin, C. M. S., J. K. Lundquist, A. Clifton, G. S. Poulos, and S. J. Schreck, 2017: Atmospheric turbulence affects wind turbine nacelle transfer functions. *Wind Energy Sci.*, **2 (1)**, 295–306, doi:10.5194/wes-2-295-2017. 1

Mauder, M., and T. Foken, 2015: Eddy-covariance software TK3. University of Bayreuth, Bayreuth, Germany, doi:10.5281/zenodo.20349. 38

Mauritsen, T., and G. Svensson, 2007: Observations of stably stratified shear-driven atmospheric turbulence at low and high Richardson Numbers. *J. Atmos. Sci.*, **64 (2)**, 645–655, doi:10.1175/JAS3856.1. 9

Mayer, S., G. Hattenberger, P. Brisset, M. Jonassen, and J. Reuder, 2012a: A 'no-flow-sensor' wind estimation algorithm for unmanned aerial systems. *Int. J. Micro Air Veh.*, **4 (1)**, 15–30, doi:10.1260/1756-8293.4.1.15. 30, 35, 36, 43

Mayer, S., M. Jonassen, A. Sandvik, and J. Reuder, 2012b: Profiling the Arctic Stable Boundary Layer in Advent Valley, Svalbard: Measurements and Simulations. *Bound.-Layer Meteor.*, **143 (3)**, 507–526, doi:10.1007/s10546-012-9709-6. 12

Mayer, S., A. Sandvik, M. Jonassen, and J. Reuder, 2012c: Atmospheric profiling with the UAS SUMO: a new perspective for the evaluation of fine-scale atmospheric models. *Meteorol. Atmos. Phys.*, **116 (1-2)**, 15–26, doi:10.1007/s00703-010-0063-2. 12

McNider, R. T., J. R. Christy, and A. Biazar, 2010: A stable boundary layer perspective on global temperature trends. *IOP Conf. Ser.: Earth Environ. Sci.*, **13 (1)**, 012 003, doi:10.1088/1755-1315/13/1/012003. 1

Monin, A. S., and A. M. Obukhov, 1954: Osnovnye zakonomernosti turbulentnogo peremeshivanija v prizemnom sloe atmosfery (Basic laws of turbulent mixing in the atmosphere near ground). *Trudy Geofiz. Inst. AN SSSR*, **24 (151)**, 163–187. 7, 9

Monin, A. S., and A. M. Yaglom, 1971: *Statistical Fluid Mechanics. Mechanics of Turbulence*, Vol. 1. MIT Press, Cambridge, Mass, 769 pp. 9

Nappo, C., J. Sun, L. Mahrt, and D. Belušić, 2014: Determining wave–turbulence interactions in the stable boundary layer. *Bull. Amer. Meteor. Soc.*, **95 (1)**, ES11–ES13, doi:10.1175/bams-d-12-00235.1. 6

Nappo, C. J., 1991: Sporadic breakdowns of stability in the PBL over simple and complex terrain. *Bound.-Layer Meteor.*, **54 (1-2)**, 69–87, doi:10.1007/bf00119413. 7

Nappo, C. J., 2012: *An Introduction to Atmospheric Gravity Waves*. Elsevier Science Publishing Co Inc, URL https://www.ebook.de/de/product/19460212/carmen_j_cjn_research_meteorology_knoxville_tennessee_37919_usa_nappo_an_introduction_to_atmospheric_gravity_waves.html. 6

Neumann, P. P., and M. Bartholmai, 2015: Real-time wind estimation on a micro unmanned aerial vehicle using its inertial measurement unit. *Sens. Actuators, A*, **235**, 300–310, doi:http://dx.doi.org/10.1016/j.sna.2015.09.036. 12, 61

Nieuwstadt, F. T. M., 1984: The turbulent structure of the stable, nocturnal boundary layer. *J. Atmos. Sci.*, **41 (14)**, 2202–2216, doi:10.1175/1520-0469(1984)041<2202:TTSOTS>2.0.CO;2. 9, 54

Obukhov, A. M., 1946: Turbulentnost' v temperaturnoj - neodnorodnoj atmosfere (Turbulence in an atmosphere with a non-uniform temperature). *Trudy Inst. Theor. Geofiz. AN SSSR*, **1**, 95–115. 7, 9

Obukhov, A. M., 1971: Turbulence in an atmosphere with a non-uniform temperature. *Bound.-Layer Meteor.*, **2**, 7–29, doi:10.1007/BF00718085. 7

Palo, T., T. Vihma, J. Jaagus, and E. Jakobson, 2017: Observations of temperature inversions over central Arctic sea ice in summer. *Quart. J. Roy. Meteor. Soc.*, **143 (708)**, 2741–2754, doi:10.1002/qj.3123, qJ-16-0260.R2. 11

Palomaki, R. T., N. T. Rose, M. van den Bossche, T. J. Sherman, and S. F. J. D. Wekker, 2017: Wind estimation in the lower atmosphere using multirotor aircraft. *J. Atmos. Oceanic Technol.*, **34 (5)**, 1183–1191, doi:10.1175/JTECH-D-16-0177.1, https://doi.org/10.1175/JTECH-D-16-0177.1. 12, 30, 31, 36, 44, 61

Persson, P. O. G., C. W. Fairall, E. L. Andreas, P. G. Guest, and D. K. Perovich, 2002: Measurements near the atmospheric surface flux group tower at SHEBA: Near-surface conditions and surface energy budget. *J. Geophys. Res.*, **107 (C10)**, doi:10.1029/2000jc000705. 11

Petenko, I., S. Argentini, G. Casasanta, C. Genthon, and M. Kallistratova, 2019: Stable surface-based turbulent layer during the polar winter at Dome C, Antarctica: Sodar and in situ observations. *Bound.-Layer Meteor.*, doi:10.1007/s10546-018-0419-6. 28

Petersen, G. N., I. A. Renfrew, and G. W. K. Moore, 2009: An overview of barrier winds off southeastern Greenland during the Greenland Flow Distortion experiment. *Quart. J. Roy. Meteor. Soc.*, **135 (645)**, 1950–1967, doi:10.1002/qj.455. 6

Pfister, L., K. Lapo, C. Sayde, J. Selker, L. Mahrt, and C. K. Thomas, 2019: Classifying the nocturnal atmospheric boundary layer into temperature and flow regimes. *Quart. J. Roy. Meteor. Soc.*, doi:10.1002/qj.3508. 9

Poulos, G. S., W. Blumen, D. C. Fritts, J. K. Lundquist, J. Sun, S. P. Burns, C. Nappo, R. Banta, R. Newsom, J. Cuxart, E. Terradellas, B. Balsley, and M. Jensen, 2002: CASES-99: A comprehensive investigation of the stable nocturnal boundary layer. *Bull. Amer. Meteor. Soc.*, **83 (4)**, 555–581, doi:10.1175/1520-0477(2002)083<0555:caciot>2.3.co;2. 10

Päschke, E., R. Leinweber, and V. Lehmann, 2015: An assessment of the performance of a 1.5 m Doppler lidar for operational vertical wind profiling based on a 1-year trial. *Atmos. Meas. Tech.*, **8 (6)**, 2251–2266, doi:10.5194/amt-8-2251-2015. 39

Rautenberg, A., M. Schön, K. zum Berge, M. Mauz, P. Manz, A. Platis, B. van Kesteren, I. Suomi, S. T. Kral, and J. Bange, 2019: The multi-purpose airborne sensor carrier MASC-3 for wind and turbulence measurements in the atmospheric boundary layer. *Sensors*, **19 (10)**, 2292, doi:10.3390/s19102292. 21, 30

Rees, J. M., P. S. Anderson, and J. C. King, 1998: Observations of solitary waves in the stable atmospheric boundary layer. *Bound.-Layer Meteor.*, **86 (1)**, 47–61, doi:10.1023/a:1000555504268. 6, 7

Renfrew, I. A., and P. S. Anderson, 2006: Profiles of katabatic flow in summer and winter over Coats Land, Antarctica. *Quart. J. Roy. Meteor. Soc.*, **132 (616)**, 779–802, doi:10.1256/qj.05.148. 6

Reuder, J., L. Båserud, M. O. Jonassen, S. T. Kral, and M. Müller, 2016a: Exploring the potential of the RPA system SUMO for multipurpose boundary-layer missions during the BLLAST campaign. *Atmos. Meas. Tech.*, **9 (6)**, 2675–2688, doi:10.5194/amt-9-2675-2016. 11, 12

Reuder, J., P. Brisset, M. Jonassen, Marius Müller, and S. Mayer, 2009: The Small Unmanned Meteorological Observer SUMO: A new tool for atmospheric boundary layer research. *Meteorol. Z.*, **18 (2)**, 141–147, doi:10.1127/0941-2948/2009/0363. 12, 30

Reuder, J., M. O. Jonassen, and H. Ólafsson, 2012a: The Small Unmanned Meteorological Observer SUMO: Recent developments and applications of a micro-UAS for atmospheric boundary layer research. *Acta Geophys.*, **60 (5)**, 1454–1473, doi:10.2478/s11600-012-0042-8. 12, 30, 37

Reuder, J., L. B. serud, S. Kral, V. Kumer, J. W. Wagenaar, and A. Knauer, 2016b: Proof of concept for wind turbine wake investigations with the RPAS SUMO. *Energy Procedia*, **94**, 452–461, doi:10.1016/j.egypro.2016.09.215, 13th Deep Sea Offshore Wind R&D Conference, EERA DeepWind'2016. 12

Reuder, J., M. Ablinger, H. Ágústsson, P. Brisset, S. Brynjólfsson, M. Garhammer, T. Jóhannesson, M. O. Jonassen, R. Kühnel, S. Lämmlein, T. Lange, C. Lindenberg, S. Malardel, S. Mayer, M. Müller, H. Óafsson, O. Rögnvaldsson, W. Schäper, T. Spengler, G. Zängl, and J. Egger, 2012b: FLOHOF 2007: an overview of the mesoscale meteorological field campaign at Hofsjökull, Central Iceland. *Meteorol. Atmos. Phys.*, **116 (1-2)**, 1–13, doi:10.1007/s00703-010-0118-4. 11

Román-Cascón, C., C. Yagüe, G.-J. Steeneveld, G. Morales, J. A. Arrillaga, M. Sastre, and G. Maqueda, 2019: Radiation and cloud-base lowering fog events: Observational analysis and evaluation of WRF and HARMONIE. *Atmos. Res.*, **229**, 190–207, doi:10.1016/j.atmosres.2019.06.018. 1

Sathe, A., J. Mann, T. Barlas, W. Bierbooms, and G. van Bussel, 2012: Influence of atmospheric stability on wind turbine loads. *Wind Energy*, **16 (7)**, 1013–1032, doi:10.1002/we.1528. 1

Sayde, C., C. K. Thomas, J. Wagner, and J. Selker, 2015: High-resolution wind speed measurements using actively heated fiber optics. *Geophys. Res. Lett.*, **42 (22)**, 10,064–10,073, doi:10.1002/2015gl066729. 62

Schafer, R., 2011: What is a Savitzky-Golay filter? *IEEE Signal Processing Magazine*, **28 (4)**, 111–117, doi:10.1109/msp.2011.941097. 42

Segales, A. R., B. R. Greene, T. M. Bell, W. Doyle, J. J. Martin, E. A. Pillar-Little, and P. B. Chilson, 2020: The CopterSonde: an insight into the development of a smart unmanned aircraft system for atmospheric boundary layer research. *Atmospheric Measurement Techniques*, **13 (5)**, 2833–2848, doi:10.5194/amt-13-2833-2020. 21, 31, 32, 61

Slinger, C., and M. Harris, 2012: Introduction to continuous-wave Doppler lidar. URL https://www.semanticscholar.org/paper/Introduction-to-continuous-wave-Doppler-lidar-Slinger-Harris/bcbb58d097c437f8831a81f8c63e01b41635ddff. 28

Sorbjan, Z., 1989: *Structure of the atmospheric boundary layer*. Prentice Hall advanced reference series: Physical and life sciences, Prentice Hall. 9

Sorbjan, Z., 2010: Gradient-based scales and similarity laws in the stable boundary layer. *Quart. J. Roy. Meteor. Soc.*, **136 (650)**, 1243–1254, doi:10.1002/qj.638. 9, 10, 54, 55, 59, 60

Sorbjan, Z., and A. Grachev, 2010: An Evaluation of the Flux-Gradient Relationship in the Stable Boundary Layer. *Bound.-Layer Meteor.*, **135 (3)**, 385–405, doi:10.1007/s10546-010-9482-3. 10, 54, 55, 60

Spiess, T., J. Bange, M. Buschmann, and P. Vörsmann, 2007: First application of the meteorological Mini-UAV 'M2AV'. *Meteorol. Z.*, **16 (2)**, 159–169, doi:10.1127/0941-2948/2007/0195. 12

Steeneveld, G.-J., 2014: Current challenges in understanding and forecasting stable boundary layers over land and ice. *Front. Environ. Sci.*, **2**, 41, doi:10.3389/fenvs.2014.00041. 1

Steeneveld, G. J., M. J. J. Wokke, C. D. G. Zwaaftink, S. Pijlman, B. G. Heusinkveld, A. F. G. Jacobs, and A. A. M. Holtslag, 2010: Observations of the radiation divergence in the surface layer and its implication for its parameterization in numerical weather prediction models. *J. Geophys. Res.*, **115 (D6)**, doi:10.1029/2009jd013074. 6, 9, 26

Stull, R. B., 1988: *An Introduction to Boundary Layer Meteorology*. Atmospheric sciences library, Kluwer Academic Publishers, doi:10.1002/qj.49711548614. 5

Sun, J., L. Mahrt, R. M. Banta, and Y. L. Pichugina, 2012: Turbulence regimes and turbulence intermittency in the stable boundary layer during CASES-99. *J. Atmos. Sci.*, **69 (1)**, 338–351, doi:10.1175/jas-d-11-082.1. 7

Sun, J., C. J. Nappo, L. Mahrt, D. Belušić, B. Grisogono, D. R. Stauffer, M. Pulido, C. Staquet, Q. Jiang, A. Pouquet, C. Yagüe, B. Galperin, R. B. Smith, J. J. Finnigan, S. D. Mayor, G. Svensson, A. A. Grachev, and W. D. Neff, 2015: Review of wave-turbulence interactions in the stable atmospheric boundary layer. *Rev. Geophys.*, **53 (3)**, 956–993, doi:10.1002/2015rg000487. 6, 7, 9

Taylor, G. I., 1938: The spectrum of turbulence. *Proc. R. Soc. A*, **164 (919)**, 476–490, doi:10.1098/rspa.1938.0032. 33, 37, 53

Thomas, C. K., A. M. Kennedy, J. S. Selker, A. Moretti, M. H. Schroth, A. R. Smoot, N. B. Tufillaro, and M. J. Zeeman, 2012: High-resolution fibre-optic temperature sensing: A new tool to study the two-dimensional structure of atmospheric surface-layer flow. *Bound.-Layer Meteor.*, **142 (2)**, 177–192, doi:10.1007/s10546-011-9672-7. 62

Uotila, P., T. Vihma, and J. Haapala, 2015: Atmospheric and oceanic conditions and the extremely low Bothnian Bay sea ice extent in 2014/2015. *Geophys. Res. Lett.*, **42 (18)**, 7740–7749, doi:10.1002/2015gl064901. 18

Uttal, T., J. A. Curry, M. G. McPhee, D. K. Perovich, R. E. Moritz, J. A. Maslanik, P. S. Guest, H. L. Stern, J. A. Moore, R. Turenne, A. Heiberg, M. C. Serreze, D. P. Wylie, O. G. Persson, C. A. Paulson, C. Halle, J. H. Morison, P. A. Wheeler, A. Makshtas, H. Welch, M. D. Shupe, J. M. Intrieri, K. Stamnes, R. W. Lindsey, R. Pinkel, W. S. Pegau, T. P. Stanton, and T. C. Grenfeld, 2002: Surface Heat Budget of the Arctic Ocean. *Bull. Amer. Meteor. Soc.*, **83 (2)**, 255–275, doi:10.1175/1520-0477(2002)083<0255:SHBOTA>2.3.CO;2. 11

Valldecabres, L., A. Peña, M. Courtney, L. von Bremen, and M. Kühn, 2018: Very short-term forecast of near-coastal flow using scanning lidars. *Wind Energy Sci.*, **3 (1)**, 313–327, doi:10.5194/wes-3-313-2018. 62

van de Wiel, B. J. H., A. F. Moene, O. K. Hartogensis, H. A. R. D. Bruin, and A. A. M. Holtslag, 2003: Intermittent turbulence in the stable boundary layer over land. part III: A classification for observations during CASES-99. *J. Atmos. Sci.*, **60 (20)**, 2509–2522, doi:10.1175/1520-0469(2003)060<2509:ititsb>2.0.co;2. 9

van den Kroonenberg, A., T. Martin, M. Buschmann, J. Bange, and P. Vörsmann, 2008: Measuring the Wind Vector Using the Autonomous Mini Aerial Vehicle M 2 AV. *J. Atmos. Oceanic Technol.*, **25 (11)**, 1969–1982, doi:10.1175/2008jtecha1114.1. 11, 12

Vasiljević, N., M. Harris, A. T. Pedersen, G. R. Thorsen, M. Pitter, J. Harris, K. Bajpai, and M. Courtney, 2020: Wind sensing with drone-mounted wind lidars: proof of concept. *Atmos. Meas. Tech.*, **13 (2)**, 521–536, doi:10.5194/amt-13-521-2020. 62

Vignon, E., F. Hourdin, C. Genthon, B. J. H. V. de Wiel, H. Gallée, J.-B. Madeleine, and J. Beaumet, 2018: Modeling the dynamics of the atmospheric boundary layer over the Antarctic plateau with a general circulation model. *J. Adv. Model. Earth Syst.*, **10 (1)**, 98–125, doi:10.1002/2017ms001184. 11

Vignon, E., B. J. H. van de Wiel, I. G. S. van Hooijdonk, C. Genthon, S. J. A. van der Linden, J. A. van Hooft, P. Baas, W. Maurel, O. Traullé, and G. Casasanta, 2017: Stable boundary-layer regimes at Dome C, Antarctica: observation and analysis. *Quart. J. Roy. Meteor. Soc.*, **143 (704)**, 1241–1253, doi:10.1002/qj.2998. 11

Vihma, T., J. Jaagus, E. Jakobson, and T. Palo, 2008: Meteorological conditions in the Arctic Ocean in spring and summer 2007 as recorded on the drifting ice station Tara. *Geophys. Res. Lett.*, **35 (18)**, doi:10.1029/2008gl034681. 11

Vihma, T., T. Kilpeläinen, M. Manninen, A. Sjöblom, E. Jakobson, T. Palo, J. Jaagus, and M. Maturilli, 2011: Characteristics of temperature and humidity inversions and low-level jets over Svalbard fjords in spring. *Adv. Meteorol.*, 14, doi:10.1155/2011/486807. 6

Vose, R. S., D. R. Easterling, and B. Gleason, 2005: Maximum and minimum temperature trends for the globe: An update through 2004. *Geophys. Res. Lett.*, **32 (23)**, doi:10.1029/2005gl024379. 1

Wang, J.-Y., B. Luo, M. Zeng, and Q.-H. Meng, 2018: A wind estimation method with an unmanned rotorcraft for environmental monitoring tasks. *Sensors*, **18 (12)**, 4504, doi:10.3390/s18124504. 61

Weill, A., C. Klapisz, B. Strauss, F. Baudin, C. Jaupart, P. V. Grunderbeeck, and J. P. Goutorbe, 1980: Measuring heat flux and structure functions of temperature fluctuations with an acoustic Doppler sodar. *J. Appl. Meteor.*, **19 (2)**, 199–205, doi:10.1175/1520-0450(1980)019<0199:mhfasf>2.0.co;2. 27

Wildmann, N., M. Hofsäß, F. Weimer, A. Joos, and J. Bange, 2014a: MASC; a small Remotely Piloted Aircraft (RPA) for wind energy research. *Adv. Sci. Res.*, **11**, 55–61, doi:10.5194/asr-11-55-2014. 12, 30

Wildmann, N., M. Mauz, and J. Bange, 2013: Two fast temperature sensors for probing of the atmospheric boundary layer using small remotely piloted aircraft (RPA). *Atmos. Meas. Tech.*, **6 (8)**, 2101–2113, doi:10.5194/amt-6-2101-2013. 30

Wildmann, N., G. A. Rau, and J. Bange, 2015: Observations of the early morning boundary-layer transition with small remotely-piloted aircraft. *Bound.-Layer Meteor.*, **157 (3)**, 345–373, doi:10.1007/s10546-015-0059-z. 12

Wildmann, N., S. Ravi, and J. Bange, 2014b: Towards higher accuracy and better frequency response with standard multi-hole probes in turbulence measurement with remotely piloted aircraft (RPA). *Atmos. Meas. Tech.*, **7 (4)**, 1027–1041, doi:10.5194/amt-7-1027-2014. 30

World Meteorological Organization, 2008: Guide to Meteorological Instruments and Methods of Observation. Publication Board of the World Meteorological Organization Geneva, Switzerland, URL http://library.wmo.int/pmb_ged/wmo_8_en-2012.pdf, updated in 2010. 33

Wrenger, B., and J. Cuxart, 2017: Evening tansition by a river sampled using a remotely-piloted multicopter. *Bound.-Layer Meteor.*, **165 (3)**, 535–543, doi:10.1007/s10546-017-0291-9. 12, 30, 31

Wyngaard, J., L. Barbieri, A. Thomer, J. Adams, D. Sullivan, C. Crosby, C. Parr, J. Klump, S. R. Shrestha, and T. Bell, 2019: Emergent challenges for science sUAS data management: Fairness through community engagement and best practices development. *Remote Sensing*, **11 (15)**, 1797, doi:10.3390/rs11151797. 39

Yagüe, C., S. Viana, G. Maqueda, and J. M. Redondo, 2006: Influence of stability on the flux-profile relationships for wind speed, ϕ_m, and temperature, ϕ_h, for the stable atmospheric boundary layer. *Nonlinear Processes Geophys.*, **13 (2)**, 185–203, doi:10.5194/npg-13-185-2006. 7

Zhou, B., and F. K. Chow, 2014: Nested large-eddy simulations of the intermittently turbulent stable atmospheric boundary layer over real terrain. *J. Atmos. Sci.*, **71 (3)**, 1021–1039, doi:10.1175/jas-d-13-0168.1. 7

Zilitinkevich, S., and P. Calanca, 2000: An extended similarity theory for the stably stratified atmospheric surface layer. *Quart. J. Roy. Meteor. Soc.*, **126 (566)**, 1913–1923, doi:10.1002/qj.49712656617. 9

Zilitinkevich, S. S., and I. N. Esau, 2005: Resistance and heat-transfer laws for stable and neutral planetary boundary layers: Old theory advanced and re-evaluated. *Quart. J. Roy. Met. Soc*, **131 (609)**, 1863–1892, doi:10.1256/qj.04.143. 9

Appendix

Table 1: A1: List of Abbreviations

ABL	Atmospheric Boundary Layer
AMOR Q13	Advanced Mission and Operation Research Quadcopter (13 inch)
ASC	Andøya Space Center
B2M	Bebop2Met
CS	CopterSonde
CNR	Carrier-to-Noise Ratio
DBS	Doppler Beam Swinging
DGPS	Dual Global Positioning System
EC	Eddy-Covariance
FMI	Finnish Meteorological Institute
GCS	Ground Control Station
GFI	Geophysical Institute, University of Bergen
GNSS	Global Navigation Satellite System
GPS	Global Positioning System
IRGA	Infra-Red Gas Analysers
IMU	Inertia Measurement Unit
IOP	Intensive Observation Period
LES	Large-Eddy Simulation
lidar	Light Detection and Ranging
LLJ	Low-Level Jet
MASC	Multi-Purpose Airborne Sensor Carrier
MOST	Monin–Obukhov Similarity Theory
NWP	Numerical Weather Prediction
OU	University of Oklahoma
PPI	Plan Position Indicator
QA/QC	Quality Assurance and Quality Check
RC	Remote Control
RHI	Range Height Indicator
RPAS	Remotely Piloted Aircraft System
RTK	Real-Time Kinematic
SBL	Stable Boundary Layer
SCM	Single-Column Model
sodar	Sound Detection and Ranging
SUMO	Small Meteorological Observer
UAS	Unmanned Aircraft System
UAV	Unmanned Aerial Vehicle
UOWL	Ostwestfalen-Lippe University of Applied Sciences and Arts
UT	University of Tübingen
VAD	Velocity Azimuth Display
VSBL	Very Stable Boundary Layer
WCv1	WINDCUBE v1
WC100S	WINDCUBE 100S
WMO	World Meteorological Organization
WSBL	Weakly Stable Boundary Layer

I

Paper I

Innovative Strategies for Observations in the Arctic Atmospheric Boundary Layer (ISOBAR) — The Hailuoto 2017 Campaign

Innovative Strategies for Observations in the Arctic Atmospheric Boundary Layer (ISOBAR)—The Hailuoto 2017 Campaign

Stephan T. Kral [1,2,*], Joachim Reuder [1], Timo Vihma [2], Irene Suomi [2], Ewan O'Connor [2], Rostislav Kouznetsov [2,3], Burkhard Wrenger [4], Alexander Rautenberg [5], Gabin Urbancic [1,2], Marius O. Jonassen [1,6], Line Båserud [1], Björn Maronga [1,7], Stephanie Mayer [8], Torge Lorenz [8], Albert A. M. Holtslag [9], Gert-Jan Steeneveld [9], Andrew Seidl [1], Martin Müller [10], Christian Lindenberg [10], Carsten Langohr [4], Hendrik Voss [4], Jens Bange [5], Marie Hundhausen [5], Philipp Hilsheimer [5] and Markus Schygulla [5]

[1] Geophysical Institute and Bjerknes Centre for Climate Research, University of Bergen, Postbox 7803, 5020 Bergen, Norway; joachim.reuder@uib.no (J.R.); gabin.urbancic@fmi.fi (G.U.); marius.jonassen@unis.no (M.O.J.); line.baserud@uib.no (L.B.); maronga@muk.uni-hannover.de (B.M.); andrew.seidl@uib.no (A.S.)

[2] Finnish Meteorological Institute, P.O. Box 503, 00101 Helsinki, Finland; timo.vihma@fmi.fi (T.V.); irene.suomi@fmi.fi (I.S.); ewan.oconnor@fmi.fi (E.O.); rostislav.kouznetsov@fmi.fi (R.K.)

[3] A.M. Obukhov Institute for Atmospheric Physics, RU-119017 Moscow, Russia

[4] Department of Environmental Engineering and Computer Science, University of Applied Sciences Ostwestfalen-Lippe, An der Wilhelmshöhe 44, 37671 Höxter, Germany; burkhard.wrenger@hs-owl.de (B.W.); carsten.langohr@hs-owl.de (C.L.); hendrik.voss@hs-owl.de (H.V.)

[5] Department of Geosciences, University of Tübingen, Hölderlinstr. 12, 72074 Tübingen, Germany; alexander.rautenberg@uni-tuebingen.de (A.R.); jens.bange@uni-tuebingen.de (J.B.); marie.hundhausen@gmx.de (M.H.); philipp.hilsheimer@googlemail.com (P.H.); markus.schygulla@web.de (M.S.)

[6] The University Centre in Svalbard, P.O. Box 156, N-9171 Longyearbyen, Norway

[7] Institute of Meteorology and Climatology, Leibniz University Hannover, P.O. Box 6009, D-30060 Hannover, Germany

[8] Uni Research Climate, Bjerknes Centre for Climate Research, P.O. Box 7810, N-5020 Bergen, Norway; stephanie.mayer@uni.no (S.M.); torge.lorenz@uni.no (T.L.)

[9] Meteorology and Air Quality Section, Wageningen University, P.O. Box 9101, NL-6700 HB Wageningen, The Netherlands; bert.holtslag@wur.nl (A.A.M.H.); gert-jan.steeneveld@wur.nl (G.-J.S.)

[10] Lindenberg und Müller GmbH & Co. KG, Fasanenweg 4, 31249 Hohenhameln, Germany; martin.mueller@lindenberg-mueller.de (M.M.); christian.lindenberg@lindenberg-mueller.de (C.L.)

* Correspondence: stephan.kral@uib.no; Tel.: +47-5558-2863

Abstract: The aim of the research project "Innovative Strategies for Observations in the Arctic Atmospheric Boundary Layer (ISOBAR)" is to substantially increase the understanding of the stable atmospheric boundary layer (SBL) through a combination of well-established and innovative observation methods as well as by models of different complexity. During three weeks in February 2017, a first field campaign was carried out over the sea ice of the Bothnian Bay in the vicinity of the Finnish island of Hailuoto. Observations were based on ground-based eddy-covariance (EC), automatic weather stations (AWS) and remote-sensing instrumentation as well as more than 150 flight missions by several different Unmanned Aerial Vehicles (UAVs) during mostly stable and very stable boundary layer conditions. The structure of the atmospheric boundary layer (ABL) and above could be resolved at a very high vertical resolution, especially close to the ground, by combining surface-based measurements with UAV observations, i.e., multicopter and fixed-wing profiles up to 200 m agl and 1800 m agl, respectively. Repeated multicopter profiles provided detailed information on the evolution of the SBL, in addition to the continuous SODAR and LIDAR wind

measurements. The paper describes the campaign and the potential of the collected data set for future SBL research and focuses on both the UAV operations and the benefits of complementing established measurement methods by UAV measurements to enable SBL observations at an unprecedented spatial and temporal resolution.

---

1. Introduction

The atmospheric boundary layer (ABL) is the lowest part of the atmosphere where the Earth's surface strongly influences the wind, temperature, and humidity through turbulent transport of air mass. Due to its superior importance for the atmosphere system, an appropriate representation of the ABL is essential for both operational numerical weather prediction (NWP) and climate models as well as for a wide range of practical applications, such as air pollution forecast and wind energy yield estimates. In contrast to the ABL, the stable boundary layer (SBL) is typically one order of magnitude shallower and can reach a vertical extent as low as 10 m. Turbulence in the SBL is typically much weaker or intermittent and is mainly produced by vertical wind shear, whereas buoyancy inhibits vertical motion. Furthermore, a number of nonturbulent motions, such as wave-like motions, solitary modes, microfronts or drainage flows, become important [1]. The principal problem in representing turbulence in those models correctly is that the length scales of the turbulent processes are typically far below model resolution and therefore need to be parameterized. While the corresponding parameterization schemes, e.g., reference [2], generally work very well for near-neutral and unstable conditions, they show significant shortcomings for the SBL, e.g., by systematically overestimating turbulent mixing rates and the height of the ABL (h_{ABL}) [3–6]. In the context of weather forecasting, this leads to, amongst others, significant errors in the prediction of near surface parameters, such as the 2-m temperature and 10-m wind speed for situations with clear skies and low wind typically occurring at night or during winter [6]. Errors in h_{ABL} might also induce considerable uncertainties in the forecast of wind profiles and the location of low-level jets (LLJ), which are crucial parameters for applications such as wind energy. Furthermore, this also leads to a typical warm bias for SBL conditions in NWP models [4,7,8], which is also of importance under the aspects of climate and climate change. One of the most dominant signals in climate records is the accelerated warming of the polar regions during wintertime and the increase in nighttime temperatures at lower latitudes [9]. This observed polar amplification may be partly related to the shallow SBL with a corresponding small heat capacity. Hence, a certain heat gain results in a relatively large temperature increase [10]. In addition, this dampens the temperature inversion infrared cooling to space [11,12]. A systematic overestimation of turbulent mixing and the ABL height thus complicates the proper attribution of the mechanisms of Arctic climate change [12–14].

Monin–Obukhov similarity theory (MOST) provides dimensionless relationships between the surface fluxes of heat and momentum, the variance and the mean gradients of temperature, moisture, and wind in the atmospheric surface layer (SL). These dimensionless relationships are a function of the height (z) above the surface, which is made dimensionless with the Monin–Obukhov length scale (L). Strictly speaking, these relationships apply only for stationary and homogeneous surface conditions. In practice, however, there is a strong need for wider application, and as such, field observations in a variety of circumstances are needed to evaluate the dimensionless relationships. Most of the surface parameterization schemes in NWP and climate models are based on the traditional MOST, which is known for its shortcomings in characterizing the SBL [15–21]. Under such conditions, continuous turbulence may break down and become intermittent e.g., [22], so that non-local features,

such as the stability at higher levels and the Coriolis effect, gain relative importance [23,24]. This may imply the occurrence of upside-down events, in which turbulence is mainly generated by the vertical wind shear associated with LLJ [23,25]. Additional processes, such as inertial oscillations and gravity waves [26] can then contribute significantly to the turbulent kinetic energy (TKE) budget. Zilitinkevich and Calanca [15] and Zilitinkevich [27] presented an attempt for a non-local theory for the SBL, taking into account the effect of internal gravity waves in the free atmosphere. In addition, other small-scale processes and phenomena, such as drainage flow, radiation divergence [1,6,28], fog, and close interactions with the surface as well as potential snow feedback [29] further increase the complexity of the SBL. The effects of all those phenomena are neither well understood, nor sufficiently captured by MOST or its extensions [15,30–32].

SBL conditions also impose challenges with respect to observations, as the typically weak turbulent fluxes close to the surface become difficult to measure precisely under very stable conditions. Gradient-based scaling schemes, as proposed by [20,33,34] and formally equivalent to the MOST approach, might overcome some of the observational issues of weak turbulent fluxes, since the vertical gradients within the SBL are usually strong and relatively easy to measure. From a modeling point of view, recent high-resolution large-eddy simulation (LES) studies have shown a lack of grid convergence under stable conditions [35–37] which might be attributed to the fact that MOST is usually applied between the surface and the first grid level in the atmosphere (i.e., typically at heights between 1 m to 10 m). This might violate basic assumptions for MOST, e.g., that the measurement level or the first grid level in LES cases must lie inside the inertial sublayer, in which the flow is spatially homogeneous and dissipation follows Kolmogorov's 5/3 law. Errors can be induced by the fact that turbulence is not properly resolved at the first couple of grid points adjacent to the surface. In such cases, turbulence is not fully resolved and the flow is dominated by the subgrid-scale model in use. It is often observed that this general deficiency of LES models to resolve turbulence near the surface leads to near-surface gradients that are too strong and inherently lead to an underestimation of the surface friction [38].

Field campaigns addressing the SBL generally face logistical challenges in taking measurements at remote sites that are difficult to reach and are often characterized by harsh weather conditions, especially in regard to low temperatures. In particular, observations over sea ice involve additional risks for equipment and people, e.g., due to sea ice motion and melt. Major campaigns with focus on the SBL over sea ice have included the Weddell ice station in the Austral autumn and winter of 1992 [39–42], the Surface Heat Budget over the Arctic Ocean (SHEBA) in the Beaufort Sea in 1997–1998 [23,43,44], the drifting ice station, Tara, in the central Arctic in the spring and summer of 2007 [45–47], and the drifting station, N-ICE2015, north of Svalbard in the winter and spring of 2015 [48]. Other land-based campaigns, e.g., ARTIST [49], CASES-99 [50], GABLS [51,52], FLOSS-II [53], the measurements at Summit Station in central Greenland [54], and recently, MATERHORN [55] have also contributed considerably to the current state of knowledge on SBLs. The typical observation methods applied in such campaigns are profile measurements using weather masts, tethersondes, and radiosondes, as well as eddy covariance (EC) measurements at one or multiple levels. Several SBL studies have also been based on manned research aircraft observations, mainly over sea ice in the Arctic [56–60] and the Baltic Sea [61,62]. Manned research aircraft may also release dropsondes and apply airborne LIDARs [63]. Over the last decade, the use of Unmanned Aerial Vehicles (UAVs) has also rapidly increased in the field of atmospheric research [64,65] and corresponding systems have been applied in ABL campaigns, both in the Arctic [66–68] and Antarctic [69–73].

The different methods for observing the SBL are generally complementary. Continuous time series of basic meteorological parameters at different temporal resolutions can be obtained in-situ by weather masts, tethersondes, or radiosonde ascents, or they can be remotely sensed by e.g., with LIDAR (Light Detection and Ranging), SODAR (Sound Detection and Ranging), RADAR (Radio Detection and Ranging), RASS (Radar-Acoustic Sounding System) or microwave radiometer observations. All these measurement methods and devices have certain shortcomings that may be at least partially overcome by proper UAV missions. Weather masts are limited in height and are rather inflexible with respect to

changes in location. Tethersondes require considerable infrastructure and their operation is limited to wind speeds below $12\,\mathrm{m\,s^{-1}}$ [47]. Continuous data are only available if the balloon is kept at a fixed altitude, which limits the vertical resolution [74]. In addition, sometimes the temperature inversions can be so strong that the buoyancy of the tethered balloon is not sufficient to penetrate it [67]. Rawinsonde soundings reach high altitudes, but pass very quickly through the interesting layers for SBL research. They only provide snapshots of vertical profiles in relatively poor temporal resolution, and are comparatively expensive for long-term use. Observations by large manned research aircraft are even more expensive. An additional drawback of those platforms for SBL research is the limitation in the lowermost possible flight altitude for safe operations and the fact that the pure size and velocity of the aircraft might massively disturb the local structure and dynamics of a shallow SBL. Doppler LIDARs and SODARs provide wind information with a vertical resolution in the order of $5\,\mathrm{m}$ to $20\,\mathrm{m}$, typically in the lowest few hundred meters above the ground, depending on wind speed and stability, and, in the case of LIDAR, also on other parameters, such as the aerosol content [75], water vapor, ozone or temperature. So far, the use of remote-sensing systems for dedicated SBL campaigns in polar regions has been rather limited, [49,76,77]. Furthermore, the minimum altitude for wind information from pulsed non-scanning LIDAR systems is in the order of $40\,\mathrm{m}$. Higher vertical resolution and lower minimum altitudes can be achieved by operating scanning Doppler LIDARs at low-elevation angles. However, the achieved data originates from a much larger area than for high elevation scans. Scintillometers are capable of measuring spatially-averaged turbulent fluxes and cross-winds close to the ground along horizontal paths of approximately $1\,\mathrm{km}$ to $10\,\mathrm{km}$. In previous years, SBLs have also been addressed by satellite-based remote-sensing, e.g., [78].

The main motivation for the ISOBAR project is to develop and apply a new and innovative observation strategy for the SBL that is based on meteorological UAVs, ground-based in-situ, and remote-sensing profiling systems. The main idea is to combine the reliability and continuity of well-established ground-based observations with the flexibility of small UAV systems. This strategy is to be applied during several campaigns in polar regions to provide extensive data sets on the turbulent structure of the SBL with unique and unprecedented spatial and temporal resolution. This will form the basis for intensive analysis of small-scale turbulent processes in the SBL and corresponding multi-scale modeling studies.

To optimize the collection of ABL data over a period of three weeks, the Hailuoto-I campaign was based on the combined use of a weather mast, equipped for gradient and flux observations; a scanning Doppler LIDAR; a vertically pointing SODAR; and several fixed-wing and multicopter UAVs equipped with different sensors. To the authors' knowledge, the Hailuoto-I campaign is the first field campaign to combine ground-based in-situ and remote-sensing instrumentation with the intensive use of multiple UAVs for systematic SBL research.

The manuscript is structured in the following way. In Section 2 we describe the experiment site, the instrumentation used, and some details on the operation of our UAVs. Data processing methods and data availability are summarized in Section 3. Section 4 describes the general synoptic situation and the sea ice conditions during Hailuoto-I. The first results are presented in Section 5 together with a brief discussion, before summarizing the main outcomes of the Hailuoto-I campaign and giving a short outlook on our future plans for specific analysis and modeling studies in Section 6.

2. Experiment Description

The Hailuoto-I campaign took place between 11 and 27 February 2017 over the sea ice of the Bothnian Bay, close to the Finnish island of Hailuoto, as part of the ISOBAR project. Hailuoto island is located roughly 20 km west of the city of Oulu and has a size of about $200\,\mathrm{km^2}$ (Figure 1). Its landscape is mainly flat heath terrain, with the highest point reaching only about 20 m asl. The field site was located at $65.0384°$ N and $24.5549°$ E, just off-shore of Hailuoto Marjaniemi, the westernmost point of the island (Figure 1), where the Finnish Meteorological Institute operates a permanent weather station. Bothnian Bay, the northernmost part of the Baltic Sea, is typically entirely frozen every winter with the

exception of the winters of 2014/2015 [79] and 2015/2016 with land-fast ice up to 0.8 m on the coast of Hailuoto.

During the observation period, the apparent sunrise changed from 6:35 to 5:39 UTC and the apparent sunset from 14:38 to 15:31 UTC, calculated with [80]. The noontime solar elevation angle ranged from 11.15° to 16.83° [81]. The apparent solar and sea ice conditions favored the formation of a SBL [61,62], underlying a weak diurnal cycle.

The instrumentation operated on site during the campaign included an eddy covariance (EC) system; a 4 m meteorological mast with three levels of slow-response sensors for temperature, humidity, and wind; a four component radiometer; and two ground flux sensors. The ground-based in-situ measurements were complemented by a scanning wind LIDAR, a vertically profiling SODAR, and several types of fixed and rotary-wing UAVs.
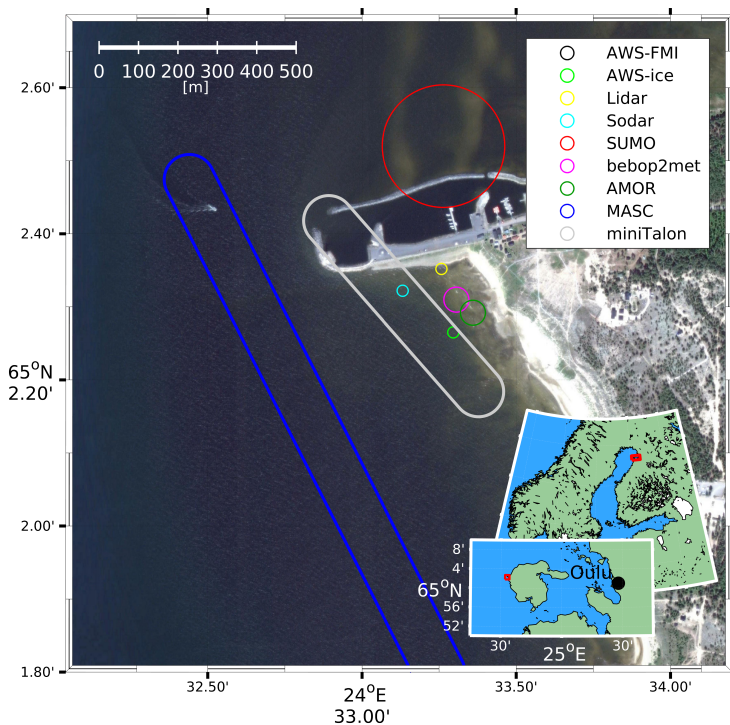
Figure 1. Overview maps showing the Hailuoto-I campaign site, the location of the ground-based instrumentation and typical locations and paths of the Unmanned Aerial Vehicle (UAV) flights.

2.1. Instrumentation

2.1.1. Basic Instrumentation

Close to the selected field site, the Finnish Meteorological Institute (FMI) operates the World Meteorological Organization (WMO) automatic weather station (AWS) Hailuoto Marjaniemi (ID 02873), henceforth referred to as AWS-FMI. The Western and Northern sectors of this station represent open water conditions during summer and typically, sea ice during winter, which was also the case during this campaign, as will be later seen in Section 4. East of the station (about 45° to 165°), the measurements are affected by the island and by some buildings at a distance of about 50 m to 100 m from the station, including a lighthouse and an ice radar tower. The measured parameters, installed instrumentation,

and their heights are listed in Table 1. All measurements, except wind, are collected at the station; the wind speed and direction are observed at the top of the ice radar tower. The anemometer is supported by a 2 m high mast attached to the railing of the tower platform, the measurement height being about 29 m asl.

Table 1. Specifications of the operational automatic weather station (WMO station ID 02873) at Hailuoto.

Parameters	Sensor	Acq. Period	Meas. Height
Cloud base height, h_{CB}	Vaisala CT25K Laser Ceilometer	10 min	
50 SYNOP codes	Vaisala FD12P Weather Sensor	10 min	
Temperature, T; relative humidity RH	Vaisala HMP155 Humidity and Temperature Probe	10 min	2.0 m agl
Pressure, p	Vaisala PTB 201A Digital Barometer	10 min	7.3 m asl
Temperature, T	Pentronic AB Pt100 Platinum Resistance Thermometer	10 min	2.0 m agl
Wind speed, U; direction, Dir; gust U_{max}	Adolf Thies GmbH & Co. KG 2D Ultrasonic Anemometer (UA2D)	10 min, 3 s	29 m agl

The Finnish Transport Agency operates a network of coastal ice radars used for ice monitoring for navigation along the Finnish coast. One of the radars is located at Marjaniemi, at the top of a 30-m high tower next to the AWS-FMI and the light house. The ice radar is a 9.375 GHz ($\lambda \approx 3$ cm), 25 kW magnetron radar manufactured by Terma A/S, Denmark. The range resolution (the pulse length) can be chosen operationally by Vessel Traffic Services depending on ice conditions and can vary from 50 ns to 1000 ns (pulse repetition frequency from about 0.7 kHz to 3.5 kHz). Rasterized images are provided with a temporal median filtering of 15 s to 20 s. However, due to the limited means of mobile data communication, preprocessed images can only be transmitted at 2-min intervals. More detailed information on the radar and image processing is provided in reference [82].

A 4 m mast, from here on referred to as AWS-ice, equipped with instrumentation for observations of wind speed, direction, temperature and relative humidity (all at 1 m agl, 2 m agl and 4 m agl), radiation balance, and ground heat flux (snow and ice), was installed on the sea ice (Figure 1). For observations of SL turbulence, the mast was additionally equipped with an EC system, consisting of a 3-dimensional sonic anemometer and an open-path gas-analyzer for H_2O and CO_2, both mounted at 2.7 m agl. The EC system faced towards $238°$ (true direction) in order to have an undisturbed fetch over the sea ice sector. The sensor specifications are summarized in Table 2.

Table 2. Specifications of the automatic weather station (AWS)-ice.

Parameters	Sensor	Acq. Period	Meas. Height
Temperature, T	Campbell ASPTC (aspirated)	1 min	1, 2 and 4 m agl
Temperature, T	PT100 (aspirated)	1 min	1, 2 and 4 m agl
Relative humidity, RH	Rotronic HC2-S (aspirated)	1 min	1, 2 and 4 m agl
Wind speed, U	Vector A100LK	1 min	1, 2 and 4 m agl
Wind direction, Dir	Vector W200P	1 min	1, 2 and 4 m agl
Up and downwelling short and longwave radiation, $SW \uparrow\downarrow$, $LW \uparrow\downarrow$	Kipp & Zonen CNR1	1 min	1 m agl
Ground flux, GF	Hukseflux HFP01-SC	1 min	snow and ice
Wind components, u, v, w; sonic temperature, T_s	Campbell CSAT-3	0.05 s	2.7 m agl
Concentrations of H_2O, CO_2; pressure, p	LI-COR LI7500	0.05 s	2.7 m agl

2.1.2. UAV Platforms

In order to obtain detailed information on the atmospheric state across the entire ABL and parts of the free atmosphere, a number of different UAV (Figure 2), both fixed and rotary-wing systems, were operated in the area around the main field site. A short description of the systems used during the campaign and their capabilities are given below.
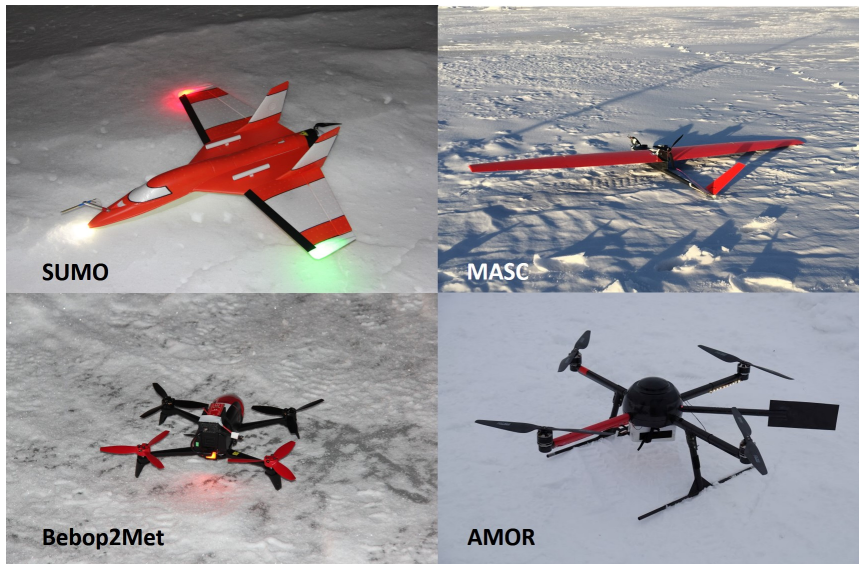
Figure 2. UAV systems used during the Hailuoto-I campaign.

The Small Unmanned Meteorological Observer (SUMO) [83,84] is a small fixed-wing UAV, equipped with the Paparazzi autopilot system and a set of basic meteorological sensors. The data acquisition system of the SUMO also records the aircraft's position and attitude, provided by an on-board Global Navigation Satellite System (GNSS) and an Inertial Measurement Unit (IMU). The SUMO is designed to take atmospheric profiles up to 5000 m and can be operated in wind speeds of more than $15 \, \text{m s}^{-1}$. Under cold environmental conditions, the flight time is typically 45 min. The most important sensor specifications are summarized in Table 3. The meteorological sensors for T and RH are placed a fair distance from the battery and motor on top of the wings to assure good ventilation during flight. In addition to the directly-measured meteorological parameters, like temperature, relative humidity, and pressure, the horizontal wind speed and direction can be estimated by applying the "no-flow-sensor" wind estimation algorithm described in reference [68].

Table 3. Specifications for the paparazzi-based UAVs: Small Unmanned Meteorological Observer (SUMO), miniTalon, and Bebop2Met.

Parameter	Sensor	Acq. Frequency	Aircraft Type
Temperature, T; relative Humidity, RH	Sensirion SHT75	2 Hz	SUMO, miniTalon, Bebop2Met
Temperature, T	Pt1000 Heraeus M222	8.5 Hz	SUMO, miniTalon
Pressure, p	MS 5611	4 Hz	SUMO, miniTalon
Infra-red temperature, T_{IR}	MLX90614	8.5 Hz	SUMO, miniTalon,
Wind components, u, v, w	Aeroprobe 5-hole probe	100 Hz	miniTalon
Position, lat, lon, alt	GNSS	4 Hz	SUMO, miniTalon, Bebop2Met
Attitude angles, θ, ϕ, ψ	IMU	4 Hz	SUMO, miniTalon, Bebop2Met

The Multi-purpose Airborne Sensor Carrier (MASC-2) is an electrically-powered, single engine, pusher aircraft of 3.5 m wing span and a total weight of 6 kg, including a scientific payload of 1.0 kg [85]. This UAV is equipped with the ROCS (Research Onboard Computer System) autopilot system developed at the University of Stuttgart. Its endurance under polar conditions is up to 90 min at a cruise speed of 22 m s^{-1}. For the measurement of turbulence along horizontal straight flight legs and other atmospheric parameters, MASC-2 carries a scientific payload, as summarized in Table 4 and described in detail in [86–88]. The sensors are placed in a special sensor holding unit which is attached to the aircraft directly above the nose to face air that is as undisturbed as possible. The 3D-wind vector and the temperature measurements are capable of resolving turbulence up to frequencies of approximately 30 Hz, allowing turbulent fluctuations to be resolved in the sub-meter range. The data from these sensors is oversampled with an acquisition frequency of 100 Hz. Each component of the measurement system aboard MASC-2 was tested in the lab and during flight. The sensors were calibrated and airborne gathered data were validated by comparison to both other measurement systems and theoretical expectations [85–87].

Table 4. Specifications for the Multi-purpose Airborne Sensor Carrier (MASC-2) UAV.

Parameter	Sensor	Acq. Frequency
Temperature, T	PT100-fine-wire	100 Hz
Temperature, T	TCE-fine-wire	100 Hz
Relative humidity, RH	P14-Rapid	100 Hz
Pressure, p	HCA-BARO	100 Hz
Wind components, u, v, w	5-hole probe	100 Hz
Position, lat, lon, alt	GNSS	100 Hz
Attitude angles, θ, ϕ, ψ	IMU	100 Hz

A new UAV based on the the miniTalon produced by X-UAV with an EPP airframe of 120 cm wingspan and 83 cm length that was designed to carry a higher payload (up to 1000 g) was tested during the campaign. The system is a further development of the SUMO by Lindenberg und Müller GmbH & Co. KG and GFI, with increased dimensions. It allows for the integration of an additional turbulence sensor package (Aerosonde five-hole probe), significantly higher air speeds (up to 25 m s^{-1}), and longer endurance (ca. 90 min). The turbulence sensors are placed in the nose facing forward, whereas the temperature and humidity sensors are mounted on top of the fuselage, well separated from the battery and motor. Aside from these differences, the miniTalon is equipped with the same Paparazzi autopilot system and the same basic sensor package as described above (Table 3).

The Bebop2Met is based on Bebop2 by Parrot, a small, commercially-available multicopter with a weight of about 500 g and a diameter of roughly 50 cm. The system was modified for our purposes by adding meteorological sensors (Table 3) integrated into a 3D-printed frame attached on top of the battery, as well as by running the Paparazzi autopilot software on the original processor. The sensors for T and RH are placed a few centimeters above one of the propellers on a thin side arm. Tests have shown that the sensors are well ventilated and that the flow at this location is fairly horizontal. The flight time under cold environmental conditions is typically in the range of 20 min, and it can only be operated safely in weak and moderate wind conditions below 10 m s^{-1}. Typical flight operations include maneuvers such as hovering at a fixed position and altitude and vertical profiles at a fixed location with a constant vertical speed.

The Advanced Mission and Operation Research (AMOR) multicopter UAV was designed to fly in environmental monitoring missions [89], including meteorological campaigns in polar regions. The central airframe, the side arms, the landing gear, and the 15 inch propellers are made of carbon-reinforced plastic. The empty weight of the UAV is 1.5 kg, and the maximum takeoff weight is 4.9 kg. Depending on the environmental conditions, the battery, and the payload, the maximum flight time is approximately 60 min, and the UAV can be operated in winds of up to 15 m s^{-1}. Due to

the cold conditions and the relatively short profiling missions during Hailuoto-I, AMOR flights took typically about 5 min. The Advanced Meteorological Onboard Computer (AMOC) receives the sensor data, fuses the data sets with the IMU and GNSS data sets, and stores them on a μSD card. A fast temperature sensor based on a 25 μm thermocouple wire, a factory calibrated HYT 271 RH sensor, and a Digi Pico P14 Rapid RH sensor provide the meteorological standard data sets. A pressure sensor provides the altitude above ground level, and a Melexis thermopile sensor provides the surface temperature data, as shown in Table 5. The sensors are mounted on a horizontal tube well outside the downwash of the propellers.

Table 5. Specifications of the sensors mounted on the Advanced Mission and Operation Research (AMOR) UAV.

Parameter	Sensor	Acq. Frequency
Temperature, T; relative humidity, RH	HYT 271	10 Hz
Temperature, T; relative humidity, RH	P14 Rapid	10 Hz
Temperature, T	K-type thermocouple	10 Hz
Pressure, p	BMP 180	10 Hz
Infra-red temperature, T_{IR}	MLX90614	10 Hz
Position, lat, lon, alt	μBlox GNSS	5 Hz
Attitude angle θ, ϕ, ψ	autopilot IMU	5 Hz

2.1.3. Remote-Sensing

For observations of the 3D-wind field over our study area, we deployed a scanning wind LIDAR (Leosphere Windcube 100s) on the shoreline (Figure 1). The Windcube 100s is a pulsed wind LIDAR system operating at a wavelength of 1.54 μm and a pulse energy of about 10 μJ. It has a maximum range for wind measurements of 3.5 km at a range gate resolution of 50 m. The LIDAR was operated in PPI (plan position indicator) mode, i.e., performing azimuth scans over 360° alternating between two elevation angles of 1° and 75°. Further details on the chosen settings are summarized in Table 6.

Table 6. Settings for the alternating PPI (plan position indicator) modes for the operation of the Windcube 100s scanning LIDAR (Light Detection and Ranging).

Parameter	Value (Low-Elevation Scan)	Value (High-Elevation Scan)
Elevation angle	1°	75°
Mode	PPI	PPI
Minimum range	50 m	50 m
Maximum range	3300 m	3300 m
Display resolution	25 m	25 m
Number of range gates	131	131
Starting azimuth angle	0°	0°
Final azimuth angle	359.9°	359.9°
Scan duration	120 s	72 s
Accumulation time	0.5 s	0.5 s

A vertically-pointing, single-antenna version of the LATAN-3M SODAR system [90] was installed on the sea ice at a distance of about 50 m from the coastline (Figure 1) on 8 February. The SODAR has a frequency-coded sounding signal which allows several measurements per range gate, thus providing higher data availability and quality compared to single-frequency signals. The frequency-coded signal includes eight consecutive 50 ms pulses with frequencies of 3.32, 3.46, 3.58, 3.66, 3.76, 3.9, 4.02 and 4.13 kHz. The vertical measurement range is from 10 m to 340 m, even though the lowest and highest levels typically suffer from poor data availability. At the lowest 3 to 4 levels, the data availability is reduced, since measurements are only based on the first few frequencies as the sampling starts immediately after the transmission of the last frequency. On the other hand, the data availability from

the upper levels is often limited by atmospheric conditions because of the lack of thermal turbulence from which the acoustic echoes originate. The measured parameters are the intensity within the main spectral peak of the return signal and the adjacent band and the Doppler shift of the peak, expressed in terms of radial velocity. The parameters are estimated for each range gate with 3 s-resolution (0.33 Hz). From the data, it is possible to derive, for example, profiles of mean vertical velocity and its variance. Previously, this SODAR has been used to detect wind shear driven turbulence, convective turbulence, strong katabatic flows, and moist air advection with wave structures in the stably stratified ABL [91].

2.2. UAV Operations

Flights taking place at altitudes of less than 150 m agl and with visual contact to the aircraft can be carried out without any restrictions. Since parts of our operations exceeded these limitations, specifically, the maximum allowed altitude, an application was made for the establishment of a temporary danger area (D-Area), which was granted by the Finnish Aviation Agency for the core period of our campaign. The D-Area (Figure 3) extended from our field site 3 km to 4 km along the coast in Southern and Northeastern directions and about 5 km off-coast to the west and northwest. The vertical extent was from the surface up to flight level 65 (6500 ft or 1981.2 m), but we limited our operations to a maximum target altitude of 1800 m to ensure a good safety margin. The D-Area had to be reserved on a daily basis on the last working day preceding the activities by sending a corresponding request to the airspace management and control (AMC) unit. Before the actual start of UAV operations, we had to contact the responsible AMC unit at Oulu airport to activate the D-Area. If aircraft were passing through or other operations compromised flight safety, the AMC unit could contact us and all operations had to be cancelled immediately. The end of the UAV activities was again reported from our side to AMC to deactivate the D-Area.

The different aircraft types were used for specific missions in the vicinity of our ground-based measurement systems. The typical locations of these flight missions are indicated in Figure 1. All UAVs applied could be operated with a few minutes delay between landing and the next launch, since this usually only requires the installation of new batteries and the start of a new flight mission in the GCS. Apart from MASC-2, which was started with the help of a bungee, all other UAVs could be launched without any technical support, i.e., from ground or hand launch for the multicopters and fixed-wing aircraft, respectively. However, only the multicopter systems, which were mainly used for ABL profiles, were operated at high repetition frequencies during intense observation periods.

The SUMO system can climb very efficiently and was mainly used to obtain vertical profiles up to an altitude of roughly 1800 m. These profiles were achieved by a helical flight pattern with a radius of 120 m and an ascent and descent rate of roughly 2 m s^{-1}. The main purpose of these missions was to obtain several atmospheric profiles per day, covering the ABL and the lower part of the free atmosphere, reflecting larger scale variations in the atmospheric background state. In total, SUMO performed 39 scientific flights during the campaign.

The flight patterns of the MASC-2 and the miniTalon, which were both designed for airborne turbulence measurements, consisted of horizontal race tracks at different altitudes between 20 m agl to 400 m agl. The race tracks, two parallel straight legs of about 600 m to 1500 m length connected by half circles for turning the aircraft, were typically aligned in the main wind direction. The data observed with the high-resolution wind and temperature sensors on these legs were used to provide turbulent parameters at higher levels. MASC-2 flights were typically carried out several times per day and partially repeated after 2 h. During the campaign, the miniTalon was only used for one day (three measurement flights) for testing and validation against the MASC-2 system, which was operated simultaneously. The data from these three miniTalon flights are not the subject of this article, since sophisticated data processing algorithms must be developed for the further analysis. The analysis of the 14 scientific MASC-2 flights is also beyond the scope of this article.

Two multicopter systems were utilized to obtain profiles at a very high vertical resolution within the ABL. In order to gain detailed information on the evolution of the ABL, these profiles were

repeated almost continuously during intensive operation periods. Due to the more sophisticated sensor package with partially very short response times, the AMOR system is capable of probing the ABL with higher accuracy, whereas the Bebop2Met profiles are comparably smooth. However, this was partially compensated by operating the Bebop2Met at a slower ascent rate. Due to technical problems, the AMOR system could only be operated during the very end of our campaign.
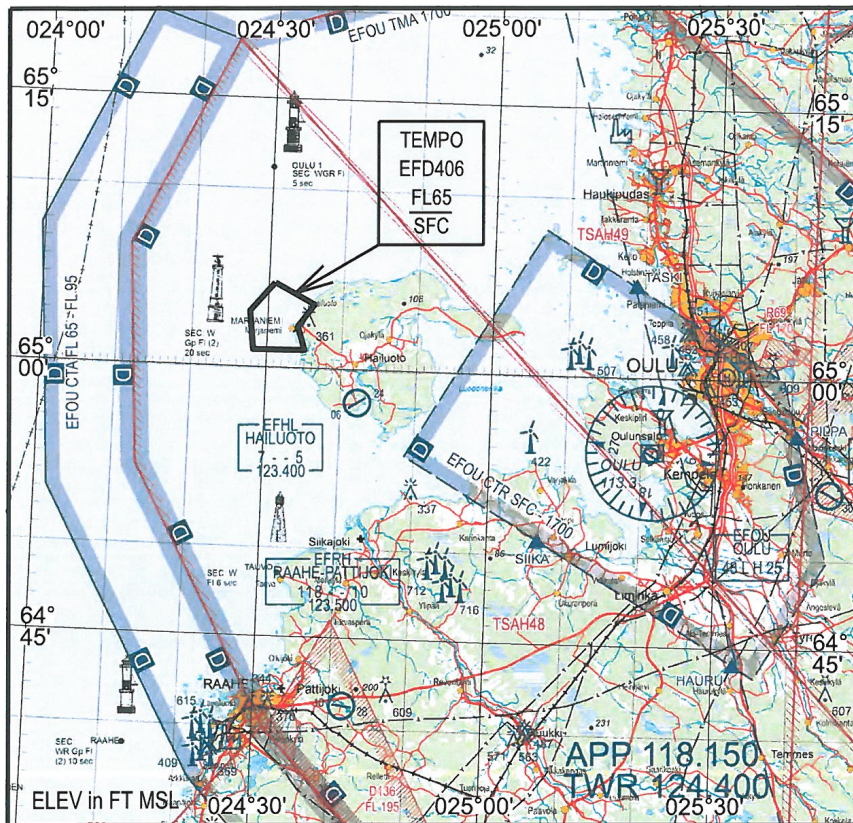
Figure 3. Aviation map of the area around Oulu airport. The danger area reserved for our UAV operations is outlined in bold and labeled as TEMPO EFD406 (Source: ANS Finland Aeronautical Information Services AIP Supplement Map).

　　The Bebop2Met UAV was operated on vertical profiles, ranging from 0 m agl and typically 200 m agl or even higher (400 m agl) when the atmospheric conditions allowed for it. The atmospheric profiles were performed at a fixed location at a distance of about 10 m to 20 m from the meteorological mast. In order to optimize the vertical resolution of these surface and boundary layer profiles, the vertical climb rate was set to $0.5\,\mathrm{m\,s^{-1}}$ below 10 m agl and $1\,\mathrm{m\,s^{-1}}$ above. The flights took typically 15 min to 20 min and could be repeated after a ground time of approximately 5 min. For comparison to the mast observations and the calibration of the (experimental) wind estimation algorithm, the Bebop2Met was held at a fixed altitude of 2 m agl to 4 m agl for 1 min to 2 min.

　　The maximum height of the AMOR multicopter profiles was typically 200 m agl. In order to operate the AMOR UAV safely in the vicinity of the other UAV and the meteorological mast on the sea ice, the start and landing site was chosen to be closer to the shore side. After the takeoff to 5 m agl, the flight was continued at the final location of the profile, approximately 20 m further towards the

seaside. The lowest part of the ABL was sampled with a vertical climb speed of $1\,\mathrm{m\,s^{-1}}$, resulting in a very high temperature resolution of approximately 0.1 m.

3. Data and Methods

3.1. Data Processing

The data from the land-based AWS-FMI is routinely checked and processed by the Finnish Meteorological Institute and can thus be used as is. All other data were visually inspected for obvious errors. Furthermore, system specific data processing procedures were applied.

The slow-response AWS-ice data were checked for their physical range, and obviously erroneous data were removed. The directional offsets of the wind vanes were corrected to face true north, and all three wind vanes were aligned to result in the same wind direction under conditions with neutral stratification. Due to the distance and large difference in measurement height, no such correction was applied in order to align our wind direction observations with the ones taken over land at AWS-FMI. The short-wave radiation (I) showed small negative values during the night, which were used to apply an offset correction to the entire data set by forcing the minimum value to equal zero.

The EC data was processed using the TK3.11 EC software package [92] producing 30-min, 10-min, and 1-min averaged turbulence quantities, like variance, turbulent fluxes of sensible and latent heat, and momentum. The following settings and corrections were applied: de-spiking by applying a 7-SD threshold; 10% maximum allowed number of missing/bad values; double rotation; Moore, Schotanus, and WPL density corrections; cross-correlation to maximize covariance; stationarity tests; and integral tests on developed turbulence. The resulting data was quality flagged using a three-level flagging system, ranging from 0 to 2. In accordance with the Spoleto agreement, a flag of 0 indicated data of high quality, 1 indicated intermediate quality and 2 indicated poor quality [92]. For the following analyses, we included all EC data with a flag of 0 or 1.

In addition to the directly measured parameters, like T, RH, and p, obtained by the SUMO, the horizontal wind speed (U) and direction (Dir) were estimated by applying the "no-flow-sensor" wind estimation algorithm described by [68]. All SUMO data were interpolated to a common frequency of 4 Hz in order to provide a consistent data set.

The Bebop2Met also provides direct profile measurements of T, RH and p, of which only data during ascent was used due to possible downwash contamination during decent. The pressure data at the time of takeoff and landing were used to remove linear trends in the surface pressure which have commonly been observed to cause altitude errors of a few meters towards the end of a flight. Getting reliable altitude information is crucial, especially for observations of the lowermost layers if, e.g., surface-based inversions are to be resolved correctly. Like for the SUMO system, all data were interpolated to a common frequency of 4 Hz. In addition, attempts were made to retrieve wind speed and direction estimates from the aircraft pitch and roll information, following the method of [93]. Due to the design of the Bebop2 with a long but slim body, this method can only be applied reliably if the cross-wind component affecting the aircraft is much smaller than the front-wind component. Since an autopilot algorithm for turning the aircraft into the wind was not implemented during the campaign, the wind speed and direction data from the Bebop2Met have to be considered experimental with corresponding larger uncertainties.

The AMOR pressure data, used to compute the height above ground level of the UAV, was smoothed by applying a moving average. The data of the humidity sensors were recomputed, taking into account the response time and thereby, mapping the correct values to the corresponding heights.

All SODAR data with a signal-to-noise ratio (SNR) below 2 dB were removed from the further analyses. From the filtered SODAR data, we computed 10-min averaged profiles of the vertical velocity and its variance. The attenuated backscatter signal, measured directly by the SODAR, was used to estimate the ABL height. When the top of a thermally-stratified ABL fell within the sounding range, the pattern of echo-signal was used to determine the ABL height. The latter was determined by

visual inspection of echograms and return-signal profiles, as the height where the echo intensity of a pronounced echoing layer sharply decreases. This method was chosen as the echo-intensity is a reliable indicator for mixing, in contrast to the standard deviation of the vertical velocity, σ_w, that is often wave-dominated in the SBL and therefore, is not a proper indicator for turbulence.

The LIDAR data obtained from the Windcube 100s were already filtered for acceptable carrier-to-noise, ratio, i.e., CNR > -23 dB. An additional check was made for the low elevation data, since this also contains clutter from hard targets such as buildings, the shore, etc. A clutter map was used to remove hard targets, which have a very high SNR and a radial velocity of zero. Furthermore, all points with an instrumental wind speed error greater than $0.5 \, \mathrm{m\,s^{-1}}$ and unphysical wind speed values exceeding $30 \, \mathrm{m\,s^{-1}}$ were removed. The radial wind speed measurements were used to compute time series of horizontal wind profiles from both PPI scanning patterns, applying the velocity-azimuth-display (VAD) technique [94]. The VAD technique assumes horizontal homogeneity, and the applied method checks this assumption by testing the collinearity. Profile time series of $\overline{w'^2}$ from the SODAR and $\overline{U}$ from the LIDAR are available as Supplementary Materials (Section 6). Furthermore, deviations from the mean state over one entire scan were used to compute turbulent statistics of the flow.

3.2. Data Availability

The data availability for the different measurement systems is shown in Figure 4. The FMI permanent weather station close to the lighthouse is part of the official Finnish weather observation network and is operational year-round. Data from this station was therefore available without major quality issues for the entire observation period. The automatic weather station, installed on the sea ice, was operated between 11 and 27 February. Due to a damaged backup battery, which was causing a drop in voltage, some data was lost. In particular, the slow-response data seemed to be affected by this issue. The EC system, running on the same data logger, stopped recording on 13 February due to a broken data cable from the sonic anemometer, which was replaced on 15 February. Furthermore, some of the EC data was of poor (flag 2, see Section 3) or intermediate quality (flag 1). Good and intermediate quality data are marked in green and orange in Figure 4 and were both used for further analysis, whereas poor quality data were removed. The optical lens of the LIDAR was subject to significant icing from the inside, especially at the beginning of the campaign. After defrosting the lens several times, this was not an issue any longer, but probably, due to very low aerosol concentration, the carrier-to-noise ratio (CNR) was rather poor for most observed levels for almost the entire campaign. The SODAR system was subject to flooding due to snow melt and water pushing up through the ice, causing some loss of data in the middle of our campaign. Green and orange colors in Figure 4 refer to the availability of instantaneous observations used to compute a 10-min average. For the good quality data, the lower threshold was 66.7% and for limited quality data, it was 33.3%.

The operation of the different UAVs requires significant manpower, typically involving one safety pilot and one ground control station operator. These systems were therefore mainly operated during intensive observational periods, when the atmospheric conditions were most interesting, i.e., strong static stability and weak winds in the SL. Smaller technical problems and human endurance during rough environmental conditions prevented higher numbers of flights. A fair amount of flights were also carried out during conditions when the stability was relatively weak. In total, 139 scientific flight missions were carried out during the campaign and were distributed as follows: 53 Bebop2Met; 39 SUMO; 30 AMOR; 14 MASC-2; and 3 miniTalon flights. Around one third of the flights (39%) were carried out during conditions with strong atmospheric stability ($Ri_B > 0.2$). For 12% of the cases, the 2-m wind speed was, in addition, below $0.5 \, \mathrm{m\,s^{-1}}$. The irregular flight times, with a focus on stable conditions and rather moderate and low wind speeds, as well as the maximum flight altitudes of the different UAV systems, may have caused a significant sampling bias. It is therefore not recommended for general conclusions to be drawn based on the UAV data alone. These data should primarily be used for the analysis of case studies.
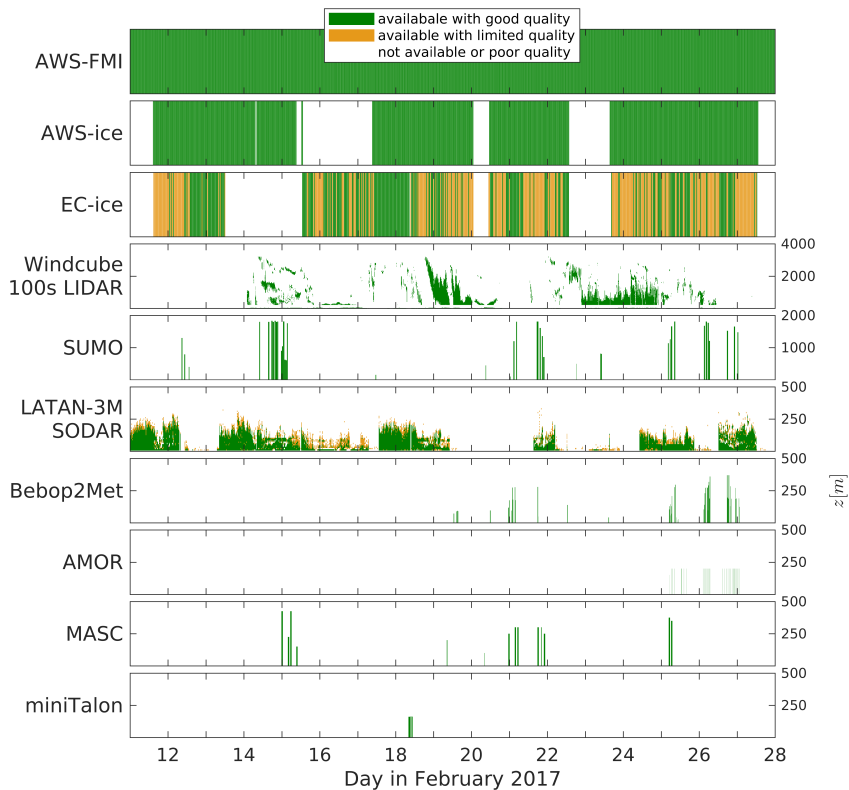
Figure 4. Data availability and corresponding altitude (only for profiling systems) for the different observation systems during the campaign period. Green indicates the availability of good quality data where applicable; orange corresponds to available data of limited quality; and the white gaps indicate poor quality or missing data.

4. Synoptic Situation and Sea Ice Conditions

The analysis of the synoptic situation, including the passages of fronts and sea ice conditions was based on the daily FMI operational weather analysis and ice charts. Until recently, the Bothnian Bay has been entirely frozen every winter. However, the ice thickness, the maximum annual ice extent, and the length of the ice season have shown decreasing trends in recent decades [95]. Winters 2014/2015 (Uotila2015) and 2015/2016 were the first for which we can be certain that parts of the Bothnian Bay remained ice-free. The maximum ice extent is typically reached in March. In the shallow waters close to the coast, land-fast ice prevails and can grow up to a thickness of 0.8 m. Even in mild winters, the level ice thickness reaches 0.3 m to 0.5 m. The land-fast ice is typically free of leads, and the compact sea ice field with snow pack on top effectively insulates the atmosphere from the relatively warm sea.

The sea ice season 2016/2017 was mild in the Baltic Sea. Its length in the Bothnian Bay was, however, close to the average of 1965–1986 (reference period used in FMI ice service). The ice growth started during the first half of November 2016 and was fast during a cold period in early January, leading to an overall ice extent of 44,000 km^2 in Bothnian Bay. Shortly thereafter, temperatures increased and for the rest of the month, mild southwesterlies prevailed, preventing new ice formation and packing the ice densely towards the coast within Bothnian Bay. By the end of January, the Baltic Sea ice extent had reduced to only 28,000 km^2.

In the beginning of February, a large high pressure system strengthened over Finland, causing fair weather and occasional extremely cold temperatures. Especially from 6 to 9 February, there were very cold temperatures in most of the country. The ice extent increased then rapidly, and a maximum ice extent in the Baltic Sea of 88,000 km^2 was observed on 12 February. At this time, Bothnian Bay was almost completely ice-covered by 10 cm to 25 cm thick drift ice, and the thickness of the land-fast ice was between 5 cm to 55 cm, as shown in Figure 5 (left panel). In the middle of February, a westerly to northwesterly flow pattern strengthened over the region, causing dry and warm Föhn wind from the Scandinavian Mountains. Over Bothnian Bay, the ice field was packed against the Northeastern coast, and a large ice-free area in the center of the Bay formed (Figure 5, right panel). Almost all ships to Oulu, Kemi, and Tornio had to be assisted by ice breakers. In the end of February, ice extent of the Baltic Sea was 77,000 km^2.
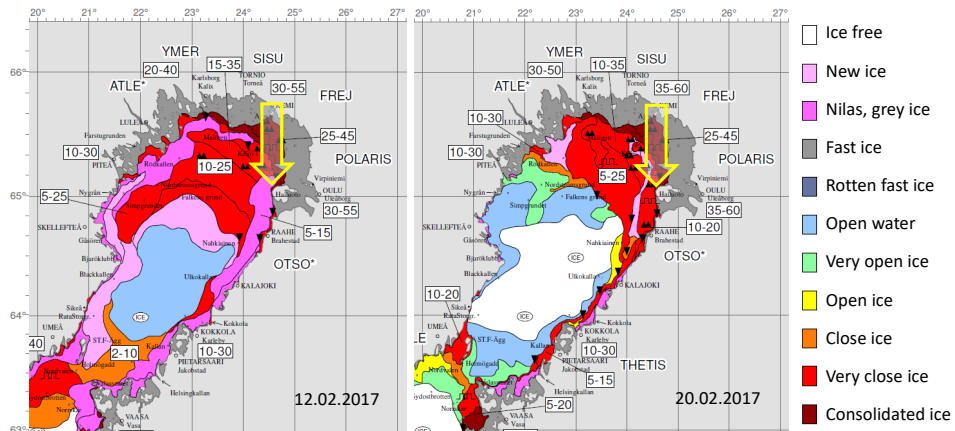
Figure 5. Examples of sea ice charts: maximum extent during the campaign on 12 February 2017 (**left panel**) and minimum on 20 February 2017 (**right panel**). The ice type is color coded; the numbers in the white boxes indicate the ice thickness in cm. The charts were provided by the Finnish Meteorological Institute on an operational basis (http://en.ilmatieteenlaitos.fi/ice-conditions). The location of the experiment site is indicated by the yellow arrow.

On Hailuoto, the 2-m air temperature was 2 °C higher and the 10-m wind speed was 0.5 m s^{-1} lower than the climatological mean values for February during 1981–2010. In the first week of the ISOBAR campaign Hailuoto-I, from 11 to 18 February, the synoptic-scale conditions were characterized by a high-pressure center, first located over Southern Scandinavia and then moving over Central and Eastern Europe. Low pressure systems were passing over the North Atlantic, Norwegian Sea, and Barents Sea from southwest to northeast, resulting in variable winds, occasionally approaching 20 m s^{-1} in Hailuoto (Figure 6). Depending on the air-mass origin, wind speed, and cloud cover, the 2-m air temperature in Hailuoto varied between −17 °C to 4 °C (Figure 6). By 19 February, the high pressure center had moved north of the Azores, and a small low pressure system passed over Europe during 19 to 24 February. A passage of a warm front resulted in snow fall (8 mm water equivalent) on 23 February. From 24 to 27 February, the synoptic situation was dominated by two large low pressure systems, one first centered over Southern Finland, moving towards the northeast, and another one moving from the Denmark Strait to the Faroe Islands. In the saddle region between the lows, clear skies and weak winds allowed the 2-m air temperature, observed at the official weather station, to drop down to −19.1 °C during the night of 27 February.

Figure 6. Overview of the meteorological conditions: (**a**) temperature, T, and surface pressure, p; (**b**) relative, RH, and specific humidity, q; (**c**) wind speed, U; and direction, Dir; (**d**) short-wave, K, long-wave, I, and net radiation balance, Net; (**e**) total cloud fraction and cloud base height. Gray shading indicates times of UAV operation. Note that the wind measurements over land were performed at 29 m above ground.

5. Potential of the Data and First Results

The deeper analysis of the comprehensive data set collected during the Hailuoto-I campaign is far beyond the scope of this overview article. Here, we aim to give a general overview of the campaign conditions, mainly based on the SL observations with the eddy covariance technique (Section 5.1). We shortly present the potential to combine the different ground-based in-situ and remote-sensing observations for a detailed characterization of the ABL structure (Section 5.2), and finally, present the results of a case study in a situation where the temperature suddenly decreased by 6 °C close to the ground (Section 5.3).

5.1. Surface Layer Observations

The conditions in the SL, observed over the sea ice, are presented in Figure 7, from top to bottom as follows: (a) the turbulent friction velocity, $u_* = (\overline{u'w'}^2 + \overline{v'w'}^2)^{1/4}$; (b) the turbulent kinetic energy per unit mass, $TKE = 1/2 \cdot (\overline{u'^2} + \overline{v'^2} + \overline{w'^2})$; (c) the turbulent sensible heat flux, $H_S = c_p \cdot \rho \cdot \overline{w'T'}$; and (d) the turbulent latent heat flux, $LE = \lambda \cdot \overline{w'a'}$. u_* and TKE were both highly correlated with

the horizontal wind speed, ranging from values close to zero up to roughly $0.75\,\mathrm{m\,s^{-1}}$ and $3\,\mathrm{m^2\,s^{-2}}$, respectively. Both parameters did not show any obvious dependency on the wind direction (see Figure 6). However, when directional aspects were considered, it has to be taken into account that the sonic anemometer was facing off-shore and that a fair amount of data with flow over the island was flagged by the post-processing software due to potential flow distortion errors from the mast [92]. H_S was mostly negative, ranging from $-73.6\,\mathrm{W\,m^{-2}}$ to $27.5\,\mathrm{W\,m^{-2}}$. The strongest negative values of H_S, associated with rapid cooling of the ABL, were reached under conditions with strong negative radiation balance (dominated by the outgoing long-wave radiation, I, see also Figure 6d), resulting in moderate values of u_* or TKE. Such situations are typically associated with large positive temperature gradients (not shown in detail here). However, the turbulent flux of the latent heat, LE, showed very different values, ranging from $-16.3\,\mathrm{W\,m^{-2}}$ to $37.0\,\mathrm{W\,m^{-2}}$. More than half of the observed values of LE were positive. This is not surprising, as sea ice and snow are saturated surfaces. Hence, if the air relative humidity is below saturation, an upward latent heat flux may occur simultaneously with a downward sensible heat flux. Over Polar oceans, the air relative humidity is at, or very close to, saturation [43], and dry air masses are often advected over the sea ice, allowing sublimation (upward latent heat flux) even if the sensible heat flux is directed downwards. For example, during a Foehn event over the Bothnian Bay in March 2004, [96] observed a relative humidity of 40 % with an upward latent heat flux simultaneous to a downward sensible heat flux. In our case, the largest upward latent heat flux was observed on 17 to 18 February 2017 (Figure 7), when the relative humidity was 70% to 80% and wind was coming from the west (Figure 6). Calculation of a three-day backward trajectory applying the Meteorological Data Explorer [97] indeed suggested a Foehn event with adiabatic subsidence heating when the air mass descended down the mountain slopes in Northern Sweden.
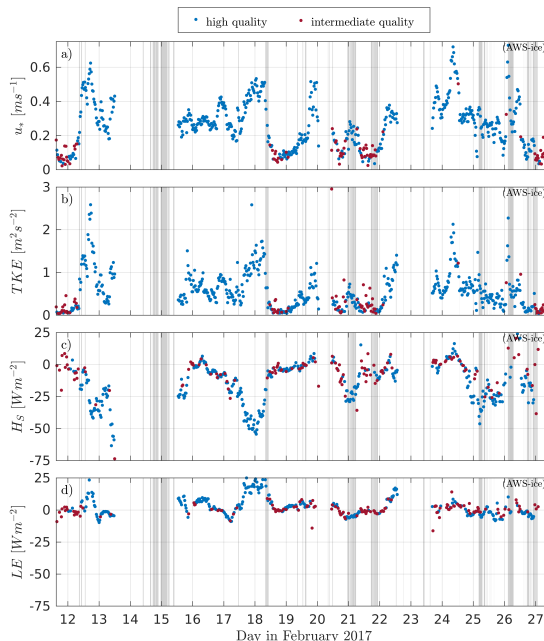
Figure 7. Time series of (**a**) 30-min averaged friction velocity, u_*; (**b**) turbulent kinetic energy per unit mass, TKE; (**c**) turbulent sensible heat flux, H_S; and (**d**) latent heat flux, LE, observed with the EC system, 2.7 m above the sea ice. The quality of the data is indicated by blue and red markers for high and intermediate quality, respectively. Poor quality data is not shown. Gray shading indicates times of UAV operation.

Figure 8 shows the time series of the stability parameters: (a) Monin–Obukhov (MO) stability parameter, $\zeta = z/L$ with z being the measurement height and L the Obukhov length, defined as $L = -(\theta_v \cdot u_*^3)/(\kappa \cdot g \cdot \overline{w'\theta_v'})$; (b) the flux Richardson Number, $Rf = (g \cdot \overline{w'\theta_v'})/(\theta_v \cdot \overline{u'w'} \cdot \partial \overline{U}/\partial z)$; (c) the bulk Richardson Number, $Ri_B = (g \cdot \Delta\theta_v \cdot \Delta z)/(\overline{\theta_v} \cdot (\Delta U)^2)$; (d) the difference in potential temperature, $\Delta\theta$, between the 4 m and 1 m levels, as observed over the sea ice; and (e) the atmospheric boundary layer (ABL) height (h_{ABL}), estimated from the SODAR observations. The gray vertical lines indicate events with $U < 0.5\,\mathrm{m\,s^{-1}}$, the threshold for the near-calm stable boundary layer (SBL), when, according to [98], the relationship between the fluxes and the weak mean flow breaks down and the use of the traditional stability parameters, e.g., ζ, Ri_B, Rf, becomes difficult. The dynamic stability, ζ, covers a wide range of different stabilities from weakly unstable (4%), $\zeta < -0.1$, to stable or very stable (29%), $\zeta \geq 0.05$, with most observations in the near-neutral range (66%), $-0.1 \leq \zeta < 0.05$.
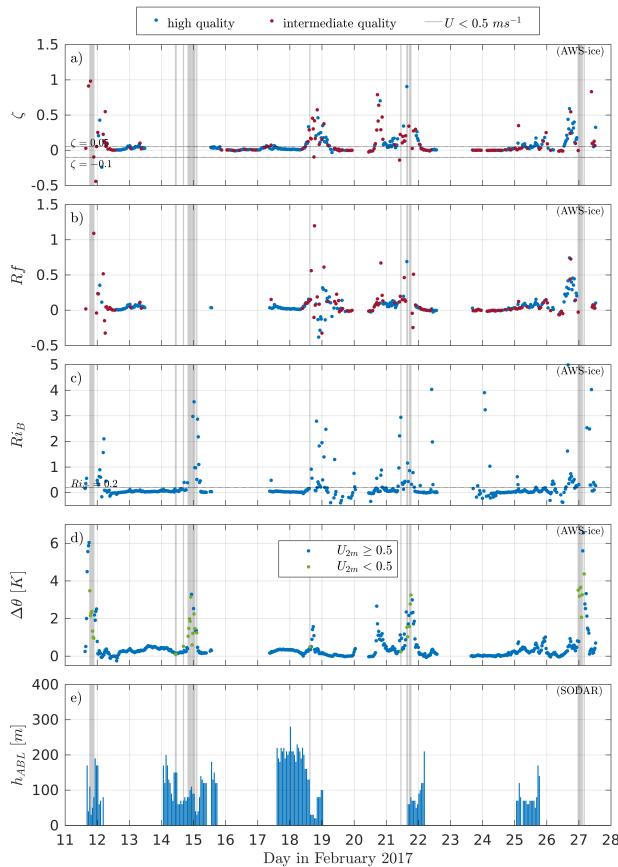
Figure 8. Time series of the stability parameters: (**a**) MO stabilty, ζ; (**b**) flux Richardson Number, Rf; (**c**) bulk Richardson Number, Ri_B; (**d**) the difference in potential temperature between the 4 m and 1 m levels, observed over the sea ice; and (**e**) the ABL height, h_{ABL}, estimated from the SODAR (Sound Detection and Ranging) observations. The quality of the underlying eddy covariance (EC) data for ζ and Rf is indicated by blue and red markers. The horizontal dashed lines for $\zeta = -0.1$ and $\zeta = 0.05$ in (**a**) and $Ri_{cr} = 0.2$ in (**c**) mark the thresholds for different stability classes. The gray vertical lines mark near-calm events with $U < 0.5\,\mathrm{m\,s^{-1}}$.

However, a fair number of cases (27%) with very stable stratification ($Ri_B > Ri_{cr} = 0.2$) were found. All such cases were related to weak wind conditions, when u_* or $\overline{u'w'}$ approach zero, resulting in high stability values. During the observation period, 34 cases (30-min averages) of a near-calm SBL were observed, which frequently resulted in very sharp surface inversions with potential temperature differences between the 4 m and 1 m levels reaching up to 6 °C and greater. h_{ABL} was typically below 100 m during these cases and reached values as low as 20 m. It has to be noted that no absolutely reliable algorithm for determining h_{ABL} from SODAR observations exists and that our estimates are partially based on human judgment and therefore, are somewhat subjective. Furthermore, no reliable estimates could be provided when the data quality of the SODAR observations was too poor or when h_{ABL} exceeded the vertical range of the instrument, i.e., $h_{ABL} > 340$ m.

5.2. Profiles

5.2.1. Composite Profiles from Multiple Systems

Figure 9 shows an example of atmospheric profile measurements for temperature, T, and wind speed, U, from different systems, i.e., AWS-ice at 1 m agl, 2 m agl and 4 m agl; AWS-FMI (only U) at 29 m asl; Bebop2Met (only T) from 0 m agl to 350 m agl; SUMO from 40 m agl to 1800 m agl; and LIDAR from roughly 200 m agl to 450 m agl. The displayed AWS and LIDAR data represent time-averaged data for the time period indicated in the legend, whereas the UAV data correspond to one single ascent. The Bebop2Met T data is bin-averaged with 10 m increments, while for the SUMO data, the bins are 25 m, and the LIDAR data points are separated by roughly 24 m. It also has to be noted that we used three different scales for the y-axis to increase the level of detail in the SL towards the surface.
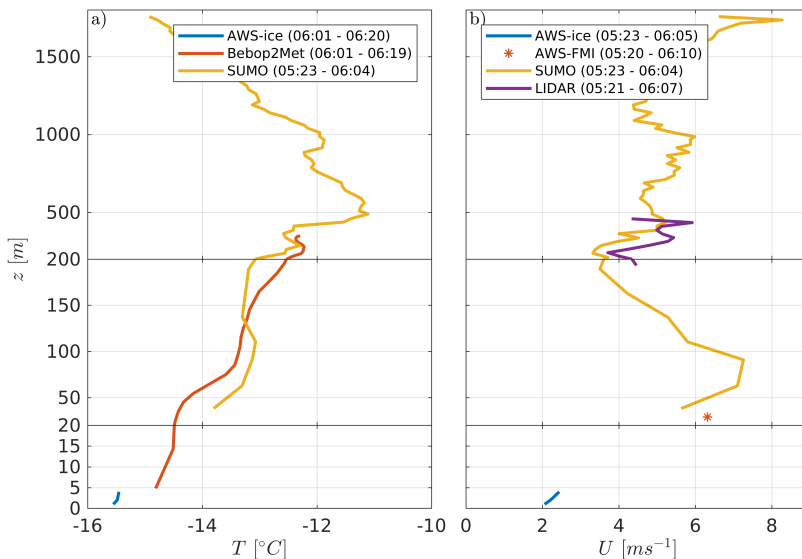
Figure 9. Combined temperature (**a**) and wind speed (**b**) profiles based on AWS-ice AWS-Finnish Meteorological Institute (FMI) (only U), Bebop2Met (T), Small Unmanned Meteorological Observer (SUMO) and LIDAR (U) observations from 26 February between 05:20 and 06:20 UTC. The AWS and LIDAR data represent averaged profiles for the periods indicated in the legend.

During the morning of 26 February, the ABL was stably stratified with a surface-based inversion reaching up to about 300 m, as well as several smaller, but also sharp inversions further above. All three systems matched very well with temperature differences in the range of 0.5 °C, which could have

been caused by differences in the sampling times and differences in the time and spatial averaging procedures applied to the data.

The profile of the horizontal wind speed has a gap from 4 m agl to 40 m agl, since no reliable estimates from the Bebop2Met UAV could be computed due to a significant cross-wind component acting on the multicopter and the lack of LIDAR data with sufficient CNR. The SUMO data, however, indicated the existence of an LLJ with a peak velocity of about $7.5\,\mathrm{m\,s^{-1}}$, located just below 100 m, which also corresponds well to the notable decrease in the vertical temperature gradient observed at this level. At the levels between the 200 m to 500 m, where LIDAR data was available, and in the vicinity of the 29-m wind measurement at AWS-FMI, the agreement between the observations within $1\,\mathrm{m\,s^{-1}}$ was fairly good, given the differences in the observation and data processing principles.

5.2.2. Evolution of Temperature Profile

The evolution of the thermal structure of the ABL during the night from 26 to 27 February is shown in Figure 10. The observations were taken by the small multicopter UAV Bebop2Met in a distance of roughly 20 m from the meteorological mast installed on the sea ice (Figure 1), and cover the time period from 17:38 UTC to 01:26 UTC (mean time of the ascent profiles). All profiles indicated a sharp, surface-based inversion reaching up to about 50 m. Above this level, the vertical temperature gradient decreased and eventually approached an isothermal gradient. The temperature above 150 m remained at roughly $-9\,°\mathrm{C}$ to $-8\,°\mathrm{C}$ for the entire 8 h period, with weak signs of warm air advection between 18:42 UTC and 19:50 UTC. The lowermost 50 m or so were, however, subject to rapid cooling, with temperatures at the surface decreasing from $-14\,°\mathrm{C}$ to $-22\,°\mathrm{C}$ after 23:04 UTC. During this event, the vertical temperature difference in the lowermost 20 m increased from values of around $2\,°\mathrm{C}$ to $6\,°\mathrm{C}$, causing a very strong static stability and inhibiting almost any vertical movement (see Section 5.3). The same behavior was also detected in the time series of profiles from the AMOR system which was operated roughly at the same time period (not shown here).
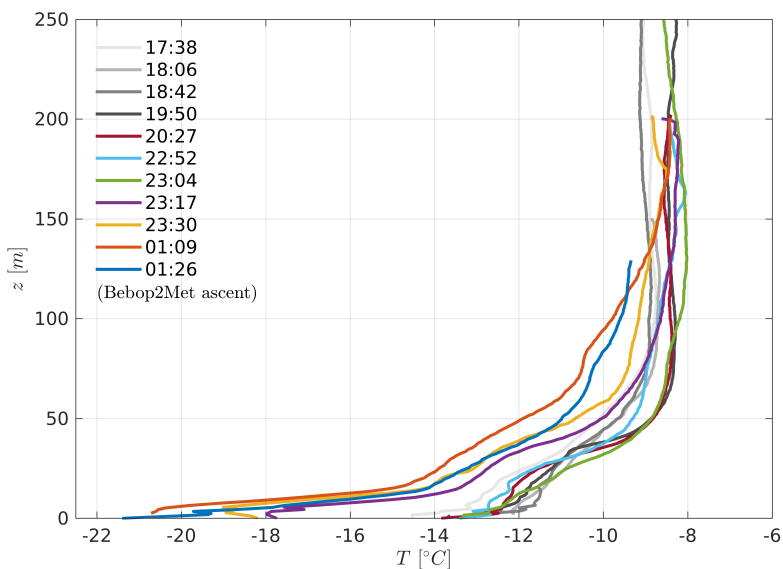
Figure 10. Evolution of the temperature profile during the night of 26 to 27 February, observed by the Bebop2Met UAV during ascent. The times in the legend refer to the mean times of each individual profile.

5.3. Case Study on Very Stable Conditions—26 to 27 February

During the last night of the campaign, 26 to 27 February, we observed a very stable case, which was characterized by strong, rapid temperature changes observed at AWS-ice. Almost the entire night was cloud-free without any indications of fog or other significant weather, according to the official weather observations from AWS-FMI. The radiation balance was strongly negative, especially until 0:00 UTC, and radiative cooling was the dominant term in the surface energy balance (compare Figure 6). Figure 11 shows the corresponding time series of (a) T; (b) U; (c) Dir; (d) RH; and (e) $\overline{w'^2}$ from the two locations over land (except for $\overline{w'^2}$) and sea ice for the period between 16:00 and 8:00 UTC. All data are based on a 1-min averaging period, except for the data from the land-based AWS-FMI, which was only available at a resolution of 10 min.
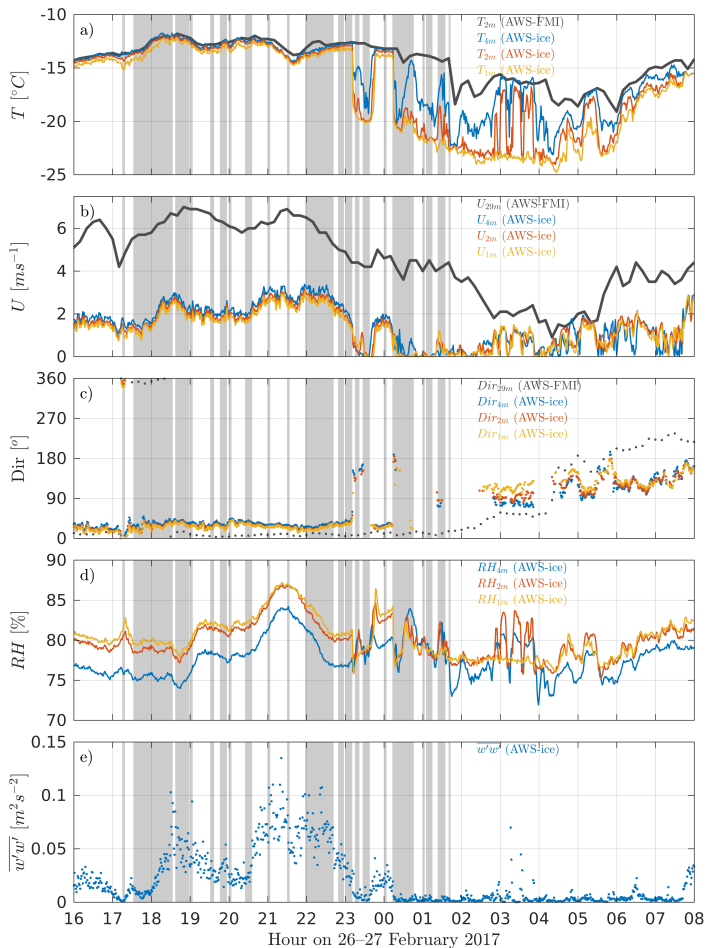
Figure 11. Time series of temperature, wind speed, wind direction, relative humidity, and vertical velocity variance (from top to bottom) during the night of 26 to 27 February. The displayed data represents 10-min and 1-min averaged data of (**a**) T; (**b**) U; (**c**) Dir; (**d**) q; and (**e**) $\overline{w'^2}$ from the permanent AWS-FMI on land and the three levels and EC of the AWS-ice, respectively. Gray shading indicates times of UAV operation.

Until around 23:00 UTC, the conditions were relatively stationary, with temperatures between $-15\,°C$ to $-12\,°C$ and wind speeds between $1\,m\,s^{-1}$ to $3\,m\,s^{-1}$ close to the ice surface and $5\,m\,s^{-1}$ to $7\,m\,s^{-1}$ at 29 m asl. The vertical gradients and local differences between land and sea ice were generally small. The 29-m wind speed decreased from $6.5\,m\,s^{-1}$ to $1.5\,m\,s^{-1}$, before it started increasing again at about 4:20 UTC.

At about 23:10, a drop in temperature from approximately $-13\,°C$ to $-18\,°C$ was observed at the 1 m level over the sea ice (Figure 11a), accompanied by a calming of the near surface winds over the ice (Figure 11b). This initial drop happened within 1 min to 2 min, but the cooling continued and temperatures of $-20\,°C$ were reached. The same kind of changes, albeit slightly weaker and slower, were observed at the 2 m and 4 m levels, whereas the observations over the slightly elevated land remained fairly constant. The near-surface temperature and wind speed stayed at low values for about 20 min and returned to their previous states at a slower rate within approximately 5 min, starting at the top and penetrating further down. The following warmer phase with a weak flow also lasted for about 20 min. During this first cold episode, the static stability in the SL was much stronger compared to the conditions before and after the episode, with temperature differences of up to $5\,°C$ and roughly $0.5\,°C$ between the 4 m and 1 m levels, respectively. The vertical gradient of U occasionally became negative during the near-calm events, indicating a decoupling of the near-surface layers. After the first cycle of rapid temperature changes, several similar events followed, which were, however, not as clearly structured as the first one, since the 1 m level and partially, the 2 m level remained at low temperatures with very weak or calm winds. Furthermore, these following events were significantly shorter and occurred with a higher frequency. At about 6:00 UTC—just after sunrise—temperatures at all observation levels started to rise again; the vertical temperature gradient decreased and the oscillations in temperature and wind became much weaker.

During the evening and throughout the night until about 2:00 UTC, the general wind direction at 29 m asl was from north (Figure 11c). During the rest of the night and the morning, the direction shifted to northeast (from about 3:00 to 4:00) and finally, to southwest (from 06:00). Over the sea ice, the wind direction deviated by a few degrees toward the east in the beginning, which might have partially been caused by a small error in the azimuthal sensor alignment. Due to the weak wind speeds below the detection range of our wind vanes, i.e., $0.6\,m\,s^{-1}$, a fair amount of wind direction observations over the sea ice had to be neglected during the calm and cold periods. The available data from these events revealed frequent direction shifts of more than $90°$ to the east and southeast, with relatively large deviations between the three observation levels. The relative humidity (Figure 11d) and specific humidity (not shown) closely followed the pattern of the temperatures at the corresponding levels, observed at the AWS-ice. The vertical velocity variance, observed with our EC system at 2.7 m asl (lowermost panel in Figure 11), indicated very weak vertical turbulent motion in the order of $\overline{w'^2} = 0.001\,m^2\,s^{-2}$ during cold episodes. The values were about one order of magnitude higher during the warmer phases. This supports the argument that vertical mixing, or its absence, is causing the observed oscillations. The values of $\overline{w'^2}$ were typically up to two orders of magnitude higher before the first event.

The last multicopter profile from this night taken with the AMOR originated from 1:40 to 1:43 UTC during one of the cold and calm events. The corresponding temperature profile is shown in Figure 12a) from ground level to 200 m, together with the AWS-ice data. The AMOR's downward facing infra-red sensor confirmed the low temperatures of the ice-covered surface ($T_{IR} = -23\,°C$). The temperature gradient within the lowermost 20 m was extremely strong with a total gradient of $\Delta T = 10\,°C$. Right above, in the layer from roughly 20 m agl to 60 m agl, there was a remarkably strong variation in temperature, with a superadiabatic lapse rate from about 20 m agl to 40 m agl. The air parcel at about 30 m agl to 40 m agl had the potential to penetrate further down to a level of approximately 5 m agl to 10 m agl, assuming a dry adiabatic descent. This can be interpreted as the signature of a strong, most likely, Kelvin–Helmholtz instability, causing local mixing, which then penetrated further down, causing the SL to switch back from the cold and calm state.
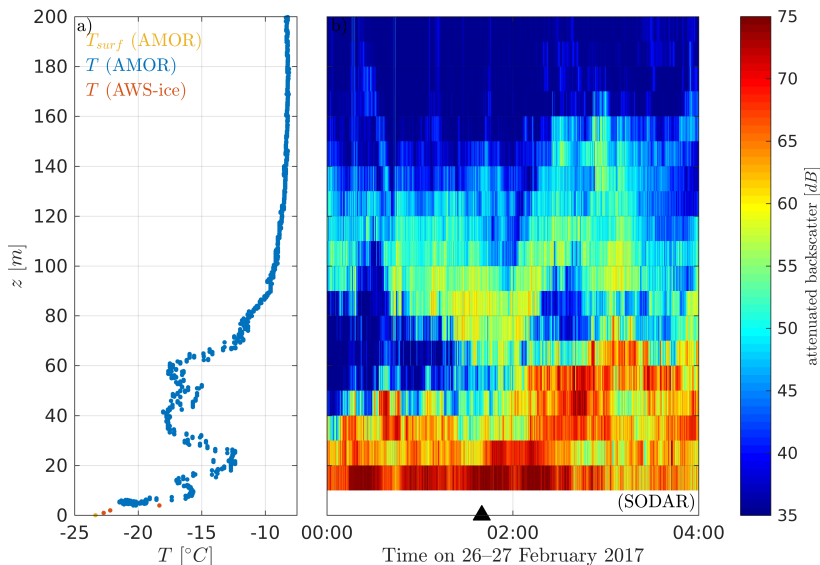
Figure 12. The structure of the ABL during 26 to 27 February: (**a**) vertical temperature profile taken by an AMOR multicopter (blue dots) and compared to the Automatic Weather Station (AWS-ice, red circles) from 1:40 UTC to 1:43 UTC, and (**b**) attenuated backscatter from the LATAN-3M SODAR between 0:00 UTC and 4:00 UTC. The black triangle marks the start time of the AMOR profile.

The time series of the attenuated backscatter from the LATAN-3M SODAR (Figure 12b) at the moment of the multicopter profile acquisition was characterized by two echoing layers: one layer within the lowest 20 m and the second one within 60 m to 100 m. The layers nicely correspond to the temperature inversion observed by the multicopter. The evolution of the attenuated backscatter profile clearly shows variability in the vertical structure of the ABL and allows for the estimation of temporal validity frame for multicopter profiles. Furthermore, the elevated inversion layer oscillated with a period of 1 h to 2 h, which could be an indication of gravity-wave activity during this night.

6. Summary and Outlook

The ISOBAR field campaign, Hailuoto-I, in February 2017 resulted in an extensive data set from several different observation systems, including ground-based in-situ and remote-sensing, in addition to airborne observations by various UAVs. The meteorological and sea ice conditions during the campaign did not represent the climatological means in the area with 2 °C higher temperatures and significantly less sea ice during most of February, compared to climatological references. Despite the relatively mild conditions, accompanied by a below average sea ice cover and the already significant diurnal cycle with notable short-wave radiation, a valuable data set on the SBL was sampled.

The stability of the SL was mostly near-neutral, but also, a fair amount of very-stable cases ($Ri_B > Ri_{cr}$) occurred during the campaign, typically related to clear sky and weak wind or near-calm conditions. Under very stable conditions, the ABL height, h_{ABL}, estimated from the SODAR data reached values as low as 20 m. In general, wind shear seems to be a very important mechanism for creating turbulence. The long-wave upwelling radiation usually dominated over the other radiation terms and the turbulent fluxes of latent and sensible heat, with the latter also being significant.

A unique approach was made in which data was combined from different profiling systems to create composite profiles, probing the atmospheric column from the surface to an altitude of 1800 m agl with very high resolution in the lowermost layers. The agreement between the different systems was very good, given the systematic differences in the measurement principle, as well as in the vertical

and temporal resolutions. Sampling the lowermost 200 m or so repeatedly over several hours gave detailed information on the evolution of the SBL structure, such as a rapid cooling of the lowermost 20 m and other relevant processes like warm air advection. The sampled data also contained at least one longer period of an SBL with very stable stratification and calm winds, which was characterized by a series of turbulent events leading to a rapid warming of the layers close to the ice surface. The UAV and SODAR profiling systems gave additional insight into the nature of these events, suggesting the existence of an elevated source of turbulence which could contribute to the occasional mixing events observed close to the surface.

The experience from this campaign motivated us to conduct a second, even more extensive field experiment. The ISOBAR campaign Hailuoto-II took place at the same site from 1 to 28 February 2018. The collected data from both ISOBAR field campaigns will be the basis for future SBL research studies. A particular focus will be on the combination of the observational data set with modeling approaches on different scales (NWP and LES) and with different levels of complexity (e.g., 3D and single column). The Weather Research and Forecasting (WRF) model [2], run with different surface and boundary layer parameterization schemes, will be evaluated against the observations to better understand the physics and dynamics behind the observed events. For that purpose, we will also perform a series of experiments with the WRF model's single-column mode, in which the atmospheric column above a single grid point from the 1 km WRF domain is resolved with very high vertical resolution. This will give a deeper insight into the sensitivity of the SBL to changes in the prescribed surface conditions and model physics.

Accompanying the LES runs will be performed with the Parallelized Large-Eddy Simulation Model (PALM) [99] to reveal SBL structure and dynamics, and virtual UAV measurements will be conducted on-the-fly during the simulation in order evaluate the representativeness of these measurements. The advantage in the LES is that the true state of the ABL is known, and errors induced by the measurement strategy can be directly evaluated. Based on the findings from this investigation, improved UAV flight strategies might be developed. Second, the problem of lacking grid convergence when simulating the SBL with LES will be addressed by applying a modified MOST-based surface boundary condition. Unlike existing boundary conditions, this will not lead to violations of the basic assumptions of MOST and inherent issues in LES modeling as outlined in the introduction. Finally, a series of LES runs shall be employed to evaluate both flux and alternative gradient-based similarity functions [33,34] in the SBL. This work will follow the methodology of the recent work for convective conditions by [100] and will elucidate whether gradient-based similarity functions might be superior to the established flux-based MOST formulation, particularly under very stable conditions.

Author Contributions: Conceptualization, S.T.K., J.R., T.V., B.W., M.O.J., B.M., S.M., A.A.M.H. and J.B.; Data curation, S.T.K., I.S., E.O., R.K., B.W., G.U. and A.S.; Formal analysis, S.T.K., I.S., E.O., R.K., B.W., G.U. and A.S.; Funding acquisition, S.T.K., J.R., T.V., B.W., M.O.J. and S.M.; Investigation, S.T.K., T.V., I.S., E.O., R.K., B.W., A.R., G.U., M.O.J., L.B., M.M., C.L. (Christian Lindenberg), C.L. (Carsten Langohr), H.V., M.H., P.H. and M.S.; Methodology, S.T.K., J.R., M.O.J., B.M., S.M., T.L., A.A.M.H. and G.-J.S.; Project administration, S.T.K., J.R., S.M. and J.B.; Resources, J.R., T.V., R.K., M.M., C.L. and J.B.; Software, S.T.K., I.S., E.O., R.K., B.W., M.O.J., A.S. and M.M.; Supervision, J.R. and T.V.; Validation, S.T.K., J.R., I.S., E.O., R.K., B.W. and G.U.; Visualization, S.T.K., J.R., R.K., B.W., G.U. and A.S.; Writing – original draft, S.T.K., J.R., T.V., I.S., R.K., B.W., A.R., G.U., B.M., S.M., T.L., A.A.M.H. and G.-J.S.; Writing—review & editing, S.T.K., J.R., T.V., I.S., R.K., B.W., A.R., M.O.J., L.B., B.M., S.M., T.L., A.A.M.H., G.-J.S. and A.S.

References

1. Mahrt, L. Stably Stratified Atmospheric Boundary Layers. *Annu. Rev. Fluid Mech.* **2014**, *46*, 23–45. [CrossRef]

2. Skamarock, W.; Klemp, J.; Dudhia, J.; Gill, D.; Barker, D.; Duda, M.; Huang, X.Y.; Wang, W. *A Description of the Advanced Research WRF Version 3*; Technical Report NCAR/TN-475+STR; NCAR: Boulder, CO, USA, 2008. [CrossRef].

3. Tjernström, M.; Žagar, M.; Svensson, G.; Cassano, J.J.; Pfeifer, S.; Rinke, A.; Wyser, K.; Dethloff, K.; Jones, C.; Semmler, T.; et al. Modelling the Arctic Boundary Layer: An Evaluation of Six ARCMIP Regional-Scale Models Using Data from the SHEBA Project. *Bound.-Layer Meteorol.* **2005**, *117*, 337–381. [CrossRef]

4. Cuxart, J.; Holtslag, A.A.M.; Beare, R.J.; Bazile, E.; Beljaars, A.; Cheng, A.; Conangla, L.; Ek, M.; Freedman, F.; Hamdi, R.; et al. Single-Column Model Intercomparison for a Stably Stratified Atmospheric Boundary Layer. *Bound.-Layer Meteorol.* **2005**, *118*, 273–303. [CrossRef]

5. Mauritsen, T.; Svensson, G.; Zilitinkevich, S.S.; Esau, I.; Enger, L.; Grisogono, B. A Total Turbulent Energy Closure Model for Neutrally and Stably Stratified Atmospheric Boundary Layers. *J. Atmos. Sci.* **2007**, *64*, 4113–4126. [CrossRef]

6. Holtslag, A.; Svensson, G.; Baas, P.; Basu, S.; Beare, B.; Beljaars, A.; Bosveld, F.; Cuxart, J.; Lindvall, J.; Steeneveld, G.; et al. Stable Atmospheric Boundary Layers and Diurnal Cycles–Challenges for Weather and Climate Models. *Bull. Am. Meteorol. Soc.* **2013**, *94*, 1691–1706. [CrossRef]

7. Lüpkes, C.; Vihma, T.; Jakobson, E.; König-Langlo, G.; Tetzlaff, A. Meteorological observations from ship cruises during summer to the central Arctic: A comparison with reanalysis data. *Geophys. Res. Lett.* **2010**, *37*. [CrossRef]

8. Atlaskin, E.; Vihma, T. Evaluation of NWP results for wintertime nocturnal boundary-layer temperatures over Europe and Finland. *Q. J. R. Meteorol. Soc.* **2012**, *138*, 1440–1451. [CrossRef]

9. McNider, R.T.; Christy, J.R.; Biazar, A. A Stable Boundary Layer Perspective on Global Temperature Trends. In *IOP Conference Series: Earth and Environmental Science*; IOP Publishing: Bristol, UK, 2010; Volume 13, p. 012003. [CrossRef].

10. Esau, I.; Davy, R.; Outten, S. Complementary Explanation of Temperature Response in the Lower Atmosphere. *Environ. Res. Lett.* **2012**, *7*, 044026. [CrossRef]

11. Pithan, F.; Mauritsen, T. Arctic amplification dominated by temperature feedbacks in contemporary climate models. *Nat. Geosci.* **2014**, *7*, 181–184. [CrossRef]

12. Boé, J.; Hall, A.; Qu, X. Current GCMs' Unrealistic Negative Feedback in the Arctic. *J. Clim.* **2009**, *22*, 4682–4695, doi:10.1175/2009JCLI2885.1. [CrossRef]

13. Esau, I.; Zilitinkevich, S. On the Role of the Planetary Boundary Layer Depth in the Climate System. *Adv. Sci. Res.* **2010**, *4*, 63–69. [CrossRef]

14. Vihma, T.; Pirazzini, R.; Fer, I.; Renfrew, I.A.; Sedlar, J.; Tjernström, M.; Lüpkes, C.; Nygård, T.; Notz, D.; Weiss, J.; et al. Advances in understanding and parameterization of small-scale physical processes in the marine Arctic climate system: A review. *Atmos. Chem. Phys.* **2014**, *14*, 9403–9450. [CrossRef]

15. Zilitinkevich, S.; Calanca, P. An Extended Similarity Theory for the Stably Stratified Atmospheric Surface Layer. *Q. J. R. Meteorol. Soc.* **2000**, *126*, 1913–1923. [CrossRef]

16. Klipp, C.L.; Mahrt, L. Flux-Gradient Relationship, Self-Correlation and Intermittency in the Stable Boundary Layer. *Q. J. R. Meteorol. Soc.* **2004**, *130*, 2087–2103. [CrossRef]

17. Sodemann, H.; Foken, T. Empirical Evaluation of an Extended Similarity Theory for the Stably Stratified Atmospheric Surface Layer. *Q. J. R. Meteorol. Soc.* **2004**, *130*, 2665–2671. [CrossRef]

18. Baas, P.; Steeneveld, G.J.; van de Wiel, B.J.H.; Holtslag, A.A.M. Exploring Self-Correlation in Flux-Gradient Relationships for Stably Stratified Conditions. *J. Atmos. Sci.* **2006**, *63*, 3045–3054. [CrossRef]

19. Foken, T. 50 Years of the Monin-Obukhov Similarity Theory. *Bound.-Layer Meteorol.* **2006**, *119*, 431–447. [CrossRef]

20. Sorbjan, Z.; Grachev, A.A. An Evaluation of the Flux-Gradient Relationship in the Stable Boundary Layer. *Bound.-Layer Meteorol.* **2010**, *135*, 385–405. [CrossRef]

21. Grachev, A.A.; Andreas, E.L.; Fairall, C.W.; Guest, P.S.; Persson, P.O.G. The Critical Richardson Number and Limits of Applicability of Local Similarity Theory in the Stable Boundary Layer. *Bound.-Layer Meteorol.* **2013**, *147*, 51–82. [CrossRef]

22. Mauritsen, T.; Svensson, G. Observations of Stably Stratified Shear-Driven Atmospheric Turbulence at Low and High Richardson Numbers. *J. Atmos. Sci.* **2007**, *64*, 645–655. [CrossRef]

23. Grachev, A.A.; Fairall, C.W.; Persson, P.O.G.; Andreas, E.L.; Guest, P.S. Stable Boundary-Layer Scaling Regimes: The SHEBA Data. *Bound.-Layer Meteorol.* **2005**, *116*, 201–235. [CrossRef]

24. Zilitinkevich, S.; Baklanov, A.; Rost, J.; Smedman, A.S.; Lykosov, V.; Calanca, P. Diagnostic and Prognostic Equations for the Depth of the Stably Stratified Ekman Boundary Layer. *Q. J. R. Meteorol. Soc.* **2002**, *128*, 25–46. [CrossRef]

25. Mahrt, L.; Vickers, D. Contrasting Vertical Structures of Nocturnal Boundary Layers. *Bound.-Layer Meteorol.* **2002**, *105*, 351–363. [CrossRef]

26. Sorbjan, Z.; Czerwinska, A. Statistics of Turbulence in the Stable Boundary Layer Affected by Gravity Waves. *Bound.-Layer Meteorol.* **2013**, *148*, 73–91. [CrossRef]

27. Zilitinkevich, S.S. Third-Order Transport due to Internal Waves and Non-Local Turbulence in the Stably Stratified Surface Layer. *Q. J. R. Meteorol. Soc.* **2002**, *128*, 913–925. [CrossRef]

28. Steeneveld, G.J.; Wokke, M.J.J.; Zwaaftink, C.D.G.; Pijlman, S.; Heusinkveld, B.G.; Jacobs, A.F.G.; Holtslag, A.A.M. Observations of the radiation divergence in the surface layer and its implication for its parameterization in numerical weather prediction models. *J. Geophys. Res.* **2010**, *115*. [CrossRef]

29. Sterk, H.A.M.; Steeneveld, G.J.; Holtslag, A.A.M. The role of snow-surface coupling, radiation, and turbulent mixing in modeling a stable boundary layer over Arctic sea ice. *J. Geophys. Res. Atmos.* **2013**, *118*, 1199–1217. [CrossRef]

30. Nieuwstadt, F.T.M. The Turbulent Structure of the Stable, Nocturnal Boundary Layer. *J. Atmos. Sci.* **1984**, *41*, 2202–2216. [CrossRef]

31. Zilitinkevich, S.S.; Esau, I.N. Similarity Theory and Calculation of Turbulent Fluxes at the Surface for the Stably Stratified Atmospheric Boundary Layer. In *Atmospheric Boundary Layers*; Baklanov, A., Grisogono, B., Eds.; Springer: New York, NY, USA, 2007; pp. 37–49. [CrossRef]

32. Sorbjan, Z. The Height Correction of Similarity Functions in the Stable Boundary Layer. *Bound.-Layer Meteorol.* **2012**, *142*, 21–31. [CrossRef]

33. Sorbjan, Z. Gradient-based Scales and Similarity Laws in the Stable Boundary Layer. *Q. J. R. Meteorol. Soc.* **2010**, *136*, 1243–1254. [CrossRef]

34. Sorbjan, Z. Gradient-Based Similarity in the Stable Atmospheric Boundary Layer. In *Achievements, History and Challenges in Geophysics*; Bialik, R., Majdaski, M., Moskalik, M., Eds.; GeoPlanet: Earth and Planetary Sciences; Springer International Publishing: Berlin, Germany, 2014; pp. 351–375. [CrossRef]

35. Beare, R.J.; Macvean, M.K.; Holtslag, A.A.M.; Cuxart, J.; Esau, I.; Golaz, J.C.; Jimenez, M.A.; Khairoutdinov, M.; Kosovic, B.; Lewellen, D.; et al. An intercomparison of large-eddy simulations of the stable boundary layer. *Bound.-Layer Meteorol.* **2006**, *118*, 247–272. [CrossRef]

36. Sullivan, P.P.; Weil, J.C.; Patton, E.G.; Jonker, H.J.J.; Mironov, D.V. Turbulent Winds and Temperature Fronts in Large-Eddy Simulations of the Stable Atmospheric Boundary Layer. *J. Atmos. Sci.* **2016**, *73*, 1815–1840. [CrossRef]

37. Maronga, B.; Bosveld, F.C. Key parameters for the life cycle of nocturnal radiation fog: A comprehensive large-eddy simulation study. *Q. J. R. Meteorol. Soc.* **2017**, *143*, 2463–2480. [CrossRef]

38. Kawai, S.; Larsson, J. Wall-modeling in large eddy simulation: Length scales, grid resolution, and accuracy. *Phys. Fluids* **2012**, *24*, 015105. [CrossRef]

39. Andreas, E.L.; Claffey, K.J. Air-ice drag coefficients in the western Weddell Sea: 1. Values deduced from profile measurements. *J. Geophys. Res.* **1995**, *100*, 4821–4831. [CrossRef]

40. Andreas, E.L.; Claffy, K.J.; Makshtas, A.P. Low-Level Atmospheric Jets and Inversions over the Western Weddell Sea. *Bound.-Layer Meteorol.* **2000**, *97*, 459–486. [CrossRef]

41. Andreas, E.L.; Jordan, R.E.; Makshtas, A.P. Simulations of Snow, Ice, and Near-Surface Atmospheric Processes on Ice Station Weddell. *J. Hydrometeorol.* **2004**, *5*, 611–624. [CrossRef]

42. Andreas, E.L.; Jordan, R.E.; Makshtas, A.P. Parameterizing turbulent exchange over sea ice: The Ice Station Weddell results. *Bound.-Layer Meteorol.* **2005**, *114*, 439–460. [CrossRef]

43. Andreas, E.L. Near-surface water vapor over polar sea ice is always near ice saturation. *J. Geophys. Res.* **2002**, *107*. [CrossRef]

44. Persson, P.O.G. Measurements near the Atmospheric Surface Flux Group tower at SHEBA: Near-surface conditions and surface energy budget. *J. Geophys. Res.* **2002**, *107*. [CrossRef]

45. Vihma, T.; Jaagus, J.; Jakobson, E.; Palo, T. Meteorological conditions in the Arctic Ocean in spring and summer 2007 as recorded on the drifting ice station Tara. *Geophys. Res. Lett.* **2008**, *35*. [CrossRef]

46. Jakobson, L.; Vihma, T.; Jakobson, E.; Palo, T.; Männik, A.; Jaagus, J. Low-level jet characteristics over the Arctic Ocean in spring and summer. *Atmos. Chem. Phys.* **2013**, *13*, 11089–11099. [CrossRef]

47. Palo, T.; Vihma, T.; Jaagus, J.; Jakobson, E. Observations of temperature inversions over central Arctic sea ice in summer. *Q. J. R. Meteorol. Soc.* **2017**, *143*, 2741–2754. [CrossRef]

48. Cohen, L.; Hudson, S.R.; Walden, V.P.; Graham, R.M.; Granskog, M.A. Meteorological conditions in a thinner Arctic sea ice regime from winter through summer during the Norwegian Young Sea Ice expedition (N-ICE2015). *J. Geophys. Res. Atmos.* **2017**, *122*, 7235–7259. [CrossRef]

49. Argentini, S.; Viola, A.P.; Mastrantonio, G.; Maurizi, A.; Georgiadis, T.; Nardino, M. Characteristics of the boundary layer at Ny-Alesund in the Arctic during the ARTIST field experiment. *Ann. Geophys.* **2003**, *46*, 185–196.

50. Balsley, B.B.; Frehlich, R.G.; Jensen, M.L.; Meillier, Y.; Muschinski, A. Extreme Gradients in the Nocturnal Boundary Layer: Structure, Evolution, and Potential Causes. *J. Atmos. Sci.* **2003**, *60*, 2496–2508. [CrossRef]

51. Bosveld, F.C.; Baas, P.; van Meijgaard, E.; de Bruijn, E.I.F.; Steeneveld, G.J.; Holtslag, A.A.M. The Third GABLS Intercomparison Case for Evaluation Studies of Boundary-Layer Models. Part A: Case Selection and Set-Up. *Bound.-Layer Meteorol.* **2014**, *152*, 133–156. [CrossRef]

52. Kleczek, M.A.; Steeneveld, G.J.; Holtslag, A.A. Evaluation of the Weather Research and Forecasting Mesoscale Model for GABLS3: Impact of Boundary-Layer Schemes, Boundary Conditions and Spin-Up. *Bound.-Layer Meteorol.* **2014**, *152*, 213–243. [CrossRef]

53. Mahrt, L. Bulk formulation of surface fluxes extended to weak-wind stable conditions. *Q. J. R. Meteorol. Soc.* **2008**, *134*, 1–10. [CrossRef]

54. Miller, N.B.; Turner, D.D.; Bennartz, R.; Shupe, M.D.; Kulie, M.S.; Cadeddu, M.P.; Walden, V.P. Surface-based inversions above central Greenland. *J. Geophys. Res. Atmos.* **2013**, *118*, 495–506. [CrossRef]

55. Lehner, M.; Whiteman, C.D.; Hoch, S.W.; Jensen, D.; Pardyjak, E.R.; Leo, L.S.; Di Sabatino, S.; Fernando, H.J. A case study of the nocturnal boundary layer evolution on a slope at the foot of a desert mountain. *J. Appl. Meteorol. Climatol.* **2015**, *54*, 732–751. [CrossRef]

56. Guest, P.S.; Glendening, J.W.; Davidson, K.L. An observational and numerical study of wind stress variations within marginal ice zones. *J. Geophys. Res. Oceans* **1995**, *100*, 10887–10904. [CrossRef]

57. Drüe, C.; Heinemann, G. Airborne investigation of arctic boundary-layer fronts over the marginal ice zone of the Davis Strait. *Bound.-Layer Meteorol.* **2001**, *101*, 261–292. [CrossRef]

58. Vihma, T.; Pirazzini, R. On the Factors Controlling the Snow Surface and 2-m Air Temperatures over the Arctic Sea Ice in Winter. *Bound.-Layer Meteorol.* **2005**, *117*, 73–90. [CrossRef]

59. Lüpkes, C.; Vihma, T.; Birnbaum, G.; Dierer, S.; Garbrecht, T.; Gryanik, V.M.; Gryschka, M.; Hartmann, J.; Heinemann, G.; Kaleschke, L.; et al. Mesoscale Modelling of the Arctic Atmospheric Boundary Layer and Its Interaction with Sea Ice. In *Arctic Climate Change*; Lemke, P., Jacobi, H.W., Eds.; Atmospheric and Oceanographic Sciences Library; Springer: Dordrecht, The Netherlands, 2012; Volume 43, pp. 279–324. [CrossRef]

60. Tetzlaff, A.; Lüpkes, C.; Hartmann, J. Aircraft-based observations of atmospheric boundary-layer modification over Arctic leads. *Q. J. R. Meteorol. Soc.* **2015**, *141*, 2839–2856. [CrossRef]

61. Brümmer, B. Temporal and spatial variability of surface fluxes over the ice edge zone in the northern Baltic Sea. *J. Geophys. Res.* **2002**, *107*. [CrossRef]

62. Vihma, T.; Brümmer, B. Observations and Modelling of the On-Ice And Off-Ice Air Flow over the Northern Baltic Sea. *Bound.-Layer Meteorol.* **2002**, *103*, 1–27. [CrossRef]

63. Lampert, A.; Maturilli, M.; Ritter, C.; Hoffmann, A.; Stock, M.; Herber, A.; Birnbaum, G.; Neuber, R.; Dethloff, K.; Orgis, T.; et al. The Spring-Time Boundary Layer in the Central Arctic Observed during PAMARCMiP 2009. *Atmosphere* **2012**, *3*, 320–351. [CrossRef]

64. Elston, J.; Argrow, B.; Stachura, M.; Weibel, D.; Lawrence, D.; Pope, D. Overview of Small Fixed-Wing Unmanned Aircraft for Meteorological Sampling. *J. Atmos. Ocean. Technol.* **2015**, *32*, 97–115. [CrossRef]

65. Villa, T.; Gonzalez, F.; Miljievic, B.; Ristovski, Z.; Morawska, L. An Overview of Small Unmanned Aerial Vehicles for Air Quality Measurements: Present Applications and Future Prospectives. *Sensors* **2016**, *16*, 1072. [CrossRef] [PubMed]

66. Curry, J.A.; Maslanik, J.; Holland, G.; Pinto, J. Applications of Aerosondes in the Arctic. *Bull. Am. Meteorol. Soc.* **2004**, *85*, 1855–1861. [CrossRef]

67. Mayer, S.; Jonassen, M.O.; Sandvik, A.; Reuder, J. Profiling the Arctic Stable Boundary Layer in Advent Valley, Svalbard: Measurements and Simulations. *Bound.-Layer Meteorol.* **2012**, *143*, 507–526. [CrossRef]

68. Mayer, S.; Hattenberger, G.; Brisset, P.; Jonassen, M.; Reuder, J. A 'no-flow-sensor' Wind Estimation Algorithm for Unmanned Aerial Systems. *Int. J. Micro Air Veh.* **2012**, *4*, 15–30. [CrossRef]

69. Cassano, J.J.; Maslanik, J.A.; Zappa, C.J.; Gordon, A.L.; Cullather, R.I.; Knuth, S.L. Observations of Antarctic polynya with unmanned aircraft systems. *Eos Trans. Am. Geophys. Union* **2010**, *91*, 245–246. [CrossRef]

70. Cassano, J.J.; Seefeldt, M.W.; Palo, S.; Knuth, S.L.; Bradley, A.C.; Herrman, P.D.; Kernebone, P.A.; Logan, N.J. Observations of the atmosphere and surface state over Terra Nova Bay, Antarctica, using unmanned aerial systems. *Earth Syst. Sci. Data* **2016**, *8*, 115–126. [CrossRef]

71. Jonassen, M.; Tisler, P.; Altstädter, B.; Scholtz, A.; Vihma, T.; Lampert, A.; König-Langlo, G.; Lüpkes, C. Application of remotely piloted aircraft systems in observing the atmospheric boundary layer over Antarctic sea ice in winter. *Polar Res.* **2015**, *34*, 25651. [CrossRef]

72. Knuth, S.; Cassano, J.; Maslanik, J.; Herrmann, P.; Kernebone, P.; Crocker, R.; Logan, N. Unmanned aircraft system measurements of the atmospheric boundary layer over Terra Nova Bay, Antarctica. *Earth Syst. Sci. Data* **2013**, *5*, 57. [CrossRef]

73. Knuth, S.L.; Cassano, J.J. Estimating Sensible and Latent Heat Fluxes Using the Integral Method from in situ Aircraft Measurements. *J. Atmos. Ocean. Technol.* **2014**, *31*, 1964–1981. [CrossRef]

74. Vihma, T.; Kilpeläinen, T.; Manninen, M.; Sjöblom, A.; Jakobson, E.; Palo, T.; Jaagus, J.; Maturilli, M. Characteristics of Temperature and Humidity Inversions and Low-Leve Jets over Svalbard Fjords in Spring. *Adv. Meteorol.* **2011**, *2011*, 14. [CrossRef]

75. Achtert, P.; Brooks, I.M.; Brooks, B.J.; Moat, B.I.; Prytherch, J.; Persson, P.O.G.; Tjernström, M. Measurement of wind profiles by motion-stabilised ship-borne Doppler lidar. *Atmos. Meas. Tech.* **2015**, *8*, 4993–5007. [CrossRef]

76. Anderson, P.S. Fine-Scale Structure Observed In A Stable Atmospheric Boundary Layer By Sodar And Kite-Borne Tethersonde. *Bound.-Layer Meteorol.* **2003**, *107*, 323–351. [CrossRef]

77. Kral, S.; Reuder, J.; Hudson, S.R.; Cohen, L. *N-ICE2015 Sodar Wind Data*; Norwegian Polar Institute: Tromsø, Norway, 2017. [CrossRef]

78. Devasthale, A.; Sedlar, J.; Kahn, B.H.; Tjernström, M.; Fetzer, E.J.; Tian, B.; Teixeira, J.; Pagano, T.S. A Decade of Spaceborne Observations of the Arctic Atmosphere: Novel Insights from NASA's AIRS Instrument. *Bull. Am. Meteorol. Soc.* **2016**, *97*, 2163–2176. [CrossRef]

79. Uotila, P.; Vihma, T.; Haapala, J. Atmospheric and oceanic conditions and the extremely low Bothnian Bay sea ice extent in 2014/2015. *Geophys. Res. Lett.* **2015**, *42*, 7740–7749. [CrossRef]

80. Cornwall, C.; Horiuchi, A.; Lehman, C. NOAA ESRL Sunrise/Sunset Calculator. Available online: https://www.esrl.noaa.gov/gmd/grad/solcalc/sunrise.html (accessed on 2 November 2017).

81. Cornwall, C.; Horiuchi, A.; Lehman, C. NOAA ESRL Solar Position Calculator. Available online: https://www.esrl.noaa.gov/gmd/grad/solcalc/azel.html (accessed on 2 November 2017).

82. Karvonen, J. Virtual radar ice buoys—A method for measuring fine-scale sea ice drift. *Cryosphere* **2016**, *10*, 29–42. [CrossRef]

83. Reuder, J.; Brisset, P.; Jonassen, M.O.; Müller, M.; Mayer, S. The Small Unmanned Meteorological Observer SUMO: A New Tool for Atmospheric Boundary Layer Research. *Meteorol. Z.* **2009**, *18*, 141–147. [CrossRef]

84. Reuder, J.; Jonassen, M.O.; Ólafsson, H. The Small Unmanned Meteorological Observer SUMO: Recent Developments and Applications of a Micro-UAS for Atmospheric Boundary Layer Research. *Acta Geophys.* **2012**, *60*, 1454–1473. [CrossRef]

85. Wildmann, N.; Hofsäß, M.; Weimer, F.; Joos, A.; Bange, J. MASC—A small Remotely Piloted Aircraft (RPA) for wind energy research. *Adv. Sci. Res.* **2014**, *11*, 55–61. [CrossRef]

86. Wildmann, N.; Mauz, M.; Bange, J. Two fast temperature sensors for probing of the atmospheric boundary layer using small remotely piloted aircraft (RPA). *Atmos. Meas. Tech.* **2013**, *6*, 2101–2113. [CrossRef]

87. Wildmann, N.; Ravi, S.; Bange, J. Towards higher accuracy and better frequency response with standard multi-hole probes in turbulence measurement with remotely piloted aircraft (RPA). *Atmos. Meas. Tech.* **2014**, *7*, 1027–1041. [CrossRef]

88. Van den Kroonenberg, A.; Martin, T.; Buschmann, M.; Bange, J.; Vörsmann, P. Measuring the wind vector using the autonomous mini aerial vehicle M2AV. *J. Atmos. Ocean. Technol.* **2008**, *25*, 1969–1982. [CrossRef]

89. Wrenger, B.; Cuxart, J. Evening Transition by a River Sampled Using a Remotely-Piloted Multicopter. *Bound.-Layer Meteorol.* **2017**, *165*, 535–543. [CrossRef]

90. Kouznetsov, R.D. The multi-frequency sodar with high temporal resolution. *Meteorol. Z.* **2009**, *18*, 169–173. [CrossRef]

91. Kouznetsov, R.D. The summertime ABL structure over an Antarctic oasis with a vertical Doppler sodar. *Meteorol. Z.* **2009**, *18*, 163–167. [CrossRef]

92. Mauder, M.; Foken, T. *Eddy-Covariance Software TK3*; University of Bayreuth: Bayreuth, Germany, 2015. [CrossRef]

93. Palomaki, R.T.; Rose, N.T.; van den Bossche, M.; Sherman, T.J.; Wekker, S.F.J.D. Wind Estimation in the Lower Atmosphere Using Multirotor Aircraft. *J. Atmos. Ocean. Technol.* **2017**, *34*, 1183–1191. [CrossRef]

94. Päschke, E.; Leinweber, R.; Lehmann, V. An assessment of the performance of a 1.5 μm Doppler lidar for operational vertical wind profiling based on a 1-year trial. *Atmos. Meas. Tech.* **2015**, *8*, 2251–2266. [CrossRef]

95. Vihma, T.; Haapala, J. Geophysics of sea ice in the Baltic Sea: A review. *Prog. Oceanogr.* **2009**, *80*, 129–148. [CrossRef]

96. Granskog, M.A.; Vihma, T.; Pirazzini, R.; Cheng, B. Superimposed ice formation and surface energy fluxes on sea ice during the spring melt–freeze period in the Baltic Sea. *J. Glaciol.* **2006**, *52*, 119–127. [CrossRef]

97. Zeng, J.; Matsunaga, T.; Mukai, H. METEX—A flexible tool for air trajectory calculation. *Environ. Model. Softw.* **2010**, *25*, 607–608. [CrossRef]

98. Mahrt, L. The Near-Calm Stable Boundary Layer. *Bound.-Layer Meteorol.* **2011**, *140*, 343–360. [CrossRef]

99. Maronga, B.; Gryschka, M.; Heinze, R.; Hoffmann, F.; Kanani-Sühring, F.; Keck, M.; Ketelsen, K.; Letzel, M.O.; Sühring, M.; Raasch, S. The Parallelized Large-Eddy Simulation Model (PALM) version 4.0 for atmospheric and oceanic flows: Model formulation, recent developments, and future perspectives. *Geosci. Model Dev.* **2015**, *8*, 2515–2551. [CrossRef]

100. Maronga, B.; Reuder, J. On the Formulation and Universality of Monin–Obukhov Similarity Functions for Mean Gradients and Standard Deviations in the Unstable Surface Layer: Results from Surface-Layer-Resolving Large-Eddy Simulations. *J. Atmos. Sci.* **2017**, *74*, 989–1010. [CrossRef]

Paper II

Intercomparison of Small Unmanned Aircraft System (sUAS) Measurements for Atmospheric Science during the LAPSE-RATE Campaign

Barbieri, L., S. T. Kral, S. C. C. Bailey, A. E. Frazier, J. D. Jacob, J. Reuder, D. Brus, P. B. Chilson, C. Crick, C. Detweiler, A. Doddi, J. Elston, H. Foroutan, J. González-Rocha, B. R. Greene, M. I. Guzman, A. L. Houston, A. Islam, O. Kemppinen, D. Lawrence, E. A. Pillar-Little, S. D. Ross, M. P. Sama, D. G. Schmale, T. J. Schuyler, A. Shankar, S. W. Smith, S. Waugh, C. Dixon, S. Borenstein and G. de Boer. *Sensors*, **19**, 2179 (2019), doi:10.3390/s19092179.

II

MDPI

Article

Intercomparison of Small Unmanned Aircraft System (sUAS) Measurements for Atmospheric Science during the LAPSE-RATE Campaign

Lindsay Barbieri [1,*,†] , Stephan T. Kral [2,†] , Sean C. C. Bailey [3] , Amy E. Frazier [4] ,
Jamey D. Jacob [5] , Joachim Reuder [2] , David Brus [6] , Phillip B. Chilson [7] ,
Christopher Crick [8] , Carrick Detweiler [9] , Abhiram Doddi [10] , Jack Elston [11] ,
Hosein Foroutan [12] , Javier González-Rocha [13] , Brian R. Greene [7] , Marcelo I. Guzman [14] ,
Adam L. Houston [15] Ashraful Islam [16] , Osku Kemppinen [17] , Dale Lawrence [10] ,
Elizabeth A. Pillar-Little [7] , Shane D. Ross [18] , Michael Sama [19] , David G. Schmale III [20] ,
Travis J. Schuyler [14] , Ajay Shankar [9] , Suzanne W. Smith [3] , Sean Waugh [21] , Cory Dixon [22] ,
Steve Borenstein [22] and Gijs de Boer [23,24]

1   Rubenstein School of Environment and Natural Resources and Gund Insitute for Environment,
    University of Vermont, Burlington, VT 05401, USA
2   Geophysical Institute and Bjerknes Centre for Climate Research, University of Bergen, Postbox 7803,
    5020 Bergen, Norway; stephan.kral@uib.no (S.T.K.); joachim.reuder@uib.no (J.R.)
3   Department of Mechanical Engineering, University of Kentucky, Lexington, KY 40506, USA;
    sean.bailey@uky.edu (S.C.C.B.); suzanne.smith@uky.edu (S.W.S.)
4   School of Geographical Sciences and Urban Planning, Arizona State University, Tempe, AZ 85281, USA;
    Amy.Frazier@asu.edu
5   Unmanned Systems Research Institute and School of Aerospace Engineering, Oklahoma State University,
    Stillwater, OK 74078, USA; jdjacob@okstate.edu
6   Finnish Meteorological Institute, Erik Palménin aukio 1, P.O. Box 503, FIN-00100 Helsinki, Finland;
    david.brus@fmi.fi
7   School of Meteorology, Advanced Radar Research Center, and Center for Autonomous Sensing and
    Sampling, University of Oklahoma, Norman, OK 73071, USA; chilson@ou.edu (P.B.C.);
    brian.greene@ou.edu (B.R.G.); epillarlittle@ou.edu (E.A.P.-L.)
8   Department of Computer Science, Oklahoma State University, Stillwater, OK 74078, USA;
    chriscrick@cs.okstate.edu
9   Department of Computer Science and Engineering, University of Nebraska–Lincoln,
    Lincoln, NE 68588, USA; carrick@cse.unl.edu (C.D.); ashankar@cse.unl.edu (A.S.)
10 Department of Aerospace Engineering, University of Colorado, Boulder, CO 80309, USA;
    Abhiram.Doddi@colorado.edu (A.D.); dale.lawrence@colorado.edu (D.L.)
11 Black Swift Technologies, Boulder, CO 80301, USA; elstonj@blackswifttech.com
12 Department of Civil and Environmental Engineering, Virginia Tech,
    Blacksburg, VA 24061, USA; hosein@vt.edu
13 Department of Aerospace and Ocean Engineering, Virginia Tech,
    Blacksburg, VA 24061, USA; javig86@vt.edu
14 Department of Chemistry, University of Kentucky, Lexington, KY 40506, USA;
    marcelo.guzman@uky.edu (M.I.G.), travis.schuyler@uky.edu (T.J.S.)
15 Department of Earth and Atmospheric Sciences, University of Nebraska–Lincoln, Bessey Hall 126,
    Lincoln, NE 68588, USA; ahouston2@unl.edu
16 Department of Mechanical and Materials Engineering, University of Nebraska–Lincoln,
    Lincoln, NE 68588, USA; mislam@huskers.unl.edu
17 Department of Physics, Kansas State University, 1228 N. 17th St., Manhattan, KS 66506, USA;
    okemppin@phys.ksu.edu
18 Department of Biomedical Engineering and Mechanics, Virginia Tech, Blacksburg, VA 24061, USA;
    sdross@vt.edu
19 Department of Biosystems and Agricultural Engineering, College of Agriculture, Food and Environment,
    University of Kentucky, Lexington, KY 40546, USA; michael.sama@uky.edu
20 School of Plant and Environmental Sciences, Virginia Tech, Blacksburg, VA 24061, USA; dschmale@vt.edu

21 NOAA National Severe Storms Laboratory, 120 David L. Boren Blvd., Norman, OK 73072, USA;
    sean.waugh@noaa.gov
22 Integrated Remote and In Situ Sensing Program, University of Colorado, Boulder, CO 80309, USA;
    cory.dixon@colorado.edu (C.D.); steve.borenstein@colorado.edu (S.B.)
23 Cooperative Institute for Research in Environmental Sciences, University of Colorado,
    Boulder, CO 80309, USA; gijs.deboer@colorado.edu
24 NOAA Physical Sciences Division, Boulder, CO 80305, USA
*   Correspondence: lindsay.barbieri@uvm.edu; Tel.: +1-508-308-8706
†   These authors contributed equally to this work.

Abstract: Small unmanned aircraft systems (sUAS) are rapidly transforming atmospheric research. With the advancement of the development and application of these systems, improving knowledge of best practices for accurate measurement is critical for achieving scientific goals. We present results from an intercomparison of atmospheric measurement data from the Lower Atmospheric Process Studies at Elevation—a Remotely piloted Aircraft Team Experiment (LAPSE-RATE) field campaign. We evaluate a total of 38 individual sUAS with 23 unique sensor and platform configurations using a meteorological tower for reference measurements. We assess precision, bias, and time response of sUAS measurements of temperature, humidity, pressure, wind speed, and wind direction. Most sUAS measurements show broad agreement with the reference, particularly temperature and wind speed, with mean value differences of 1.6 $\pm$2.6 °C and 0.22 $\pm$ 0.59 m/s for all sUAS, respectively. sUAS platform and sensor configurations were found to contribute significantly to measurement accuracy. Sensor configurations, which included proper aspiration and radiation shielding of sensors, were found to provide the most accurate thermodynamic measurements (temperature and relative humidity), whereas sonic anemometers on multirotor platforms provided the most accurate wind measurements (horizontal speed and direction). We contribute both a characterization and assessment of sUAS for measuring atmospheric parameters, and identify important challenges and opportunities for improving scientific measurements with sUAS.

Keywords: sUAS; unmanned aircraft systems; unmanned aerial vehicles; UAV; sensor intercomparison; atmospheric measurements

---

1. Introduction

Small unmanned aircraft systems (sUAS) are transforming the paradigm of atmospheric research. Their importance for meteorological studies has been highlighted in several recent reports [1,2], and their ability to contribute high quality measurements across spatial and temporal domains is unequivocal [3]. Initial efforts to measure the atmosphere with remotely piloted aircraft began a half century ago [4,5], and activities have continued through the 20th century [6]. However, the last decade has seen a rapid increase in the rate of sUAS development and application for lower atmospheric studies due to reductions in cost of systems and sensors associated with the advancement of consumer electronics. A main benefit of sUAS is their ability to operate in airspaces or situations that are too difficult or hazardous for manned aircraft [7] such as in and around thunderstorms [8], active volcanoes [9], or chemical plumes. Since they are more maneuverable than other types of platforms, they are able to sample portions of the atmosphere that have previously been either limited in observation or inaccessible through traditional monitoring methods such as meteorological towers, weather balloons, or satellites. They also permit the capture of atmospheric variables and data at finer spatial and temporal scales compared to other measurement technologies, and often at lower cost, allowing enhanced investigations of boundary layer processes. In sum, sUAS are providing critical information on the vertical and horizontal structure and variability of the atmosphere, which in turn is

spurring new areas of engineering and science related to the development, deployment, and application of these systems for atmospheric studies.

sUAS have been employed to address a range of theoretical, methodological, and applied atmospheric science research questions. In particular, they have proven instrumental for advancing boundary layer research [10–19], gas and aerosol investigations [20–23], cloud microphysics [24,25], understanding of severe storm development [8,26,27], turbulence research [28,29], and the impact of wind turbines on atmospheric structure [30,31]. From a methodological perspective, sUAS are fostering development of new methods for measurement, such as acoustic atmospheric tomography [32], and capturing the spatial structure of thermodynamic variables [33]. In response to the growing application of sUAS technology, the European Union sponsored a COST (Cooperation in Science and Technology) Action [34] to support the development of a community around sUAS use for atmospheric science in 2008. Stemming from this action, the International Society for Atmospheric Research using Remotely piloted Aircraft (ISARRA) was established. The first meeting of ISARRA was held in Palma de Mallorca, Spain in 2013, and since then meetings have been held annually in Europe and the United States.

A key factor in the development of ISARRA was the integration of synergistic community knowledge related to atmospheric sensors, best practices for integration of sensors onboard unmanned aircraft platforms, and general measurement techniques and principles when using sUAS for atmospheric sampling, as discussed above. Critical to achieving scientific goals with sUAS is ensuring accurate measurements through proper characterization of system and sensor performance. A variety of commercial off-the-shelf (COTS) and custom-built sensor payloads for sUAS have been developed specifically to measure atmospheric variables such as thermodynamics, wind velocity/direction, turbulence, gas concentrations, and aerosol properties. An overview of some of these sensors was provided in Ref. [7] and a recent community white paper [35]. In addition, scientific capability can be impacted by the sUAS itself, with both fixed-wing and multirotor sUAS platforms used. In general, fixed-wing platforms currently have an advantage over multirotor platforms in terms of endurance and payload potential, whereas multirotor platforms typically require less operator infrastructure and expertise as well as have hovering and ascent flight capabilities that cannot be matched by fixed-wing platforms. Thus, obtaining accurate measurements depends not only on the integrity of the sensor technology but also on intrinsic factors such as the manner in which the sensor is integrated into the platform, as well as extrinsic factors such as flight patterns and weather conditions. Beyond the sensors themselves, platforms can add additional uncertainties to the measurements. For example, multirotor sUAS can introduce localized mixing of the atmosphere from the propellers, which alters the environment being sampled. Additionally, the reduced forward motion of multirotor platforms compared to fixed-wing aircraft can also impact measurements by reducing airflow over sensors and contributing to directional solar effects. Studies have begun investigating the impacts of these and other factors on the quality of thermodynamic measurements [36,37], but a greater understanding of how platform and sensor characteristics affect measurement quality is needed.

Given the rapid expansion in the use of sUAS for atmospheric research, there is a pressing need to continually assess and improve the quality of the instrumentation and measurement devices to advance collective understanding of the robustness of data being captured from sUAS. As part of the most recent ISARRA meeting, hosted by the University of Colorado-Boulder (CU-Boulder) during summer 2018, a community field campaign was organized in which a primary scientific goal was the characterization of system and sensor performance for improving the quality of atmospheric measurements. The field campaign, titled 'Lower Atmospheric Process Studies at Elevation—a Remotely piloted Aircraft Team Experiment (LAPSE-RATE)', took place in the San Luis Valley of Colorado (Figure 1) from 14–19 July, 2018, and included participation by a variety of university, government, and industry teams. Over the course of six days, more than 100 participants from 13 institutions and organizations supported the coordinated deployment of over 35 unmanned aircraft and completed 1287 flights, accumulating more than 260 flight hours. Flight operations spanned a large area of the San Luis Valley (approximately

3500 km^2), and distributed research flights were organized to observe several interesting atmospheric phenomena, including the morning boundary layer transition in a high-altitude mountain valley, the diurnal cycle of valley flows, convective initiation, and aerosol properties.

In addition to these scientific objectives, coordinated missions were organized between the participating teams to compare measurements across sensors and platforms and validate these measurements against reference measurements from ground-based instrumentation, in particular from a 18 m meteorological tower. The purpose of these intercomparisons was to not only compare the performance of different sensors to the ground-based references but also to compare sensor performance across platforms. The objectives of this study were to evaluate the measurements collected during intercomparison flights to provide a deeper understanding of the accuracy related to capturing atmospheric measurements via sUAS and to identify factors that may contribute uncertainties or error to meteorological measurements. In the next section, 2, we provide an overview of the site information, a detailed description of the sUAS and ground-based systems used for intercomparison as well as information on the flight patterns and analysis techniques. Section 3 presents the results of these comparisons including evaluation of intercomparisons between sUAS-based measurements and ground-based measurements as well as statistical comparisons between measurements captured by different aircraft systems. In addition, this section discusses these intercomparison results in detail and reflects on the potential causes of the observed differences, best practices based on the results of this intercomparison study, and additional perspectives on the future direction of sUAS-based atmospheric measurement.

2. Materials and Methods

2.1. Study Site Information

2.1.1. Operations Area and Ground Instrumentation

The comprehensive LAPSE-RATE campaign took place across the northern half of the San Luis Valley, but all intercomparison flights analyzed in this study were conducted at the Leach Airfield (37°47′06″ N 106°02′49″ W) located in Center, Colorado (Figure 1). The local time during this study at this site was MDT, and all times reported in this study are in UTC, which is +8 h from MDT. The airfield is a county-owned, public-use airport located approximately 3.2 km ENE of the commercial district of Center, Colorado and 32 km NNW of Alamosa, Colorado. The site is situated approximately 2330 m above sea level (MSL) and, true to its name, sits in the center of the expansive elevated San Luis valley. The airfield is surrounded by irrigated agricultural land with very little topography in the immediate vicinity, although substantial mountain ranges (some peaks over 4300 m) are located approximately 32 km to the east and west, 40 km to the north, and 112 km to the south. The open space around Leach Airfield supported simultaneous deployment of several sUAS at a time.

The Mobile UAS Research Collaboratory (MURC) was the primary ground-based system providing instrumentation for reference comparisons. The MURC is an instrumented van that was added to CU-Boulder's Integrated Remote and In-Situ Sensing (IRISS) program vehicle fleet in early 2018 (Figure 1d). The MURC was designed to operate independently during sUAS operations and serve as a mobile command station on larger deployments, overseeing field teams and providing situational awareness. The MURC is equipped with a 15 m extendable mast, at the top of which several meteorological sensors are mounted (Figure 1d). These include a Gill MetPak Pro Base Station that provides barometric pressure (±0.5 hPa), temperature (±0.1 °C), and humidity (±0.8% of RH); a Gill 3D sonic anemometer (<1.5% RMS accuracy at 12 m/s, ±2° accuracy at 12 m/s) for 3D wind measurements; and an R.M. Young Wind Monitor anemometer (±0.3 m/s, ±3°), which provides a redundant horizontal wind measurement. All meteorological sensors were purchased and installed a few months prior to the LAPSE-RATE campaign, and instrument accuracy is provided from the manufacturers specifications. All together termed the MURC Tower, the vehicle and mast with this instrumentation was 18 m tall. The MURC also contained a large communications suite that

increases the range of the UHF/VHF vehicle to vehicle radios, increases bandwidth on the cellular data connection, and improves the ground station to sUAS communication link. For field computing and campaign support, the MURC was equipped with two workstations serving as sUAS ground stations. Additionally, there were two servers for more intensive computing tasks, with one dedicated to graphics intensive processes (such as photogrammetry) and the other dedicated to general computing and data processing.
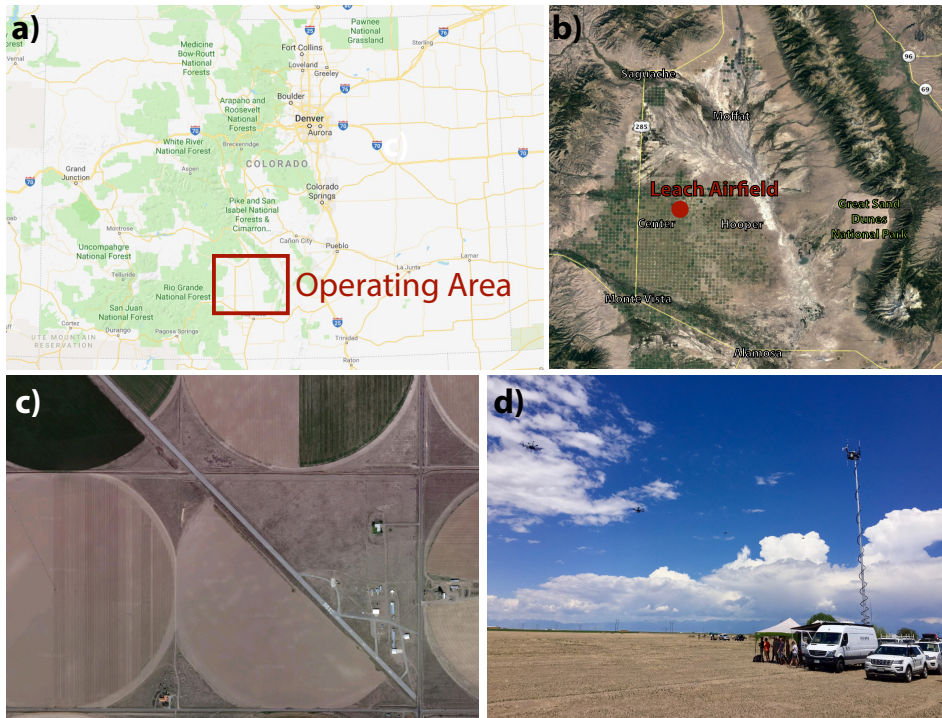
Figure 1. Maps illustrating the location of flight operations during Lower Atmospheric Process Studies at Elevation—a Remotely piloted Aircraft Team Experiment (LAPSE-RATE). (**a**) Operating area. (**b**) Leach Airfield. (**c**) The largest map (right) shows a satellite image of the area around Leach Airfield [Images courtesy of Google Maps]. (**d**) Mobile UAS Research Collaboratory (MURC) facility.

The Integrated Mesonet and Tracker (CoMet-2) was an additional mobile ground-based system that was operational during the intercomparison flights at Leach Airfield. This unit provided near-ground observations with slow temperature and humidity at ~2 m altitude measured using a Vaisala HMP155A, pressure at 2.5 m altitude using a Vaisala PTB210, and wind at 3.25 m altitude using an R.M. Young 05103 propellor anemometer. While this ground-based system did provide important contextual atmospheric measurements, especially for the multirotor platforms, these data were not used in our primary analysis. Several additional ground-based observational assets were also deployed throughout the week, including two ground-based Doppler LiDAR (Windcube) systems operated by CU-Boulder, the Collaborative Lower Atmospheric Mobile Profiling System (CLAMPS) operated by the University of Oklahoma and the National Oceanic and Atmospheric Administration (NOAA) National Severe Storms Laboratory (NSSL), ground vehicles outfitted with meteorological sensors operated by the University of Nebraska–Lincoln and NSSL (following Ref. [38]), and regular radiosonde launches. While these data again served to better contextualize the meteorological conditions, they were not used directly in the intercomparison analyses.

The majority of the intercomparison flights were conducted on 14 July 2018, with additional intercomparison flights taking place on 15 and 17 July 2018. While it was not possible to fly all platforms simultaneously given space constraints and Federal Aviation Administration (FAA) sUAS operating procedures, all platforms were flown in similar flight patterns and at approximately the same altitude and distance from the ground instrumentation to standardize comparisons. All intercomparison flights were conducted under FAA Part 107 [39].

2.1.2. Weather Conditions

Forecasting and modeling support for the entire LAPSE-RATE campaign was provided by the National Weather Service forecast office in Pueblo, CO, and the National Center for Atmospheric Research. Summer conditions in the San Luis Valley are generally dry but with frequent afternoon convection over the surrounding mountains. Some mountain storms advect over the valley itself, depending on wind and moisture conditions. Radiosonde data from the week are presented in Figure 2b, along with MURC observations of pressure (Psfc), temperature (T), relative humidity (RH), and wind speed (Wspd) and direction (Wdir) for the same time period. On 14 and 15 July, the area was impacted by a cold front to the north and monsoonal moisture advected in from the Pacific. This combination resulted in the development of widespread afternoon thunderstorms over the mountains surrounding the valley, with some storms producing heavy precipitation and gusty winds. For 17 July, a region of high pressure established over Colorado, with some storms developing over surrounding mountains. Radiosondes launched at Leach Airfield (Figure 2b) throughout the entire week of the campaign show a consistent lower atmosphere featuring a strong (15–20 °C) diurnal cycle in temperature, with early morning temperatures around 10–12 °C and afternoon temperatures reaching over 30 °C. In general, winds during the intercomparison flights were light and variable, with some elevated wind speeds associated with afternoon convective events.

As stated previously, most intercomparison flights took place on 14 July 2018, with some additional flights on 15 and 17 July. A radiosonde launched on 14 July (17:43 UTC launch time, (Figure 2a) reveals a well-mixed, dry-adiabatic boundary layer extending up to around 550 m above ground level (AGL) (Figure 2a—insert), where a small temperature inversion is present. The atmosphere above this inversion layer is well-mixed up to around 4000 m AGL. The radiosonde and comparison data from surface instrumentation show the presence of a super-adiabatic surface layer extending to nearly 40 m AGL. As a result, there were generally warm and clear conditions throughout the morning and early afternoon hours. Thunderstorms formed over adjacent mountains during the afternoon, with the largest storms developing over the Sangre de Cristo range to the east of Leach Airfield (Figure 1). Some of these storms advected over the valley throughout the course of the late afternoon, resulting in gusty winds and precipitation, particularly over the eastern half of the valley. All intercomparison flights were carried out during conditions with a well-mixed lower atmosphere over the extent of the altitudes sampled.

2.2. sUAS Platforms, Payloads and Flight Patterns

The teams participating in the LAPSE-RATE campaign aimed to explore a wide variety of scientific objectives throughout the week, and thus there was a variety of platforms and sensors included in the intercomparison. A total of 37 individual platforms were flown including 14 different airframes and 23 unique configurations of airframes and sensor payloads. The majority of the platforms (27) were multirotor airframes, and the remaining were fixed-wing. Seventeen different types of sensors were used to measure pressure (*P*), temperature (*T*), and relative humidity (*RH*), and another eight different types of sensors were used to measure (horizontal) wind speed (*U*) and wind direction (*dir*). An overview of the different systems and operators is provided in Table 1, with more detail provided below.
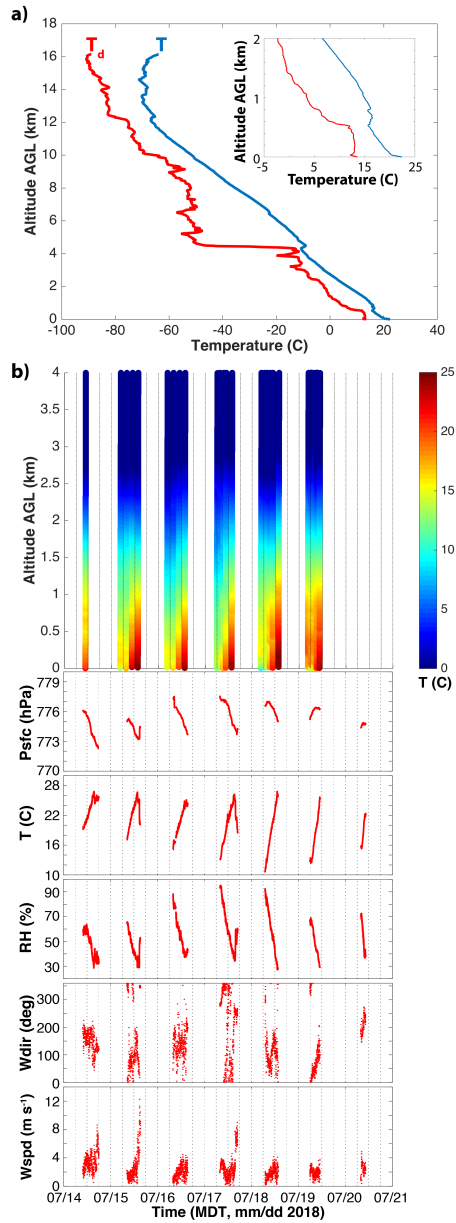
Figure 2. Radiosonde data. (**a**) Radiosonde data, including temperature (*T*, blue line) and dew point temperature (*T_d*, red line), from 14 July (17:43 UTC launch time) and (**a**)—insert focuses on the radiosonde data from surface to 2 km above ground level (AGL). (**b**) Data from radiosonde launches (top) and MURC (bottom) for each day during the week-long campaign.

Table 1. Aircraft participating in intercomparison experiment. Operators were: CU, University of Colorado-Boulder; CU-BST, University of Colorado-Boulder and Black Swift Technologies; EGM, EngeniusMicro LLC; FMI, Finnish Meteorological Institute; KSU, Kansas State University; OSU-A, Oklahoma State University Team A; OSU-B, Oklahoma State University Team B; OSU-C, Oklahoma State University Team C; OU, University of Oklahoma; UNL, University of Nebraska–Lincoln; UKY, University of Kentucky; VT, Virginia Tech; UVA, University of Virginia. Nomenclature in table includes: R, multirotor; FW, fixed-wing; P, pressure; T, temperature; RH humidity; U, wind velocity; MHP, multi-hole probe. Configuration types refer to the configuration of the temperature and humidity sensors and are: 1—sensor packages where aspiration and solar shielding are not relevant; 2—no special sensor placement, aspiration, radiation protection; 3—sensors have aspiration and solar shielding; 4—sensors have solar shielding but no forced aspiration; 5—sensors have aspiration but no solar shielding; *—indicates data not available at time of manuscript preparation; # - indicates where numbers used in figure legends to denote different aircraft or sensors as appropriate.

Operator	Airframe	Type	QTY	Measures	Sensor				Config.	Legend
					P	RH	T	U		
CU	Data Hawk2	FW	3	PTHU	TE MS-5611	Sensiron SHT-31	Sensiron SHT-31		3	CU_DH_SHT31 CU_DH_MS5611
							Cold-wire	Aircraft Dynamics	3 *	CU_DH_IMU
CU	Mistral	FW	1	PTHU			BST MHP		5 *	
	TTwistor	FW	1	PTHU	Vaisala PTU module			Aeroprobe MHP	3 * *	
	Talon-3	FW	1	PTH	TE MS8607	Vaisala PTU module			3 * *	
CU-BST	S1	FW	1	PTHU			BST MHP		5	CU_S1_MHP
	S2	FW	1	PTHU			BST MHP		5 *	
EGM	Intense Eye V2	R	1	PTHU			DTS Flex (×2) TriSonica Mini WS		4 1	EGM_IE2_DTS_# EGM_IE2_tris
FMI	Tarot Hex	R	2	PTH		Bosch BME 280 Vaisala AQT400			4 4	FMI_P# BME280 FMI_P2_AQT400
KSU	M600	R	1	PTH		OSU MDASS			3	KSU_M600_ds_09
OSU-A, OSU-C	SOLO	R	6	PTH		OSU MDASS			3	OSU#_SOLO_ds_##
OSU-A	M600	R	1	PTHU		iMetXQ2 OSU MDASS		FT205	2 3 * 1 *	OSUa_M600P1_xq2
	M600	R	1	PTHU		OSU MDASS		Young 81000	3 * 1	OSUa_M600P2_Y81

Table 1. *Cont.*

Operator	Airframe	Type	QTY	Measures	Sensor				Config.	Legend
					P	*RH*	*T*	*U*		
OSU-B	SOLO	R	3	*PTH*	TE MS5611	iMet XQ2			4	OSU_SOLO_xq2_#
OU	Coptersonde 2	R	3	*PTHU*		IS HYT271	iMet Therm. (×3)	Aircraft Dynamics		OU_CS2#_MS5611
									4	OU_CS2#_HYT271_#
									3	OU_CS2#_PT100_#
										OU_CS2#_IMU
UKY	M600	R	1	*PTH*		iMetXQ2 (×2)			3	UKY_M600P_xq2_#
	SOLO	R	1	*PTHU*		iMetXQ2		TriSonica Mini	3	UKY_SOLO_xq2
									1	UKY_SOLO_tris
	SOLO	R	1	*PTH*	Bosch BME 280				4	UKY_SOLO_BME280
	S1000	R	1	*PTH*		iMetXQ			3	UKY_S1000_xq1
	BLUECAT5	FW	3	*PTHU*		iMetXQ		Custom MHP	3	UKY_BC5#_xq1
										UKY_BC5#_MHP
UNL	M600	R	1	*PTH*		iMetXQ			3	UNL_M600P1_xq1
						iMetXQ2			3	UNL_M600P1_xq2
	M600	R	1	*PTH*		iMetXQ2			3	UNL_M600P2_xq2
						Nimbus PTH			3	UNL_M600P2_nim_1
						Nimbus PTH			4	UNL_M600P2_nim_2
VT, VT-UVA	SOLO	R	1	*PTHU*		iMet XQ		Aircraft Dynamics	5	VT_UVA_SOLO_xq2
	Inspire 2	R	2	*TU*			Meter Atmos 22		1	VT_I2#_MA22

2.2.1. Multirotor Aircraft

The multirotor aircraft primarily consisted of COTS quadcopters (3DR SOLO, DJI Inspire 2, LynxMotion HQuad500), hexacopters (Tarot X6, DJI Matrice M600P), and octocopters (DJI S1000), with the EngeniusMicro, LLC team operating an Intense Eye V2 quadcopter manufactured by Emergent RC. The flight controllers were mainly 3DR Pixhawk, DJI proprietary, or A3 controllers. Flight times for these aircraft ranged from 12 min to 40 min, depending on their payload and rotor blade configuration.

While many of these aircraft carried sensors specific to the scientific objectives of the operating team (e.g., gas concentration, aerosols, etc.), in this study we considered only pressure, temperature, humidity, and 2D wind vector measurements. The most commonly used COTS *P*,*T*, and *RH* sensor was the iMetXQ/iMetXQ-2 (International Met Systems, Grand Rapids, MI, USA). These sensors log data at 1 Hz, with a stated response and accuracy of 10 ms, ±1.5 hPa for pressure; 2 s, ±0.3 °C for temperature; and 5 s, ±0.5% of *RH* for relative humidity for the iMetXQ and improved temperature and humidity response of 1 s and 0.6 s respectively for the iMetXQ-2. Several teams also used the Bosch BME280 sensor, which has a manufacturer-stated response and accuracy of 6 ms, ±1 hPa for pressure, 1 s, ±0.5 °C for temperature, and 1 s, ±3% of RH for relative humidity. Additional *P*, *T*, and *H* sensing on the Finnish Meteorological Institute (FMI) aircraft was also provided by a Vaisala AQT400 gas sensor, which has a manufacturer-stated accuracy of ±10 hPa for pressure, ±0.3 °C for temperature, and ±5% to 8% of *RH* for relative humidity and manufacturer-stated response time <60 s. It is important to note that there are nuances and limitations to manufacturer-stated sensor specifications, for example, humidity response time is dependent on temperature (e.g., for the iMetXQ-2 humidity response is 0.6 s at 25 °C, but 5.2 s at 5 °C), and this information is not always provided in the manufacturer specifications for all sensors.

Many of the teams participating in the LAPSE-RATE field campaign also developed their own integrated systems for meteorological measurements. For example, the University of Oklahoma (OU) operated the LynxMotion HQuad500 (CopterSonde 2), which was equipped with three Innovative Sensor Technology HYT 271 humidity sensors, three InterMet Bead Thermistors, and an TE Connectivity MS-5611 Barometer to measure pressure (8 ms, ±1.5 hPa for pressure, 1 s, ±0.3 °C for temperature, 4 s and ±1.8% of *RH* for humidity). This platform also utilized aircraft dynamics to extract wind speed and direction. The University of Nebraska–Lincoln (UNL) fielded a custom-built two-node pressure, temperature and humidity sensor, here referred to as the Nimbus PTH sensor. Similarly, Oklahoma State University developed the MDASS, Meteorological Data Acquisition Sonde System, to measure *P*, *T*, and *RH*, in addition to other user defined parameters such as GPS, radiation, wind speed, or turbulence [40]. This modular sensor was flown on several of their platforms as well as onboard the DJI M600Pro operated by Kansas State University. The OSU MDASS system has a reported accuracy of ±0.3 °C, ±2% of *RH* and ±0.12 hPa, an onboard fan for sensor aspiration, and shielding. The Intense Eye V2 operated by EngeniusMicro, LLC was equipped with a Differential Temperature Sensor System V2 Low Mass Flex to measure temperature at a resolution of 0.00625 °C and also included a TriSonica Mini Weather Station to measure pressure, temperature, and humidity (±3 hPa, ±0.5 °C, ±3% of *RH*), and also wind speed and direction.

Several multirotors utilized sonic anemometers for measuring wind speed and direction [41]. Sonic anemometers used included the Trisonica Mini (±0.5 m/s magnitude, ±1° direction, ±2 °C temperature), FT Technologies FT205 (±0.3 m/s magnitude, ±4° direction, ±2 °C temperature), Meter Atmos 22 (±0.5 m/s magnitude, ±1° direction) [41], and R.M. Young 81000 (±0.05 m/s magnitude, ±2° direction, ±2 °C, temperature. All sonic anemometers used in this study were located on masts above the plane of the rotors to avoid rotor wash effects. In addition, these sensors also provide a temperature measurement capability, which is included in this study. However, it should be noted that this sonic temperature is an inferred value that is also influenced by humidity, and is not a direct temperature measurement, but very close to virtual temperature.

Wind velocity estimates from the motion of an sUAS platform in flight can also be obtained either by using a kinematic or dynamic model [42–46]. Kinematic models are used to measure wind

velocity solely from a sUAS platform orientation obtained from IMU measurements, whereas dynamic models consider the flight dynamics of the sUAS platform (i.e., how forces and moments relate to vehicle accelerations) in addition IMU measurements to estimate the wind. There are advantages and disadvantages to each with primary limitations arising from IMU accuracy and vehicle inertial response times [47].

2.2.2. Fixed-Wing Aircraft

The fixed-wing aircraft included a combination of modified, COTS, and custom airframes. CU-Boulder (CU) operated four types of fixed-wing aircraft: TTwistor-3, Talon-3, Mistral, and Datahawk2. The TTwistor is an update to the field proven Tempest sUAS but with increased performance [48,49]. The TTwistor-3 and Mistral airframes are made from composites, while the DataHawk2 and Talon-3 are foam construction. TTwistor-3 has an endurance of up to 3 h at 17 m/s, the Mistral's endurance is about 2 h, the DataHawk2's is about 60 min, and the Talon's is about 30–45 min. The TTwistor-3, Mistral, and Talon-3 aircraft make use of the Pixhawk autopilot, while the Datahawk2 employs custom-developed avionics software. TTwistor-3 is equipped with a PTU module that is based upon the sensors employed by the National Center for Atmospheric Research (NCAR) mini Dropsonde. This system uses a Vaisala RSS904 sensor module, which is near identical to the same sensors used in the standard RS-92 radiosonde [50] except for the temperature sensor, which is a larger and more mechanically robust sensor. Additionally, TTwistor-3 carries an Aeroprobe 5-hole multi-hole probe [51,52] for 3D relative wind measurements; and a Vectornav VN200 [53,54] for position and orientation. The Mistral is equipped with a BlackSwift Technologies multi-hole probe (MHP), which provides 3D relative wind along with *P*, *T*, and *RH*. Talon-3 is also equipped with the Vaisala PTU module under one wing and a Microsonde board under the other. The Microsonde board has a TE connectivity MS-8607 *P*, *T*, and *RH* sensor, [55], along with a uBlox Global Navigation Satellite System (GNSS) module [56].

The Datahawk2 sUAS, [57] is a small pusher-prop foam aircraft. This platform has been used for a variety of purposes, including the study of turbulence [58,59] and high latitude [10,23] deployments. The DataHawk2 carries a variety of sensors to make measurements of the atmospheric and surface states. Custom instrumentation includes a fine wire sensor employing two cold-wires and one hot-wire. These provide high frequency (800 Hz) information on temperature and wind speed. High bandwidth is enabled by small surface-area-to-volume ratios of very thin (5 μm diameter) wires. In addition, the DataHawk2 carries a custom integrated circuit that includes commercial Sensiron SHT-31 sensor for temperature and humidity ($\pm$1.5% of RH, $\pm$0.1 °C, 8 s response time) and a TE Connectivity MS-5611 for barometric pressure ($\pm$1.5 hPa, 8 ms response time). For information on surface and sky temperatures, DataHawk2s are also equipped with upward- and downward-looking thermopile sensors. Wind speed and direction is determined from the measured ground velocity vector, aircraft attitude, and measured air speed relative to the aircraft.

Black Swift Technologies (BST) worked with CU-Boulder (CU) to operate two additional fixed-wing aircraft, the S1 and S2. The S1 is a foam airframe based on the commercially available Skywalker X8 platform and outfitted with the Black Swift Technologies SwiftPilot autopilot. It has a flying-wing design with a 2.1 m wingspan and gross takeoff weight of 5 kg, and 0.5 kg available for carrying sensors. In the S1 configuration, the aircraft can operate for up to 90 min at a cruise speed of 15 m/s. The S2 is a fully composite airframe purpose-built for flying scientific payloads in demanding atmospheric environments (high-altitude, corrosive particulates, and strong turbulence). It is also outfitted with the SwiftCore autopilot system. The aircraft has a maximum take off weight of 8.1 kg and a wingspan of 3.0 m, providing an 18 m/s cruise speed for up to 110 min. Both the S1 and S2 were equipped with the BST multi-hole probe which provides wind speed, direction, magnetometer, accelerometer, gyroscope, barometric pressure, temperature and humidity measurements at 100 Hz. The sensors were placed on the top of the aircraft, with the probe tip extending beyond the front of the aircraft to reduce body effects on the probe measurements. State measurements from the SwiftCore

autopilot were used to provide the necessary information for conversion of the wind vectors to the inertial frame.

The University of Kentucky (UKY) operated three fixed-wing aircraft, which are virtually identical and are referred to as the BLUECAT5 design [29]. These aircraft were also built around the Skywalker X8 airframe, ruggedized and modified for autonomous flight using a 3DR Pixhawk PX4 autopilot. In their current configuration, the aircraft can operate for 45 min at a cruise speed of 20 m/s. Each BLUECAT5 was equipped with an iMet-XQ sensor to measure P, T, and RH. The sensor was located on top of the aircraft fuselage in a housing designed to protect the sensor from solar radiation, while also leaving it exposed to air flowing over the aircraft. Wind velocity and direction were determined by a custom five-hole probe to measure the air velocity vector relative to the aircraft, working with a VectorNav VN-300 dual GNSS inertial sensor to measure the aircraft ground speed and aircraft orientation in the Earth-fixed inertial frame.

2.2.3. Sensor Locations

Sensor location varied for each aircraft with each team designing their own solutions. For simplicity, we assign them to the following categories: (1) indicates systems where T and RH sensors are not impacted by solar radiation shielding or forced aspiration; (2) indicates no special sensor placement, aspiration, or solar radiation protection for T, and RH sensors; (3) indicates aspiration and solar shielding for T, and RH sensors; (4) indicates system has solar shielding but no forced aspiration for T, and RH sensors; and (5) indicates system with aspiration but no solar shielding for T and RH sensors. Generally speaking, forced aspiration is assumed for all fixed-wing aircraft, as the sensors were located external to the airframe. The most common configuration for aspirating the multirotor sensors was by placing them within the rotor wash. Approaches to solar shielding T and RH sensors varied considerably by aircraft.

2.2.4. Flight Patterns

All sUAS platforms with payload packages conducted their intercomparison flights under the guidance of pre-defined flight patterns. The two standard patterns for fixed-wing and multirotor platforms are described below and visualized in Figure 3. Pilots adhered to those patterns as closely as possible, and any deviations that occurred during individual intercomparison flights, e.g., due to operational limitations, were recorded.

The primary comparison measurements were extracted from flight loiters conducted at approximately 18 m, to match the height of the MURC. In some cases, particularly for fixed-wing platforms, 18 m was too low for safe flight operations and slightly higher altitudes were chosen. Pilots loitered for 10 min to stabilize and obtain equilibrated sensor measurements for comparison with MURC. In the case of the multirotor platforms, an additional loiter at 3.4 m was performed to match with CoMeT-2. If sUAS battery operations or other flight conditions did not allow for the full 10 min, then 8 min was acceptable for loiters with the MURC for the primary time of measurement comparison, and 2 min for other altitudes. In addition to loiters, sUAS platforms ascended to 120 m and descended through the altitude point of 18 m to correspond with MURC tower heights to compare lag effects of sUAS sensor measurements. Flight patterns were conducted at least once for every sUAS platform and sensor payload. Specifically, the nominal flight patterns were as follows. *Fixed-Wing*: Launch and fly to stabilize at loiter altitude. Loiter at 18 m for 10 min. Ascend at 1 m/s to 120 m. Loiter at 120 m for 2 min. Descend 1 m/s to 18 m. Loiter at 18 m for 2 min. Ascend at own rate to 120 m. Descend at own rate to pass through 18 m. Land. *Multirotor*: Launch and fly to stabilize at loiter altitude. Loiter at 18 m for 8–10 min. Descend 1 m/s to 3.4 m. Loiter 3.4 for 2 min. Ascend at 1 m/s to pass through 18 m to reach 120 m. Loiter at 120 m for 2 min (as battery allows). Descend at 1 m/s to pass through 18 m to reach 3.4 m. Loiter 2 min at 3.4 m (as battery allows). Land.
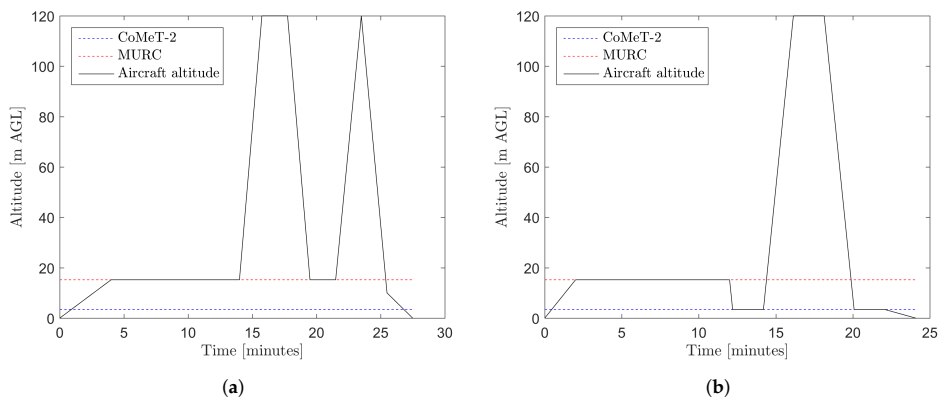
Figure 3. Example flight profiles. (**a**) Fixed-Wing; (**b**) Rotorcraft.

2.3. Data Analysis

As noted above, we grouped the sUAS platforms with sensor payloads by the platform configuration (fixed-wing or multirotor) and the sensor placement configuration. We then analyzed each sUAS platform and sensor payload by each atmospheric parameter measured: temperature, relative humidity, pressure, wind speed, wind direction. For each atmospheric parameter, we compared the sUAS measurements with the MURC reference measurements during sUAS flight loiter time. In some cases it was hard to identify a time period during the loiter where clear steady-state sensor values had been reached. In such cases we selected a intercomparison period covering roughly the second half of the loiter period. Comparisons of overall time series were made and a measurement difference plot was produced using the mean values from the intercomparison period. A Wilcoxon rank-sum test, also known as a Mann–Whitney U, test was then performed on sUAS mean measurement differences from the MURC reference to test for significant differences between (a) aircraft platform type (fixed-wing and multirotor) and (b) sensor configurations. These tests were repeated for all parameters.

Due to the fact that the analyzed parameters may vary significantly with altitude and since the algorithms for determining of the flight altitude may be very different for the sUAS in use, we applied a uniform post-processing algorithm to determine the flight altitude from pressure and temperature data. For the sUAS not sampling both of these parameters the originally provided altitude, mostly GNSS based, was used. In the applied method we first detrend the pressure time series linearly based on the pressure just before the start and right after the landing to remove a potential sensor drift or temporal atmospheric changes. We then compute the vertical thickness between two adjacent pressure levels of $\Delta p = 0.5$ hPa increments:

$$\Delta z_i = -\frac{\Delta p}{g \cdot \rho_i} \tag{1}$$

with the density, $\rho_i = \overline{p_i}/R \cdot \overline{T_i}$, calculated based on the mean pressure, $\overline{p_i}$, and mean temperature, $\overline{T_i}$, of each layer i and the specific gas constant of dry air, $R = 287.058$ J kg^{-1} K^{-1}. The integration of Δz_i yields an altitude z_i for each pressure level p_i. By interpolating between the pressure levels p_i for each $p(t)$ we get a new time vector $z(t)$. Apart from improving the comparability of our data, to our experience this method usually gives a much more stable altitude than the pure GNSS reading and assures that start and landing are at the same level. Furthermore, taking the ambient temperature into account improves the accuracy under conditions deviating significantly from the typically assumed standard atmosphere profile.

To compare sUAS measurements to the reference MURC data, precision and bias analysis was constrained to data from the portion of the flight when the sUAS was at the same altitude as the

MURC (approximately 10 min). As sensors had variable response times, with some responding more slowly upon reaching loiter altitude, we further constrained the measurement data to the period of time in which parameter measurements were determined to be stable and in equilibrium. Further, it is important to note that many wind estimates from these platforms require extensive post-processing.

To assess time response we compared the ascent and descent portion of the flight profile. We base our analysis on the assumption that the mean profile was stationary during this portion of the flight paired with using concurrent MURC data as a reference, and that therefore large statistical deviations between the profiles measured during ascent and descent could be attributed solely to lag caused by insufficient measurement system time response, with increasing deviation reflecting increased time lag. Note that this difference is influenced by the sensor itself, as well as the intricacies of the sensor placement on the aircraft. Thus, the profile data was split into ascent and descent portions of the flight using visual inspection of the altitude, temperature, humidity and pressure time series. Then, the ascent and descent data were bin-averaged using 1 m vertical bins between 19.5 m and 120.5 m. Where data were not available within these bins due to high ascent/descent rates relative to the sensor acquisition rate, linear interpolation was used to ensure at least one measurement point was present.

To generate a single, simple measure of sensor response, the absolute-mean-deviation (*amd*) between the bin-averaged ascent and descent data of a particular quantity, X, was calculated as

$$amd(X^{\uparrow\downarrow}) = |\langle X_i^{\uparrow} - X_i^{\downarrow} \rangle_i| \qquad (2)$$

where the $\uparrow$ indicates data from ascent, the $\downarrow$ indicates data from descent, the X_i indicates the quantity measured for each altitude bin, and the $\langle \cdot \rangle_i$ brackets indicate an average over all bins. Note that averaging before taking the absolute value is important to account for the fact that fast-response sensors resolving fine-scale turbulence may produce ascent and descent profiles very close together, but the profiles may cross each other several times. By calculating the absolute-mean-deviation, positive and negative deviations may cancel each other out, leading to a low value for the entire profile. Hence, following the assumption of a stationary mean profile, a low *amd* value should reflect faster temporal response of the measurement system.

Since each comparison flight took place at a different time, the mean-absolute deviation (*mad*) from the time-series data measured by the MURC was computed to provide an indication of the natural variability of X that may have occurred during each profiling flight. For the portion of the MURC time-series, $X_M(t)$, corresponding to the ascent and descent portion of each specific sUAS flight, we calculate

$$mad(X_M) = \langle |X_M(t) - \langle X_M(t) \rangle_t| \rangle_t, \qquad (3)$$

where $X_M(t)$ is the quantity measured during the portion of the time series being considered and $\langle \cdot \rangle_t$ indicates a time average over that portion of the time series. A higher *mad* value will indicate increasing deviation from the assumed stationary mean profile and therefore indicates that there is a contribution of non-stationarity for the *amd* value for a particular measurement system.

3. Results and Discussion

3.1. Overview of Precision and Bias Results

The majority of the intercomparison analyses presented here are from each sUAS intercomparison flight using the MURC data as a consistent reference. By using the measurements from when the flight altitude was at, or close to, the altitude of the MURC tower, we assume statistical convergence of measured parameters, and focus on precision and bias differences between the sUAS and the MURC measurements. The horizontal separation between the sUAS and the MURC, in the order of 15 m for multirotors and typically 100 m for fixed-wings, is assumed to be insignificant with respect to the averaging times and the prevailing wind speeds. However, it has to be noted that averaging fixed-wing

data, which are sampled along a circular trajectory, implies spatial averaging as well which is not the case for stationary platforms such as the MURC tower or a loitering multirotor system.

Comparisons of measured temperature, T, humidity RH, and pressure P are presented in Figures 4–6, respectively. Humidity is presented as relative humidity, RH, as this is the common sensor output quantity for RH. Comparisons of measured (horizontal) wind speed, U, and direction, dir, are also presented in Figures 7 and 8, respectively. In Figure 4 through Figure 8, the comparison is presented in two ways. Subfigures (a) through (c) show time series of the corresponding MURC measured parameter and the different sUAS measurements of the same parameter during the intercomparison period. Here, the solid black line represents the reference data from the MURC, and the solid colored lines reference the corresponding data from the sUAS platforms. The colored symbols at the top mark the start time of the intercomparison time period and identify the sUAS conducting flight operations. In subfigure (d), the mean value over the intercomparison time period measured by the sUAS is compared to the mean value measured by the MURC for the same intercomparison time period. Error bars in (d) represent the standard deviation of the measured values over the same time period. In Figures 4–8, the same symbol nomenclature is used for consistency. In this nomenclature, a △ is used to indicate fixed-wing systems, and a ◯ is used to indicate multirotor systems. The T and RH sensor configurations are further indicated by additional white markers on top of the colored symbols: • for no aspiration and radiation shielding; × for aspiration only; + for radiation shielding only; ∗ for aspiration and radiation shielding; ◇ for sensors not impacted by aspiration or solar radiation shielding (e.g., sonic anemometer temperature).

3.2. Overview of Time Response Results

To allow assessment of the time response of the measurement systems, Figure 9 shows the results from the analysis of the difference between ascent and descent portions of the flight. We focus this comparison on the measured values of T and RH as these measurements are most commonly subject to slow sensor response times, and can be substantially impacted by multiple factors, including sensor type (e.g., small-bead thermistor vs integrated circuit temperature measurement) as well as the placement on the aircraft (which can impact sensor aspiration, thermal radiation from the airframe, recycling of sampled air, etc.). Hence this comparison we present is a comprehensive assessment of the entire measurement system in operation, and is important in addition to testing of sensor response time in a controlled environment.

In Figures 9a,b the T and RH measurements made by each sUAS during ascent and descent are compared as profiles of $T(z)$ and $RH(z)$ respectively, where z is the height AGL. To improve readability, $T(z)$ and $RH(z)$ have been artificially offset, with the offset varying by aircraft to minimize overlap of the profiles. The values $amd(T)$ and $amd(RH)$ calculated for each sUAS are presented with blue bars and with additional markers in Figures 9c,d, respectively. In Figures 9e,f, these values have been compensated by subtracting $mad(T_M)$ and $mad(RH_M)$ respectively, to account for non-stationarities in T or RH due to large-scale turbulent or synoptic scale changes that may have occurred during the flight. $mad(T_M)$ and $mad(RH_M)$ are also shown as black bars in Figures 9c,d. The symbol and color nomenclature used in this figure follows the one used in Figures 4 and 5.

3.3. Temperature, Relative Humidity and Pressure

Most of the sUAS in this study carried one or more sensor payloads to measure at least three parameters: T (38), RH (36), and P (36). The intercomparisons of these parameter measurements shown in Figures 4–6 indicate that the sUAS provide consistent results, with broad general agreement with the MURC reference measurements, with mean value and standard deviation of the difference between all sUAS and MURC of: $T = 1.65 \pm 2.6$ °C; $RH = -3.15 \pm 12.12$%; and $P = 1.01 \pm 1.16$ hPa. In general, higher variability of T measurements was reported by the sUAS as compared to the MURC during the intercomparison flight period. This result may be due to differences in sensor response times, as well as overall movement of the sUAS with respect to altitude as the sUAS often experienced

altitude changes while loitering, as the mean standard deviation in altitude for all sUAS over their intercomparison time periods was 1.09 m $\pm$0.95 m. Under well mixed conditions, resulting in a dry adiabatic lapse rate, a height difference of 1.0 m corresponds to an approximate temperature difference of 0.01 °C at the prevailing pressure levels. It is important to note that the multirotor systems, similar to the MURC, conduct point measurements, whereas the fixed-wing aircraft were necessarily flying orbits around the MURC instruments, which can add variability due to the continually changing orientation of the aircraft.
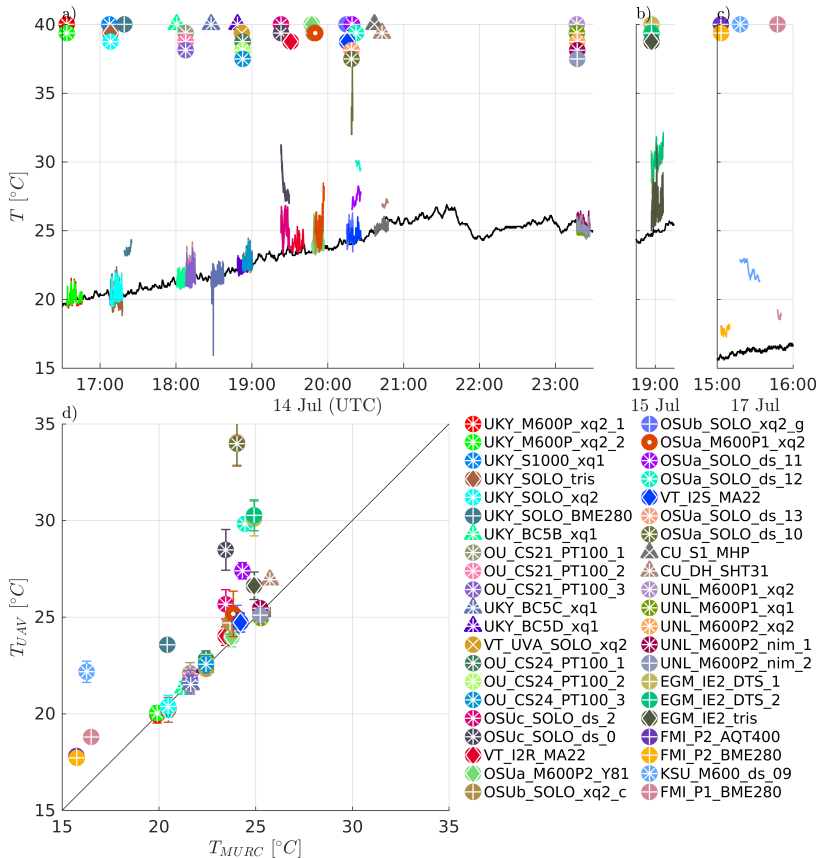
Figure 4. Time series of temperature measurements during July 14 (**a**), 15 (**b**), and 17 (**c**). The black solid line shows the reference observations from the MURC at 18 m AGL, whereas the colored solid lines represent the small unmanned aircraft system (sUAS) observations from the comparison period when the sUAS was flying next to the tower at approximately the same height. The colored symbols at the top mark the start time of the comparison period and their shape indicates the type of sUAS: △ for fixed-wing systems, and a ◯ for multirotor systems. The different white markers on top of the colored symbols indicate the different types of T and relative humidity (*RH*) sensor setups: · for no aspiration and radiation shielding; × for aspiration only; + for radiation shielding only; ∗ for aspiration and radiation shielding; ◇ for sensors not impacted by aspiration or solar radiation shielding. The mean differences between the sUAS and the MURC reference observations are shown in (**d**) with error bars indicating standard deviation.

The agreement between the sUAS and MURC mean values of measured *T* is highlighted in Figure 4d, where a perfect agreement between the two would lie along the diagonal reference line. The results indicate good agreement, with the majority (27/42) of the sUAS platforms measuring within $\pm 1\,^\circ$C of the MURC, and nearly half of the systems (11/42) measuring within $\pm 0.25\,^\circ$C. Notably, where disagreement occurred, the sUAS sensors had a positive bias, with few of the sUAS reporting mean *T* values below that of the MURC reference. In addition, these sensors tended to be of the integrated circuit-type (BME280, AQT400, MDASS). A high bias could be caused by absorption of direct solar radiation from the sun, infrared radiation from the surface, atmosphere, or warm sUAS parts (e.g., motors, battery) all of which could possibly be reduced by altering sensor placement, radiation shielding and aspiration. In at least two cases, the warmer *T* bias can be attributed to a poor sensor response (i.e., with the OSUa_SOLO_ds_10 and OSUa_SOLO_ds_13 demonstrating this in Figure 4). For these systems, the sUAS did not fully adapt to the temperature change from the warmer initial conditions close to ground to the cooler ambient air at the target loiter altitude, and we therefore did not include them in the assessment of sensor configuration.
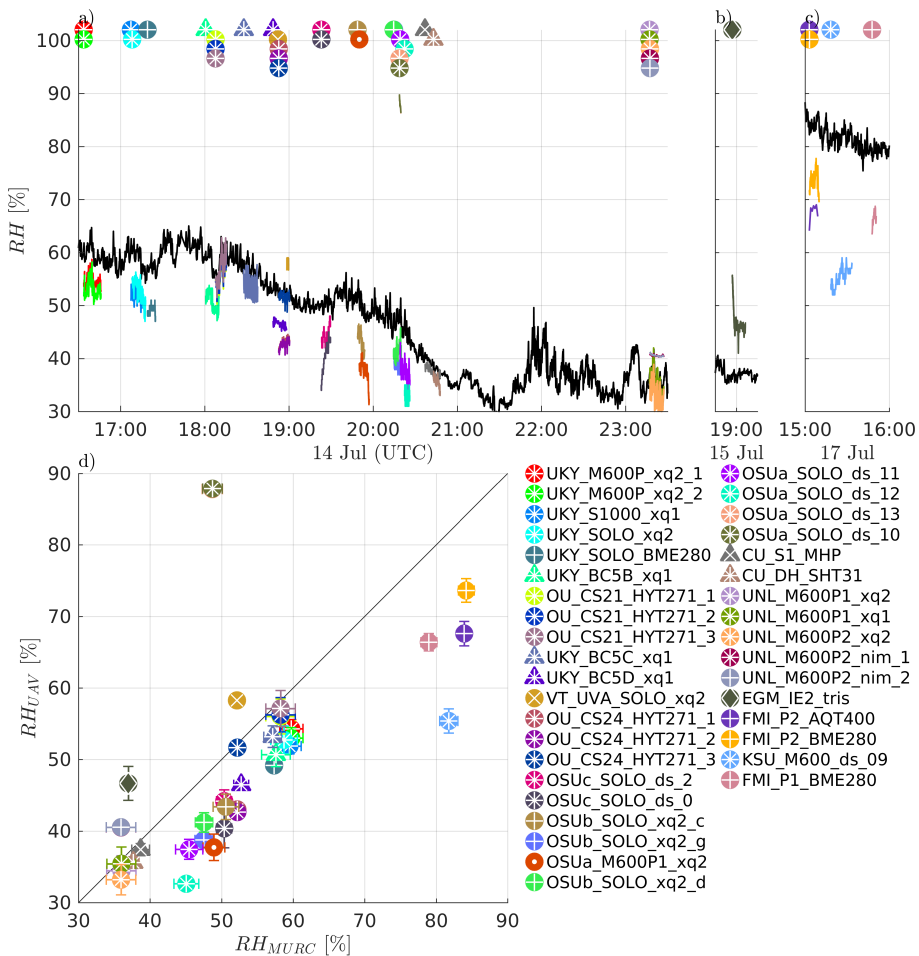
Figure 5. Time series of relative humidity measurements from July 14 (**a**), 15 (**b**), and 17 (**c**) and comparison of mean values to MURC reference measurements (**d**). The colors and markers follow the same scheme as in Figure 4.
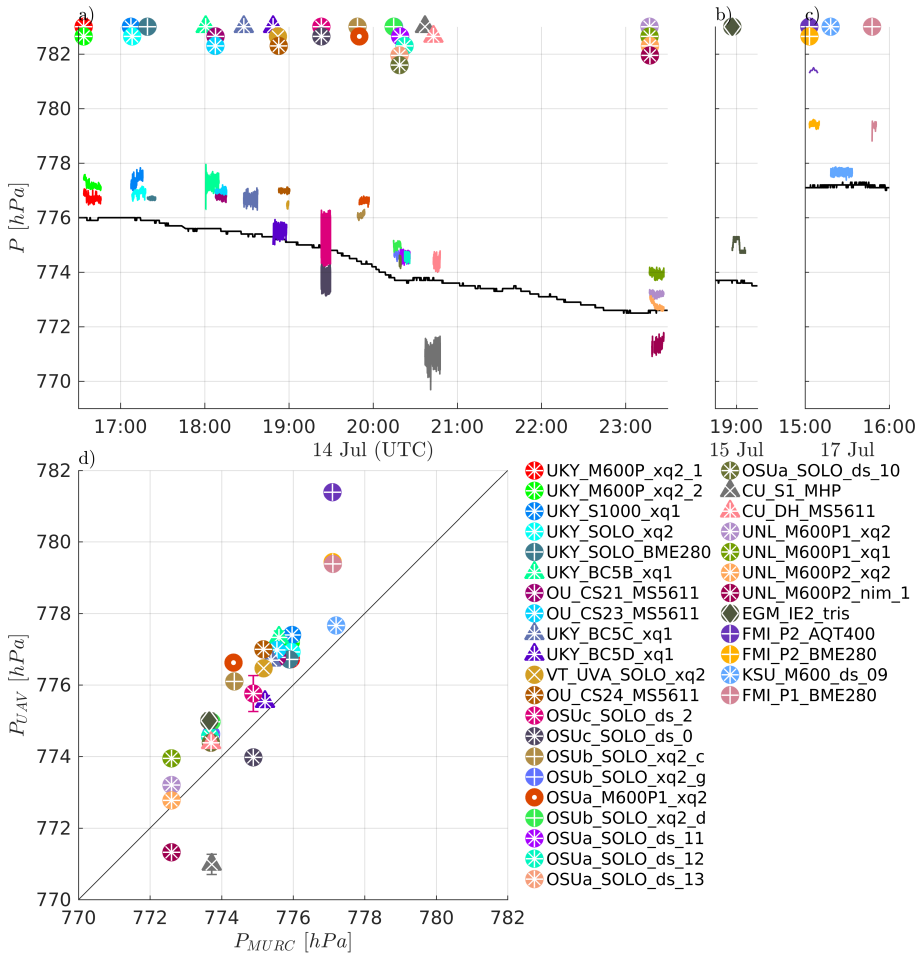
Figure 6. Time series of pressure measurements during July 14 (**a**), 15 (**b**), and 17 (**c**) and differences to MURC reference measurements (**d**). The colors and markers follow the same scheme as in Figure 4.

The differences between fixed-wing and multirotor aircraft configuration are detailed further in Figure 10a, which shows the larger spread in *T* measurements from multirotors, with a positive bias predominantly measured by multirotors. When examined in further detail, by delineating whether the sensors were aspirated and solar shielded, as done in Figure 10b, a potential source of the bias emerges. *T* measurements from unaspirated sUAS sensors were significantly different than from aspirated ones ($p < 0.009$), and had a high positive bias compared to the reference. In addition, as noted above and although exceptions occurred, sUAS sensor payloads generally biasing high also largely utilized integrated circuit temperature sensing, with the small-bead thermistor and sonic anemometer sensors being in better agreement with the reference.

The sUAS and MURC intercomparison of measured *RH*, shown in Figure 5, indicates much less agreement between the sUAS and MURC than was observed for temperature. The same general degree of fluctuations as for *T* can be observed in the time series of *RH* in Figure 5a, with some systems showing more or less fluctuation in value, and nearly all reached a steady state value during the loiter period. No trend was observed in the fluctuations, potentially indicating that the different amount of *RH* variations observed was due to intrinsic differences between system configurations. It is clear

from Figure 5d that the majority of the sUAS sensor payloads report *RH* mean values below that of the MURC, as mean value measurements lying along the diagonal reference line indicate perfect agreement between the MURC and sUAS, as with Figure 4d. However, only 9 of the 37 sUAS systems report *RH* mean values within ±5% of the MURC mean value, with most of these measured when *RH* < 40%. Twenty sUAS systems reported mean *RH* values 5% to 10% lower than the MURC, in the range of *RH* 45% to 65%, with one system as a clear outlier measuring almost 40% higher than the MURC. The remaining four sUAS systems reported mean *RH* values > 10% lower than the MURC, at the highest and lowest extents of the *RH* range.
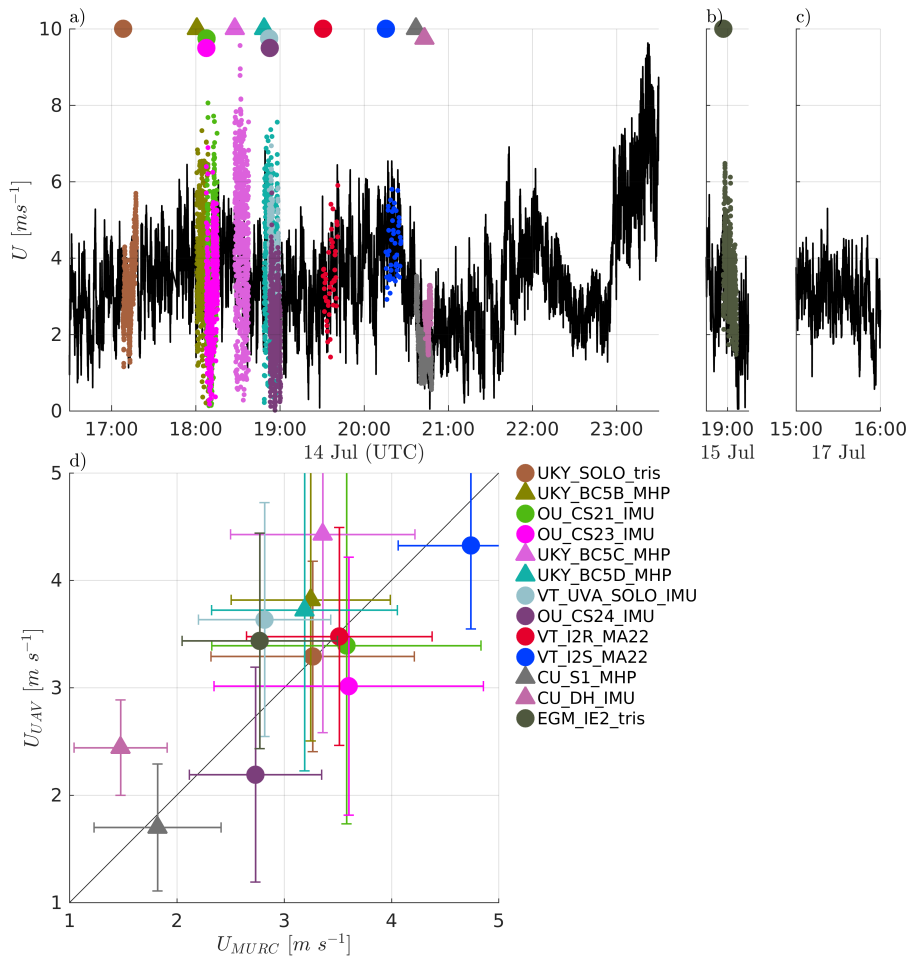
Figure 7. Time series of wind speed measurements during July 14 (**a**), 15 (**b**), and 17 (**c**) and differences to MURC reference measurements (**d**). The colors and markers follow the same scheme as in Figure 4, although without indication of the sensor setup (white markers).
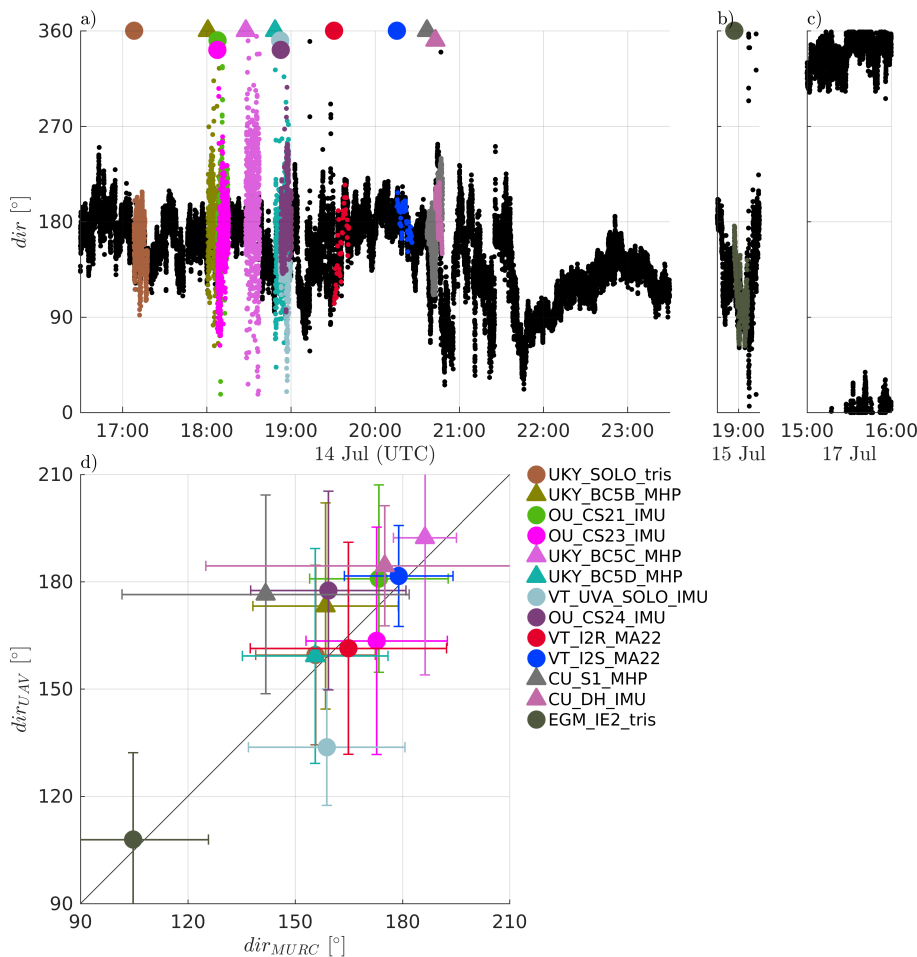
Figure 8. Time series of wind direction measurements (represented as dots for better interpretability) during July 14 (**a**), 15 (**b**), and 17 (**c**) and differences to MURC reference measurements (**d**). The colors and markers follow the same scheme as in Figure 7.

The differences between fixed-wing and multirotor aircraft configuration are compared in Figure 10c for RH. The multirotor platforms demonstrated more variability than the fixed-wing platforms for this measurement parameter, although substantially more aircraft fall into this category. When the distributions for different sensor configurations are compared, as done in Figure 10d, it becomes apparent that much of this variability can be attributed to platforms without aspiration, with almost all platforms measuring RH mean values over 10% below that of the MURC having no aspiration. However, the measured value of RH is dependent on the measured value of T, and therefore the similar influence of sensor aspiration on both parameters is not unexpected.

The sUAS and MURC intercomparison of measured P, shown in Figure 6, indicates generally good agreement, with 24 of the 33 sUAS payload systems reporting mean values within ± 1.5 hPa of the MURC reference, with all but three of those biasing higher than the MURC. There was considerable variation for the other 9 sUAS payload systems; although, all but two were within 3 hPa and most showed a positive bias as compared with the MURC reference. As shown in Figure 10e and consistent with T and RH, there were no statistically significant differences between P measurements between

sUAS platforms. Similarly, the sensor configuration of *T* and *RH* sensors (which are commonly packaged with the *P* sensor) did have a significant impact on the measurement of *P*, as indicated in Figure 10f. Further, the sensor payloads that were placed under the body of the multirotor reported the greatest deviation from the MURC reference value and outside the range of manufacturer uncertainty for this quantity. Outside of this observation, and noting that the same types of sensors can produce different amounts of fluctuation in the measurement of *P*, the observed variability may be attributed to differences in individual sensor manufacture and intrinsic sensor properties. However, unlike *RH*, the difference between MURC and sUAS measurements are predominantly within the uncertainty of the majority of sensors used.
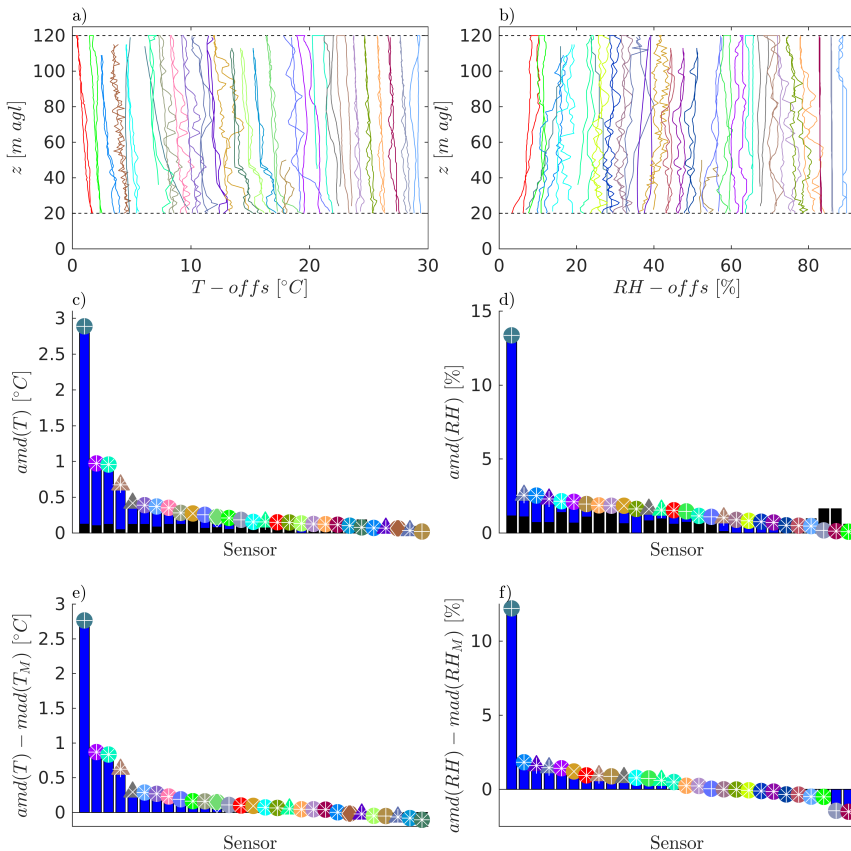
Figure 9. Comparison of temperature and relative humidity profiles taken during ascent and descent. Profile data between 20 m and 120 m AGL for temperature and relative humidity are shown in (**a**,**b**), respectively. The colors of the profiles are the same as in Figures 4 and 5. The profile data is shifted by an artificial temperature/humidity offset to increase the visibility of the profiles. The second row shows the absolute-mean-deviation between ascent and descent data (blue) and the corresponding mean-absolute-deviation of the MURC data for the corresponding times (black) for temperature (**c**) and relative humidity (**d**). The same markers as in Figures 4 and 5 are used to identify the different platform-sensor configurations. The last row shows the difference between the profile's absolute-mean-deviation and the MURC mean-absolute-deviation for temperature (**e**) and relative humidity (**f**).
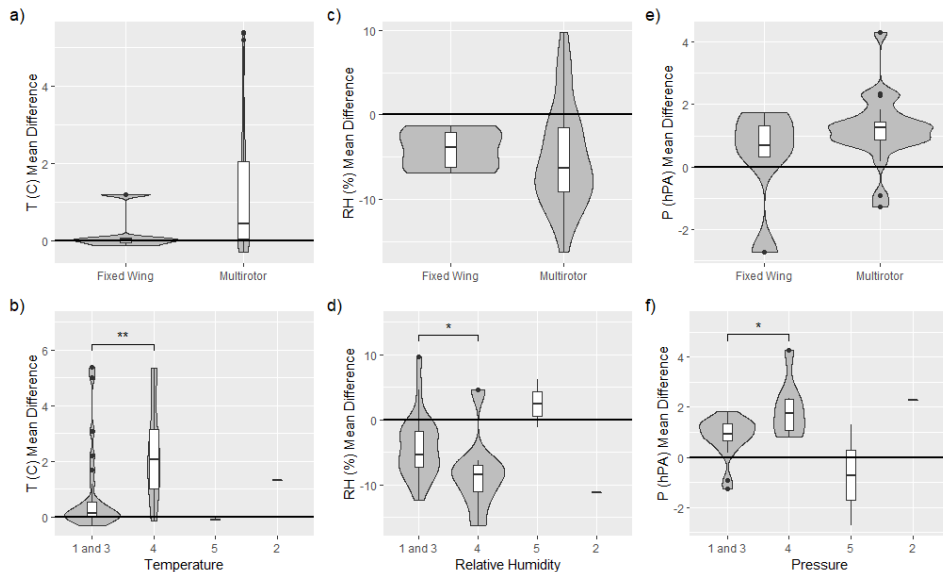
Figure 10. Comparison of temperature, relative humidity, and pressure measurement differences in relation to the MURC measurements, represented with the black line at 0. Averages of parameter measurement differences over each platform's MURC intercomparison loiter period are compared between platform and sensor configuration groups. For sensor configurations, 1 and 3 are sensors with solar radiation shielding and aspiration (3) or are not impacted (1), 4 are sensors with solar radiation shielding only, 5 are sensors with aspiration only, and 2 are sensors with neither solar radiation shielding or aspiration. Wilcoxon rank-sum tests were performed ($p(T) = 0.009$; $p(RH) = 0.039$; $p(P) = 0.036$).

The ultimate drivers of these differences in sUAS T, RH, and P measurement agreement relative to the MURC reference measurements may be difficult to untangle. The variability in the sensor measurements over the intercomparison loiter period and the variability in the altitude may have a joint effect. The degree of variability for both T and RH measurements during the intercomparison loiter varies between platform and sensor configuration, and no clear trend was observed in the standard deviation of the measurements. There is no clear trend that might indicate the source of disagreement, with no observed dependence on platform type or sensor. That said, the unaspirated sensors generally reported lower values of RH, and higher values of T. However, this finding is not exclusive to the aspiration. Furthermore, one sensor that reported a high positive bias relative to the MURC in RH was one that had no solar shielding, although the temperature measurement, which should be most significantly impacted by solar shielding, was in close agreement for this system. An additional factor not controlled for in Figure 10 is the type of sensor itself (e.g., integrated circuit or small-bead thermistor temperature sensing, resistive or capacitive humidity sensing, etc.). Among the possible influences that sensor type could have include, susceptibility to self-heating, sensitivity to location on the aircraft (e.g., proximity to electrical noise or thermal sources), and temporal response of the sensor.

3.4. Wind Speed and Direction

As a vector quantity that is influenced by the motion of the sUAS, the measurement of wind speed and direction tends to require more sophisticated measurement systems. Hence, fewer systems (13) were capable of measuring wind velocity and direction as compared to the number of systems capable of measuring pressure, temperature and humidity (36). These 13 systems utilized only three types of

measurement approaches, with multi-hole probes used by fixed-wing sUAS (4), sonic anemometers used by multirotor sUAS (4), and aircraft dynamics used by both types of systems (5). The last type can be further divided into three different approaches: (i) a comparison between the ground speed vector and the attitude measured by the global navigation satellite system (GNSS) and the inertial measurement unit (IMU) and the air speed, as used for the CU_DH fixed-wing sUAS; (ii) a calibrated conversion of the multirotor attitude angles for wind speed and direction while keeping the aircraft level with respect to its roll axis by yawing into the wind, as used for the three OU_CS systems; and (iii) a calibrated conversion of motor response to wind speed and direction, as used by the VT_UVA_SOLO multirotor.

Winds during the intercomparison measurements were consistent with super-adiabatic conditions at the MURC location (thereby lowering the sensitivity to altitude variability due to a well-mixed boundary layer minimizing the vertical gradient of the mean wind), with wind speeds between 2 to 4 m/s, gusting ±1 m/s over the period of each flight. In general, all measured winds showed good agreement between the MURC and sUAS, as evidenced in the time series of Figure 7a,b and scatter plot of Figure 7d. The difference in average U measured by all sUAS and the MURC was 0.22 ±0.59 m/s. Furthermore, the fluctuations measured by the systems were generally in good agreement as well, although some of the fixed-wing aircraft systems report higher variability than the MURC within the same time period.

A more quantitative compilation of the differences between the sUAS and MURC is provided in Figure 11a, which shows that the sUAS were generally in close agreement with the MURC with respect to mean wind speed measured during the loiter period. A comparison of the measured mean and fluctuating velocity magnitude shows no obvious bias between sUAS and MURC measurements. The majority of the mean values measured by the sUAS are within ±0.5 m/s of the MURC mean value with a predominantly positive bias, as evident in Figure 11a.

A slightly more nuanced view is presented in Figure 11b, which divides the comparison into fixed-wing and multirotor platforms. Higher variability was reported in the fixed-wing systems, which tended to bias high. The difference in sampling flights has already been noted (e.g., multirotor systems conduct point measurements, whereas the fixed-wing aircraft fly orbits around reference instruments) but it is important to highlight that a time series measured along a horizontal circular trajectory adds variability in both wind speed and direction due to the continually changing orientation of the aircraft during each orbit, and potential horizontal inhomogeneities in the wind field. The degree of bias appears to be dependent on specifics of each aircraft, as three identical physical systems (the BC5# systems) produced bias relative to the MURC of +0.5 m/s, +0.5 m/s, and +1 m/s, suggesting potential sensitivity to the individual multi-hole probe calibrations and alignment.

The sonic anemometers on the hovering multirotors provided the most consistent results with only small deviations from the MURC values (Figure 7d). This result suggests that concerns about biasing sonic anemometer wind measurements by rotorwash can be alleviated by careful placement of the sonic anemometer, at least for mean horizontal winds. The highest variability was observed in the systems using aircraft dynamics to extract the wind velocity. Again, individual calibrations may play a role in the accuracy of the reported wind magnitude, as three identical systems reported biases relative to the MURC of −0.2 m/s, −0.5 m/s, and −0.5 m/s.

The wind direction comparison, presented in Figure 8, shows similar trends to those observed for wind speed, with an average difference between all sUAS and the MURC of 5.09 ±14.07°. The time series comparison in Figure 8a again shows higher fluctuations in time for the fixed-wing aircraft compared to the multirotor aircraft, with these additional fluctuations attributed to the necessity of the aircraft to orbit around the MURC tower.

The distributions of average measured wind direction in Figure 11c show a tendency to measure a slightly larger angle in wind direction relative to that reported by the MURC. However, the majority of the sUAS systems measured wind direction within ±15° of the MURC value. As with wind speed, the distribution for all sUAS was divided into separate fixed-wing and multirotor distributions

in Figure 11d. Here it can be observed that the multirotor aircraft had better agreement than the fixed-wing aircraft. Again, it is possible that the orbits flown by the fixed-wing aircraft contribute to the bias and higher variability observed in the measured wind direction.
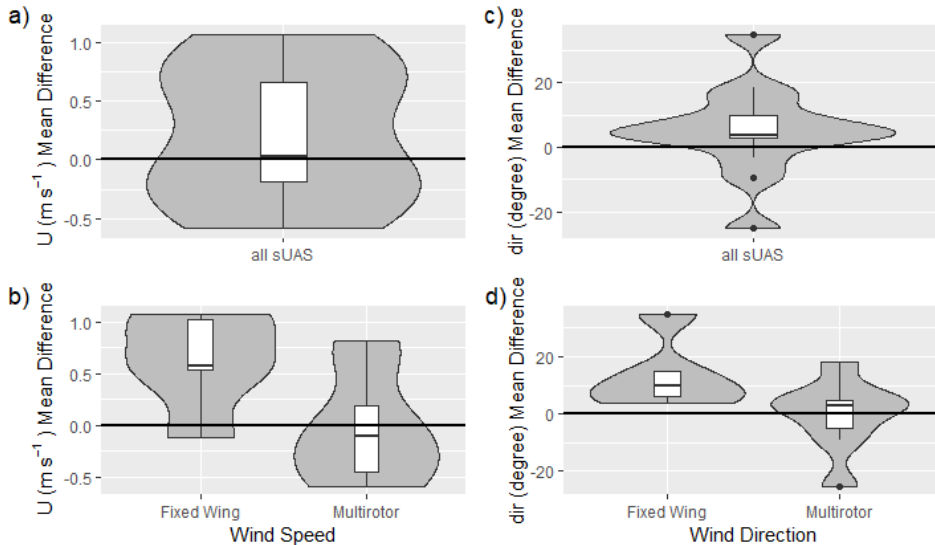
Figure 11. Comparison of difference (MURC – sUAS) in wind speed and wind direction measurement in relation to the MURC measurements—represented with the black line at 0. Averages of parameter measurement differences over each platform's MURC intercomparison loiter period are shown for all sUAS and then compared by platform. Wilcoxon rank-sum tests were performed, no significant differences were reported although near-significant differences were observed: $p(U) = 0.09$; $p(dir) = 0.07$.

3.5. Time Response of Measurement Systems

The comparison in Figure 9 provides an opportunity to assess the impact of the different sensor configurations on the time response of the temperature and humidity measurements. Note that this assessment does not take into account all possible influencing factors and is an attempt to quantify some of the effects of time response qualitatively observed when examining the data. In addition, we aim to assess the system as a whole (sensors and their arrangement on the aircraft), with the expectation that this integrated response will be quite different from manufacturer stated response.

In Figure 9c,d the higher the *amd*, the greater the mean difference between the ascent and descent measured profiles shown in Figure 9a,b, respectively. Assuming a stationary profile of *T* or *RH*, this would reflect slower response of the measurement systems. To account for non-stationarity of the true profile, these results are presented in Figure 9e,f compensated for the variability during the measurement using the *mad* in time reported by the MURC. This step implies the assumption that the variability observed at the height of the MURC platform is representative for the variability of the vertical column that has been profiled. It should also be noted that this analysis will not highlight systems with response times on the order of the ascent/descent times of the flight, as these systems will report the same values for both ascent and descent. Similarly, a very uniform profile, without any significant vertical gradients, is also likely to be reflected in a very good agreement between the ascent and descent profiles.

Generally, no clear trends were evident, with identical systems presenting different values. However, it does appear that the fine-bead thermistor-based temperature measurements (e.g., _xq, _xq2, and _pt100), which have faster manufacturer-stated response times, slightly outperformed the integrated-circuit-based temperature sensors (e.g., _BME280, _AQT400, _SHT31, _ds). In addition, systems with no aspiration demonstrated greater symptoms of sensor lag than those incorporating similar sensors without some form of aspiration. For example, the system that produced the largest $amd(T)$ and $amd(RH)$ values had the sensors mounted underneath the body of the multirotor airframe and out of the rotorwash. The systems that provided values of $amd(T) - mad(T_M)$ and $amd(RH) - mad(RH_M)$ near zero were predominantly those with some sort of aspiration of the sensors. In addition, it was observed that sUAS-sensor combinations with high negative $amd(T) - mad(T_M)$ and $amd(RH) - mad(RH_M)$ values did not seem to resolve temporal and spatial variations well (see the very straight relative humidity profiles in Figure 9b.)

3.6. Trends and Broader Discussion

In summary, the sUAS systems show broad agreement with the MURC values, particularly for temperature. There were no clear differences between fixed-wing and mutirotor platforms in the measurement of P, T, and RH, although wind measurements made by hovering multirotor aircraft were found to be in closer agreement to the MURC measured wind speed and direction than those made by orbiting fixed-wing platforms. Variability between the wind measured by nearly identical different aircraft also suggests that individual aircraft calibrations may play a considerable role in the accuracy of these measurements.

The time response and overall accuracy of T and RH measurements is dependent on the aspiration and solar shielding of the sensors, which is consistent with previous work [3]. Some differences were also observed between systems using integrated-circuit-based temperature sensors and those utilizing fine-bead thermistor sensors. Non-aspirated and unshielded sensors generally deviated from the MURC reference value to a greater degree, and unaspirated sensors demonstrated symptoms of measurement lag, particularly for T. Bias was generally observed between the sUAS and MURC T, RH, and P measurements. The sUAS measurements were, on average, higher than the MURC measurements in T, and P, with the sUAS measurement values of RH generally lower than the MURC value. Further, the RH disagreement exceeds the stated uncertainty for the sensors used. Hence, some caution is advised when interpreting reported accuracy of RH sensors when deployed on sUAS. It should be mentioned that these biases are consistent with the sUAS being slightly lower in altitude than the MURC sensors.

4. Limitations and Future Work

4.1. Measurement Accuracy

Understanding the potential accuracy limitations of altitude measurements is particularly critical for proper assessment of all other parameters, and altitude is not trivial to measure accurately. Depending on the system, altitude is based either on GNSS or pressure alone, or a fusion of both e.g., by Kalman filtering. The corresponding altitude estimates provided by the various autopilot systems are thus prone to different types of uncertainties that might be of particular importance for the required high precision of altitude attribution in the atmospheric surface layer. The experience during the LAPSE-RATE intercomparison flights, mainly based on the mean deviation in altitude for all sUAS, suggests that some platforms had difficulties maintaining stability at the loiter height. While this was particularly true for sUAS platforms where pilots were using manual controls, sensor drift is a known challenge for sUAS altitude measurements more broadly [60].

Opportunities may exist to better capture altitude for more accurate intercomparisons with ground-based systems for future studies. For platforms and sensors where altitude is determined based on pressure, an important practice would be to validate P readings from sUAS simultaneously with ground-based systems while platforms are on the ground before and after intercomparison flights. These simultaneous measurements could provide a better assessment of the deviations in altitude readings when platforms are airborne and thereby may have helped to improve assessment of other atmospheric measurements. Further, we highly recommend to post-process the altitude based on the measured temperature and pressure profile if ambient atmospheric conditions are significantly deviating from the assumed temperature profile (e.g., the often assumed International Civil Aviation Organization (ICAO) Standard atmosphere is characterized by a surface temperature of 15 °C and a lapse rate of −6.5 K/km), and are used for the pressure to altitude conversion. For low-altitude flights, a laser altimeter may help, and some of the platforms were equipped with these during the intercomparison flights (e.g., UKY's fixed-wing sUAS). While laser altimeters are currently used to enable more precise autonomous landing (e.g., [61]), they present an opportunity for future research and development for measuring altitude for low-altitude flights. Further, a more robust assessment of dual GNSS/INS systems, GNSS systems operating under real-time kinematic positioning, and magnetometer drift could aid in better atmospheric measurements as sUAS altitude and orientation is critical for accurate sensor intercomparison measurements.

A response rate comparison with the sUAS sensor measurements compared with the MURC measurement was intended using information gathered as the sUAS platform passed through the MURC point of altitude on ascent and descent, however, we were not able to conduct detailed analysis using this data. Rigorous analysis of the sensor response time using flight data was inhibited by the well-mixed prevailing conditions during the intercomparison flights causing weak vertical gradients. Detailed analysis of time response of the measurement systems using this portion of the flights is therefore not possible in this study, but is an important area for future research. Related to response time, for the intercomparison loiter period, measurements were used when the aircraft was determined to be at the appropriate loiter altitude and where sensor readings appeared to reach a measurement equilibrium. Further characterization and assessment of the time for sensor systems to reach the measurement equilibrium upon reaching the loiter altitude may provide useful insights for developing the best flight plans for atmospheric measurement data capture.

An important practice to explore for future intercomparison studies would be to include comparisons of the atmospheric measurements between all sensors while the sUAS are on the ground, and to do so under a variety of meteorological conditions. This could provide a useful baseline for assessing the accuracy and robustness of sensor measurements in flight. Further, future intercomparison studies may be able to determine a calibration factor that could be used based on the reference data in order to make the measurement data from all sUAS platforms align with the reference system. This would be helpful to a research study or operations team aiming to use data from different platforms collectively to address broader scientific inquiries. However, with the current intercomarison data, we are unable to make this described calibration factor. To do so in the future, intercomparison flights would need to be conducted in a variety of atmospheric conditions (e.g., at night with no solar radiation) and repeated more than once in order to determine a robust calibration factor. One important limitation to note is the lack of robust validation of the MURC reference measurements. While MURC instrumentation was calibrated as described in Section 2, and radiosondes and other mobile ground-based systems (e.g., CoMeT) provided important contextual comparison measurements, more comprehensive validation of the MURC reference measurements may have benefited this intercomparison analysis.

4.2. Measurement Robustness

Addressing temporal drift of intercomparison results (e.g., comparing intercomparison flights between the first day and final day of the week-long LAPSE-RATE campaign) is another important consideration. Comparing these same sUAS sensor payloads over the course of the longer campaign would allow for important discussions of the affect of 'wear and tear' of sensor systems on measurement accuracy. It is critical to extend the assessment of these sensor systems beyond laboratory or ground-based conditions, to more comprehensively evaluate sensor robustness under flight operation conditions. While we did attempt an intercomparison event on the final day of the LAPSE-RATE campaign (20 July 2018), operational challenges prevented several teams from participating. Flight tests conducted on this final day demonstrated the utility of calibrating multiple sensors on a single platform, providing improved confidence (or at least understanding) of intercomparisons between sensor systems. Even in these cases, however, mounting on small platforms may introduce discrepancies due to differences in aspiration and radiation shielding.

Additionally, as sensor payloads are occasionally exchanged between platforms during longer campaigns, it may also be beneficial to conduct intercomparison flights with the same sensor payloads flown on different aircraft frames. Examples of calibration experiments to evaluate for characterizing sensor response have been addressed elsewhere, primarily by utilizing simple calibration and validation experiments to determine the impact of response times and drift over limited times [3]. However, longer-term experiments are needed to better understand the impact of sensor behavior and associated measurement confidence. Utilization of Observational System Simulation Experiments (OSSEs) is one way, as it provides the ability to investigate the optimal observational sUAS deployment and sensor requirements in a simulated setting, including number and spatial distribution of weather observations, cadence of the measurements, spatial and temporal resolution, and vertical sampling resolution, for example [62–64].

4.3. Data and Information Management

There are many other potential sources and drivers of measurement error to consider. Additional sensor configuration considerations are likely relevant beyond solar radiation shielding and aspiration, and more comprehensive assessment of instrumentation handling is worth highlighting for future work (e.g., internal heating of sensors, as sUAS sensors measuring higher T and lower RH than the MURC, which can potentially be due to internal heating caused by their locations and configurations within the sUAS). Further, instrument calibration methodology, data corrections, and post-processing differ by sensor, system, and operator. To evaluate sensor system performance, there is great need to better represent the data processing levels involved (e.g., sensor manufacturer corrections, post-processing corrections) and whether intercomparison assessments are occurring with minimum data post-processing, or to what extent data are subjected to post-processing routines including quality assurance and quality control routines.

All sUAS platforms in this study had varying instrument handling and data management processes and workflows, with differing levels of automation regarding on-board data processing and post-processing. All together, this auxiliary information is likely critical for characterizing sUAS measurement accuracy, but is often difficult to capture as usable metadata, as operators may have a variety of different methods and expectations for documenting this information. However, it is clear that capturing relevant metadata in more detail and in a standardized way is critical to better assess sUAS measurement accuracy, error, and uncertainty and to improve future scientific goals (e.g., integrating sUAS data into weather models). To advance the use of sUAS for scientific data collection, future work will need to address these and other relevant data and information management challenges.

5. Conclusions

As small unmanned aircraft become more prominent platforms for atmospheric data collection, this paper highlights results from one of the largest collaborative flight campaigns with in-field intercomparison measurements to date, with a wide variety of differing platforms, sensors, and data collection workflows. We demonstrate the important role of coordinated intercomparison flights to support and enable the overall progression of sUAS collecting scientific measurements of atmospheric parameters. In particular, we show that while sUAS are broadly providing accurate atmospheric measurements, sensor configuration is important and proper aspiration and solar radiation shielding are likely more important than sUAS platform or specific sensor type. These significant differences highlight the need for more comprehensive sUAS design and development, with careful consideration for sensor integration to minimize measurement accuracy differences between platforms and enable more robust atmospheric data collection. Important challenges we highlight are managing all of the scientifically relevant data from the sUAS and capturing the specifics of important data-collection operations details (e.g., sensor specifications and configurations, instrument calibration, and data-processing workflows). Overall, we conclude that the future is bright for the use of sUAS for atmospheric science and expanding our understanding of best-practices in sUAS data collection via this and future intercomparision studies will lead to increasing the usefulness for sUAS-collected data in augmenting and expanding atmospheric knowledge, and for the potential for integrating these data for broader scientific insights.

Abbreviations

The following abbreviations are used in this manuscript:

AGL	Above Ground Level
CLAMPS	Collaborative Lower Atmospheric Mobile Profiling System
COA	Certificate of Authorization
COST	European Cooperation in Science and Technology
COTS	commercial off the shelf
FAA	Federal Aviation Administration
GNSS	Global Navigation Satellite System
ICAO	International Civil Aviation Organization
IMU	Inertial Measurement Unit
INU	Inertial Navigation Unit
IRISS	Integrated Remote and In-Situ Sensing program
ISARRA	International Society for Atmospheric Research using Remotely piloted Aircraft
LAPSE-RATE	Lower Atmospheric Process Studies at Elevation—a Remotely piloted Aircraft Team Experiment
MDT	Mountain Daylight Time
MSL	Meters above Sea Level
MURC	Mobile UAS Research Collaboratory
NOAA	National Oceanic and Atmospheric Administration
NSSL	NOAA National Severe Storms Laboratory
OSSEs	Observational System Simulation Experiments
RPAS	Remotely Piloted Aircraft System
sUAS	small Unmanned Aircraft System

References

1. National Academies of Sciences and Medicine. *The Future of Atmospheric Boundary Layer Observing, Understanding, and Modeling: Proceedings of a Workshop*; The National Academies Press: Washington, DC, USA, 2018.

2. De Boer, G.; Dalfflon, B.; Guenther, A.; Moore, D.; Schmid, B.; Serbin, S.; Vogelmann, A. *Aerial Observation Needs Workshop*; Technical Report; Department of Energy Climate and Environmental Sciences Division: Upton, NY, USA, 2015.

3. Jacob, J.D.; Chilson, P.B.; Houston, A.L.; Smith, S.W. Considerations for Atmospheric Measurements with Small Unmanned Aircraft Systems. *Atmosphere* **2018**, *9*, 252.

4. Hill, M.; Konrad, T.; Meyer, J.; Rowland, J. Radio controlled small aircraft as measurement platform for meteorological sensors, discussing development and performance from field tests. *Appl. Tech. Dig.* **1970**, *10*, 11–19.

5. Konrad, T.; Hill, M.; Meyer, J.; Rowland, J. A small, radio-controlled aircraft as a platform for meteorological sensors. *Appl. Tech. Dig.* **1970**, *10*, 11–19.

6. Holland, G.; Webster, P.; Curry, J.; Tyrell, G.; Gauntlett, D.; Brett, G.; Becker, J.; Hoag, R.; Vaglienti, W. The Aerosonde robotic aircraft: A new paradigm for environmental observations. *Bull. Am. Meteorol. Soc.* **2001**, *82*, 889–902.

7. Elston, J.; Argrow, B.; Stachura, M.; Weibel, D.; Lawrence, D.; Pope, D. Overview of small fixed-wing unmanned aircraft for meteorological sampling. *J. Atmos. Ocean. Technol.* **2015**, *32*, 97–115.

8. Elston, J.S.; Roadman, J.; Stachura, M.; Argrow, B.; Houston, A.; Frew, E. The tempest unmanned aircraft system for in situ observations of tornadic supercells: Design and VORTEX2 flight results. *J. Field Robot.* **2011**, *28*, 461–483.

9. Pieri, D.C.; Diaz, J.; Bland, G.; Fladeland, M.; Makel, D.; Schwandner, F.; Buongiorno, M.; Elston, J. *Unmanned Aerial Technologies for Observations at Active Volcanoes: Advances and Prospects*; American Geophysical Union Fall Meeting: New Orleans, LA, USA, 2017.

10. De Boer, G.; Ivey, M.; Schmid, B.; Lawrence, D.; Dexheimer, D.; Mei, F.; Hubbe, J.; Bendure, A.; Hardesty, J.; Shupe, M.D.; et al. A Bird's-Eye View: Development of an Operational ARM Unmanned Aerial Capability for Atmospheric Research in Arctic Alaska. *Bull. Am. Meteorol. Soc.* **2018**, *99*, 1197–1212, doi:10.1175/BAMS-D-17-0156.1.

11. Kral, S.; Reuder, J.; Vihma, T.; Suomi, I.; O'Connor, E.; Kouznetsov, R.; Wrenger, B.; Rautenberg, A.; Urbancic, G.; Jonassen, M.; et al. Innovative Strategies for Observations in the Arctic Atmospheric Boundary Layer (ISOBAR)—The Hailuoto 2017 Campaign. *Atmosphere* **2018**, *9*, 268.

12. Bonin, T.; Chilson, P.; Zielke, B.; Fedorovich, E. Observations of the Early Evening Boundary-Layer Transition Using a Small Unmanned Aerial System. *Bound.-Layer Meteorol.* **2013**, *146*, 119–132.

13. Bonin, T.A.; Goines, D.C.; Scott, A.K.; Wainwright, C.E.; Gibbs, J.A.; Chilson, P.B. Measurements of the temperature structure-function parameters with a small unmanned aerial system compared with a sodar. *Bound.-Layer Meteorol.* **2015**, *155*, 417–434.

14. Wildmann, N.; Rau, G.A.; Bange, J. Observations of the Early Morning Boundary-Layer Transition with Small Remotely-Piloted Aircraft. *Bound.-Layer Meteorol.* **2015**, *157*, 345–373.

15. Lothon, M.; Lohou, F.; Pino, D.; Couvreux, F.; Pardyjak, E.; Reuder, J.; Vilà-Guerau De Arellano, J.; Durand, P.; Hartogensis, O.; Legain, D.; et al. The BLLAST field experiment: boundary-layer late afternoon and sunset turbulence. *Atmos. Chem. Phys.* **2014**, *14*, 10931–10960.

16. Cassano, J.J.; Maslanik, J.A.; Zappa, C.J.; Gordon, A.L.; Cullather, R.I.; Knuth, S.L. Observations of Antarctic polynya with unmanned aircraft systems. *EOS Trans. Am. Geophys. Union* **2010**, *91*, 245–246.

17. Van den Kroonenberg, A.; Martin, T.; Buschmann, M.; Bange, J.; Vörsmann, P. Measuring the wind vector using the autonomous mini aerial vehicle M2AV. *J. Atmos. Ocean. Technol.* **2008**, *25*, 1969–1982.

18. Van den Kroonenberg, A.; Bange, J. Turbulent flux calculation in the polar stable boundary layer: Multiresolution flux decomposition and wavelet analysis. *J. Geophys. Res. Atmos.* **2007**, *112*, D06112.

19. Jonassen, M.O.; Tisler, P.; Altstädter, B.; Scholtz, A.; Vihma, T.; Lampert, A.; König-Langlo, G.; Lüpkes, C. Application of remotely piloted aircraft systems in observing the atmospheric boundary layer over Antarctic sea ice in winter. *Polar Res.* **2015**, *34*, 25651.

20. Schuyler, T.J.; Guzman, M.I. Unmanned Aerial Systems for Monitoring Trace Tropospheric Gases. *Atmosphere* **2017**, *8*, 206.

21. Platis, A.; Altstädter, B.; Wehner, B.; Wildmann, N.; Lampert, A.; Hermann, M.; Birmili, W.; Bange, J. An observational case study on the influence of atmospheric boundary-layer dynamics on new particle formation. *Bound.-Layer Meteorol.* **2016**, *158*, 67–92.

22. Corrigan, C.; Roberts, G.; Ramana, M.; Kim, D.; Ramanathan, V. Capturing vertical profiles of aerosols and black carbon over the Indian Ocean using autonomous unmanned aerial vehicles. *Atmos. Chem. Phys.* **2008**, *8*, 737–747.

23. De Boer, G.; Ivey, M.; Schmid, B.; McFarlane, S.; Petty, R. Unmanned Platforms Monitor the Arctic Atmosphere. *EOS* **2016**, *97*, 1033–1056.

24. Ramanathan, V.; Ramana, M.V.; Roberts, G.; Kim, D.; Corrigan, C.; Chung, C.; Winker, D. Warming trends in Asia amplified by brown cloud solar absorption. *Nature* **2007**, *448*, 575.

25. Roberts, G.; Ramana, M.; Corrigan, C.; Kim, D.; Ramanathan, V. Simultaneous observations of aerosol–cloud–albedo interactions with three stacked unmanned aerial vehicles. *Proc. Natl. Acad. Sci. USA* **2008**, *105*, 7370–7375.

26. Cione, J.; Kalina, E.; Uhlhorn, E.; Farber, A.; Damiano, B. Coyote unmanned aircraft system observations in Hurricane Edouard (2014). *Earth Space Sci.* **2016**, *3*, 370–380.

27. Houston, A.L.; Argrow, B.; Elston, J.; Lahowetz, J.; Frew, E.W.; Kennedy, P.C. The collaborative Colorado–Nebraska unmanned aircraft system experiment. *Bull. Am. Meteorol. Soc.* **2012**, *93*, 39–54.

28. Balsley, B.B.; Lawrence, D.A.; Woodman, R.F.; Fritts, D.C. Fine-scale characteristics of temperature, wind, and turbulence in the lower atmosphere (0–1300 m) over the south Peruvian coast. *Bound.-Layer Meteorol.* **2013**, *147*, 165–178.

29. Witte, B.M.; Singler, R.F.; Bailey, S.C. Development of an Unmanned Aerial Vehicle for the Measurement of Turbulence in the Atmospheric Boundary Layer. *Atmosphere* **2017**, *8*, 195.

30. Wildmann, N.; Hofsäß, M.; Weimer, F.; Joos, A.; Bange, J. MASC—A small Remotely Piloted Aircraft (RPA) for wind energy research. *Adv. Sci. Res.* **2014**, *11*, 55–61.

31. Reuder, J.; Båserud, L.; Kral, S.; Kumer, V.; Wagenaar, J.W.; Knauer, A. Proof of concept for wind turbine wake investigations with the RPAS SUMO. *Energy Procedia* **2016**, *94*, 452–461.

32. Finn, A.; Rogers, K. Improving Unmanned Aerial Vehicle–Based Acoustic Atmospheric Tomography by Varying the Engine Firing Rate of the Aircraft. *J. Atmos. Ocean. Technol.* **2016**, *33*, 803–816.

33. Hemingway, B.L.; Frazier, A.E.; Elbing, B.R.; Jacob, J.D. Vertical sampling scales for atmospheric boundary layer measurements from small unmanned aircraft systems (sUAS). *Atmosphere* **2017**, *8*, 176.

34. Lange, M.; Reuder, J. *UAS Report COST Action ES0802 Unmanned Aerial Systems in Atmospheric Research*; Technical Report; COST: Brussels, Belgium, 2013.

35. Vömel, H.; Argrow, B.; Axisa, D.; Chlson, P.; Ellis, S.; Fladeland, M.; Frew, E.; Jacob, J.; Lord, M.; Moore, J.; et al. The NCAR/EOL Community Workshop On Unmanned Aircraft Systems For Atmospheric Research. 2018. Available online: https://www.eol.ucar.edu/node/13299 (accessed on 30 April 2019).

36. Greene, B.R.; Segales, A.R.; Waugh, S.; Duthoit, S.; Chilson, P.B. Considerations for temperature sensor placement on rotary-wing unmanned aircraft systems. *Atmos. Meas. Tech.* **2018**, *11*, 5519–5530.

37. Greene, B.R.; Segales, A.R.; Bell, T.M.; Pillar-Little, E.A.; Chilson, P.B. Environmental and sensor integration influences on temperature measurements by rotary-wing unmanned aircraft systems. *Sensors* **2019**, *19*, 1470.

38. Straka, J.M.; Rasmussen, E.N.; Fredrickson, S.E. A mobile mesonet for finescale meteorological observations. *J. Atmos. Ocean. Technol.* **1996**, *13*, 921–936.

39. Administration, F.A. Part 107 of the Small Unmanned Aircraft Regulations; 2016. Available Online: https://www.faa.gov/news/fact_sheets/news_story.cfm?newsId=20516 (accessed on 26 April 2019)

40. Foster, N.P.; Pinkerman, C.W.; Jacob, J.D. Meteorological Data Collection for Three-Dimensional Forecasting Advancements. In Proceedings of the 8th AIAA Atmospheric and Space Environments Conference, Washington, DC, USA, 13–17 June 2016; American Institute of Aeronautics and Astronautics: Reston, VA, USA, 2016.

41. Nolan, P.; Pinto, J.; González-Rocha, J.; Jensen, A.; Vezzi, C.; Bailey, S.; de Boer, G.; Diehl, C.; Laurence, R.; Powers, C.; et al. Coordinated Unmanned Aircraft System (UAS) and Ground-Based Weather Measurements to Predict Lagrangian Coherent Structures (LCSs). *Sensors* **2018**, *18*, 4448.

42. Langelaan, J.W.; Alley, N.; Neidhoefer, J. Wind Field Estimation for Small Unmanned Aerial Vehicles. *J. Guid. Control Dyn.* **2011**, *34*, 1016–1030.

43. Palomaki, R.T.; Rose, N.T.; van den Bossche, M.; Sherman, T.J.; Wekker, S.F.J.D. Wind Estimation in the Lower Atmosphere Using Multirotor Aircraft. *J. Atmos. Ocean. Technol.* **2017**, *34*, 1183–1191.

44. Johansen, T.A.; Cristofaro, A.; Sorensen, K.L.; Hansen, J.M.; Fossen, T.I. On estimation of wind velocity, angle-of-attack and sideslip angle of small UAVs using standard sensors. In Proceedings of the 2015 International Conference on Unmanned Aircraft Systems (ICUAS), Denver, CO, USA, 9–12 June 2015; pp. 510–519.

45. Neumann, P.P.; Bartholmai, M. Real-time wind estimation on a micro unmanned aerial vehicle using its inertial measurement unit. *Sens. Actuators A Phys.* **2015**, *235*, 300–310.

46. González-Rocha, J.; Woolsey, C.A.; Sultan, C.; De Wekker, S.F. Sensing Wind from Quadrotor Motion. *J. Guid. Control Dyn.* **2019**, *42*, 836–852, doi:10.2514/1.G003542.

47. Donnell, G.W.; Feight, J.A.; Lannan, N.; Jacob, J.D. Wind Characterization Using Onboard IMU of sUAS. In Proceedings of the 2018 Atmospheric Flight Mechanics Conference. American Institute of Aeronautics and Astronautics, Atlanta, GA, USA, 25–29 June 2018.

48. Roadman, J.; Elston, J.; Argrow, B.; Frew, E. Mission Performance of the Tempest Unmanned Aircraft System in Supercell Storms. *J. Aircr.* **2012**, *49*, 1821–1830.

49. Elston, J.; Argrow, B.; Frew, E.; Houston, A.; Straka, J. Evaluation of unmanned aircraft systems for severe storm sampling using hardware-in-the-loop simulations. *J. Aerosp. Comput. Inf. Commun.* **2011**, *8*, 269–294.

50. Vaisala. *Vaisala Radiosonde RS92*; Vaisala: Vantaa, Finland, 2013.

51. Aeroprobe. *Aeroprobe Micro Air Data System User Manual*, 2nd ed.; Aeroprobe Corporation: Christiansburg, VA, USA, 2016.

52. Telionis, D.; Yang, Y.; Rediniotis, O. Recent Developments in Multi-Hole Probe (MHP) Technology. In Proceedings of the 20th International Congress of Mechanical Engineering, Gramado, Brazil, 15–20 November 2009.

53. VectorNav Technologies.   VN-200 User Manual; Document Revision 2.03; 2015.   Available online: https://www.vectornav.com/docs/default-source/documentation/vn-200-documentation/vn-200-user-manual-(um004).pdf?sfvrsn=3a9ee6b9_23 (accessed on 30 April 2019).

54. VectorNav Technologies. VN-200 GPS/INS Specifications. 2017. Available online: http://www.vectornav.com/products/vn-200/specifications (accessed on 26 June 2017).

55. TE Connectivity.   MS8607-02BA01.   2015.   Available online: https://www.te.com/commerce/DocumentDelivery/DDEController?Action=showdoc&DocId=Data+Sheet%7FMS8607-02BA01%7FB3%7Fpdf%7FEnglish%7FENG_DS_MS8607-02BA01_B3.pdf%7FCAT-BLPS0018 (accessed on 30 April 2019).

56. Ublox. CAM-M8. 2016. Available online: https://www.u-blox.com/sites/default/files/CAM-M8-FW3_DataSheet_%28UBX-15031574%29.pdf (accessed on 30 April 2019).

57. Lawrence, D.A.; Balsley, B.B. High-Resolution Atmospheric Sensing of Multiple Atmospheric Variables Using the DataHawk Small Airborne Measurement System. *J. Atmos. Ocean. Technol.* **2013**, *30*, 2352–2366, doi:10.1175/JTECH-D-12-00089.1.

58. Luce, H.; Kantha, L.; Hashiguchi, H.; Lawrence, D.; Yabuki, M.; Tsuda, T.; Mixa, T. Comparisons between high-resolution profiles of squared refractive index gradient M^2 measured by the Middle and Upper Atmosphere Radar and unmanned aerial vehicles (UAVs) during the Shigaraki UAV-Radar Experiment 2015 campaign. *Ann. Geophys.* **2017**, *35*, 423–441.

59. Balsley, B.B.; Lawrence, D.A.; Fritts, D.C.; Wang, L.; Wan, K.; Werne, J. Fine Structure, Instabilities, and Turbulence in the Lower Atmosphere: High-Resolution In Situ Slant-Path Measurements with the DataHawk UAV and Comparisons with Numerical Modeling. *J. Atmos. Ocean. Technol.* **2018**, *35*, 619–642, doi:10.1175/JTECH-D-16-0037.1.

60. Nichols, T.; Argrow, B.; Kingston, D. Error Sensitivity Analysis of Small UAS Wind-Sensing Systems. In Proceedings of the AIAA Information Systems-AIAA Infotech @ Aerospace, Grapevine, TX, USA, 9–13 January 2017; p. 0647.

61. Geske, J.; MacDougal, M.; Stahl, R.; Wagener, J.; Snyder, D.R. Miniature laser rangefinders and laser altimeters. In Proceedings of the 2008 IEEE Avionics, Fiber-Optics and Photonics Technology Conference, San Diego, CA, USA, 30 September–2 October 2008; pp. 53–54.

62. Privé, N.C.; Xie, Y.; Koch, S.; Atlas, R.; Majumdar, S.J.; Hoffman, R.N. An Observing System Simulation Experiment for the Unmanned Aircraft System Data Impact on Tropical Cyclone Track Forecasts. *Mon. Weather Rev.* **2014**, *142*, 4357–4363.

63. Houston, A.; Keeler, J. Assimilation of UAS-Supercell Datasets in an OSSE Framework. In Proceedings of the AMS 22nd Conference on Integrated Observing and Assimilation Systems for the Atmosphere, Oceans, and Land Surface, Austin, TX, USA, 9 January 2018.

64. Houston, A.; Keeler, J. The Impact of Sensor Response and Airspeed on the Representation of Atmospheric Boundary Layer Phenomena by Airborne Instruments. *J. Atmos. Ocean. Technol.* **2018**, *35*, 1687–1699..

Paper III

The Innovative Strategies for Observations in the Arctic Atmospheric Boundary Layer Project (ISOBAR) — Unique fine-scale observations under stable and very stable conditions

Kral, S. T., J. Reuder, T. Vihma, I. Suomi, K. Flacké Haualand, G. H. Urbancic, B. R. Greene, G.-J. Steeneveld, T. Lorenz, B. Maronga, M. O. Jonassen, H. Ajosenpää, L. Båserud, P. B. Chilson, A. A. M. Holtslag, A. D. Jenkins, R. Kouznetsov, S. Mayer, E. A. Pillar-Little, A. Rautenberg, J. Schwenkel, A. Seidl and B. Wrenger.

III

1 **The Innovative Strategies for Observations in the Arctic Atmospheric**

2 **Boundary Layer Project (ISOBAR) — Unique fine-scale observations under**

3 **stable and very stable conditions**

4 Stephan T. Kral[*]

5 *Geophysical Institute and Bjerknes Centre for Climate Research, University of Bergen, Bergen,*

6 *Norway*

7 Joachim Reuder

8 *Geophysical Institute and Bjerknes Centre for Climate Research, University of Bergen, Bergen,*

9 *Norway*

10 Timo Vihma

11 *Finnish Meteorological Institute, Helsinki, Finland*

12 Irene Suomi

13 *Finnish Meteorological Institute, Helsinki, Finland*

14 Kristine Flacké Haualand

15 *Geophysical Institute and Bjerknes Centre for Climate Research, University of Bergen, Bergen,*

16 *Norway*

17 Gabin H. Urbancic

1

Geophysical Institute, University of Bergen, Bergen, Norway, and Finnish Meteorological

Institute, Helsinki, Finland

Brian R. Greene

School of Meteorology, Advanced Radar Research Center, and Center for Autonomous Sensing

and Sampling, University of Oklahoma, Norman, Oklahoma, USA

Gert-Jan Steeneveld

Meteorology and Air Quality Section, Wageningen University, Wageningen, Netherlands

Torge Lorenz

NORCE Norwegian Research Centre and Bjerknes Centre for Climate Research, Bergen, Norway

Björn Maronga

Institute of Meteorology and Climatology, Leibniz University Hannover, Hannover, Germany, and

Geophysical Institute, University of Bergen, Bergen, Norway

Marius O. Jonassen

The University Centre in Svalbard, Longyearbyen, Norway and Geophysical Institute, University

of Bergen, Bergen, Norway

Hada Ajosenpää

Finnish Meteorological Institute, Helsinki, Finland

Line Båserud

Geophysical Institute and Bjerknes Centre for Climate Research, University of Bergen, Bergen,

Norway, and Norwegian Meteorological Institute, Oslo, Norway

2

Phillip B. Chilson

School of Meteorology, Advanced Radar Research Center, and Center for Autonomous Sensing and Sampling, University of Oklahoma, Norman, Oklahoma, USA

Albert A. M. Holtslag

Meteorology and Air Quality Section, Wageningen University, Wageningen, Netherlands

Alastair D. Jenkins

Geophysical Institute, University of Bergen, Bergen, Norway

Rostislav Kouznetsov

Finnish Meteorological Institute, Helsinki, Finland, and Obukhov Institute for Atmospheric Physics, Moscow, Russia

Stephanie Mayer

NORCE Norwegian Research Centre and Bjerknes Centre for Climate Research, Bergen, Norway

Elizabeth A. Pillar-Little

School of Meteorology and Center for Autonomous Sensing and Sampling, University of Oklahoma, Norman, Oklahoma, USA

Alexander Rautenberg

Center for Applied Geoscience, Eberhard-Karls-Universität Tübingen, Tübingen, Germany

Johannes Schwenkel

Institute of Meteorology and Climatology, Leibniz University Hannover, Hannover, Germany

3

Andrew W. Seidl

Geophysical Institute and Bjerknes Centre for Climate Research, University of Bergen, Bergen,

Norway

Burkhard Wrenger

Ostwestfalen-Lippe University of Applied Sciences and Arts, Höxter, Germany

Corresponding author: Stephan T. Kral, stephan.kral@uib.no

4

ABSTRACT

The Innovative Strategies for Observations in the Arctic Atmospheric Boundary Layer Program (ISOBAR) is a research project investigating stable atmospheric boundary layer (SBL) processes, whose representation still poses significant challenges in state-of-the-art numerical weather prediction (NWP) models. In ISOBAR ground-based flux and profile observations are combined with boundary-layer remote sensing methods and the extensive usage of different unmanned aircraft systems (UAS). During February 2017 and 2018 we carried out two major field campaigns over the sea ice of the northern Baltic Sea, close to the Finnish island of Hailuoto at 65 °N. In total 14 intensive observational periods (IOPs) resulted in extensive SBL datasets with unprecedented spatiotemporal resolution, which will form the basis for various numerical modeling experiments. First results from the campaigns indicate numerous very stable boundary layer (VSBL) cases, characterized by strong stratification, weak winds, and clear skies, and give detailed insight in the temporal evolution and vertical structure of the entire SBL. The SBL is subject to rapid changes in its vertical structure, responding to a variety of different processes. In particular, we study cases involving a shear instability associated with a low-level jet, a rapid strong cooling event observed a few meters above ground, and a strong wave-breaking event that triggers intensive near-surface turbulence. Furthermore, we use observations from one IOP to validate three different atmospheric models. The unique fine-scale observations resulting from the ISOBAR observational approach will aid future research activities, focusing on a better understanding of the SBL and its implementation in numerical models.

5

Capsule summary. Combining ground-based micrometeorological instrumentation with boundary layer remote sensing and unmanned aircraft systems for high-resolution observations on the stable boundary layer over sea ice and corresponding modelling experiments.

Background and Motivation

The stably-stratified atmospheric boundary layer (SBL) is common in the Arctic, where the absence of solar radiation during winter causes a negative net radiation at the surface. Even during daylight seasons, the high surface albedo of snow and ice favors SBL formation (Persson et al. 2002). The SBL is of particular interest for our understanding of the Arctic climate system (e.g., Bintanja et al. 2012; Lesins et al. 2012; Davy and Esau 2016), which experiences a significantly stronger warming than the rest of the globe, commonly referred to as Arctic Amplification (Serreze et al. 2009; Serreze and Barry 2011; Pithan and Mauritsen 2014; Dai et al. 2019). The state of and the processes in the ABL affect the turbulent and radiative heat fluxes from the atmosphere to the Earth's surface and, accordingly, the surface mass balance of sea ice, ice sheets, glaciers, and terrestrial snow. Hence, the correct understanding and parameterization of the SBL and its coupling to the underlying snow, ice, or land surface is crucial for the reliability of climate model projections in polar regions. Another strong indication for the importance of the SBL is the fact that the observed global warming trend over the last decades is most pronounced at nighttime and in polar regions, both when SBL prevail (McNider et al. 2010).

Climate and numerical weather prediction (NWP) models suffer from insufficient ABL parameterizations and have a strong need for an improved representation of the SBL, in particular in very stable boundary layer (VSBL) conditions. This is demonstrated by large errors under VSBL conditions, where 2-m air temperature errors (ΔT_{2m}) of the order of $10\,\mathrm{K}$ are common even in short-term (24-h) NWP products (Atlaskin and Vihma 2012). In atmospheric reanalyses, broadly

6

applied in diagnostics of climate variability and change, the monthly/seasonal means of ΔT_{2m} in the Arctic (Jakobson et al. 2012; Graham et al. 2019) and Antarctic (Jonassen et al. 2019) typically show values of a few kelvins, and can even reach 20 K, strongly depending on the VSBL parameterization applied (Uppala et al. 2005). The common positive temperature biases are typically related to excessively large downward sensible heat flux (Cuxart et al. 2005; Tjernström et al. 2005), whereas large negative biases may be generated via thermal decoupling between the atmosphere and the snow/ice surface (Mahrt 2003; Uppala et al. 2005). In addition to problems in the turbulence parameterization, most climate models use a too coarse vertical resolution for an appropriate representation of the VSBL (Byrkjedal et al. 2007).

The numerical models used for weather prediction and climate scenarios rely on turbulence closure and surface-layer exchange schemes based on Monin-Obukhov similarity theory (MOST, Monin and Obukhov 1954), which relates the non-dimensional vertical gradients of wind, temperature and humidity to their respective surface fluxes. MOST is, however, theoretically only valid for stationary, homogeneous flow fields in the atmospheric surface layer, where variations of the turbulent fluxes with height can be neglected. Because the SBL rarely satisfies these conditions, there is substantial need for improvement in the description, characterization, and parameterization of the relevant SBL processes. Moreover, empirical studies evaluating MOST commonly indicate an inability to differentiate between near-neutral and very stable regimes (Foken 2006; Sorbjan and Grachev 2010; Sorbjan 2010; Grachev et al. 2013), which this is largely related to the very weak turbulent heat fluxes present in both situations.

The motivation of the Innovative Strategies for Observations in the Arctic Atmospheric Boundary Layer (ISOBAR) project is to improve our understanding of the SBL by applying new observation techniques and numerical modelling experiments, based on the collected data. In combination with well-established ground-based micrometeorological instrumentation and boundary layer remote

7

sensing, we utilize multiple unmanned aircraft systems (UAS) — designed for boundary layer observations — to intensively sample the SBL over sea ice. Through this endeavor, we aim to advance our understanding of the myriad of different processes relevant under very stable stratification. The potential of such observational approaches has been emphasised in a number of SBL review articles (e.g., Fernando and Weil 2010; Mahrt 2014). n particular, we investigate the role of wave–turbulence interaction, the formation and variability of low-level jets (LLJ), intermittency, the spatiotemporal evolution of the SBL structure, and interaction between the SBL and the free atmosphere.

The atmospheric boundary layer (ABL) is in general characterized by turbulence generated by wind shear that is either enhanced or suppressed by buoyancy effects, with surface friction and surface heating or cooling as the main drivers. SBL formation is favoured by clear sky and weak wind conditions, typically associated with high pressure synoptic situations characterized by large-scale subsidence and weak pressure gradients. Warm air advection may also contribute to the formation or strengthening of a SBL. In SBL research, it is common to distinguish between the weakly stable boundary layer (WSBL), where turbulence is still the dominating process, and the VSBL, in which turbulence is weak or intermittent. Transitions between WSBL and VSBL take place under clear skies when the net radiative heat loss at the surface becomes larger than the maximum turbulent heat flux that can be maintained by wind shear (de Wiel et al. 2017). As turbulence in the VSBL is typically weak, other processes — such as radiation divergence, surface coupling, wave phenomena, and fog — may become more important. If present, the turbulence is often intermittent.

Hoch et al. (2007), Steeneveld et al. (2010) and Gentine et al. (2018) address the substantial role of radiation divergence on the temperature budget under these conditions. Moreover, the lack of turbulent drag in the VSBL coincides with the emergence of LLJ. Bosveld et al. (2014)

8

showed that even for a relatively straightforward LLJ event at Cabauw (The Netherlands), different single-column models (SCM) represent this event rather differently and with considerable biases compared to observations. In addition, gravity waves might propagate under stratified conditions and transport momentum vertically (Nappo 2012; Lapworth and Osborne 2019). The sheer number of involved processes, and their often local nature, results in a rather poor understanding of the SBL in general (Mahrt 2014). An improved understanding of the SBL archetypes and their evolution is in particular hampered by the lack of available vertical profile observations of temperature, humidity and wind speed at an appropriate vertical resolution and at high enough sampling rates, as these variables may vary strongly in time and space.

In the WSBL, turbulence can be properly scaled following the local scaling hypothesis proposed by Nieuwstadt (1984), an extension of the original MOST. For the VSBL, classical scaling relations break down and a comprehensive theory is virtually absent. Previous studies successfully applied gradient-based scaling as a function of the gradient Richardson number, Ri (Sorbjan and Grachev 2010; Sorbjan 2010). This method is formally equivalent to MOST, but does not suffer from poorly defined scaling parameters (i.e., fluxes that are particularly difficult to measure in the VSBL) and it is also not affected by self-correlation (Sorbjan and Grachev 2010).

Further insights into the SBL are crucial for further progress in climate modelling and NWP (Holtslag et al. 2013). Atmospheric circulation models tend to require more drag at the surface than can be justified from local field observations on drag due to vertical shear (Beare 2007; Svensson and Holtslag 2009). This may be due to differences between processes captured by local observations and those acting on the scale of a grid cell, in particular over complex terrain with additional drag resulting from horizontal shear (Goger et al. 2018) or gravity waves (Steeneveld et al. 2008). Without the enhanced drag, the predicted weather systems are typically too persistent. Hence, climate and NWP models have utilized a so-called enhanced mixing approach (Louis 1979)

9

for decades. This approach comes, however, at the cost of the representation of the SBL that is often too warm near the surface, too deep, and the modelled LLJ are often "diluted". This has large consequences for applications such as air quality modelling (Fernando and Weil 2010), road state forecasting (Karsisto et al. 2017), wind energy production (Heppelmann et al. 2017) and visibility forecasts for aviation (Román-Cascón et al. 2019). In climate models, enhanced mixing may result in a positive surface temperature bias (Holtslag et al. 2013), increasing the upwelling longwave radiation (temperature feedback) and decreasing the reflected shortwave radiation through enhanced snow and ice melt (albedo feedback). To overcome the shortcomings of the enhanced mixing approach without impacting the model performance on larger scales, future SBL parameterizations would have to take into account all sources of mechanical drag, for which detailed observations are essential.

A number of earlier field campaigns have been dedicated to SBL studies, either over mid-latitude grass fields, such as CASES-99 in Kansas (Poulos et al. 2002) and SABLES 98 in Spain (Cuxart et al. 2000); in hilly terrain with a focus on mountain weather, such as MATERHORN in Utah (Fernando et al. 2015); or in polar regions such as SHEBA in the Arctic Ocean (Uttal et al. 2002). These studies provided a wealth of observational data and their analysis offered highly valuable insights into SBL behavior. All these campaigns were, however, limited by their in-situ measurements being from rather low meteorological masts and with supporting atmospheric profiling, e.g., by radiosondes, having rather poor temporal resolution. The availability of new instruments, observation techniques and measurement platforms for probing the SBL, UAS in particular, now offers unique and unrivaled opportunities for a new generation of polar SBL observations (Kral et al. 2018).

The application of unmanned, at that time remotely controlled, aircraft for atmospheric research, started at the end of the 1960s. Konrad et al. (1970) used a commercially available hobby model

10

airplane with a wingspan of around 2.5 m to measure profiles of temperature and humidity up to 3 km above ground. About two decades later, more systematic attempts for atmospheric investigations were conducted, mainly based on relatively large military drones modified for scientific applications (Langford and Emanuel 1993; Stephens et al. 2000). A breakthrough on the path towards smaller and more cost-efficient systems was the Aerosonde, with a wingspan of 2.9 m, an overall take-off weight of 15 kg, and about 5 kg of scientific payload capacity (Holland et al. 2001).

A rapid development of small airframes, autopilots and meteorological sensors from around 2000 is the direct result of the substantial progress in micro-electronics and component miniaturization. One of the pioneering attempts was the still remotely-controlled system Kali that performed more than 150 flights in Nepal and Bolivia to investigate thermally driven flows in the Himalayas and the Andes (Egger et al. 2002, 2005). During the following decade, a number of different research groups developed small meteorological UAS systems with the aim of providing reasonably priced airborne sensing capabilities for boundary layer research. Some of the most prominent examples are SUMO (Small Unmanned Meteorological Observer, Reuder et al. 2009), M^{2}AV (Meteorolocial Mini Aerial Vehicle, Spiess et al. 2007), MASC (Multi-purpose Airborne Sensor Carrier, Wildmann et al. 2014), Smartsonde (Chilson et al. 2009; Bonin et al. 2013), and Pilatus (de Boer et al. 2015). A comprehensive overview of small UAS for atmospheric research can be found in Elston et al. (2015).

Many ABL campaigns have relied on UAS based data sampling (e.g., Houston et al. 2012; Reuder et al. 2012b; Bonin et al. 2013; Lothon et al. 2014; Reuder et al. 2016; de Boer et al. 2019). Several of the aforementioned systems have also been operated successfully in polar environments and provided unique profiles of basic meteorological parameters that have been used for process studies (Curry et al. 2004; Cassano et al. 2010; Cassano 2013; Knuth and Cassano 2014; Jonassen et al. 2015; de Boer et al. 2018), meso-scale model validation (Mayer et al. 2012b,c)

11

and the evaluation of the benefit of UAS data assimilation (Jonassen et al. 2012; Sun et al. 2020). However, as fixed-wing systems, they have shortcomings and limitations with respect to accurate measurements in the stable surface layer close to the ground. Rotary-wing multi-copter systems, with their ability to hover and to slowly ascend and descend vertically, have here clear advantages (Neumann and Bartholmai 2015; Palomaki et al. 2017; Wrenger and Cuxart 2017; Bell et al. 2020; Segales et al. 2020).

On the basis of previous field campaigns, it is evident that the SBL is often highly heterogeneous over a variety of horizontal scales (e.g., Martínez et al. 2010; Cuxart et al. 2016). Hence, we have to question the classical assumption that sampling over time at one point is equivalent to sampling instantly in space. Accordingly, there is a need for the use of mobile sensor platforms, allowing for observations over a broad range of spatial scales. In ISOBAR we respond to this need by operating a variety of UAS with different capabilities, supported by point and profile observations.

The ISOBAR17 and ISOBAR18 field campaigns

As an integral part of the ISOBAR project, we carried out two field campaigns over the sea ice of the northern Baltic Sea close to the Finnish island Hailuoto in February 2017 and 2018 (see Table 1 for a list of all participants). Hailuoto is located in the Bothnian Bay, the northernmost part of the Baltic Sea, about 20 km west of the city of Oulu (Figure 1). It covers roughly 200 km^2, with its highest point reaching only about 20 m asl. Our field site was located at 65.037°N and 24.555°E, just off-shore of Hailuoto Marjaniemi, the westernmost point of the island, which is also the location of a WMO weather station, operated by the Finnish Meteorological Institute (FMI). Besides the solid sea ice conditions that can be expected for the Bothnian Bay in February (Uotila et al. 2015), the daylight periods are still relatively short, favoring the VSBL development. In addition, this field site provided a solid infrastructure, easy access and the Finnish air traffic

12

regulations allowed for an unbureaucratic flight permission process that enabled very flexible and science-driven UAS operations during the two campaigns.

The observational setup largely relied on micrometeorological masts installed on the sea ice, a few hundred meters southwest of the FMI weather station (Figure 1). In 2017 we installed a 4-m mast on the sea ice, equipped with one eddy-covariance (EC) system, three levels of slow-response instrumentation, net radiation and its components (upward and downward for both solar shortwave and thermal longwave radiation), and two ground heat flux sensors. This setup was extended in 2018 by erecting a 10-m mast (referred to as GFI2), equipped with the same set of sensors and two additional EC systems. An additional 2-m mast (GFI1), consisting of an EC system and a net radiometer, was placed about 65 m to the north-northwest of the 10-m mast. The nearby WMO station provides observations of temperature, humidity, pressure, cloud base height, cloud fraction, visibility, and precipitation every 10 min at the height of 2 m agl and observations of wind speed, direction and sonic temperature at the height of 46 m asl. Details on station location, sensor placement and specifications for the two campaigns and the different automatic weather stations are summarized in Table 2.

For continuous observations of the vertical wind profile and the turbulent structure of the lower atmosphere, we deployed a number of different ABL remote sensing systems: a vertically point-ing 1D LATAN-3M sodar in 2017 and 2018 (Kouznetsov 2009; Kral et al. 2018), a Leosphere WindCube 100S (WC100s) scanning wind lidar in 2017 (Kumer et al. 2014; Kral et al. 2018), a 3D Scintec MFAS phased array sodar in 2018, and a 3D Leosphere WindCube v1 (WCv1) doppler wind lidar in 2018 (Kumer et al. 2014, 2016). Table 3 provides an overview of the specifications of these systems and the observed variables.

Complementing the observations from the stationary systems, we made intensive use of a number of meteorological UAS, in order to sample profiles of the most important thermodynamic and

13

dynamic properties of the ABL and the lower free atmosphere. A summary of the different UAS and their specifications with corresponding references is given in Table 4 and Figure 2. The three UAS shown in Figure 2 but not listed in Table 4 were still at an experimental stage and their data were not shown in this article.

For atmospheric profiles of temperature, humidity and wind up to 1800 m (just below flight level 65, our altitude operation limit defined by the aviation authorities) we used the fixed-wing system SUMO, with repeated profiles every 3 h to 4 h during intensive observational periods (IOPs). Multi-copter profiles based on the Bebop2Met (abbreviated B2M), Q13 and CopterSonde (CS) were carried out roughly every 15 min to 30 min during IOPs to gain profiles of the lowermost 200 m to 300 m at high vertical resolution. To capture prevailing strong gradients within the SBL, we operated the multi-copters at fairly low climb rates between $0.5\,\mathrm{m\,s^{-1}}$ and $1\,\mathrm{m\,s^{-1}}$. The second fixed-wing UAS, MASC-2/3, measured turbulence properties along horizontal straight legs at fixed altitudes between 10 m and 425 m, vertically separated by 10 m to 25 m. An overview of the different IOPs, including a basic description of the observed conditions and the number of performed UAS flights is given in Table 5.

Post-processing including thorough quality checks resulted in two extensive datasets on the SBL over sea-ice. The overall data availability (see Figure 3 for an overview for the different systems) was significantly improved for ISOBAR18 compared to the previous year. UAS data availability during the first days of the campaigns is very limited since the preparation of the UAS was started after the installation of most ground-based systems was finished. The UOWL team operating the Q13 UAS could not participate for the full campaign period and decided to focus on the last week of ISOBAR17 and the last two weeks of ISOBAR18. In addition, the Bebop2Met (in 2017) and the CopterSonde (in 2018) were operated for the first time during a scientific campaign and required extensive preparation, resulting in limited data availability from these UAS during approximately

14

the first week of the corresponding campaign. Furthermore, icing on the inside of the WindCube 100S lense (in 2017) and the late arrival of the WindCube v1 (in 2018) caused the major data gaps in the remotely sensed wind profiles.

Meteorological and sea ice conditions

ISOBAR17 was exposed to varying weather conditions (Figure 4a). Around the start of the campaign, a large high pressure pattern strengthened over Finland, resulting in a few days with clear skies and cold temperatures. From mid February and onward, several low pressure systems passed Scandinavia and Finland, causing high variations in wind speed and direction. From 24 February on, the Bothnian Bay was again under the influence of high pressure, creating favorable conditions for SBL development. Relatively, the temperature was mostly mild, with only few days below $-10\,°C$. Consistent with the mild weather, the sea ice extent of the Baltic sea in February 2017 was considerably smaller than usual (compared to a reference period of 2006-2018, not shown). The sea ice concentration in the Bothnian Bay grew rapidly from 5-12 February (Figure 4b, c) during the relatively cold period associated with the high pressure system in the beginning of the campaign. From mid February, the large-scale flow packed the ice towards the northeast of the Bothnian Bay, resulting in a local minimum in the sea ice concentration on 18 February (Figure 4d). Afterwards, the sea ice concentration gradually increased until the end of the month (Figure 4e).

In contrast to the varying synoptic conditions the year before, the weather during ISOBAR18 was dominated by high pressure (Figure 4f). In February 2018 temperatures were low, winds were relatively weak and mostly from the north and there were many days with clear skies. An exception to these meteorological conditions occurred during the passage of a low pressure system from the North Sea toward northern Sweden and Finland around 8-16 February, resulting in strong southerly

15

319 winds and temperatures up to 0 °C. Before and after this period, daily mean temperatures were

320 typically below −10 °C and the wind speed was mostly low to moderate. The high pressure blocking

321 situation during ISOBAR18 is consistent with a colder sea ice season compared to ISOBAR17, with

322 gradually increasing sea ice concentration and thickness during the cold periods of 1-8 February

323 (Figure 4g, h) and 15-23 February (Figure 4i, j). The Bothnian Bay was more or less ice covered

324 throughout the ISOBAR18 campaign.

325 Overall, the sea ice conditions and weather situation were more favorable for the formation

326 of VSBL during ISOBAR18. An overview of the large-scale and corresponding boundary-layer

327 conditions during the 14 IOPs is provided in Table 5.

328 **Synthesis of UAS and ground-based in-situ and remote sensing observations**

329 The two ISOBAR field campaigns comprised a variety of observation systems, thus the synthesis

330 of observations on the basic meteorological parameters, such as wind speed, direction, temperature

331 and humidity, required carefully designed post-processing procedures. In particular the UAS

332 data underwent procedures for sensor calibration, reprocessing of altitude data based on observed

333 pressure and air temperature instead of assuming a standard atmosphere lapse rate, response time

334 correction (UAS thermodynamic parameters) and QA/QC procedures, especially for the wind

335 estimation algorithms. Excellent examples for the quality of this synthesis are the profiles from

336 1510 to 1530 UTC 20 February 2018 when all four profiling UAS (SUMO, B2M, CS2 and Q13)

337 were operated quasi-simultaneously together with the ground-based observations from GFI2, FMI,

338 MFAS and WCv1. The resulting profiles in Figure 5, reveal a very good agreement between the

339 different systems. All UASs and the 10-m mast sample a well-mixed layer up to ∼ 100 m topped by

340 a sharp inversion. The observed wind speed profiles also agree very well with light winds below

341 $2\,\mathrm{m\,s^{-1}}$ in the lowermost 60 m and increasing wind speeds up to $4\,\mathrm{m\,s^{-1}}$ to $5\,\mathrm{m\,s^{-1}}$, peaking at about

16

200 m. CopterSonde, lidar (WCv1) and sodar (MFAS) show slightly higher wind speeds at this level with the CopterSonde indicating this being related to a LLJ. The SUMO did not reproduce the same peak wind speed at this level, as its wind estimation algorithm (Mayer et al. 2012a) takes data over one full circular flight track into account, which results in a smoother wind profile. Furthermore, the presented wind speed profiles from MFAS and WCv1 represent 30-min averages, whereas UAS profiles are based on quasi-instantaneous observations.

Science highlights

SBL evolution

During IOP-14, 1615 to 2030 UTC 23 February 2018, UAS based atmospheric profiling with high temporal resolution gives detailed insight into the temporal evolution of the SBL at a spatial resolution on the order of 1 m. This allows for the direct capture of a considerable portion of the turbulent fluctuations, in particular at higher levels, as the size of turbulent eddies is expected to increase with height. Hailuoto was located at the south-eastern flank close to the centre of the high pressure system and under the influence of weak northeasterly flow (Table 5). Clear-sky conditions favored the development of an SBL, transitioning between the weakly stable and very stable regime. Temperature profiles from the three UAS operated during this IOP, i.e., SUMO, B2M and Q13, indicate an overall cooling of the ABL associated with strengthening of the surface-based inversion and increase in inversion depth (Figure 6a). The corresponding near-surface temperature observations (Figure 6b) confirm the trend of surface cooling and intensification of the inversion, which is initiated by long-wave radiative cooling after sunset. Various UAS profiles indicate remarkable, fine-scale structures of thermal instabilities in layers between the surface and approximately 70 m. In particular, the profiles at 1718, 1741 and 1819 UTC consistently

17

resemble these features. At the same time, we observe a series of rapid temperature changes, most pronounced at the 0.6-m and 2.0-m levels. During the cold episodes, the near-surface wind directions change from about 60° to 10° and exhibit a signature of wind veer resembling an Ekman spiral (Figure 6b). The observed shift in wind direction occurs, however, on time scales much shorter than expected from pure Ekman adjustment, indicating the importance of local advective processes. With the geostrophic wind shifting gradually from roughly 60° to 100°, this results in a surface angle of at least 50°. Note that NWP models in GABLS1 show roughly a surface angle of 30° (Svensson and Holtslag 2009), while theory of Nieuwstadt (1985) predicts 60°. The period from about 1815 until 2000 UTC is characterized by a strong surface inversion and meandering of the flow can be observed at all levels up to 46 m. The second weather station on the sea ice (GFI-1, not shown) recorded a very similar temperature and wind signal, however, the changes occur a couple of minutes earlier and the cold periods last longer. Based on these observations, we conclude that these events are related to the passage of microfronts (i.e., the advection of airmasses with different properties). The measured wind direction suggests the warmer airmass being modified by the presence of land, whereas the colder air originates from a rather clean sea-ice fetch. The observed fine-scale instabilities in the vertical profiles lead us to the hypothesis that these microfronts are rather irregular in their shape, potentially triggered by directional shear.

Disentangling the complexity of the SBL

During IOP-10, 18-19 February 2018, ground-based in-situ and remote sensing systems alongside UAS captured a variety of SBL phenomena during two major periods with very stable stratification, the first of which was from 1330 to 1615 UTC while the second was from about 1930 to 0040 UTC. The large-scale situation was characterized by a high pressure system forming in the Barents Sea and associated weak pressure gradients at its southeastern flank, but varying cloud cover (Table 5).

18

The start of these periods correspond well with strongly negative net-radiation (indicated as colored shading at the top of Figure 7a), due to clear sky conditions. The temperatures observed at GFI2 (10-m mast on the sea ice) and FMI (permanent 46-m tower) reveal strong vertical gradients during the VSBL cases and are subject to rapid variations, especially at the 4.5-m and 6.9-m levels. The LATAN-3M sodar echogram indicates a surface-based turbulent layer extending to a maximum altitude of roughly 100 m, but frequently as shallow as 20 m (or even lower) and with occasional elevated turbulent layers above (Figure 7c). The wind profile above the ABL is fairly constant with a weak flow from east-northeast (wind barbs in Figure 7d). Within the ABL, the wind profile is, however, influenced by a variety of processes (e.g., LLJ or submeso motions) resulting in strong variability in both wind direction and magnitude (Figure 7b). In general, IOP-10 was characterized by near-calm conditions, with 31 % (63 %) of the 10 min averaged 2-m wind speed below $0.5\,\mathrm{m\,s^{-1}}(1.0\,\mathrm{m\,s^{-1}})$, which makes the SBL susceptible to sporadic mixing events generated by wave-like and other submeso motions (Mahrt 2011). In the following paragraphs we will highlight some of the observations during the subintervals I–III. The complexity of these cases (i.e., non-linear interactions between a variety of different scales, including turbulent and non-turbulent motions) is likely to cause severe problems not only in state-of-the-art NWP but also in other atmospheric research models (e.g., Fernando and Weil 2010; Sun et al. 2015).

IOP-10/I, intensification and collapse of the LLJ

The first VSBL-interval is initiated by a rapid temperature drop close to the surface of 2 K within 20 s to 30 s (Figure 8a), accompanied by a reduction in wind speed (Figure 8b) and a wind direction shift of 180° from north to south (Figure 8c). During the following minutes (until ca. 1400 UTC) the near-surface winds almost completely calm down, thus increasing the dynamic stability, while the flow at elevated layers around 100 m slightly accelerates and forms a weak LLJ. All three EC

19

systems of GFI2 show weak intermittent turbulence during this period (see w' in Figure 8d and

$\overline{w'T'}$ in Figure 8e). Nevertheless, the lowest layers remain at a rather constant temperature; the

reason for this is not quite clear. Our mast observations, however, show small-scale oscillations in

wind speed and direction at the three lowest levels, which seem rather independent of each other.

Occasionally, the local wind and directional shear might be large enough to trigger small-scale

mixing events.

At about 1535 UTC, the 10-m wind speed accelerates to about $2 \, \mathrm{m \, s^{-1}}$ triggering a strong

intermittent event, which also influences the two EC levels below, although to a weaker extent.

Investigating the evolution of the vertical wind profile (Figure 8g) based on WCv1 lidar and 10-m

mast data, suggests that the acceleration of the 10-m wind is related to an increase in wind shear

due to the intensification and lowering of the LLJ; eventually this causes a shear instability. The

sodar echogram (Figure 7c) supports this interpretation, as it indicates an elevated weak turbulent

layer merging with lower levels around 1440 UTC, followed by an increase in turbulence below

80 m and the lowering of the elevated inversion layer (Figure 8f). After this event, the wind speed

profiles take a more logarithmic shape again. The vertical temperature profiles in Figure 8f also

feature a shift from a very shallow and strong surface-based and an additional elevated inversion to

a more logarithmic profile after this event. A reduction in radiative cooling due to increased cloud

cover initiates the end of this VSBL-period.

IOP-10/II, near-surface wave instability

During IOP-10 the instrumentation on the 10-m mast recorded a series of amplifying temperature

oscillations, most pronounced at 4.5 m, 6.9 m and 10.3 m (Figure 9a). At 2234 UTC this oscillation

results in an remarkable cooling of the 10.3-m temperature, dropping by 4 K within approximately

1 min. Associated with this main cooling event is a temporary shift to neutral static stability

20

and enhanced near surface turbulence (Figure 9b). The near-surface stability before this event was characterized by a sharp temperature gradient, $\Delta T_{10m\text{-}0.6m} \approx 4.5\,\mathrm{K}$ and weak winds at about $1\,\mathrm{m\,s^{-1}}$, meandering between south-southwest and north-northeast (Figure 9a). The three sonic anemometers of GFI2 sampled very weak to intermittent turbulence (Figure 9b), whereas the remote sensing systems (e.g., 45-m and 85-m lidar levels in Figure 9b) indicate some wave activity aloft (see also Figure 7b). The signature of this wave can also be detected in the 10-m vertical velocity data.

From 2232 UTC the wind at the lowermost levels shifts to a northerly direction, whereas at 10 m it stays south-southeast for two more minutes. This results in enhanced local shear as shown in Figure 9c, while the bulk shear is still fairly weak. At the same time, the amplitude of the wave starts to grow rapidly, causing an upward transport of cold, near-surface air at the wave crest at 2233 UTC. This is also associated with a shift to near-neutral stratification as reflected in the substantial drop in the gradient Richardson number (Figure 9d). During the next wave trough, the static stability becomes stable again but the directional shear remains. The following wave crest results in the aforementioned strong elevated cooling event, contributing to further destabilisation of the surface layer (Figure 9d) and the breaking of the wave at 2234 UTC. This wave instability causes enhanced turbulence and a uniform northerly wind direction at all observation levels of the 10-m mast. Also the gradient and bulk Richardson numbers drop to values between 0 and 0.25. The following period is characterized by weak but increasing stability with continuous turbulence. Some weaker wave activity remains clearly visible in our observations.

Although the origin of the process leading to the shift in wind direction near the surface and the resulting enhanced directional wind shear remains unclear, this case nicely illustrates the importance of local wind shear for triggering the instability of near-surface wave.

21

The LATAN-3M sodar recorded a very clear and strong harmonic signal starting at 0010 UTC (Figure 10f) between 100 m and 200 m, which resulted in a major instability at 0037 UTC. Near the surface, the turbulence was enhanced substantially, as observed by the EC systems at 2.0 m, 4.5 m and 10.3 m (Figure 10d, e). The harmonic oscillations with a period of about 4 min can also be observed in the horizontal and vertical velocity components (Figure 10b and d) of the WCv1 and the 10-m mast. The oscillations in horizontal and vertical velocity are 180° out of phase, consistent with internal gravity waves (Sun et al. 2015).

The preceding period is at first characterized by a strong, surface-based inversion (Figure 10a) topping out at about 100 m with light, meandering winds roughly from southeast (Figure 10b and c), occasionally showing the signature of wind veer resembling an Ekman spiral (e.g., as seen around 2310 UTC). The turbulence detected by the three sonic anemometers is very weak and of intermittent character. Between 2340 and 2350 UTC the wind direction shifts to a rather northerly direction at all levels below 200 m (see also Figure 7d) and the wind speeds drop. The upper level winds, at heights between 46 m and 85 m, accelerate gently until the wave breaks at 0037 UTC.

For an in-depth analysis, the UAS temperature and lidar wind speed profiles sampled at 2342, 0009 and 0030 UTC (mean UAS flight time) offer further insight in the dynamics of this event (Figure 11a). These profiles indicate some cooling above 50 m, whereas wind speeds increase below 75 m and decrease above this level, resulting in the formation of a LLJ as seen in the last profile. This corresponds to strong downward transport of momentum as seen in the time height diagram for wind speed (Figure 11c). Estimates of Ri for the three profiles (Figure 11b) indicate the formation of a dynamically weakly stable layer (Ri < 0.25) right below 150 m, between the time of the first and second profile, which then propagates downwards. This locally weakly stable

22

layer is largely related to the sharp wind speed gradients above the LLJ core. Just about 7 min after the last UAS profile, the wave breaks and strongly enhances the turbulence near the surface. The wavelet spectral energy estimate of the vertical wind component observed at 10 m (Figure 11d) indicates very weak turbulence before 0037 UTC. The wave-breaking event is characterized by a very strong signal with a period of about 3 min, which triggers a turbulence cascade to smaller scales. After 0100 UTC, the strong 3 min signal begins to vanish and the small-scale turbulence weakens again.

The wave breaking event ends at 0050 UTC and after this the wave appears to have higher frequency (Figure 10f). This is most likely due to the Doppler shift caused by the increasing wind speeds at the levels above 125 m (Figure 11c).

Summary and outlook

ISOBAR is an experimental research project targeting the SBL over Arctic sea ice by means of a novel observational approach based on a combination of ground-based in-situ and remote sensing instrumentation with multiple unmanned aircraft systems. Two major field campaigns, ISOBAR17 and ISOBAR18, were carried out at the Finnish island Hailuoto in the ice-covered Bothnian Bay, each lasting for about one month in February 2017 and 2018. These campaigns were characterized by contrasting conditions, with little sea ice and relatively mild temperatures in 2017, whereas conditions were closer to the climatological mean in 2018, favoring more frequent VSBL formation. With our observation strategy of extensive UAS-based measurements supplemented by surface-based mast and remote sensing observations, we have sampled comprehensive SBL datasets, including 14 IOPs; these datasets offer unprecedented spatiotemporal resolution, while also displaying good agreement between the different systems.

23

Frequent UAS profiles allow for detailed insight into the evolution of the SBL, which may be subject to rapid temperature changes affecting the entire ABL, and small-scale thermal instabilities within the otherwise stably stratified ABL. These data also allow for detailed studies on various VSBL processes and their interaction with near-surface turbulence, of which we highlight three examples, all observed during the same IOP: first, a shear instability caused by the lowering and intensification of the LLJ; second, an unusual rapid-cooling event at elevated levels around 10 m, which appears to be caused by the interaction of a near-surface wave with local shear and the modulation of the surface layer static stability associated with this non-linear wave; third, a wave instability related to the intensification of shear at the top of a forming LLJ, triggering enhanced turbulence near the surface. The nature and interactions of such VSBL processes, as well as the potential deviations from similarity theory associated with them, will be subject to more systematic studies also making use of other SBL datasets such as SHEBA (Grachev et al. 2008) or CASES-99 (Poulos et al. 2002).

Furthermore, the ISOBAR datasets provide an excellent opportunity to study the transition from WSBL to VSBL, which is important for a better understanding of the conditions leading to strong surface-based temperature inversions and associated extremely cold temperatures. In particular, we aim to investigate the relative importance of local and large-scale conditions. In a follow-up project, we aim to identify and classify the various mechanisms behind the generation of intermittency in the VSBL, based on the ISOBAR and other data sets. This classification should form the basis for a stochastic parameterization for intermittent turbulence in meso-scale NWP models. Additionally, the UAS profiles gathered during ISOBAR — with such unique spatiotemporal resolution — offer a new perspective for SBL studies by applying an alternative gradient-based scaling scheme (Sorbjan 2010). The application of this method allows the determination of vertical profiles of turbulent parameters, which could aid the development of new NWP parameterizations.

24

Initial numerical modelling experiments have confirmed that the structure of the VSBL is inadequately represented in state-of-the-art NWP and SCM. A complementary LES experiment showed that turbulence-resolving simulations are able to reproduce even very shallow stable layers and thus provide a powerful tool for studying turbulent processes in such conditions. In a next step we thus plan to perform an LES study to evaluate the gradient-based similarity relationships. In this way, we hope to develop a turbulence parameterization, to be implemented in both NWP and SCM models and finally to be evaluated against measurement data obtained during the IOP periods. Moreover, we strive to analyze LES data with respect to phenomena observed during the IOPs and to perform virtual flights in the LES model to evaluate and improve flight strategies for future UAS campaigns.

Sidebar: SBL model simulations

To illustrate current challenges in SBL modelling, three different types of numerical models were used to simulate the SBL evolution during IOP-14 (23-24 February 2018): the MetCoOp Ensemble Prediction System (MEPS), the Weather Research and Forecasting model in its single-column mode (WRF-SCM), and the large-eddy simulation (LES) model PALM. MEPS (Müller et al. 2017) is an operational NWP system covering the Nordic countries, forced at its boundaries by the global ECMWF-IFS (Bauer et al. 2013). There are 65 vertical model levels, with the first level at 12.5 m agl and decreasing vertical resolution aloft. Surface-atmosphere and surface-soil processes are described by the SURFEX model (Masson et al. 2013). WRF-SCM utilizes the full WRF physics (Skamarock et al. 2008), with Mellor–Yamada–Nakanishi–Niino turbulence parameterization (Nakanishi and Niino 2006), within an atmospheric column with 200 vertical levels. The vertical spacing is about 2 m in the lower atmosphere. Hourly geostrophic winds and advection of momentum, temperature and humidity are derived from a meso-scale WRF simulation

25

548 (Sterk et al. 2015). PALM (Maronga et al. 2015, 2020) runs at a grid spacing of 2 m and a model

549 domain of 500^3 m^3 using a standard configuration but with a modified Deardorff subgrid-scale

550 closure as described by Dai et al. (2020) and coupled to the Rapid Radiative Transfer Model

551 (Clough et al. 2005). PALM is initialized by the same vertical profiles as WRF-SCM and forced

552 by skin temperatures observed during IOP-14.

553 Figure 12 shows that even though all three models are capable of forming a very stable strati-

554 fication and cold air at the surface, the model results differ considerably. The formation of cold

555 air above the surface and the associated strong vertical (temperature) gradients are best captured

556 by PALM, while both MEPS and WRF-SCM display a deeper SBL with weaker gradients. At

557 heights between 50 m and 300 m, both WRF-SCM and PALM produce weaker temperature gra-

558 dients, which can be ascribed to deficiencies in the model initialization. MEPS here captures the

559 stratification much better. Overall, the three different models show substantial deviations from the

560 observations in the lower atmosphere.

561 Likely sources for these deviations are the turbulence parameterizations which overestimate

562 turbulent mixing and the associated downward heat flux from the atmosphere to the cold surface,

563 and the different boundary conditions and initial conditions applied. As PALM resolves most of

564 the turbulent transport, it can more adequately represent the SBL evolution close to the surface. It

565 is noteworthy that PALM and WRF-SCM, despite being initialized with the same profiles, produce

566 quite different SBLs. Research models like WRF-SCM and PALM are highly sensitive to the

567 initial profiles and boundary conditions, which are either derived from measurements or larger-

568 scale model data and thus come with an inherent uncertainty. All three models depend on accurate

569 surface properties, for which a combination of measurements and ad-hoc estimations was used

570 here. The differences present in these simulations epitomise the necessity for deeper understanding

571 of the SBL and its representation in atmospheric models; an understanding which is expedited

26

by unique, fine-scale observational datasets, such as ISOBAR. Sensitivities to model physics and surface properties during IOP-14 are subject of an ongoing study, following the process-based analysis by Sterk et al. (2016).

27

APPENDIX

List of Abbreviations

References

Atlaskin, E., and T. Vihma, 2012: Evaluation of NWP results for wintertime nocturnal boundary-layer temperatures over Europe and Finland. *Quart. J. Roy. Meteor. Soc.*, **138 (667)**, 1440–1451, doi:10.1002/qj.1885.

Bauer, P., and Coauthors, 2013: *Model Cycle 38r2: Components and Performance*. European Centre for Medium-Range Weather Forecasts.

Beare, R. J., 2007: Boundary layer mechanisms in extratropical cyclones. *Quart. J. Roy. Meteor. Soc.*, **133 (623)**, 503–515, doi:10.1002/qj.30.

Bell, T. M., B. R. Greene, P. M. Klein, M. Carney, and P. B. Chilson, 2020: Confronting the boundary layer data gap: evaluating new and existing methodologies of probing the lower atmosphere. *Atmos. Meas. Tech.*, **13 (7)**, 3855–3872, doi:10.5194/amt-13-3855-2020.

28

Bintanja, R., E. C. van der Linden, and W. Hazeleger, 2012: Boundary layer stability and Arctic climate change: A feedback study using EC-Earth. *Climate Dyn.*, **39 (11)**, 2659–2673, doi: 10.1007/s00382-011-1272-1.

Bonin, T., P. Chilson, B. Zielke, and E. Fedorovich, 2013: Observations of the early evening boundary-layer transition using a small unmanned aerial system. *Bound.-Layer Meteor.*, **146 (1)**, 119–132, doi:10.1007/s10546-012-9760-3.

Bosveld, F. C., and Coauthors, 2014: The third GABLS intercomparison case for evaluation studies of boundary-layer models. Part B: Results and process understanding. *Bound.-Layer Meteor.*, **152 (2)**, 157–187, doi:10.1007/s10546-014-9919-1.

Byrkjedal, Ø., I. Esau, and N. G. Kvamstø, 2007: Sensitivity of simulated wintertime Arctic atmosphere to vertical resolution in the ARPEGE/IFS model. *Climate Dyn.*, **30 (7-8)**, 687–701, doi:10.1007/s00382-007-0316-z.

Cassano, J. J., 2013: Observations of atmospheric boundary layer temperature profiles with a small unmanned aerial vehicle. *Antarct. Sci.*, **26 (02)**, 205–213.

Cassano, J. J., J. A. Maslanik, C. J. Zappa, A. L. Gordon, R. I. Cullather, and S. L. Knuth, 2010: Observations of Antarctic polynya with unmanned aircraft systems. *EOS, Trans., Amer. Geophys. Union*, **91 (28)**, 245, doi:10.1029/2010eo280001.

Chilson, P. B., and Coauthors, 2009: SMARTSonde: A small UAS platform to support radar research. *Proceedings of the 34th Conference on Radar Meteorology*, URL http://ams.confex. com/ams/34Radar/techprogram/paper_156396.htm.

Clough, S. A., M. W. Shephard, E. J. Mlawer, J. S. Delamere, M. J. Iacono, K. Cady-Pereira, S. Boukabara, and P. D. Brown, 2005: Atmospheric radiative transfer modeling: A summary

29

of the AER codes. *J. Quant. Spectrosc. Radiat. Transfer*, **91 (2)**, 233–244, doi:10.1016/j.jqsrt. 2004.05.058.

Curry, J. A., J. Maslanik, G. Holland, and J. Pinto, 2004: Applications of aerosondes in the arctic. *Bull. Amer. Meteor. Soc.*, **85 (12)**, 1855–1862, doi:10.1175/bams-85-12-1855.

Cuxart, J., and Coauthors, 2000: Stable atmospheric boundary-layer experiment in Spain (SABLES 98): A report. *Bound.-Layer Meteor.*, **96 (3)**, 337–370, doi:10.1023/a:1002609509707.

Cuxart, J., and Coauthors, 2005: Single-column model intercomparison for a stably strat- ified atmospheric boundary layer. *Bound.-Layer Meteor.*, **118 (2)**, 273–303, doi:10.1007/ s10546-005-3780-1.

Cuxart, J., and Coauthors, 2016: Estimation of the advection effects induced by surface het- erogeneities in the surface energy budget. *Atmos. Chem. Phys.*, **16 (14)**, 9489–9504, doi: 10.5194/acp-16-9489-2016.

Dai, A., D. Luo, M. Song, and J. Liu, 2019: Arctic amplification is caused by sea-ice loss under increasing CO2. *Nat. Commun.*, **10 (1)**, doi:10.1038/s41467-018-07954-9.

Dai, Y., S. Basu, B. Maronga, and S. R. de Roode, 2020: Addressing the grid-size sensitivity issue in large-eddy simulations of stable boundary layers. *Bound.-Layer Meteor.*, in review, 2003.09463v1.

Davy, R., and I. Esau, 2016: Differences in the efficacy of climate forcings explained by variations in atmospheric boundary layer depth. *Nat. Commun.*, **7 (1)**, 11 690, doi:10.1038/ncomms11690.

de Boer, G., and Coauthors, 2015: The Pilatus unmanned aircraft system for lower atmospheric research. *Atmos. Meas. Tech.*, **9**, 1845–1857, doi:10.5194/amtd-8-11987-2015.

30

de Boer, G., and Coauthors, 2018: A bird's-eye view: Development of an operational ARM unmanned aerial capability for atmospheric research in Arctic Alaska. *Bull. Amer. Meteor. Soc.*, **99 (6)**, 1197–1212, doi:10.1175/BAMS-D-17-0156.1, https://doi.org/10.1175/BAMS-D-17-0156.1.

de Boer, G., and Coauthors, 2019: Development of community, capabilities and understanding through unmanned aircraft-based atmospheric research: The LAPSE-RATE campaign. *Bull. Amer. Meteor. Soc.*, doi:10.1175/bams-d-19-0050.1.

de Wiel, B. J. H. V., and Coauthors, 2017: Regime transitions in near-surface temperature inversions: A conceptual model. *J. Atmos. Sci.*, **74 (4)**, 1057–1073, doi:10.1175/jas-d-16-0180.1.

Egger, J., and Coauthors, 2002: Diurnal winds in the Himalayan Kali Gandaki Valley. Part III: Remotely piloted aircraft soundings. *Mon. Wea. Rev.*, **130 (8)**, 2042–2058, doi:10.1175/1520-0493(2002)130<2042:DWITHK>2.0.CO;2.

Egger, J., and Coauthors, 2005: Diurnal circulation of the Bolivian altiplano. Part I: Observations. *Mon. Wea. Rev.*, **133 (4)**, 911–924, doi:10.1175/MWR2894.1.

Elston, J., B. Argrow, M. Stachura, D. Weibel, D. Lawrence, and D. Pope, 2015: Overview of small fixed-wing unmanned aircraft for meteorological sampling. *J. Atmos. Oceanic Technol.*, **32 (1)**, 97–115, doi:10.1175/JTECH-D-13-00236.1.

Fernando, H. J. S., and J. C. Weil, 2010: Whither the stable boundary layer? *Bull. Amer. Meteor. Soc.*, **91 (11)**, 1475–1484, doi:10.1175/2010BAMS2770.1, https://doi.org/10.1175/2010BAMS2770.1.

Fernando, H. J. S., and Coauthors, 2015: The MATERHORN: Unraveling the intricacies of mountain weather. *Bull. Amer. Meteor. Soc.*, **96 (11)**, 1945–1967, doi:10.1175/BAMS-D-13-00131.1.

31

Foken, T., 2006: 50 years of the Monin–Obukhov similarity theory. *Bound.-Layer Meteor.*, **119**, 431–447, doi:10.1007/s10546-006-9048-6.

Gentine, P., G.-J. Steeneveld, B. G. Heusinkveld, and A. A. Holtslag, 2018: Coupling between radiative flux divergence and turbulence near the surface. *Quart. J. Roy. Meteor. Soc.*, **144 (717)**, 2491–2507, doi:10.1002/qj.3333.

Goger, B., M. W. Rotach, A. Gohm, O. Fuhrer, I. Stiperski, and A. A. M. Holtslag, 2018: The impact of three-dimensional effects on the simulation of turbulence kinetic energy in a major Alpine valley. *Bound.-Layer Meteor.*, **168 (1)**, 1–27, doi:10.1007/s10546-018-0341-y.

Grachev, A. A., E. L. Andreas, C. W. Fairall, P. S. Guest, and P. O. G. Persson, 2008: Turbulent measurements in the stable atmospheric boundary layer during SHEBA: Ten years after. *Acta Geophys.*, **56 (1)**, 142–166, doi:10.2478/s11600-007-0048-9.

Grachev, A. A., E. L. Andreas, C. W. Fairall, P. S. Guest, and P. O. G. Persson, 2013: The critical richardson number and limits of applicability of local similarity theory in the stable boundary layer. *Bound.-Layer Meteor.*, **147 (1)**, 51–82, doi:10.1007/s10546-012-9771-0.

Graham, R. M., and Coauthors, 2019: Evaluation of six atmospheric reanalyses over Arctic sea ice from winter to early summer. *J. Climate*, **32 (14)**, 4121–4143, doi:10.1175/jcli-d-18-0643.1.

Greene, B., A. Segales, T. Bell, E. Pillar-Little, and P. Chilson, 2019: Environmental and sensor integration influences on temperature measurements by rotary-wing unmanned aircraft systems. *Sensors*, **19 (6)**, 1470, doi:10.3390/s19061470.

Heppelmann, T., A. Steiner, and S. Vogt, 2017: Application of numerical weather prediction in wind power forecasting: Assessment of the diurnal cycle. *Meteorol. Z.*, **26 (3)**, 319–331, doi:10.1127/metz/2017/0820.

Hersbach, H., and Coauthors, 2020: The ERA5 global reanalysis. *Quart. J. Roy. Meteor. Soc.*, doi:10.1002/qj.3803.

Hoch, S. W., P. Calanca, R. Philipona, and A. Ohmura, 2007: Year-round observation of longwave radiative flux divergence in Greenland. *J. Appl. Meteor. Climatol.*, **46 (9)**, 1469–1479, doi: 10.1175/JAM2542.1.

Holland, G. J., and Coauthors, 2001: The Aerosonde Robotic Aircraft: A new paradigm for environmental observations. *Bull. Amer. Meteor. Soc.*, **82 (5)**, 889–901, doi:10.1175/1520-0477(2001) 082<0889:TARAAN>2.3.CO;2.

Holtslag, A., and Coauthors, 2013: Stable atmospheric boundary layers and diurnal cycles – challenges for weather and climate models. *Bull. Amer. Meteor. Soc.*, **94 (11)**, 1691–1706, doi:10.1175/BAMS-D-11-00187.1.

Houston, A. L., B. Argrow, J. Elston, J. Lahowetz, E. W. Frew, and P. C. Kennedy, 2012: The collaborative Colorado–Nebraska unmanned aircraft system experiment. *Bull. Amer. Meteor. Soc.*, **93 (1)**, 39–54, doi:10.1175/2011bams3073.1.

Jakobson, E., T. Vihma, T. Palo, L. Jakobson, H. Keernik, and J. Jaagus, 2012: Validation of atmospheric reanalyses over the central Arctic Ocean. *Geophys. Res. Lett.*, **39 (10)**, n/a–n/a, doi:10.1029/2012gl051591.

Jonassen, M., P. Tisler, B. Altstädter, A. Scholtz, T. Vihma, A. Lampert, G. König-Langlo, and C. Lüpkes, 2015: Application of remotely piloted aircraft systems in observing the atmospheric boundary layer over Antarctic sea ice in winter. *Polar Res.*, **34 (0)**, doi:10.3402/polar.v34.25651.

33

Jonassen, M. O., H. Ólafsson, H. Ágústsson, O. Rögnvaldsson, and J. Reuder, 2012: Improving high-resolution numerical weather simulations by assimilating data from an unmanned aerial system. *Mon. Wea. Rev.*, **140 (11)**, 3734–3756, doi:10.1175/MWR-D-11-00344.1.

Jonassen, M. O., I. Välisuo, T. Vihma, P. Uotila, A. P. Makshtas, and J. Launiainen, 2019: Assessment of atmospheric reanalyses with independent observations in the Weddell Sea, the Antarctic. *J. Geophys. Res.: Atmos.*, doi:10.1029/2019jd030897.

Karsisto, V., S. Tijm, and P. Nurmi, 2017: Comparing the performance of two road weather models in the Netherlands. *Wea. Forecasting*, **32 (3)**, 991–1006, doi:10.1175/WAF-D-16-0158.1.

Knuth, S. L., and J. J. Cassano, 2014: Estimating sensible and latent heat fluxes using the integral method from in situ aircraft measurements. *J. Atmos. Oceanic Technol.*, **31 (9)**, 1964–1981, doi:10.1175/JTECH-D-14-00008.1, http://dx.doi.org/10.1175/JTECH-D-14-00008.1.

Konrad, T. G., M. L. Hill, J. R. Rowland, and J. H. Meyer, 1970: A small, radio-controlled aircraft as a platform for meteorological sensor. *APL Technical Digest*, **10**, 11–19, 19710054637.

Kouznetsov, R. D., 2009: The multi-frequency sodar with high temporal resolution. *Meteorol. Z.*, **18 (2)**, 169–173, doi:10.1127/0941-2948/2009/0373.

Kral, S., and Coauthors, 2018: Innovative strategies for observations in the arctic atmospheric boundary layer (ISOBAR)—the Hailuoto 2017 campaign. *Atmosphere*, **9 (7)**, 268, doi:10.3390/atmos9070268.

Kumer, V.-M., J. Reuder, M. Dorninger, R. Zauner, and V. Grubišić, 2016: Turbulent kinetic energy estimates from profiling wind LiDAR measurements and their potential for wind energy applications. *Renewable Energy*, **99**, 898–910, doi:10.1016/j.renene.2016.07.014.

34

Kumer, V.-M., J. Reuder, and B. R. Furevik, 2014: A comparison of LiDAR and radiosonde wind measurements. *Energy Procedia*, **53**, 214–220, doi:10.1016/j.egypro.2014.07.230.

Langford, J. S., and K. A. Emanuel, 1993: An unmanned aircraft for dropwindsonde deployment and hurricane reconnaissance. *Bull. Amer. Meteor. Soc.*, **74 (3)**, 367–375, doi: 10.1175/1520-0477(1993)074<0367:AUAFDD>2.0.CO;2.

Lapworth, A., and S. R. Osborne, 2019: Gravity-wave drag in the stable boundary layer over moderate terrain. *Bound.-Layer Meteor.*, **171 (2)**, 175–189, doi:10.1007/s10546-018-00422-3.

Lesins, G., T. J. Duck, and J. R. Drummond, 2012: Surface energy balance framework for Arctic amplification of climate change. *J. Climate*, **25 (23)**, 8277–8288, doi:10.1175/JCLI-D-11-00711. 1.

Lothon, M., and Coauthors, 2014: The BLLAST field experiment: Boundary-layer late afternoon and sunset turbulence. *Atmos. Chem. Phys.*, **14 (20)**, 10 931–10 960, doi:10.5194/ acp-14-10931-2014.

Louis, J.-F., 1979: A parametric model of vertical eddy fluxes in the atmosphere. *Bound.-Layer Meteor.*, **17 (2)**, 187–202, doi:10.1007/BF00117978.

Mahrt, L., 2003: BOUNDARY LAYERS | stably stratified boundary layer. *Encyclopedia of Atmospheric Sciences*, Elsevier, 298–305, doi:10.1016/b0-12-227090-8/00091-9.

Mahrt, L., 2011: The near-calm stable boundary layer. *Bound.-Layer Meteor.*, **140 (3)**, 343–360, doi:10.1007/s10546-011-9616-2.

Mahrt, L., 2014: Stably stratified atmospheric boundary layers. *Annu. Rev. Fluid Mech.*, **46**, 23–45, doi:10.1146/annurev-fluid-010313-141354.

35

Maronga, B., and Coauthors, 2015: The Parallelized Large-Eddy Simulation Model (PALM) version 4.0 for atmospheric and oceanic flows: Model formulation, recent developments, and future perspectives. *Geosci. Model Dev.*, **8 (8)**, 2515–2551, doi:10.5194/gmd-8-2515-2015.

Maronga, B., and Coauthors, 2020: Overview of the PALM model system 6.0. *Geosci. Model. Dev.*, **13**, 1335–1372, doi:10.5194/gmd-13-1335-2020.

Martínez, D., M. A. Jiménez, J. Cuxart, and L. Mahrt, 2010: Heterogeneous nocturnal cooling in a large basin under very stable conditions. *Bound.-Layer Meteor.*, **137 (1)**, 97–113, doi: 10.1007/s10546-010-9522-z.

Masson, V., and Coauthors, 2013: The SURFEXv7.2 land and ocean surface platform for coupled or offline simulation of earth surface variables and fluxes. *Geoscientific Model Development*, **6 (4)**, 929–960, doi:10.5194/gmd-6-929-2013.

Mayer, S., G. Hattenberger, P. Brisset, M. Jonassen, and J. Reuder, 2012a: A 'no-flow-sensor' wind estimation algorithm for unmanned aerial systems. *International Journal of Micro Air Vehicles*, **4 (1)**, 15–30, doi:10.1260/1756-8293.4.1.15.

Mayer, S., M. Jonassen, A. Sandvik, and J. Reuder, 2012b: Profiling the Arctic stable boundary layer in Advent Valley, Svalbard: Measurements and simulations. *Bound.-Layer Meteor.*, **143 (3)**, 507–526, doi:10.1007/s10546-012-9709-6.

Mayer, S., A. Sandvik, M. Jonassen, and J. Reuder, 2012c: Atmospheric profiling with the UAS SUMO: a new perspective for the evaluation of fine-scale atmospheric models. *Meteorol. Atmos. Phys.*, **116 (1-2)**, 15–26, doi:10.1007/s00703-010-0063-2.

36

McNider, R. T., J. R. Christy, and A. Biazar, 2010: A stable boundary layer perspective on global temperature trends. *IOP Conference Series: Earth and Environmental Science*, **13 (1)**, 012 003, doi:10.1088/1755-1315/13/1/012003.

Monin, A. S., and A. M. Obukhov, 1954: Osnovnye zakonomernosti turbulentnogo peremeshivanija v prizemnom sloe atmosfery (Basic laws of turbulent mixing in the atmosphere near the ground). *TRUDY GEOFIZ. INST. AKAD. NAUK SSSR*, **24 (151)**, 163–187.

Müller, M., and Coauthors, 2017: AROME-MetCoOp: A Nordic convective-scale operational weather prediction model. *Wea. Forecasting*, **32 (2)**, 609–627.

Nakanishi, M., and H. Niino, 2006: An improved Mellor–Yamada level-3 model: Its numerical stability and application to a regional prediction of advection fog. *Bound.-Layer Meteor.*, **119 (2)**, 397–407, doi:10.1007/s10546-005-9030-8.

Nappo, C., 2012: *An Introduction to Atmospheric Gravity Waves*. Academic Press, 400 pp.

Neumann, P. P., and M. Bartholmai, 2015: Real-time wind estimation on a micro unmanned aerial vehicle using its inertial measurement unit. *Sens. Actuators, A*, **235**, 300–310, doi:http://dx.doi.org/10.1016/j.sna.2015.09.036.

Nieuwstadt, F. T. M., 1984: The turbulent structure of the stable, nocturnal boundary layer. *J. Atmos. Sci.*, **41 (14)**, 2202–2216, doi:10.1175/1520-0469(1984)041<2202:TTSOTS>2.0.CO;2.

Nieuwstadt, F. T. M., 1985: A model for the stationary, stable boundary layer. *Turbulence and diffusion in stable environments.*, J. C. R. Hunt, Ed., Clarendon Press, Oxford, 149–179.

Palomaki, R. T., N. T. Rose, M. van den Bossche, T. J. Sherman, and S. F. J. D. Wekker, 2017: Wind estimation in the lower atmosphere using multirotor aircraft. *J. Atmos. Oceanic Technol.*, **34 (5)**, 1183–1191, doi:10.1175/JTECH-D-16-0177.1, https://doi.org/10.1175/JTECH-D-16-0177.1.

37

Persson, P. O. G., C. W. Fairall, E. L. Andreas, P. G. Guest, and D. K. Perovich, 2002: Measurements near the atmospheric surface flux group tower at SHEBA: Near-surface conditions and surface energy budget. *J. Geophys. Res.*, **107 (C10)**, doi:10.1029/2000jc000705.

Pithan, F., and T. Mauritsen, 2014: Arctic amplification dominated by temperature feedbacks in contemporary climate models. *Nat. Geosci.*, **7 (3)**, 181–184, doi:10.1038/ngeo2071.

Poulos, G. S., and Coauthors, 2002: CASES-99: A comprehensive investigation of the stable nocturnal boundary layer. *Bull. Amer. Meteor. Soc.*, **83 (4)**, 555–581, doi:10.1175/1520-0477(2002) 083<0555:caciot>2.3.co;2.

Rautenberg, A., and Coauthors, 2019: The multi-purpose airborne sensor carrier MASC-3 for wind and turbulence measurements in the atmospheric boundary layer. *Sensors*, **19 (10)**, 2292, doi:10.3390/s19102292.

Reuder, J., L. Båserud, M. O. Jonassen, S. T. Kral, and M. Müller, 2016: Exploring the potential of the RPA system SUMO for multipurpose boundary-layer missions during the BLLAST campaign. *Atmos. Meas. Tech.*, **9 (6)**, 2675–2688, doi:10.5194/amt-9-2675-2016.

Reuder, J., P. Brisset, M. Jonassen, Marius Müller, and S. Mayer, 2009: The Small Unmanned Meteorological Observer SUMO: A new tool for atmospheric boundary layer research. *Meteorol. Z.*, **18 (2)**, 141–147, doi:10.1127/0941-2948/2009/0363.

Reuder, J., M. O. Jonassen, and H. Ólafsson, 2012a: The Small Unmanned Meteorological Observer SUMO: Recent developments and applications of a micro-UAS for atmospheric boundary layer research. *Acta Geophys.*, **60 (5)**, 1454–1473, doi:10.2478/s11600-012-0042-8.

Reuder, J., and Coauthors, 2012b: FLOHOF 2007: An overview of the mesoscale meteorological field campaign at Hofsjökull, Central Iceland. *Meteorol. Atmos. Phys.*, **116 (1-2)**, 1–13, doi:10.1007/s00703-010-0118-4.

Román-Cascón, C., C. Yagüe, G.-J. Steeneveld, G. Morales, J. A. Arrillaga, M. Sastre, and G. Maqueda, 2019: Radiation and cloud-base lowering fog events: Observational analysis and evaluation of WRF and HARMONIE. *Atmos. Res.*, **229**, 190–207, doi:10.1016/j.atmosres.2019.06.018.

Segales, A. R., B. R. Greene, T. M. Bell, W. Doyle, J. J. Martin, E. A. Pillar-Little, and P. B. Chilson, 2020: The CopterSonde: An insight into the development of a smart unmanned aircraft system for atmospheric boundary layer research. *Atmospheric Measurement Techniques*, **13 (5)**, 2833–2848, doi:10.5194/amt-13-2833-2020.

Serreze, M. C., A. P. Barrett, J. C. Stroeve, D. N. Kindig, and M. M. Holland, 2009: The emergence of surface-based Arctic amplification. *The Cryosphere*, **3 (1)**, 11–19, doi:10.5194/tc-3-11-2009.

Serreze, M. C., and R. G. Barry, 2011: Processes and impacts of Arctic amplification: A research synthesis. *Global Planet. Change*, **77 (1-2)**, 85–96, doi:10.1016/j.gloplacha.2011.03.004.

Skamarock, W., J. Klemp, J. Dudhia, D. Gill, D. Barker, M. Duda, X.-Y. Huang, and W. Wang, 2008: A Description of the Advanced Research WRF Version 3. Tech. Rep. NCAR/TN-475+STR, NCAR. doi:10.5065/D68S4MVH, technical note.

Sorbjan, Z., 2010: Gradient-based scales and similarity laws in the stable boundary layer. *Quart. J. Roy. Meteor. Soc.*, **136 (650)**, 1243–1254, doi:10.1002/qj.638.

Sorbjan, Z., and A. Grachev, 2010: An evaluation of the flux–gradient relationship in the stable boundary layer. *Bound.-Layer Meteor.*, **135 (3)**, 385–405, doi:10.1007/s10546-010-9482-3.

39

Spiess, T., J. Bange, M. Buschmann, and P. Vörsmann, 2007: First application of the meteorological Mini-UAV 'M2AV'. *Meteorol. Z.*, **16 (2)**, 159–169, doi:10.1127/0941-2948/2007/0195.

Steeneveld, G. J., A. A. M. Holtslag, C. J. Nappo, B. J. H. van de Wiel, and L. Mahrt, 2008: Exploring the possible role of small-scale terrain drag on stable boundary layers over land. *J. Appl. Meteor. Climate*, **47 (10)**, 2518–2530, doi:10.1175/2008jamc1816.1.

Steeneveld, G. J., M. J. J. Wokke, C. D. G. Zwaaftink, S. Pijlman, B. G. Heusinkveld, A. F. G. Jacobs, and A. A. M. Holtslag, 2010: Observations of the radiation divergence in the surface layer and its implication for its parameterization in numerical weather prediction models. *J. Geophys. Res.*, **115 (D6)**, doi:10.1029/2009jd013074.

Stephens, G. L., and Coauthors, 2000: The Department of Energy's atmospheric radiation measurement (ARM) unmanned aerospace vehicle (UAV) program. *Bull. Amer. Meteor. Soc.*, **81 (12)**, 2915–2938, doi:10.1175/1520-0477(2000)081<2915:tdoesa>2.3.co;2.

Sterk, H. A. M., G. J. Steeneveld, F. C. Bosveld, T. Vihma, P. S. Anderson, and A. A. M. Holtslag, 2016: Clear-sky stable boundary layers with low winds over snow-covered surfaces. Part 2: Process sensitivity. *Quart. J. Roy. Meteor. Soc.*, **142 (695)**, 821–835, doi:10.1002/qj.2684.

Sterk, H. A. M., G. J. Steeneveld, T. Vihma, P. S. Anderson, F. C. Bosveld, and A. A. M. Holtslag, 2015: Clear-sky stable boundary layers with low winds over snow-covered surfaces. Part 1: WRF model evaluation. *Quart. J. Roy. Meteor. Soc.*, **141 (691)**, 2165–2184, doi:10.1002/qj.2513.

Sun, J., and Coauthors, 2015: Review of wave–turbulence interactions in the stable atmospheric boundary layer. *Rev. Geophys.*, **53 (3)**, 956–993, doi:10.1002/2015rg000487.

40

Sun, Q. Z., T. Vihma, M. O. Jonassen, and Z. H. Zhang, 2020: Impact of assimilation of radiosonde and UAV-observations from the Southern Ocean in the polar WRF model. *Adv. Atmos. Sci.*, **37**, doi:10.1007/s00376-020-9213-8.

Svensson, G., and A. A. M. Holtslag, 2009: Analysis of model results for the turning of the wind and related momentum fluxes in the stable boundary layer. *Bound.-Layer Meteor.*, **132 (2)**, 261–277, doi:10.1007/s10546-009-9395-1.

Tjernström, M., and Coauthors, 2005: Modelling the Arctic boundary layer: An evaluation of six ARCMIP regional-scale models using data from the SHEBA project. *Bound.-Layer Meteor.*, **117 (2)**, 337–381, doi:10.1007/s10546-004-7954-z.

Uotila, P., T. Vihma, and J. Haapala, 2015: Atmospheric and oceanic conditions and the extremely low Bothnian Bay sea ice extent in 2014/2015. *Geophys. Res. Lett.*, **42 (18)**, 7740–7749, doi:10.1002/2015gl064901.

Uppala, S. M., and Coauthors, 2005: The ERA-40 re-analysis. *Quart. J. Roy. Meteor. Soc.*, **131 (612)**, 2961–3012, doi:10.1256/qj.04.176.

Uttal, T., and Coauthors, 2002: Surface heat budget of the Arctic Ocean. *Bull. Amer. Meteor. Soc.*, **83 (2)**, 255–275, doi:10.1175/1520-0477(2002)083<0255:SHBOTA>2.3.CO;2.

Wildmann, N., M. Hofsäß, F. Weimer, A. Joos, and J. Bange, 2014: MASC – a small re-motely piloted aircraft (RPA) for wind energy research. *Adv. Sci. Res.*, **11**, 55–61, doi:10.5194/asr-11-55-2014.

Wrenger, B., and J. Cuxart, 2017: Evening transition by a river sampled using a remotely-piloted multicopter. *Bound.-Layer Meteor.*, doi:10.1007/s10546-017-0291-9.

41

LIST OF TABLES

TABLE 1. Alphabetic list of campaign participants.

Name	Affiliation	Year
Jan Ahrens	Ostwestfalen-Lippe UASA	2018
Kjell zum Berge	University of Tübingen	2018
Elise Mogster Braaten	University of Bergen	2018
Line Båserud	University of Bergen	2017/2018
Phil Chilson	University of Oklahoma	2018
Ewan O'Connor	Finnish Meteorological Institute	2017
William Doyle	University of Oklahoma	2018
Heidi Midtgarden Golid	University of Bergen	2018
Brian Greene	University of Oklahoma	2018
Kristine Flacké Haualand	University of Bergen	2018
Philipp Hilsheimer	University of Tübingen	2017
Marie Hundhausen	University of Tübingen	2017
Stephan T. Kral	University of Bergen	2017/2018
Marius O. Jonassen	University Centre in Svalbard	2017
Carsten Langohr	Ostwestfalen-Lippe UASA	2017/2018
Christian Lindenberg	Lindenberg und Müller GmbH & Co. KG	2017/2018
Patrick Manz	University of Tübingen	2018
Hasan Mashni	University of Tübingen	2018
Santiago Mazuera	University of Oklahoma	2018
Martin Müller	Lindenberg und Müller GmbH & Co. KG	2017/2018
Elizabeth Pillar-Little	University of Oklahoma	2018
Alexander Rautenberg	University of Tübingen	2017/2018
Joachim Reuder	University of Bergen	2018
Martin Schön	University of Tübingen	2018
Markus Schygulla	University of Tübingen	2017
Antonio Segalés	University of Oklahoma	2018
Andrew Seidl	University of Bergen	2018
Irene Suomi	Finnish Meteorological Institute	2017/2018
Gabin H. Urbancic	University of Bergen	2017
Timo Vihma	Finnish Meteorological Institute	2017/2018
Hendrik Voss	Ostwestfalen-Lippe UASA	2017/2018
Burkhard Wrenger	Ostwestfalen-Lippe UASA	2017/2018

43

TABLE 2. Specifications of the AWS instrumentation with measured parameters: temperature, T; sonic temperature, T_s; relative humidity, RH; pressure, p; wind components, u, v, w; wind speed, ws; wind direction, wd; cloud base height, h_{CB} and fraction CF; SYNOP weather codes, syn; precipitation, prec; visibility, vis, H_2O and CO_2 concentration; up and downwelling short and longwave radiation, $SW^{\uparrow\downarrow}$, $LW^{\uparrow\downarrow}$; ground heat flux, GF.

AWS	Parameters	Sensor	Acq. Period	Meas. Height
FMI (2017/18)	T, RH	Vaisala HMP155	10 min	2.0 m agl (9 m asl)
@65.0399 °N, 24.5592 °E	p	Vaisala PTB 201A	10 min	7 m asl
	T	Pentronic AB Pt100	10 min	2.0 m agl (9 m asl)
	ws, wd, T_s	Adolf Thies UA2D	1 s	38.5 m agl (45.5 m asl)
	h_{CB}, CF	Vaisala CT25K Laser Ceilometer	10 min	
	syn, prec, vis	Vaisala FD12P Weather Sensor	10 min	
GFI (2017)	T	Campbell ASPTC (aspirated)	1 min	1.0, 2.0, 4.0 m agl
@65.0378 °N, 24.5549 °E	T	PT100 (aspirated)	1 min	1.0, 2.0, 4.0 m agl
	RH	Rotronic HC2-S (aspirated)	1 min	1.0, 2.0, 4.0 m agl
	ws	Vector A100LK	1 min	1.0, 2.0, 4.0 m agl
	wd	Vector W200P	1 min	1.0, 2.0, 4.0 m agl
	$SW^{\uparrow\downarrow}$, $LW^{\uparrow\downarrow}$	Kipp & Zonen CNR1	1 min	1.0 m agl
	GF	Hukseflux HFP01	1 min	snow and ice
	u, v, w, T_s	Campbell CSAT-3	0.05 s	2.7 m agl
	H_2O, CO_2, p	LI-COR LI7500	0.05 s	2.7 m agl
GFI1 (2018)	T	Campbell ASPTC (aspirated)	1 s	2.0 m agl
@65.0365 °N, 24.5548 °E	$SW^{\uparrow\downarrow}$, $LW^{\uparrow\downarrow}$	Kipp & Zonen CNR1	1 s	1.0 m agl
	u, v, w, T_s	Campbell CSAT-3	0.05 s	2.0 m agl
	H_2O, CO_2, p	LI-COR LI7500	0.05 s	2.0 m agl
GFI2 (2018)	T	Campbell ASPTC (aspirated)	1 s	0.6, 2.0, 6.8 m agl
@65.0360 °N, 24.5556 °E	T	PT100 (aspirated)	1 s	0.6, 2.0, 6.8 m agl
	RH	Rotronic HC2-S (aspirated)	1 s	0.6, 2.0, 6.8 m agl
	ws	Vector A100LK	1 s	0.6, 2.0, 6.8 m agl
	wd	Vector W200P	1 s	0.6, 2.0, 6.8 m agl
	$SW^{\uparrow\downarrow}$, $LW^{\uparrow\downarrow}$	Kipp & Zonen CNR1	1 s	6.4 m agl
	GF	Hukseflux HFP01	snow and ice	
	u, v, w, T_s	Campbell CSAT-3	0.05 s	2.0, 4.6, 10.3 m agl
	H_2O, CO_2, p	LI-COR LI7500	0.05 s	2.0 m agl

44

TABLE 3. Remote sensing systems specifications with measured parameters as in Table 2 and radial wind speed, u_{rad}; standard deviation of wind velocity components, σu, σv, σw; attenuated backscatter signal strength, bsc; carrier to noise ratio, CNR.

Instrument	Type	Parameters	Range	Resolution	Acq. Period
LATAN-3M (2017/18)	1D sodar	w, σw, bsc	10–340 magl	10 m (vertical)	3 s
WindCube 100S (2017)	3D scanning doppler lidar	u_{rad}, CNR	50–3300 m (radial)	25 m (radial)	1 s
WindCube v1 (2018)	3D doppler lidar	u, v, w, σu, σv, σw, CNR	40–250 magl	20 m (vertical)	4 s
MFAS (2018)	3D sodar	u, v, w, σw, bsc	40–1000 magl	10 m (vertical)	10 min

920
921

45

TABLE 4. UAS specifications with measured parameters as in Table 2 and infra-red temperature, T_{IR}. In addition to the listed sensors each UAS is equipped with a GNSS to measure the aircraft's position (latitude, lat; longitude, lon; altitude, alt) and an IMU for the aircraft's attitude angles (pitch θ; roll, ϕ; yaw, ψ). See listed references for more detailed information.

UAS	Operator	Parameter	Sensor	Acq. Freq.	Reference
SUMO (Fixed-wing)	GFI	T, RH	Sensirion SHT75	2 Hz	Reuder et al. (2009)
		T	Pt1000 Heraeus M222	8.5 Hz	Reuder et al. (2012a)
		p	MS 5611	4 Hz	
		T_{IR}	MLX90614	8.5 Hz	
		ws, wd	Aircraft Dynamics	4 Hz	
Bebop2Met (Rotary-wing)	GFI	T, RH	Sensirion SHT75	2 Hz	Kral et al. (2018)
		p	MS 5607	0.77 Hz	
		ws, wd	Aircraft Dynamics	4 Hz	
Q13a (Rotary-wing)	UOWL	T, RH	HYT 271	10 Hz	Wrenger and Cuxart (2017)
		p	BMP 180	10 Hz	
		ws	Modern Device Wind Sensor Rev. P	10 Hz	
Q13b (Rotary-wing)	UOWL	T, RH	HYT 271	10 Hz	Wrenger and Cuxart (2017)
		T	K-type thermocouple 25 μm	10 Hz	
		p	BMP 180	10 Hz	
		T_{IR}	MLX90614	10 Hz	
CopterSonde (Rotary-wing)	OU	T	iMet XF PT 100	10 Hz	Greene et al. (2019)
		T, RH	HYT 271	10 Hz	Segales et al. (2020)
		p	Pixracer barometer	10 Hz	
		ws, wd	Aircraft Dynamics	10 Hz	
MASC-2/3 (Fixed-wing)	UT	T	Pt-fine-wire	100 Hz	Wildmann et al. (2014)
		T, RH	Sensirion SHT31	10 Hz	Rautenberg et al. (2019)
		RH	P14 Rapid	10 Hz	
		p	HCA-BARO	100 Hz	
		u, v, w	custom 5-hole probe	100 Hz	

46

TABLE 5. List of IOPs during ISOBAR17 and ISOBAR18, summarizing the observed ABL conditions (i.e., stability regime; wind regime; relevant phenomena; and maximum near-surface vertical temperature difference and lapse rate) and the corresponding large-scale conditions (i.e., average wind speed and direction (850 hPa to 925 hPa); subsidence ($\overline{\omega}$); horizontal temperature-advection (adv); cloud cover; and synoptic situation). Additional information on the evolution of the large-scale conditions is given in parentheses. The large-scale conditions are extracted from ERA5 reanalysis data (Hersbach et al. 2020).

IOP No.	Start date time UTC	End date time UTC	Boundary-layer conditions	Large-scale conditions	No. UAS flights
1	14 Feb 2017 1500	15 Feb 2017 0630	near-neutral to very stable; light to calm winds; $\Delta T_{\text{4m-1m}} = 3.8\,K$ ($\Lambda = 1.3\,K\,m^{-1}$)	6 (11–4) m s^{-1} NNW(NNW–WSW); $\overline{\omega} = 0.07\,Pa\,s^{-1}$ adv $= 0.01\,Kh^{-1}$; broken cloud cover; high pressure ridge	15
2	20 Feb 2017 2300	21 Feb 2017 0600	near-neutral; moderate winds; $\Delta T_{\text{4m-1m}} = 0.8\,K$ ($\Lambda = 0.3\,K\,m^{-1}$)	10(9–11) m s^{-1} NNW; $\overline{\omega} = 0.07\,Pa\,s^{-1}$; adv $= 0.13\,Kh^{-1}$; clear sky; weak eastward-propagating trough	13
3	21 Feb 2017 1700	21 Feb 2017 2300	partially very stable; calm to light winds; $\Delta T_{\text{4m-1m}} = 6.4\,K$ ($\Lambda = 2.1\,K\,m^{-1}$)	10(6–18) m s^{-1} SSW (NW–S); $\overline{\omega} = 0.02\,Pa\,s^{-1}$; adv $= -0.06\,K\,h^{-1}$; scattered clouds; weak eastward-propagating trough	9
4	25 Feb 2017 0400	25 Feb 2017 1100	near-neutral; moderate winds; $\Delta T_{\text{4m-1m}} = 0.5\,K$ ($\Lambda = 0.2\,K\,m^{-1}$)	13(14–12) m s^{-1} NNW; $\overline{\omega} = 0\,Pa\,s^{-1}$; adv $= 0.56\,Kh^{-1}$; clear sky; low pressure influence	24
5	26 Feb 2017 0200	26 Feb 2017 0730	near-neutral to weakly stable; moderate winds; rapid-cooling ($\sim 10\,K$ in 3h); $\Delta T_{\text{4m-1m}} = 0.3\,K$ ($\Lambda = 0.1\,K\,m^{-1}$)	6(9–4) m s^{-1} NNW; $\overline{\omega} = 0.01\,Pa\,s^{-1}$; adv $= -0.12\,K\,h^{-1}$; scattered clouds; weak trough	23
6	26 Feb 2017 1400	27 Feb 2017 0200	near-neutral to very stable; light to calm winds; wave breaking (Kelvin-Helmholtz billows); $\Delta T_{\text{4m-1m}} = 6.2\,K$ ($\Lambda = 2.1\,K\,m^{-1}$)	5(6–4) m s^{-1} NNE; $\overline{\omega} = 0.08\,Pa\,s^{-1}$; adv $= 0.16\,Kh^{-1}$; clear sky; weak pressure gradients	32

47

7	10 Feb 2018 1130	11 Feb 2018 0100	near-neutral to weakly stable; moderate winds; $\Delta\overline{T}_{6.9m-0.6m} = 3.2\,K\ (\Lambda = 0.5\,K\,m^{-1})$	$13(17–8)\ ms^{-1}$ SW; $\overline{\omega} = -0.06\,Pa\,s^{-1}$; $adv = 0.47\,K\,h^{-1}$; overcast, intermittent clear sky periods; strong pressure gradient (decreasing)	13
8	16 Feb 2018 0500	17 Feb 2018 0400	near-neutral to weakly stable; elevated inversion> 50m; LLJ; $\Delta\overline{T}_{6.9m-0.6m} = 5.6\,K\ (\Lambda = 0.9\,K\,m^{-1})$	$2(4–1)\ ms^{-1}$ NE; $\overline{\omega} = 0.06\,Pa\,s^{-1}$; $adv = 0.05\,K\,h^{-1}$; broken cloud cover, weak pressure ridge	28
9	17 Feb 2018 1400	18 Feb 2018 0230	weakly to very stable; light to calm winds; $\Delta\overline{T}_{6.9m-0.6m} = 1.5\,K\ (\Lambda = 0.2\,K\,m^{-1})$	$2(3–2)\ ms^{-1}$ NE; $\overline{\omega} = 0.01\,Pa\,s^{-1}$; $adv = 0.01\,K\,h^{-1}$; clear sky to overcast; weak high pressure ridge	38
10	18 Feb 2018 1330	19 Feb 2018 0230	weakly to very stable; very light to calm winds; LLJ (upside-down mixing); wave breaking; $\Delta\overline{T}_{6.9m-0.6m} = 5.1\,K\ (\Lambda = 0.8\,K\,m^{-1})$	$5(4–6)\ ms^{-1}$ NNE; $\overline{\omega} = 0.03\,Pa\,s^{-1}$; $adv = -0.23\,K\,h^{-1}$; overcast, intermittent clear sky periods; high pressure influence (developing)	45
11	19 Feb 2018 1500	19 Feb 2018 2200	weakly stable; moderate winds; LLJ; $\Delta\overline{T}_{6.9m-0.6m} = 3.5\,K\ (\Lambda = 0.5\,K\,m^{-1})$	$6(8–5)\ ms^{-1}$ ENE; $\overline{\omega} = 0.1\,Pa\,s^{-1}$; $adv = 0.15\,K\,h^{-1}$; clear sky; high pressure influence	14
12	20 Feb 2018 1100	21 Feb 2018 0600	near-neutral to very stable; light winds; elevated inversion 100m to 180m; $\Delta\overline{T}_{6.9m-0.6m} = 5.4\,K\ (\Lambda = 0.9\,K\,m^{-1})$	$2(2–3)\ ms^{-1}$ N(NE–NW); $\overline{\omega} = 0.01\,Pa\,s^{-1}$; $adv = 0.01\,K\,h^{-1}$; overcast, clear sky after 0400; high pressure influence	51
13	22 Feb 2018 0500	22 Feb 2018 1800	near-neutral to weakly stable; light winds; $\Delta\overline{T}_{6.9m-0.6m} = 2.1\,K\ (\Lambda = 0.3\,K\,m^{-1})$	$6(5–7)\ ms^{-1}$ N; $\overline{\omega} = -0.06\,Pa\,s^{-1}$; $adv = 0.19\,K\,h^{-1}$; broken cloud cover, clear sky after 1200; high pressure influence	9
14	23 Feb 2018 1300	24 Feb 2018 0600	weakly to very stable; light winds; LLJ; waves; $\Delta\overline{T}_{6.9m-0.6m} = 4.3\,K\ (\Lambda = 0.7\,K\,m^{-1})$	$6(6–5)\ ms^{-1}$ NE; $\overline{\omega} = 0.14\,Pa\,s^{-1}$; $adv = -0.17\,K\,h^{-1}$; clear sky, intermittent scattered cloud cover; high pressure influence	44

48

Table A1. List of Abbreviations

AMOR Q13	Advanced Mission and Operation Research Quadcopter (13-inch propellers)
B2M	Bebop2Met
CS	CopterSonde
EC	Eddy-Covariance
ECMWF-IFS	ECMWF Integrated Forecasting System
FMI	Finnish Meteorological Institute
GFI	Geophysical Institute, University of Bergen
ISOBAR	Innovative Strategies for Observations in the Arctic Atmospheric Boundary Layer
lidar	Light Detection and Ranging
LLJ	Low-Level Jet
MASC	Multi-Purpose Airborne Sensor Carrier
MEPS	MetCoOp Ensemble Prediction System
MFAS	Medium Size Flat Array Sodar
MOST	Monin-Obukhov Similarity Theory
OU	University of Oklahoma
QA/QC	Quality Assurance and Quality Check

|	
RRTMG	Rapid Radiative Transfer Model Global
SBL	Stable Boundary Layer
SCM	Single-Column Model
sodar	Sound Detection and Ranging
SUMO	Small Meteorological Observer
UAS	Unmanned Aircraft System
UOWL	Ostwestfalen-Lippe UASA
UT	University of Tübingen
VSBL	Very Stable Boundary Layer
WCv1	Windcube v1
WC100S	Windcube 100S
WSBL	Weakly Stable Boundary Layer

LIST OF FIGURES

51

52

FIG. 1. Overview maps showing the ISOBAR field site: The two inlay maps at the top display the area of Northern Europe (left) and around Hailuoto and Oulu (right). The large map is based on a Sentinel-2 L2A satellite image from 18 Feb 2019 (https://apps.sentinel-hub.com/eo-browser)

53

SUMO/GFI (39/46)
Profiles 1800 m

Q13/UOWL (30/80)
Profiles 300 m

Q17/UOWL (-/3)
Infrared thermography 100 m

Bebop2Met/GFI (55/88)
Profiles 300 m

CopterSonde/OU (-/43)
Profiles 300 m

Tuffwing/OU (-/15)
CO2, Photogrametry

miniTalon/GFI (3/-)
Turbulence 300m

MASC2/UT (14/-)
Turbulence 450 m

MASC3/UT (-/13)
Turbulence 150 m

FIG. 2. The different UAS systems used during the two campaigns. The numbers of flights are indicated in parentheses for ISOBAR17 and ISOBAR18, respectively.
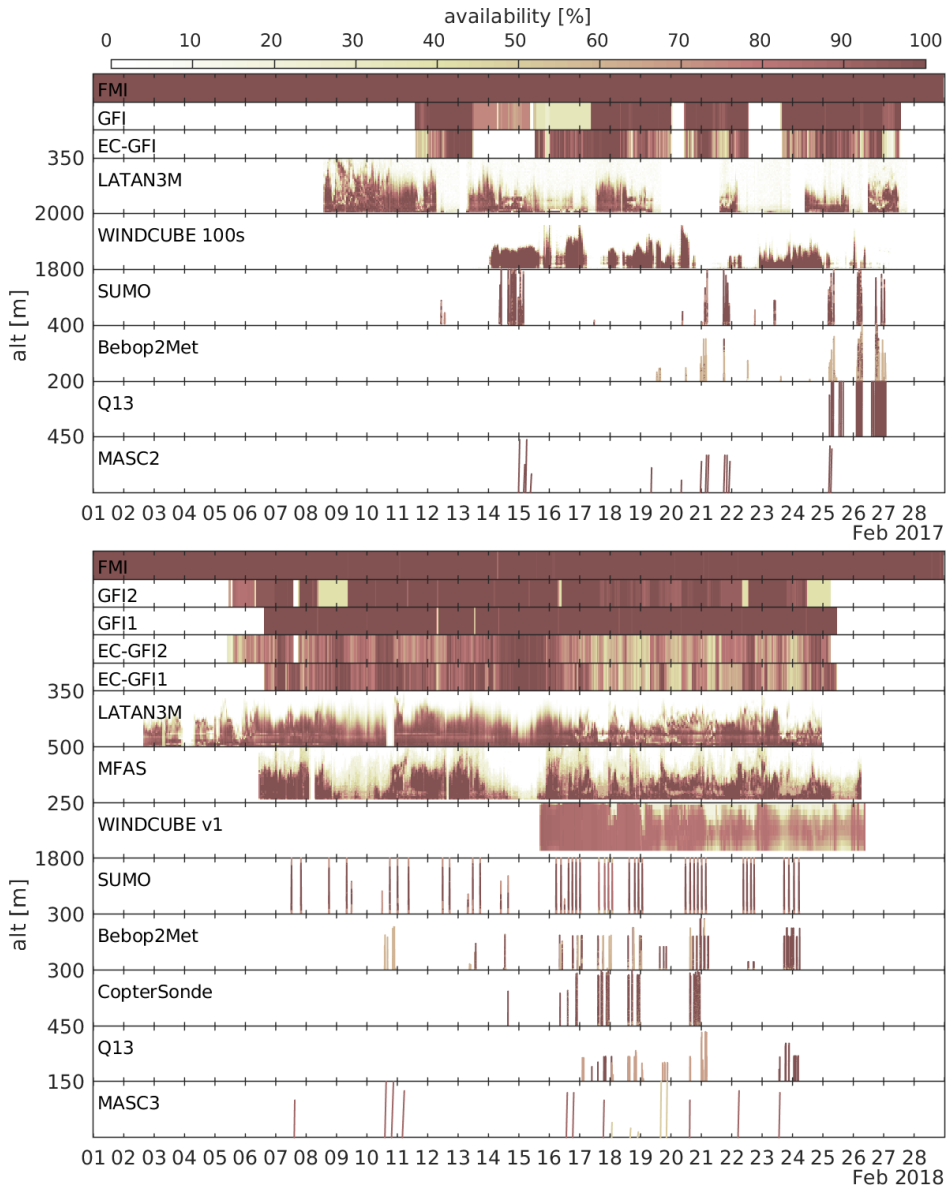
996   FIG. 3. Data availability for the measurement systems during the ISOBAR17 and ISOBAR18 campaigns. For

997   the profiling systems the data availability is given as a function of height.

55
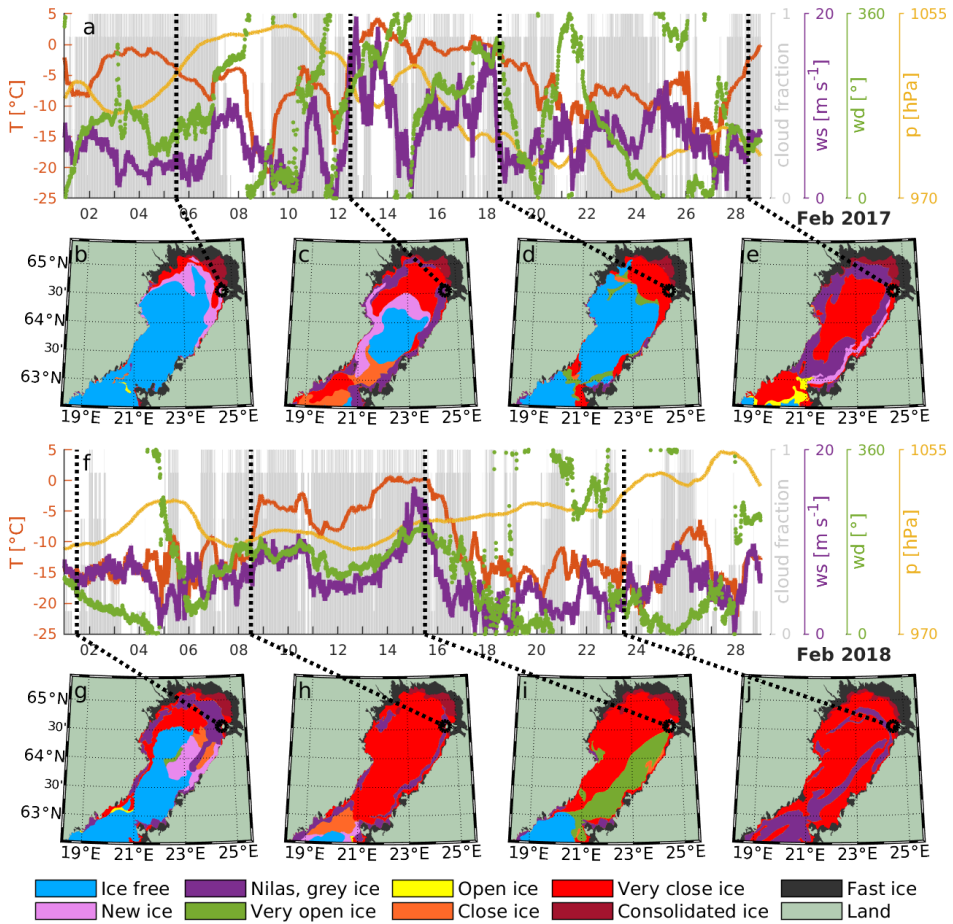
Fɪɢ. 4. Overview of the meteorological and sea-ice conditions during the two campaigns in February 2017 and 2018. The first and third rows show the time series of temperature, cloud cover, wind speed and direction and pressure observed by the WMO weather station (FMI) during February 2017 and 2018, respectively. The ice charts in the second and fourth rows represent the extrema of the ice coverage during the corresponding period based on data provided by the Finnish Meteorological Institute. Black dotted lines indicate the time of observation and the corresponding location on the maps.

56
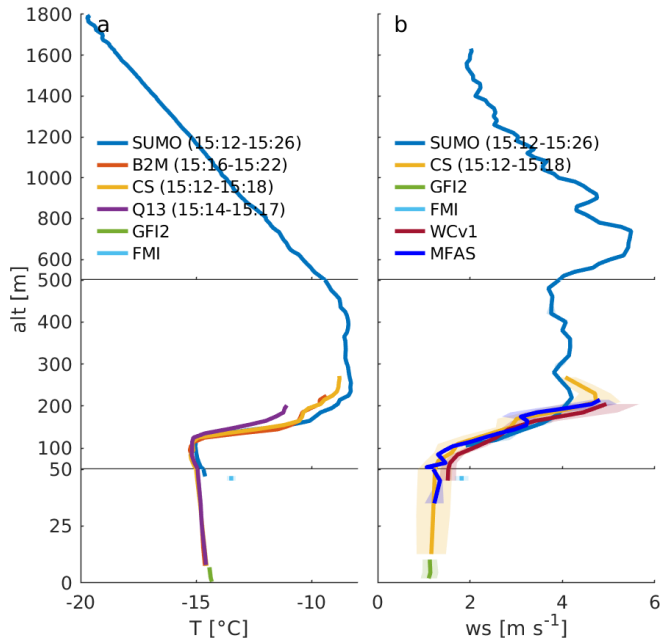
FIG. 5. Combined temperature, T, and wind speed, ws, profiles based on mast, UAS and remote sensing (wind only) data, observed between 1510 and 1530 UTC 23 Feb 2018. Solid lines and shaded areas indicate the mean and standard deviation (bin-averaged for all UAS and time-averaged for ground based systems), respectively. The observation period for the ground based systems is given in the title, the slightly shorter periods for the UAS flights are given in the legends.

57
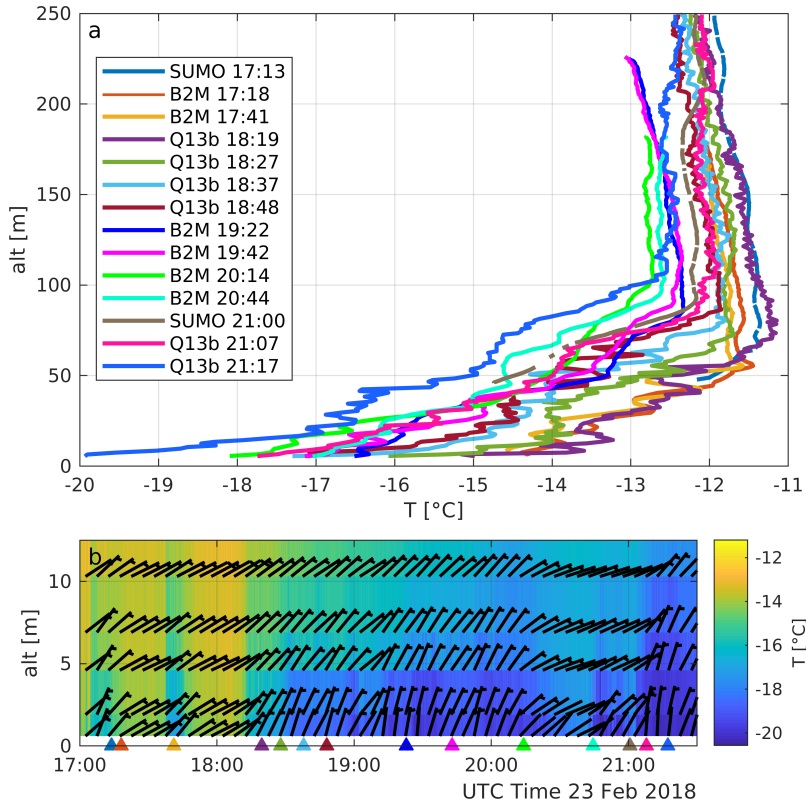
FIG. 6. Series of (a) UAS boundary layer profiles and (b) corresponding time series of surface based measurements of T (contours) and ws (wind barbs), observed during IOP-14, 1615 to 2130 UTC 23 Feb 2018. The UAS flight times for the data presented in the top panel (ascent up to 250 m) are indicated by shades and additional markers in the bottom panel, applying the corresponding color scheme.

58
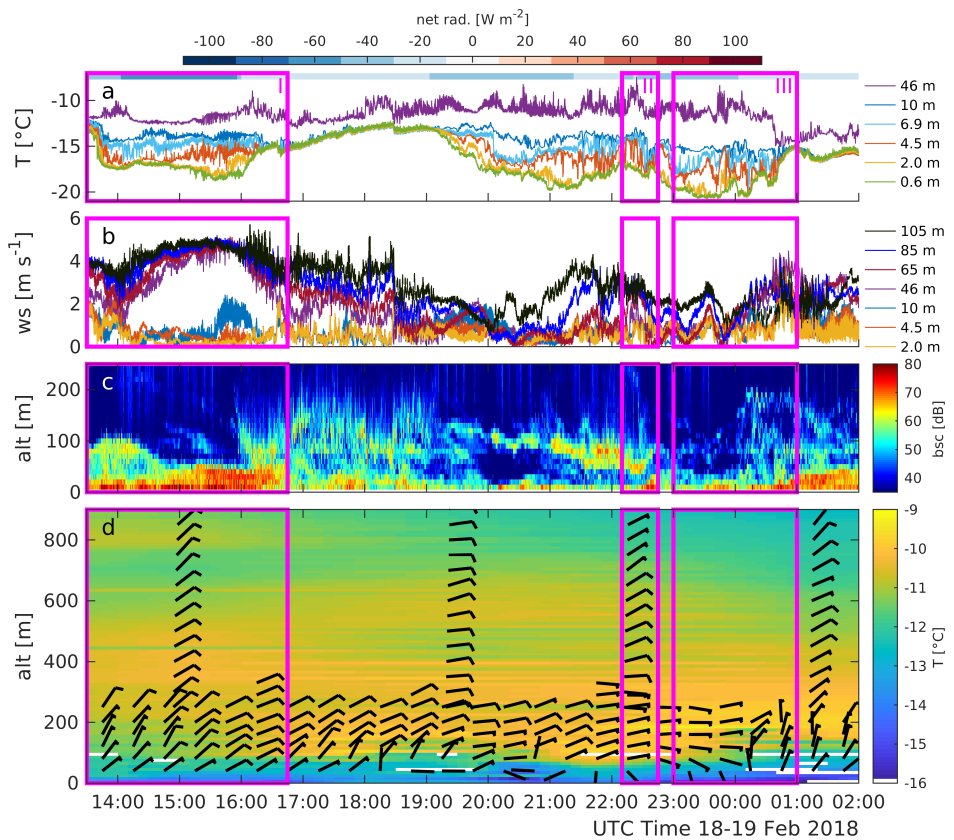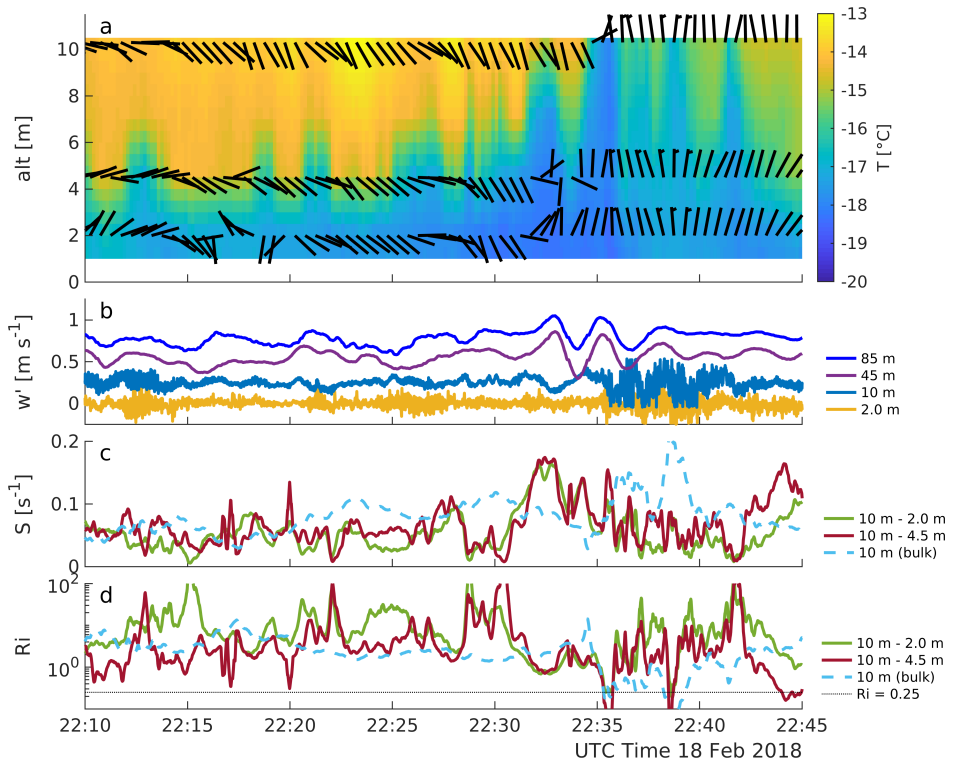
FIG. 7. Time series of various atmospheric parameters during IOP-10, 18-19 Feb 2018: (a) *T* (observed by GFI2 and FMI); (b) ws (GFI2, FMI and WCv1); (c) sodar attenuated backscatter, bsc, profiles (LATAN-3M); (d) composite profiles of *T* (UAS, GFI2) and horizontal wind (SUMO, WCv1, MFAS). Magenta boxes indicate the periods of interest analyzed in the following figures.
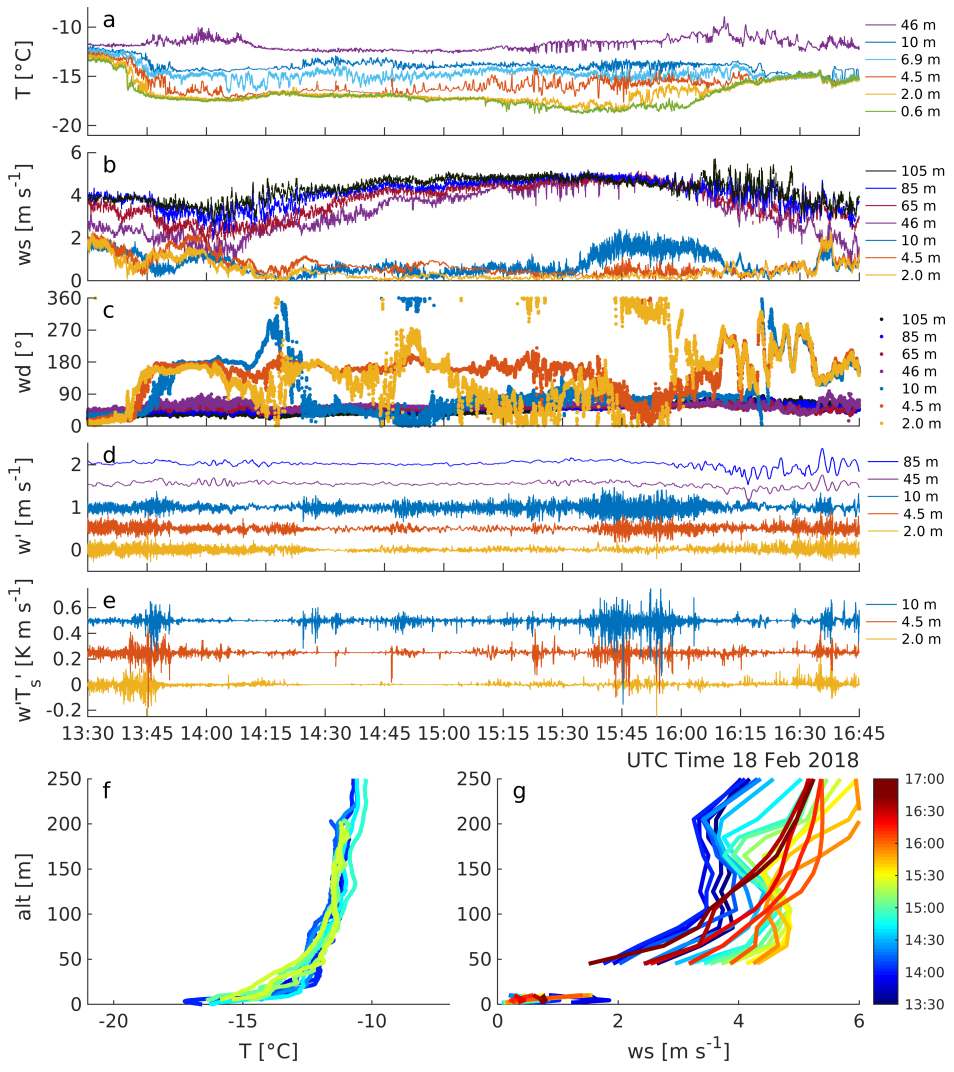
FIG. 8. Time series of various atmospheric parameters during IOP-10, 1330 to 1615 UTC 18 Feb 2018: (a) T (observed by GFI2 and FMI); (b) ws (GFI2, FMI and WCv1); (c) wd (GFI2, FMI and WCv1); (d) vertical velocity perturbation, w' (GFI2, WCv1); (e) instantaneous kinematic heat flux, $\overline{w'T'}$ (GFI2); (f) vertical profiles of T (UAS); (g) vertical profiles of ws (GFI2, WCv1). w' and $\overline{w'T'}$ data are shifted by increments of $0.5\,\mathrm{m\,s^{-1}}$ and $0.25\,\mathrm{K\,m\,s^{-1}}$, respectively, to reveal structures.

60

FIG. 9. Time series of various atmospheric parameters during IOP-10, 2210 to 2245 UTC 18 Feb 2018: (a) temperature, T, (contours) and wind speed and direction (wind barbs), observed by GFI2; (b) vertical velocity perturbation, w' (GFI2, WCv1); (c) wind shear, S (GFI2); (d) Richardson number, Ri (GFI2). The w' data are shifted by increments of $0.25\,\mathrm{m\,s^{-1}}$ to reveal structures. Wind speed at all levels and w' data at the upper two levels are smoothed applying a 1-min sliding mean average. T, S, and Ri data are 10-s sliding mean averages.
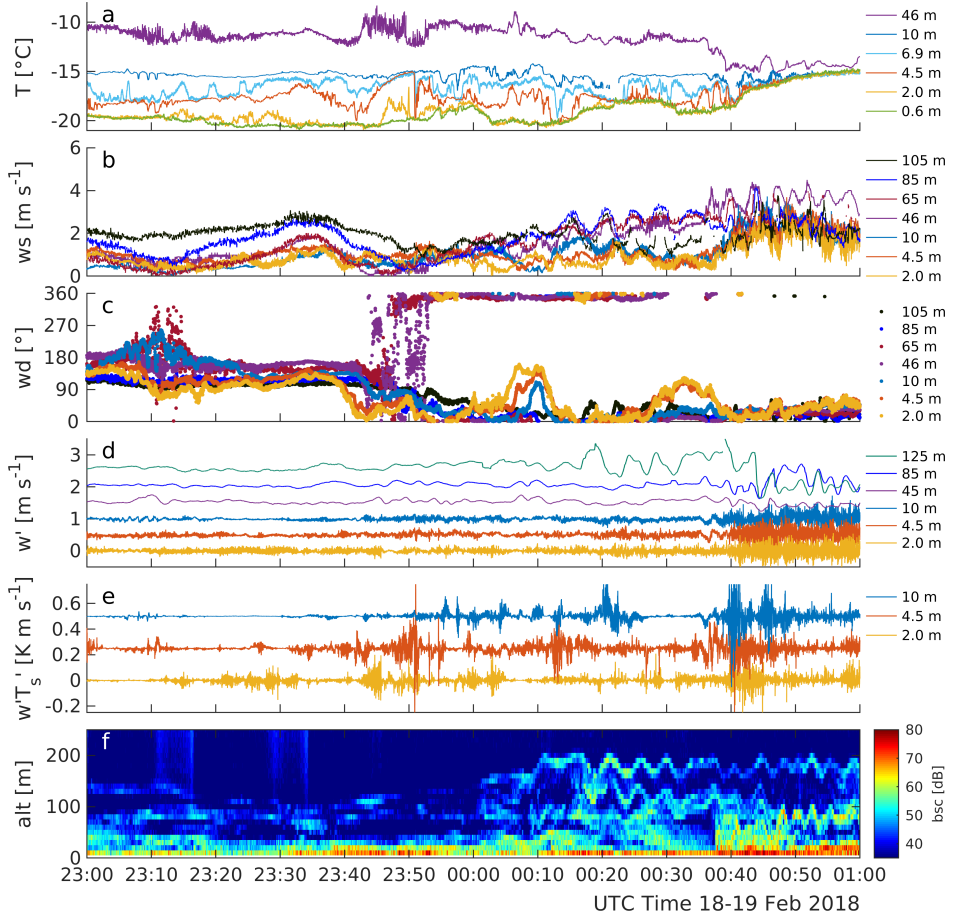
FIG. 10. Time series of various atmospheric parameters during IOP-10, 2300 UTC 18 Feb 2018 to 0100 UTC 19 Feb 2018. (a) temperature (observed by GFI2 and FMI); (b) wind speed (GFI2, FMI and WCv1); (c) wind direction (GFI2, FMI and WCv1); (d) vertical velocity (GFI2, WCv1); (e) instantaneous kinematic heat flux (GFI2); (f) sodar attenuated backscatter profiles (LATAN-3M). The vertical velocity and kinematic heat flux data are shifted by increments of $0.5\,\mathrm{m\,s^{-1}}$ and $0.25\,\mathrm{K\,m\,s^{-1}}$ respectively, to reveal structures.
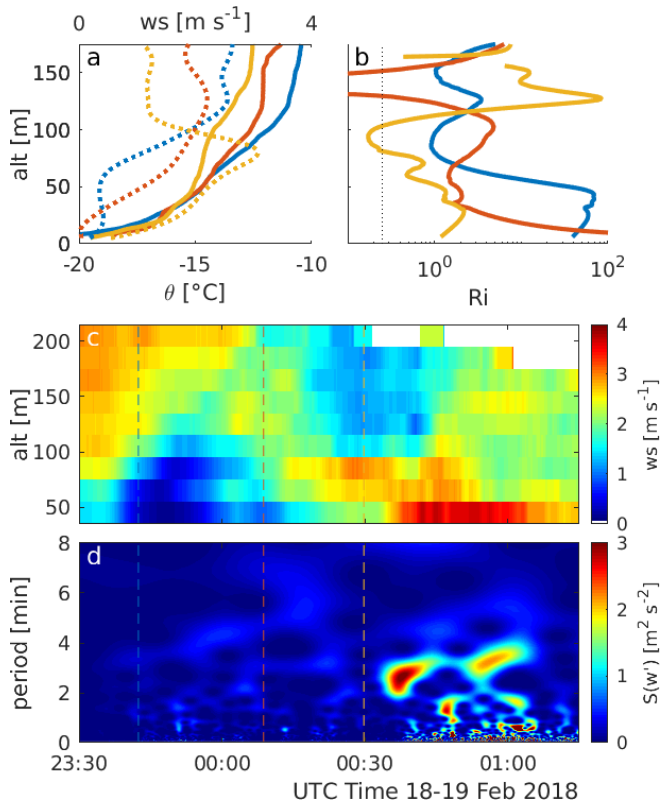
62

FIG. 11. Observations of: (a) UAS profiles of potential temperature and corresponding lidar wind speed profiles; (b) resulting profiles of Ri; (c) time–height diagram of lidar wind speed; and (d) wavelet energy of 10-m sonic vertical velocity component during IOP-10, 2330 UTC 18 Feb 2018 to 0130 UTC 19 Feb 2018. The black dotted line in (b) indicates Ri = 0.25. The UAS flight times from (a) and (b) are indicated as vertical lines in the same color in (c) and (d).

63
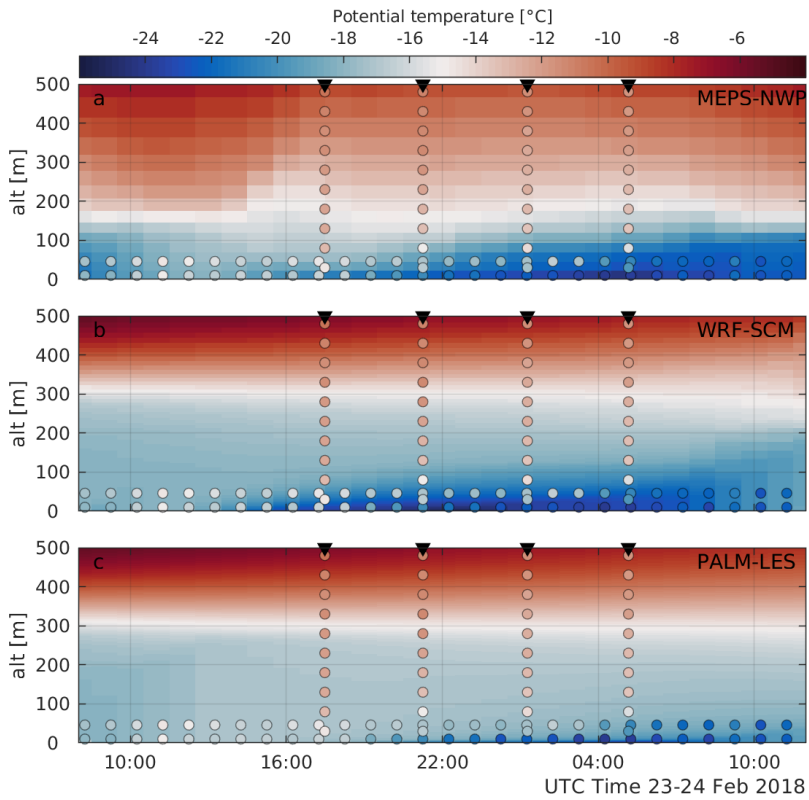
FIG. 12. Time–height plots of potential temperature from the MEPS forecast (MEPS-NWP), the WRF single-column simulation (WRF-SCM) and the PALM LES simulation (PALM-LES). The data cover the lowermost 500 m and the first 24 h at the measurement site. Observations from SUMO, GFI, FMI are superimposed as circles.

Paper IV

The Multi-Purpose Airborne Sensor Carrier MASC-3 for Wind and Turbulence Measurements in the Atmospheric Boundary Layer

IV

MDPI

Article

The Multi-Purpose Airborne Sensor Carrier MASC-3 for Wind and Turbulence Measurements in the Atmospheric Boundary Layer

Alexander Rautenberg [1,*], **Martin Schön** [1], **Kjell zum Berge** [1], **Moritz Mauz** [1], **Patrick Manz** [1], **Andreas Platis** [1], **Bram van Kesteren** [1], **Irene Suomi** [2], **Stephan T. Kral** [3] and **Jens Bange** [1]

[1] Center for Applied Geoscience, Eberhard-Karls-Universität Tübingen, Hölderlinstr. 12, 72074 Tübingen, Germany; martin.schoen@uni-tuebingen.de (M.S.); kjell.zum.berge@uni-tuebingen.de (K.z.B.); moritz.mauz@uni-tuebingen.de (M.M.); manzp@gmx.de (P.M.); andreas.platis@uni-tuebingen.de (A.P.); bram.vankesteren@uni-tuebingen.de (B.v.K.); jens.bange@uni-tuebingen.de (J.B.)

[2] Finnish Meteorological Institute, P.O. Box 503, 00101 Helsinki, Finland; irene.suomi@fmi.fi

[3] Geophysical Institute and Bjerknes Centre for Climate Research, University of Bergen, Postbox 7803, 5020 Bergen, Norway; stephan.kral@uib.no

* Correspondence: alexander.rautenberg@uni-tuebingen.de; Tel.: +49-7071-29-74339

check for
updates

Abstract: For atmospheric boundary-layer (ABL) studies, unmanned aircraft systems (UAS) can provide new information in addition to traditional in-situ measurements, or by ground- or satellite-based remote sensing techniques. The ability of fixed-wing UAS to transect the ABL in short time supplement ground-based measurements and the ability to extent the data horizontally and vertically allows manifold investigations. Thus, the measurements can provide many new possibilities for investigating the ABL. This study presents the new mark of the Multi-Purpose Airborne Sensor Carrier (MASC-3) for wind and turbulence measurements and describes the subsystems designed to improve the wind measurement, to gain endurance and to allow operations under an enlarged range of environmental conditions. The airframe, the capabilities of the autopilot Pixhawk 2.1, the sensor system and the data acquisition software, as well as the post-processing software, provide the basis for flight experiments and are described in detail. Two flights in a stable boundary-layer and a close comparison to a measurement tower and a Sodar system depict the accuracy of the wind speed and direction measurements, as well as the turbulence measurements. Mean values, variances, covariance, turbulent kinetic energy and the integral length scale agree well with measurements from a meteorological measurement tower. MASC-3 performs valuable measurements of stable boundary layers with high temporal resolution and supplements the measurements of meteorological towers and sodar systems.

Keywords: fixed-wing unmanned aircraft; turbulence measurement; 3D wind vector measurement; stable boundary layer; comparison with measurement tower; unmanned aircraft system (UAS); remotely piloted aircraft (RPA)

1. Introduction

For atmospheric boundary-layer (ABL) studies, unmanned aircraft systems (UAS) can provide new information in addition to traditional in-situ measurements or ground- and satellite-based remote sensing techniques. Recent developments of UAS and high-performance high-resolution in-situ sensors allow the observation of processes at different levels within the ABL, which so far can only be accomplished by tall meteorological towers or to some extent, although with limited spatial and temporal resolution, by ground based remote sensing systems. The ability of fixed-wing UAS to

sample data of the ABL along the flight path supplements ground based measurements and the ability to extend the data horizontally and vertically allows manifold investigations. Representative samples of the ABL can be gathered with a high temporal resolution, or area representative evaluations without the need for multiple measurement platforms. Turbulence along a straight horizontal flight path is not precisely a spatial snapshot, nor a temporally averaged snapshot, but a mixture of both, which can be labeled as quasi-spatial snapshot. The use of such data presumes the following assumptions, pros and cons. The most important compendium is Taylor's hypothesis of frozen turbulence [1,2] which must be questioned for low frequencies (or low wavenumber) of the spectrum of atmospheric turbulence [3]. Even the inertial subrange of the spectrum according to Reference [4] may not follow Taylor's hypothesis of frozen turbulence and if eddies of different sizes travel at different velocities, the turbulent wave number spectrum cannot be simply interpreted as the frequency spectrum [5,6]. With aircraft measurements, Taylor's hypothesis is rather valid, since a long distance is covered within a short time period [7,8]. The downside of transecting the turbulence regime is the shift of the spectrum towards higher frequencies and the need of sensors to be accordingly faster than those of stationary measurement systems. A moving platform in general may be technically more challenging than a stationary measurement system, since the wind vector must be transformed from a moving into an earth bound coordinate system. On the other hand, turbulence measurements along a straight horizontal flight path sampled with a fixed-wing UAS, compared to turbulence measured at a stationary point, enables a faster measurement of the quantity, since the same amount of data can be sampled in shorter time. The UAS moves with its airspeed through the ABL and the measurement at a fixed point samples the air which is advected with the mean flow. This correlation can be beneficial for example, for measurements of transition phases of the ABL, where the state of the ABL changes quickly. The need of statistical significance when calculating turbulence statistics [9] implements further challenges for UAS, because the flight distances along flight paths may be limited due to technical restrictions or legal issues. Generally, heterogeneity of the surface and inhomogeneous footprints of moving and stationary systems also implement difficulties and cause discrepancies for a direct comparison of the two systems. This study aims to validate the measurements of the new mark of the Multi-Purpose Airborne Sensor Carrier (MASC-3) by closely comparing them with measurements from a meteorological tower and subsequently being able to fuse both systems for investigations of stable boundary layers (SBL).

Like micro-meteorological stations, remotely piloted aircraft (RPA) can be equipped with fast and accurate sensors in order to measure atmospheric turbulence. The airframe of the vehicle is referred to as RPA and if the sensor systems and ground control systems are also referred to, the terminology is UAS. UAS can be equipped with similar measurement systems than manned aircraft but are limited by the size of the UAS. Since the beginning of the millennium, the rapid progress in micro-electronics and component miniaturization allowed for a fast development of airframes, autopilots and meteorological sensors for research in the ABL. One of the first low-cost attempts was the remotely-controlled, but not auto-piloted system, KALI, which performed more than 150 flights in Nepal and Bolivia to investigate thermally driven flows modified by orography [10,11]. The following years showed rapidly increasing activities by various research groups, making their sensors and instrumentation airborne within a reasonable budget. Most of those earlier systems are based on fixed-wing airframes as for example, M2AV [12], SUMO [13,14], Smartsonde [15,16], Manta [17], MASC [18], ALADINA [19,20], Pilatus [21] and BLUECAT5 [22]. UAS were used for research in the field of atmospheric physics and chemistry [23–26], boundary layer meteorology [17,27–38], and more recently also to wind-energy meteorology [39–41]. The capabilities of UAS for meteorological sampling are broad. The UAS designs range from a more accurate and diverse—but larger—sensor payload, down to small aircraft that can be operated with minimal logistical overhead. Since 2010, the use of rotary-wing multi-copter systems for atmospheric research has increased [38,42–44]. With their ability to hover and to slowly ascend and descend vertically, they are the preferred choice for many measurement tasks related to boundary- and surface-layer profiling, but are limited when measuring turbulence.

Measuring the wind speed and direction is a fundamental and elaborate requirement for understanding the processes of the ABL. The common method to measure the turbulent 3D wind vector from research aircraft is a multi-hole probe in combination with an inertial navigation system (INS). By calibration, the pressure readings are used to estimate the airspeed vector of the UAS and with the INS data, multiple coordinate transformations yield the 3D wind vector [45]. This technique originates from manned research aircraft [46] and was adopted by UAS [22,47]. Simplified algorithms to measure the temporally averaged horizontal wind speed and direction such as the "no-flow-sensor" or the "pitot-tube" algorithm, also exist and were compared to the direct 3D wind vector measurement using a five-hole probe by Reference [48].

UAS have the potential to provide new information about the SBL, when applied together with traditional in-situ measurement techniques. Parametrizations of the processes in numerical weather prediction and climate models, yet only apply for stationary and homogeneous surface conditions. The parametrization schemes, for example, the Monin–Obukhov similarity theory (MOST) are known for their shortcomings in characterizing the SBL [49]. Continuous turbulence as a quasi-stationary state may break down and become intermittent. Non-local features such as the stability at higher levels and gravity waves become important, the Coriolis effect and inertial oscillations influence the structure of the SBL and Low Level Jets (LLJ) can develop and generate turbulence by the vertical wind shear [50–54]. For weakly stable boundary layers, transition phases and very stable boundary layers [55] UAS can supplement the limited spatial or temporal coverage of ground-based measurements. On the other hand, SBL conditions also impose challenges for both stationary measurement systems and UAS, since weak turbulent fluxes are difficult to measure and require a high accuracy of the measurement system. Precise and fast measurements of the turbulent 3D wind vector from UAS in combination with meteorological towers and ground-based remote sensing techniques yield new possibilities [56].

The main aim of this study is to validate the turbulent 3D wind vector measurement with MASC-3. To do so, mean values, statistical moments of second order, integral length scales and a spectral analysis can be performed. A comparison to established measurement systems and theory leads towards validation. Firstly, a close comparison with the measurements of a meteorological tower are presented and secondly the data of the tower and the phased array 3D wind Sodar are plotted together with profiles of MASC-3 in a SBL. MASC-3 aims to improve the wind measurement, to gain endurance, to allow operations under an enlarged range of environmental conditions and to enable easy implementation of further sensors by the following measures. The influence on the 3D wind vector measuremnt by the flow field around the aircraft [57] is an important criterion and therefore the new airframe of MASC-3 features a pusher engine in the very back (behind the tail unit) of the UAS as well as a forward-spaced and streamlined sensor hat, where a five-hole probe is mounted (see Section 2.1). Also the flight guidance and the autopilot are of major importance for the 3D wind vector measurement, since the attitude of the UAS, as well as the vehicle velocity, are directly inherited in the calculations. A steady and precise flight of MASC-3 is implemented by the Pixhawk 2.1 "Cube" autopilot (see Section 2.2). The fuselage and the installed sensor hat allow for different payloads, making MASC-3 versatile for many scenarios. The standard payload is described in Section 2.3 and includes an inertial navigation system (INS) Ellipse2-N from sbg-systems [58], a five-hole probe manufactured by the Institute of Fluid Mechanics at the Technische Universität Braunschweig, Germany [59], a fine wire platinum resistance thermometer (FWPRT) developed by Reference [60] and further temperature, surface temperature and humidity sensors. The software architecture is described in Section 2.4 and runs on a Raspberry Pi 3, which allows an easy implementation of future sensors. The in-house developed post-processing software MADA (see Section 2.5) provides a standardized quality control of the gathered data within min after the flight experiment and enables comprehensive quick-looks of mean values and turbulence statistics of the flight experiment.

The measurements of this study were collected during an intensive measurement campaign—"Hailuoto-II"—of the project called Innovative Strategies for Observations in the Arctic

Atmospheric Boundary Layer (ISOBAR). The campaign took place over sea ice at the western shore of Hailuoto island in the northern Bothnian Bay on the coast of Finland in February 2018. The main motivation for the ISOBAR project is to develop and apply a new and innovative observation strategy for the stably stratified boundary layer that is based on meteorological UAS, ground-based in-situ and remote-sensing profiling systems [38]. Two flight experiments were dedicated to closely comparing the MASC-3 measurements with the meteorological tower measurements and were conducted in the evening of the 10 February 2018 over the completely frozen bay area of Hailuoto. The methods for the comparison are described in Section 3.2 and are based on a comparative duration of the time series for the stationary and the moving measurement systems, which correspond to the individual fetch of both systems. Section 4.1 compares the measurements by means of time series analysis for mean values of wind speed and direction, variances, turbulent kinetic energy, covariances and integral length scales of the 3D wind vector measurement. The analysis of a fast evolving SBL during the second flight is given in Section 4.2, where the height profiles performed with MASC-3 are supplemented with the tower and Sodar measurements on the ground, illuminating the vast potential of turbulence measurements with MASC-3 in SBL.

2. Multi-Purpose Airborne Sensor Carrier—MASC-3

A detailed description of the Multi-Purpose Airborne Sensor Carrier (MASC-3) is presented. The design criteria and capabilities of the airframe are given in Section 2.1, followed by a description of the autopilot system Pixhawk 2.1 "Cube" in Section 2.2. The airframe and the autopilot system, as well as the embedded sensor system of MASC-3, were completely reworked compared to the previous version of MASC. The sketch in Figure 1 provides an overview of the new setup. The core of the data acquisition unit is a Raspberry Pi 3, allowing the use of various interfaces to sensor applications, telemetry modules and on-board data processing algorithms. We describe the sensor system in Section 2.3, the data acquisition procedure in Section 2.4 and the post-processing procedure in Section 2.5.

2.1. Airframe Design

MASC-3 is a further development of the environment-physics group at the Center for Applied Geo-Science (ZAG), University of Tübingen, Germany and is based on the previous UAS, which was described, for example, in Reference [18,48]. The overall goals for the new design were increasing the accuracy of the wind measurement, gaining endurance, having more flexibility in implementing further sensors in future applications and allowing operations under an enlarged range of environmental conditions. Figure 1 shows the airframe with its sensor nose in the very front of the fuselage. The positioning was chosen in order to be as far away as possible from potential influences on the measurement. Figure 1 shows the sensor system with the five-hole probe, temperature and humidity sensors. Moreover, the engine is positioned in the back, behind the V-tail of the UAV. Due to the significantly increased distance between the measurement system in the nose and the engine position (see Figure 1), compared to the previous version of MASC, potential influences on the measurements are minimized.

The prop wash, vibrations and the magnetic field of the engine are further away from the sensor system. The power unit consists of a highly efficient electrical pusher setup with a gear unit in order to use a large diameter for the propellers, while keeping the engine speed low. The aerodynamic efficiency is high for cruising speeds around 20 ms^{-1}, since a propeller requires large diameters at rather slow drive rates, resulting, with Li-Ion battery packs, in a highly improved overall efficiency of the drive train, compared to the previous version of MASC. Besides, the point of application of the thrust vector has a much smaller lever arm onto the center of gravity compared to the previous MASC with a pusher engine above and behind the main wings, improving the stability of the flight during acceleration and deceleration of the engine. Due to non-zero vertical wind velocity and changes in

the horizontal wind speed on turbulent scales, or other motions, for example, thermals or up- and down-drafts due to orography, the aircraft reacts with acceleration or deceleration relative to the air.

Figure 1. Multi-Purpose Airborne Sensor Carrier (MASC-3) sketch (**top**) and pictures of the airframe with the sensor system (**middle**) and five-hole probe (**bottom**).

To fulfill the requirements of constant altitude, constant flight direction and constant airspeed, the autopilot system of the UAS controls the angle of attack and the throttle. The reactions of the UAS on changes in the wind field, correlate and are proportional to the momentum and the aerodynamic

drag of the UAS. Also, the individual flight mechanical behaviour of the UAS and its ability to be susceptible to interaction with turbulence are important. Therefore, the aerodynamic drag must be low and the flight mechanical performance of the wing design with a high lift/drag ratio are very important issues for the precision of the wind and turbulence measurement with five-hole probes [45]. MASC-3 meets these requirements superior to the previous version, since the wings and tail are from an aircraft (XPLORER 3 by NAN Models) of international championships in F3J and F5J glider competitions. The wingspan is 4 m. The streamlined fuselage design offers space for versatile configurations and with the broad range of possible wing loads, the total weight can range from 3.5 kg with a standard measurement setup and small battery capacity, up to ≈ 8 kg. The maximum flight duration with 18 ms^{-1} cruising airspeed was proven to be 2 h and is estimated to be 3 h and more. The wings, tail and fuselage are manufactured with fibreglass and carbon fibre composite materials, providing high durability and a light weight construction. With the thermodynamic management of the electrical components, MASC-3 can operate under polar conditions as well as in hot environments. Take-off is performed with a bungee or a winch, if for example, cold temperatures below $\approx -10\,^{\circ}\mathrm{C}$ cause the rubber bungee to fail. Trained pilots can land MASC-3 on a strip of less than 10×4 m, since large air brakes allow fast descents and precise steering during the approach. High manoeuvrability and a broad range of cruising airspeeds between 14 ms^{-1} and more than 30 ms^{-1} allow sampling with high resolution as well as operations in high wind speeds and extreme turbulence.

A new feature of MASC-3 is that it can be equipped with position and strobe lights . Figure 1 shows the lights following the conventions of manned aircraft, allowing take off and landing during night time. As the lighting of MASC-3 fulfills the requirements of the SERA 923/2012 regulation, (see for more details Reference [61]) the aircraft can obtain special permission of the local civil flight authorities for UAS operations during night time and beyond visual line of sight (BVLOS).

Since reduced visibility is challenging for the pilot, the flight guidance with the autopilot system PixHawk 2.1 (see also Section 2.2) allows automatic mode just after release from the take-off rope and automatic approach for manual landing procedures or even entirely autonomous landing, as shown in Figure 2.
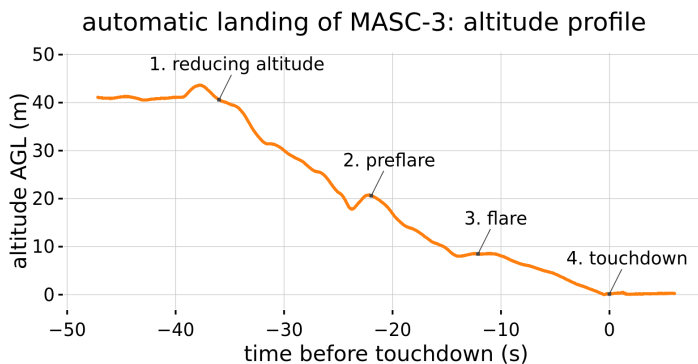

Figure 2. MASC-3 altitude profile during automatic landing procedure.

2.2. Flight Guidance, Autopilot System and Flight Patterns

When measuring wind and turbulence with a five-hole probe, the UAS needs to be able to repeat a flight pattern over the course of multiple flights to increase the statistical validity of the captured data and to allow for comparisons between different measurement flights. These requirements are met by the autopilot system. Common UAS autopilot systems use an INS (Inertial Navigation System) consisting of one or multiple triple-axis accelerometers, gyroscopes and magnetometers (IMU) for attitude and heading control as well as a GNSS (global navigation satellite system) reciever (GPS,

GLONASS, Beidou and/or Galileo) to measure ground speed and location. Some systems may also include a laser altimeter to measure altitude above ground or infrared receivers for communication with ground-based beacons for precision landing. The autopilot system of MASC-3 consists of a Pixhawk 2.1 "Cube" autopilot using a Here+ RTK GPS and magnetometer for position, velocity and heading and a mrobotics MS5525 digital airspeed sensor connected to a pitot-static tube for airspeed measurement. The heated IMU of the Cube allows MASC-3 to operate reliably in very low temperatures and the RTK GPS improves location accuracy over standard GNSS solutions. The Cube is running the open-source Ardupilot autopilot firmware and flight patterns can be programmed before take-off or wirelessly during the flight. Figure 3 shows the flight patterns used for MASC-3 and performed during the ISOBAR campaign Hailuoto-II. The "Rectangle" pattern is the most common one with MASC-3, performing long up- and downwind measurement legs. A rectangle (also called racetrack) is repeated several times at one altitude and one measurement flight normally consists of several racetracks at different altitudes. The up- and downwind portions of one racetrack are called measurement legs. The track marked as Flight #10/#11 shows the flight path of the upwind legs of a rectangle pattern that is used for the comparison in Section 4. The length of the flight legs is ≈1100 m and the northern edge (next to the measurement tower) is the starting point for the southward orientation of the flight legs. The locations of the meteorological tower and the Sodar are also marked in Figure 3 and are used to compared the data with the MASC-3 measurements. The "Circle" pattern is used for profiling with constant vertical ascent rate. With a large enough radius and consequently a low bank angle of the UAS, this pattern can be used for continuous profiles of wind speed, direction, temperature and other quantities. For complex terrain and inhomogeneous conditions, the "Kite" pattern is advantageous over the standard rectangle pattern due to its lack of lateral displacement of the up- and downwind leg. However, while flying Kite patterns, the UAV spends more time in turns, and subsequently, the time spent flying measurement legs per flight is lower than with the rectangle pattern.
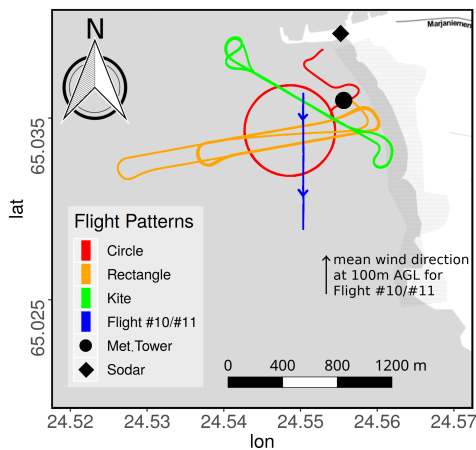
Figure 3. MASC-3 flight paths during the Hailuoto-II campaign. The island is indicated in white color and the grey area indicates water, which was completely frozen during the measurements allowing the installation of the indicated measurement tower. The sodar was installed on the island. The flight paths are plotted from the longitude and latitude readings of the inertial navigation system. The flight path section (leg) of Flight #10 and Flight #11 was used for the comparison between the tower, the Sodar and MASC-3. During Flight #10 and Flight #11 the mean wind direction at 100 m above ground level (AGL) is indicated. Map tiles by Stamen Design (http://stamen.com/) under CC BY 3.0 (http://creativecommons.org/licenses/by/3.0). Data by Open Street Map (http://openstreetmap.org/) under ODbL (http://www.openstreetmap.org/copyright).

The Ardupilot firmware running on the Cube features automatic landings. Figure 2 shows the automatic landing process of MASC-3, which was continuously performed for nocturnal operations during the Hailuoto-II campaign. While approaching the landing spot, MASC-3 engages its flaps and reduces its altitude to 20 m above ground level (AGL). It then executes a preflare by reducing throttle and increasing the pitch angle to reduce its airspeed to 16 ms^{-1}. After further descent to 8 m AGL it executes a flare with further reduction of airspeed to 12.5 ms^{-1}.

The remaining altitude is reduced until touchdown with 12.5 ms^{-1} airspeed. This implemented procedure assures reliable landings of MASC-3 and therefore increases the efficiency of a measurement campaign, especially during operations at night.

2.3. Sensor System Setup

Attached to the Raspberry Pi 3, the standard setup of MASC-3 has a variety of meteorological sensors and power handling devices. The flow diagram in Figure 4 shows the schematic powering and the data flow of the sensor system. The whole system is powered by a single 3S lithium polymer battery with a nominal capacity of 2700 mAh, allowing up-times of ≈4 h. The inertial navigation system (INS) Ellipse2-N from sbg-systems is directly powered by the battery. Since sensors and other periphery are running with 5V, the voltage coming from the battery is stepped done by a Traco Power (2 Ampere maximum current) DC-DC converter, providing a low noise power source. A USB Hub and the Raspberry Pi are directly powered from the 5V DC source. The USB Hub powers the CEBO-LC analogue-digital converter which handles the analogue signals and an Arduino which controls the digital sensors. The USB connections are also the data interfaces, for the CEBO-LC and the Arduino . The INS Ellipse2-N is also connected via USB to the Raspberry Pi.
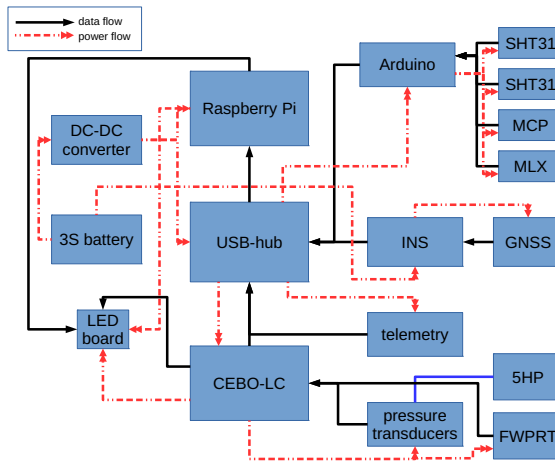
Figure 4. Data and power flow diagram of the MASC-3 sensor system

The standard sensor system consists of the following sensors:

- Inertial navigation system (INS) Ellipse2-N from sbg-systems [58]; consisting of an inertial measurement unit, a GNSS receiver and an extended Kalman Filter, measuring attitude, position and velocity of MASC-3. With 3 Axis Gyroscopes, 3 Axis Accelerometers, 3 Axis Magnetometers, a pressure sensor and an external GNSS receiver, the INS has $0.1°$ roll and pitch accuracy, $\approx 0.5°$ heading accuracy, 0.1 ms^{-1} velocity accuracy and 2 m position accuracy. The accuracy is provided by the manufacturer and the test conditions for these specifications are proprietary and may not represent the performance during flight.

- Five-hole probe; manufactured by the Institute of Fluid Mechanics at the Technische Universität Braunschweig, Germany, measuring the flow angles and magnitude (airspeed vector) onto the probe at turbulent scales [59].

- Pressure transducers; $5\times$ LDE-E 500, $1\times$ LDE-E 250 for the static pressure port and a HCA0811ARG8 barometer. The differential pressure transducers are rated with an offset long term stability of ± 0.05 Pa and a response time ($\tau 63$) of 5 ms.

- Fine wire platinum resistance thermometer (FWPRT); developed by Reference [60] with a 12.5 micrometer platinum wire, in order to measure the air temperature at turbulent scales.

- CEBO-LC from CESYS; providing an analogue-digital conversion of 14 single-ended or 7 differential analogue inputs with a measurement resolution of 16 bit. The accuracy is rated 0.005% Full Scale (typical) after Calibration and provides high-impedance operational amplifier inputs with a total sample-rate of 65 to 85 kSPS and a response-time (latency) of typically 0.9 ms and maximum 4 ms.

- SHT31 temperature and humidity sensor from Sensirion; fully calibrated, linearized, and temperature compensated digital output of temperature and relative humidity with a typical accuracy of $\pm 2\%$ RH and ± 0.3 °C. The response time for humidity ($\tau 63$) is rated to be 8 s and the response time of the temperature ($\tau 63$) is 2 s.

- MLX90614 infrared object temperature sensor; facing downwards surface temperature measurement with a resolution of 0.02 °C and a measurement accuracy of 0.5 °C

- MCP9808 temperature sensor; additional temperature measurement for surveillance of the temperature of the electrical components of the sensor system.

The analogue signals of the turbulence measurements of the temperature and the 3D wind vector, acquired by the FWPRT and the five-hole probe together with the pressure transducers, are sampled with 500 Hz and converted by the CEBO-LC analogue-digital converter. The data stream is buffered by the CEBO-LC microcontroller, using a 32 Bit counter to ensure accurate temporal progression, and is logged by the Raspberry Pi 3. The digital sensors (SHT31, MLX, MCP) are controlled by an Arduino and logged with 10 Hz. The INS data has an update rate of 100 Hz (can be set to maximum 200 Hz) and is logged directly by the Raspberry Pi 3. Besides, a telemetry link to a laptop with a ground-station software allows the surveillance of an abstract of the data at 1 Hz.

Malfunctions of the sensors can be detected during flight and preliminary results can be plotted and, if needed, the flight strategy can be adapted. This telemetry link is provided by a small radio module (XBee) within the 2.4 Ghz band. The ground station software is also capable of calculating and displaying the potential temperature profile of the ABL on the fly, making it possible to sample more often in the layers of interest. The SHT31 sensor is mounted in two positions on the sensor system. One of them is mounted outside in a tube (see Figures 1 and 5), acting as radiation shield, in order to measure the ambient air temperature and humidity alike the FWPRT. The other one is mounted inside the sensor hat to measure the temperature and humidity close to the other hardware and to monitor the temperature inside, which might be crucial in very hot or very cold conditions. The MCP9808 temperature sensor is mounted close to the pressure transducers, which are further in the front of the sensor hat, in order to monitor changes of the temperature also there. Figure 5 shows the sensor hat that is mounted on the MASC-3.
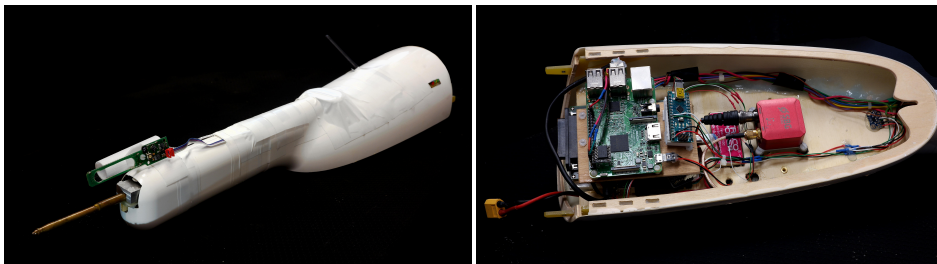

Figure 5. Sensor system hat (**left**) and mounted electronics inside the sensor hat (**right**).

2.4. Sensor System Software

The data acquisition on board the sensor hat of MASC-3 is managed by the open-source single-board computer Raspberry Pi 3. The software is designed to be a modular system that allows for switching between different sensor configurations as well as installing new sensors. A large pool of open source code examples and ready made application programming interfaces (API) allow fast implementation of new sensors. Figure 6 shows the schematic architecture of the software. The data acquisition of each individual sensor is managed by a self-contained process that connects to the sensor, logs the data on the SD card and transmits a reduced live data stream to the ground station. This design was chosen to allow for maximum freedom in choosing sensors without the restriction of being dependent on a specific programming language used by the available API of the sensor. The data acquisition software for a sensor can be written in any programming language supported by that sensors API, instead of having to create a new and potentially unreliable interface in a different programming language. The transmission of the live data stream from each sensor to the ground station software is handled by the Sensor Manager. This process is launched after the Raspberry Pi booted and starts the respective data acquisition program for each sensor in the current configuration.

The live data stream from the sensor data acquisition processes is then captured and forwarded to the ground station via telemetry modules. The ground station software detects the incoming data streams and allows plotting them against each other. To ensure the modularity of the system, the logged data is not synchronized on-board. Instead, all data is oversampled and has both, the timestamp or counter of the underlying sensor, as well as the timestamp of the system time of the operating system, which itself is updated and checked against an external hardware clock. The data is synchronized during post processing by cross-checking the timestamps and counters of each of the sensors. The Raspberry Pi 3 provides data of critical parameters of the Hardware and the operating system, including for example, CPU (central processing unit) working load, CPU temperature and so forth. Along with the remaining capacity on the SD-card, which helps the ground station observer to see whether the logging process runs properly, this data is also logged and partially transmitted to the ground station.
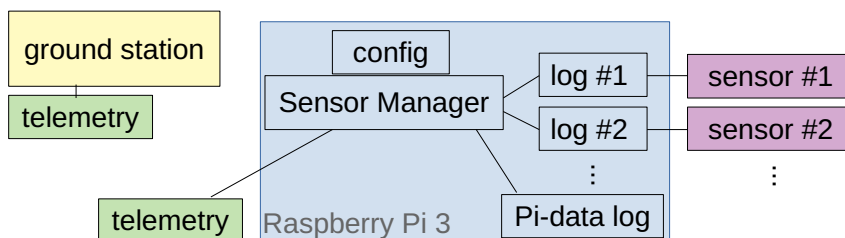

Figure 6. Schematic software setup of the sensor system on-board MASC-3.

2.5. Meteorological Airborne Data Analysis (MADA)

After each flight experiment, the stored data on the SD-Card of the Raspberry Pi 3 can be for example, downloaded via Ethernet. Since the CEBO-LC, the INS Ellipse2-N and the Arduino have separated log files, the data has to be merged. The first post-processing is done with the developed software MADA (Meteorological Airborne Data Analysis) which is a cumulative series of scripts based on the open source software R. The most important issue is the temporal synchronization of the data to one common time vector. The accuracy of the 32 Bit counter of the CEBO-LC and the INS, which also includes a 32 Bit counter as well as GNSS-time, ensures the accuracy of the synchronization, making the timestamps of the Raspberry Pi itself almost obsolete. Only the first and last timestamps of the Raspberry Pi inside the individual sensor log files are used to initially synchronise the logs. Subsequently the Pi time is used to double check the accurate temporal progression of the fused data. After synchronization, MADA provides scaling of the analogue sensors (e.g., FWPRT, pressure transducers, etc.) according to the calibration and data sheets. Then all data is sorted and meteorological data is calculated (e.g., air density etc.). After this pre-post-processing a first wind calculation is performed.

The 3D wind vector, using five-hole probes, is calculated by the summation of the ground speed vector of the UAS and the true airspeed vector of the UAS. The ground speed vector is directly given by the INS Ellipse2-N. By calibration, the pressure readings of the individual holes of the probe are used to estimate the true airspeed vector. To find a relationship between the measured pressure differences on the prope's pressure holes and the airflow angles, as well as the dynamic and static pressure at any airflow angle within the calibration range, wind-tunnel calibrations were conducted. In the wind tunnel, the airspeed is set for the calibration. With dimensionless coefficients, a set of polynomial functions for the airflow angles and the dynamic and static pressure are determined. These calibration polynomials are finally used to convert the pressure readings of the measurement to the true airspeed vector of the UAS [45]. With the attitude, position and velocity of the UAS, measured by the INS,

multiple coordinate transformations finally yield the wind vector. This method is widely used with UAS [18,22,47] and was originally used with manned aircraft [62]. A detailed description of the method is given in the study described in Reference [48], which also compares this direct method of the 3D wind vector measurement with simplified algorithms.

After the initial calculation of the 3D wind vector, a set of plots is printed out in order to get a first overview of the flight. Subsequently, suitable pairs of flight legs (straight, horizontal flight sections) for the wind correction [47] are identified by the software MADA. Since a misalignment between the five-hole probe's orientation and the UAS cannot be avoided, three offset corrections for the Euler Angles $\Delta\Phi$ (roll), $\Delta\Theta$ (pitch) and $\Delta\Psi$ (yaw or heading) must be determined. A fourth correction factor f_{tas} for the norm of the true airspeed vector accounts mostly for the calibration in the wind tunnel, which never matches exactly the conditions during the measurements. The assumptions for the in-flight calibration are a constant mean horizontal wind, a mean vertical wind near zero and low turbulence or turbulent transport. This allows a comparison of the wind components for two consecutive straights in opposite directions (star pattern), or identical legs in reverse direction. The correction offsets and factor for the presented flights in Section 4 were each determined with two pairs of legs in reverse direction on $\approx$100 m AGL. The procedure to calculate the correction factors was explained in detail in Reference [47] and analyzed with regard to the calibration of the five-hole probe and turbulence measurements in Reference [45]. If the meteorological conditions did not change substantially, the correction offsets and factor can be taken from previous flights, at least for a preliminary analysis in the field.

Afterwards, the meteorological data is processed again, including the corrections for the wind vector components. A first quality control with several plots of the measured quantities along the flight legs are printed out. Additionally, the power spectra and structure functions of the main quantities are plotted for a the quality control just after the measurements. Furthermore, vertical profiles of wind speed, wind direction and turbulence quantities are provided, containing the data of each flight leg. These quick looks are essential to get a brief overview of the meteorological conditions. An adaption of the flight patterns for consecutive flights can be considered, or a sensor malfunction can be identified. The set of plots is at hand, minutes after landing the UAV. The MADA software concept and the first analysis on sight is the foundation for a detailed post-processing of all measured data but also a key element for successful field campaigns. Uncertainty analysis of the wind vector measurement, such as the influence of the calibration procedures of the five-hole probe, airspeed variations of the UAS during the measurement, the influence of dynamic motion of the UAS and an estimation for the error propagation is given in References [45,47].

3. Methods and Data

An important difference, when comparing turbulence measurements with fixed-wing UAS along a straight, horizontal flight path (leg), with measurements of meteorological towers is, that the UAS transects the air with its cruising airspeed and the tower measures the air that is advected with the mean flow. Since MASC-3 is not dependant on the mean flow it is capable of gathering quasi-spatial snapshots with higher temporal resolution than the tower. The most important criteria to do so is a fast sensor, able to capture most of the energy inheriting fraction of the inertial sub-range of turbulence. The most important underlying assumption for a comparison is Taylor's hypothesis of frozen turbulence [1], which was found to be applicable to the smallest scales of turbulence at high frequencies or low wave numbers [2]. For the larger scales, especially for atmospheric flow under the influence of the diurnal cycle, coherent structures or the variability of the geostrophic wind, differences due to production and diffusion processes of turbulence persist if a quasi-spatial snapshot is sampled with an aircraft and compared to fixed-point measuremnt with a tower [3,63]. Coming along with that, the important question of how long is long enough for a horizontal flight leg [9] when calculating turbulence statistics, causes further complexity, making comparisons between the moving UAS and a stationary tower challenging.

3.1. Statistical Methods

The wind vector components can be compared separately and a differentiation between the horizontal components u (positive eastward) and v (positive northward) and the vertical wind component w (positive when facing upwards) is insightful. The horizontal wind speed v_h is calculated with the wind vector components u and v by

$$v_h = \sqrt{u^2 + v^2}. \tag{1}$$

Furthermore, the variances for the wind vector components must be compared for a validation. The variance of a variable X is

$$\text{Var}_X = \sigma_X^2 = \frac{1}{N-1} \sum_{i=1}^{N} (X_i - \overline{X})^2, \tag{2}$$

where N is the number of data points and $\overline{X}$ denotes the mean of the variable within the data window which, in this case, is the length of individual flight leg. The covariance Cov_{XY} of two variables is

$$\text{Cov}_{XY} = \frac{1}{N-1} \sum_{i=1}^{N} (X_i - \overline{X})(Y_i - \overline{Y}). \tag{3}$$

The turbulent kinetic energy TKE is

$$\text{TKE} = \frac{1}{2} \left(\text{Var}_u + \text{Var}_v + \text{Var}_w \right). \tag{4}$$

The integral time scale $I(X)$ of a quantity X is defined by

$$I(X) = \int_0^{\tau_1} \frac{\sigma_X(t+\tau)\,\sigma_X(t)}{\sigma_X^2} \, d\tau. \tag{5}$$

The integral time scale $I(X)$ is the autocorrelation function of the variable X and calculated by integration from zero lag to the first crossing with zero at τ_1 [64] and is multiplied by the mean true airspeed $|\overline{\vec{u}_a}|$, calculated for example, according to Reference [45],

$$L(X) = I(X) \, |\overline{\vec{u}_a}| \tag{6}$$

or, respectively for the measurement tower, by the mean horizontal wind speed $\overline{v_h}$ in order to get the integral length scale $L(X)$ [3,64–66].

The integral length scales of the horizontal wind speed $L(v_h)$ and the vertical wind $L(w)$ are considered in this study. The integral length scale can be interpreted as the typical size of the largest, or most energy-transporting eddy. To analyse the scale dependence of turbulence and to evaluate whether the inertial sub-range is sufficently resolved [4], spectra and structure functions of the horizontal v_h and vertical wind w are analysed and compared to the measurements of the tower. The frequency spectrum—or power spectrum $S_X(f)$—of a quantity X is calculated for a time series of length Δt with the time steps t and after applying a Hann window by

$$S_w(f) = \int_0^{\Delta t} \text{Cov}_{XX}(t) e^{2\pi i f t} \, dt = \frac{1}{\Delta t} \tilde{X}^*(f) \, \tilde{X}(f) = \frac{1}{\Delta t} |\tilde{X}(f)|^2 \tag{7}$$

with the frequency f, imaginary unit i, covariance function from Equation (3) and the Fourier transformed frequency series $\tilde{X}(f)$ and its complex conjugate $\tilde{X}^*(f)$. For locally isotropic turbulence, the inertial subrange is characterized by the $-5/3$ slope in the spectrum. In order to compare the data

of a moving UAS with the data of a stationary measurement tower, the frequency spectra $S_X(f)$ are transformed into wavenumber spectra $S_X(k)$ by

$$k = \frac{2\pi f}{\overline{v}} \tag{8}$$

using for the transformation of the evaluated period the mean velocity $\overline{v} = \overline{v_h}$ of the horizontal wind speed of the measurement tower and the mean true airspeed $\overline{v} = |\overline{\vec{u}_a}|$ of the UAS measurements. The structure function $D_X(s)$ of a quantity X is calculated for a time series with N data points, the time steps t and the temporal shift or lag s by

$$D_X(s) = \frac{1}{N-n} \sum_{i=1}^{N-n} (X(t) - X(t+s))^2, \tag{9}$$

where n is the number of data points associated with the lag s. For locally isotropic turbulence, the inertial subrange is characterized by the a 2/3 slope in the structure function.

To compare the structure function $D_X(s)$ of a time series between the moving UAS data and the stationary tower data, the temporal shift or lag s is transformed into a spacial lag r by

$$r = s\,\overline{v} \tag{10}$$

also using for the transformation of the evaluated period the mean velocity $\overline{v} = \overline{v_h}$ measured by the tower and $\overline{v} = |\overline{\vec{u}_a}|$ measured by the UAS. The structure function and the power spectra of the horizontal wind D_{v_h}, S_{v_h} and the vertical wind D_w, S_w are considered in this study.

Differences concerning the fact that MASC-3 samples a quasi-spatial snapshot along a straight and horizontal flight leg with its cruising airspeed and that the stationary tower samples the advected air flow can be considered by comparing the quantities of interest for time series that have the same temporal fetch. The temporal fetch is represented by the approximated time interval for the individual measurement system during which the same volume of air was sampled. To account for that, the considered duration of the time series Δt for the comparisons in Section 4 inherit the same temporal fetch calculated by

$$\Delta t_{\text{tower}} = \Delta t_{\text{UAS}} \frac{v_{\text{UAS}}}{v_{\text{tower}}} = \Delta t_{\text{UAS}} \frac{|\overline{\vec{u}_a}|}{\overline{v_h}}, \tag{11}$$

using the mean true airspeed $|\overline{\vec{u}_a}|$ of the UAS divided by the mean horizontal wind speed $\overline{v_h}$, measured by the UAS.

This factorization for defining the duration of the compared time series complies with the full duration of the MASC-3 flight leg and the corresponding duration of the time series of the tower measurement Δt_{tower} is calculated with Equation (11).

3.2. Meteorological Tower and Sodar Measurements for Comparison

During the Hailuoto-II measurement campaign at the eastern coast of the north Bothnian Bay, Finland, two flight experiments were dedicated to compare the MASC-3 measurements with the meteorological tower (see Figure 7) measurements. Both flights, Flight #10 and #11 (Figure 3), were conducted on the 10 February 2018 around 17:00 (EET) and 22:00 (EET) over the completely frozen bay area west of the island Hailuoto. Civil Twilight started at 17:25 (EET) and night started at 19:21 (EET) on the measurement day.

The meteorological conditions during the evening of the 10 February 2018 were characterized by a high pressure system over Siberia and a low pressure system just south of Iceland with a relatively weak pressure gradient at our observation site. The local conditions were mostly cloudy or partially cloudy with a cloud base height below 500 m before 17:00 UTC. Between 17:00–18:30 UTC the sky opened

up and became clear. Temperatures were quite moderate, slightly below freezing and decreasing throughout the evening and night . The wind direction was from south with a weak shift towards SSW and SW during the night. Relatively high wind speeds of up to 10 ms^{-1}, observed at the permanent weather station at 46 m above sea level declined and stabilized at 5–7 ms^{-1} after 22:00 UTC.

Figure 7. Meteorological measurement tower during the Hailuoto-II campaign. Viewing direction is north-north-east towards the harbour and the village Marjaniemi. The picture was taken by Kristine Flacké Haualand.

The MASC-3 measurements were synchronized with the mast measurements using the Equation (11), because the aim is to sample the same volume of air with both systems. Since both flights started nearby the mast (Figure 3), the first timestamp was chosen to be the same for both systems.

CSAT3 (Campbell Scientific, Inc., Shepshed, UK) sonic anemometers were deployed at three levels of the meteorological tower, at 2.0 m, 4.5 m and 10.3 m heights. These instruments provide measurements of the three wind velocity components and the sonic temperature at 20 Hz frequency. The data were first checked for unphysical values and spikes. The thresholds for unphysical values were ±30 ms^{-1} for horizontal wind components, ±10 ms^{-1} for the vertical wind component and ±30 °C for the sonic temperature. Spikes were detected using the method described by Reference [7]. The value of the next point in the time series was predicted based on weighted average of the last value and the mean of the last 80 values (which corresponds to a time interval of 4 s with 20 Hz sampling frequency). The weight of the last value depends on the auto-covariance between the consecutive values in the window of 80 values. If the absolute difference between the predicted and the observed value exceeds a certain threshold times the standard deviation of the last 80 values, the observation is considered as a spike. The detection algorithm was applied with a moving window of 80 values and a spike detection threshold of 4.0 and 5.5 (and an increase in threshold by 0.1 and 0.5 after each iteration, to account for the decreased standard deviation after removal of spikes) for the wind components and the sonic temperature, respectively. Spike detection was first applied forward in time and then backwards. Only those spikes that were detected as spikes from both directions were finally considered as spikes. During the selected period, 14:30–22:00 UTC on 10 February 2018, only a few (from 0 to 4 out of 540,000) individual suspicious values were detected for each variable and measurement height. These individual spikes in the 20 Hz data were replaced by linear interpolation using neighboring good quality values. After the quality control, momentum flux convergence was evaluated by ogive test [67]. Ogive function is the cumulative integral of the co-spectrum starting from the highest frequencies. The convergence is achieved when the function reaches a certain level where

no more energy is gained by including larger scales. In ideal conditions, ogive function can be used to detect the location of the spectral gap between the turbulent scales and diurnal/synoptic scales. Results of the ogive method are shown in Figure 8 for the 3 different heights of the tower indicated by different colors.

The ogive functions are normalized by the value at the point closest to the frequency corresponding to 10 min period. At all levels, the ogive function reached the value 1.0, that is, the convergence, in less than 10 min. As expected, the convergence was reached faster closer to the surface than at higher levels of the tower. Further, at least 80% of the total flux was covered already within 60 s, which makes the data set suitable for comparison of turbulence measurements from the tower and MASC-3. Based on the results from the ogive test, we chose a fixed 10 min sample length for the tower measurements. For each 10-min sample, the wind components (originally in the inertial coordinate system) were rotated using 2D rotation method to align the wind components along the mean wind ($\overline{u_{rot}}=\overline{v_h}$) and perpendicular to it ($\overline{v_{rot}} = \overline{w_{rot}} = 0$). The turbulence statistics were then calculated using these rotated 10 min samples.
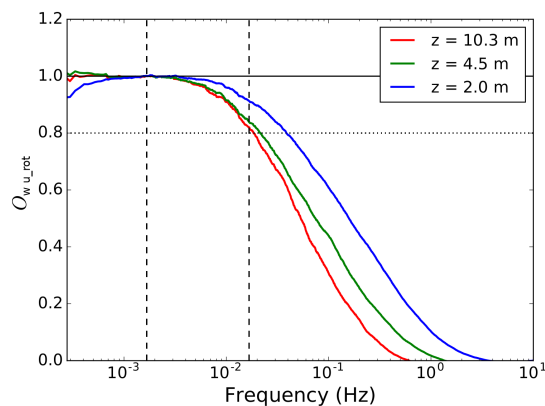

Figure 8. Results of the ogive test between vertical w and the horizontal u_{rot} wind components using all observations from the three tower heights during the period 10 February 2018 14:30–22:00 UTC. Ogives are normalized by the value at the point closest to the frequency corresponding to 10 min, indicated by the first vertical dashed line from left. The second vertical dashed line represents the frequency corresponding to 60 s.

With the prevailing wind direction for both Flights #10/#11 of $\phi \approx 150°$ at the height level of the comparison between the tower and MASC-3, the flow is advected over the south-western edge of the island Hailuoto (see Figure 3). For these conditions, the shore of Hailuoto was $\approx$1500 m away from the tower. The shore area is not forested but the structure of the surface comprises unevenness. Generally, the structure of the surface and its roughness was not totally homogeneous. Apart from the shore of Hailuoto and the harbor, the vicinity of the measurement site was covered with isolated ice features with heights of $\leq$0.5 m. Close to the shore area, some bigger ice ridges of up to 3 m persisted. The footprint for both systems, MASC-3 and the tower may therefore influence the comparison.

A MFAS Sodar system (Scintec AG) was installed at the Hailuoto-II field site on the shore line (see Figure 3) with a base height of approximately 5 m above the sea level. The acoustic Sodar antenna of the MFAS consists of 64 piezo-electric transducers, emitting and receiving sound pulses at 10 different frequencies in the range 1650 Hz–2750 Hz and an output power of 7.5 W. The MFAS can emit acoustic signals in 5 different directions, vertically and tilted in N, E, S and W direction. This enables for the computation of 3-dimensional wind profiles at a vertical resolution of 10 m,

ranging from 30 m to 1000 m. However the maximum range of the system was typically below 600 m. The temporal resolution of the Sodar data is 10 min, due to measurement sequence chosen for Hailuto-II. The manufacturer stated the accuracy for the wind speed and direction to be ± 0.3 ms^{-1} and $\pm 1.5°$, repsectively. For the comparison of the vertical profiles of the horizontal wind we chose one or two Sodar profiles, that matched the time periods of the MASC-3 ascents or descents. Only high quality Sodar data (i.e. high cumulative significance and significance density; temporal and spatial consistency) are taken into account for the analyses presented in Section 4.2.

4. Results

In this Section, we will first compare measurements from two horizontal low level flight legs of Flight #10 with measurements from the meteorological tower (Section 4.1). This will provide an overview of the quality of the MASC-3 data. Then, in Section 4.2, we will illustrate the potential of MASC-3 to complement meteorological mast and Sodar measurements by providing measurements from several heights of Flight #11. From these horizontal flights at multiple heights it is possible to derive profiles of mean atmospheric quantities that can be compared to the sodar measurements, as well as profiles of turbulence quantities.

4.1. Comparison of Measurements from MASC-3 and the Meteorological Tower

For Flight #10, with a mean sampling time for the two flight legs of $\Delta t_{\text{UAS}} = 80$ s, the corresponding sampling time of the measurement tower is $\Delta t_{\text{tower}} = 170$ s, since the true airspeed was $|\overline{\vec{u}_a}| = 19.7$ ms^{-1} and the mean horizontal wind speed $\overline{v_h} = 9.25$ ms^{-1} (Equation (11)). The first part in Section 4.1 analyses the power spectra (see Equation (7)) and the structure function (see Equation (9)) of the horizontal and vertical wind of one flight leg of MASC-3 and the corresponding data of the measurement tower in Figure 9. To allow comparability, the frequency spectra are transformed into a wavenumber spectra, using Equation (8) and the structure functions, computed over temporal lags, are transformed into spatial legs with Equation (10). To closely compare the two measurement systems, the time series of the measurement tower is plotted and the data of the two spatially closest flight legs of Flight #10 are included in the set of plots in the Figures 10–13. The time series inherited in the power spectra and the structure functions is the same than the first flight leg in the following set of figures.

The set of figures consist of the two neighboring sets of data points, which are the 10 min periods of the tower measurement on the three height levels (10.3 m, 4.5 m, 2 m AGL). Additionally, the data at 10.3 m AGL is plotted as moving average, variances covariance and TKE calculated on a moving window. The window size for the moving calculation of the quantities is $\Delta t_{\text{tower}} = 170$ s, allowing a close comparison with the data points of the MASC-3 measurement. Further, the integral length scales of the horizontal $L(v_h)$ and vertical $L(w)$ wind are plotted A moving calculation of the integral length scale according to Equation (5) is not feasible, since the autocorrelation function must be manually checked for plausibility since it may fail and not converge to a τ_1 [64]. Therefore, a moving integral length scale is not feasible, but the actual comparison with MASC-3 and the additional calculations of L on time series of length $\Delta t_{\text{tower}} = 170$ s are given to analyze the temporal variability during the comparison.

The wavenumber spectra and the structure functions for the horizontal wind v_h and the vertical wind component w in Figure 9 give insight in the resolution of both measurement systems. The inertial subrange of turbulence in an isotropic flow is characterized by the $k^{-5/3}$ slope in the power spectrum and by the $r^{2/3}$ slope in the structure function, indicating the ability and quality of the measurement system to resolve the spectrum of turbulent fluctuations in the atmospheric boundary layer. Generally, the discretization of the structure function is sparse towards small lags and the influence of sensor noise is better visible in the power spectrum. Vice versa, the power spectrum is sparsely discretised for small wave numbers and to study the production subrange and the onset of the inertial subrange, the structure function is beneficial.

The power spectrum of v_h of the tower measurement is located slightly higher than the spectrum of the MASC-3 data, since the variances of the vertical wind Var_{v_h} (visible in Figure 11) of the tower measurement are also slightly higher. The structure functions of both time series for v_h agree well in the inertial subrange but in the production subrange the curve of the tower data lies above the curve of MASC-3, which can also be explained by the difference in the variance measurements of both systems of ≈ 0.05 m^2 s^{-2}. If the variance, as an indicator of turbulence, is higher, the spectra is located higher and the production subrange is elevated. Although only ≈ 2 m altitude offset persist between the sonic anemometer and the average flight level of MASC-3, this can explain the differences, since the structure of the surface layer changes strongly with height (indicated e.g., by the 10 min averages at the three tower levels in the set of plots in the Figures 10 and 11). The power spectra and the production subrange in the structure functions lie close together for the vertical wind component w, since the variances of the vertical wind Var_w are almost identical. Also the gradient $\Delta\text{Var}_w/\Delta z$ is smaller than $\Delta\text{Var}_{v_h}/\Delta z$, when looking at the ten minute averages of the tower measurements (see Figure 11).

The ability to resolve the smallest structures can be closely compared when looking at the power spectra and towards growing wavenumbers. For v_h and w and for both measurement systems, a flattening of the spectra into the horizontal, indicating sensor noise, can be observed starting from $k \approx 4$ m^{-1} for the tower and from $k \approx 10$ m^{-1} for MASC-3. Both measurement systems seem to resolve the fluctuations of w slightly further. The structure functions indicate, that the onset of the inertial subrange of v_h starts at lags of ≈ 20 m for MASC-3 and the tower. Discrepancies can be seen in the structure functions of w, where the $r^{2/3}$ slope is reached only at smaller lags for MASC-3 ($r \approx 20$ m) than for the tower ($r \approx 10$ m). The inertial subrange for the vertical wind component close to the ground is shifted towards smaller structures due to the stability of the boundary layer. The length scales of the vertical wind are smaller than for the horizontal wind, which is also reflected in Figure 13. Following that, the inter-comparison of the structure functions for the MASC-3 data between v_h and w does reflect this. For the tower data, this feature is less pronounced. The structure functions of v_h and w of the MASC-3 data become steeper towards the lowest lags, also indicating the onset of sensor noise. The structure functions of the tower data do not indicate the onset of sensor noise as clear as the power spectra do. With sensor noise starting from $k \approx 4$ m^{-1} for the tower and from $k \approx 10$ m^{-1} for MASC-3 and by using Equation (8) it can be stated that, MASC-3 has, with 30 Hz, a significantly higher temporal resolution as the sonic anemometer with 6 Hz.

Figure 10 shows the horizontal wind v_h and the wind direction ϕ during the period when MASC-3 performed the flight legs of Flight #10 at the lowest level. The graph consists of the 10 min averages for the tower measurement at the height levels 10.3 m, 4.5 m and 2 m AGL, as well as of the moving average and the moving standard deviation at 10.3 m of v_h and ϕ. The wind speed, calculated from the MASC-3 flight legs, is higher than the curve of the moving average of the tower but the error bars are overlapping. One reason is the strong gradient of the horizontal wind speed, as indicated by the 10 min averages of the tower measurement. The height offset of the flight path and the highest level of the tower is only 1–2 m and the offset of v_h is 0.75–1 ms^{-1}. Although considering the gradient of the 10 min averages of the tower, a slight discrepancy of the wind speed with MASC-3 persists. The longitudinal offset of ≈ 100 m between the flight path and the tower and the slightly different footprint of the flow may explain this remaining small offsets. The wind direction ϕ agrees with the moving average of the tower for the first leg and differs by only 2° for the second leg. For both legs, the values of MASC-3 are within the error band of the tower measurement. Figure 10 shows, that the wind direction and speed was quite stationary during the period of comparison. The average flight level of MASC-3 with 11.7 ± 0.2 m AGL for the first leg and 11.4 ± 0.3 m AGL for the second leg indicate that the flight level is held precisely by the autopilot. Especially in SBL with large vertical gradients, this is important for the accuracy of the measurements with MASC-3.
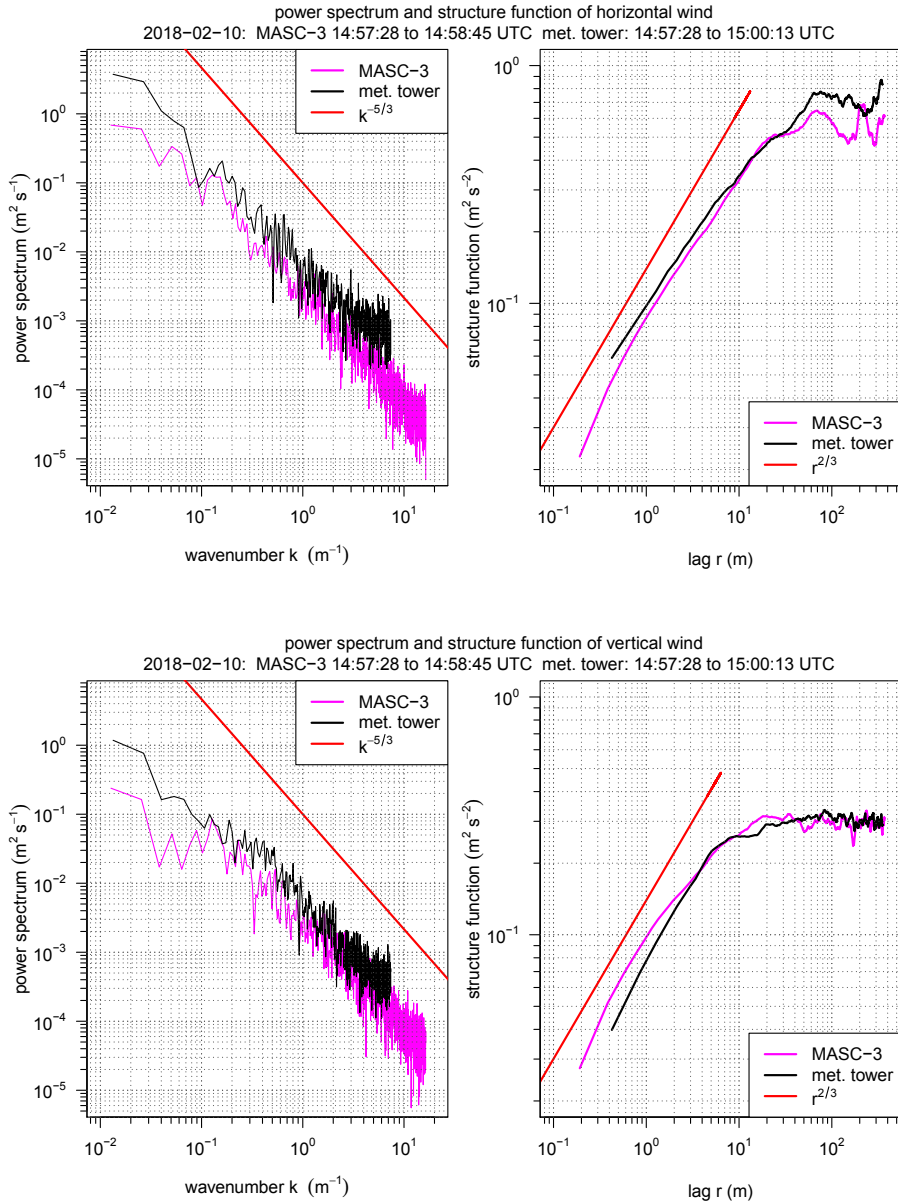
Figure 9. Wavenumber spectra (**left**) and structure functions (**right**) for the horizontal wind v_h (**top**) and the vertical wind vector component w (**bottom**). The data of the tower at the 10.3 m level inherits a time series of $\Delta t_{tower} = 165$ s, corresponding to the fetch of the MASC-3 flight leg with a duration of $\Delta t_{UAS} = 77$ s. Flight #10 and the first leg at 11.7 m AGL is given.
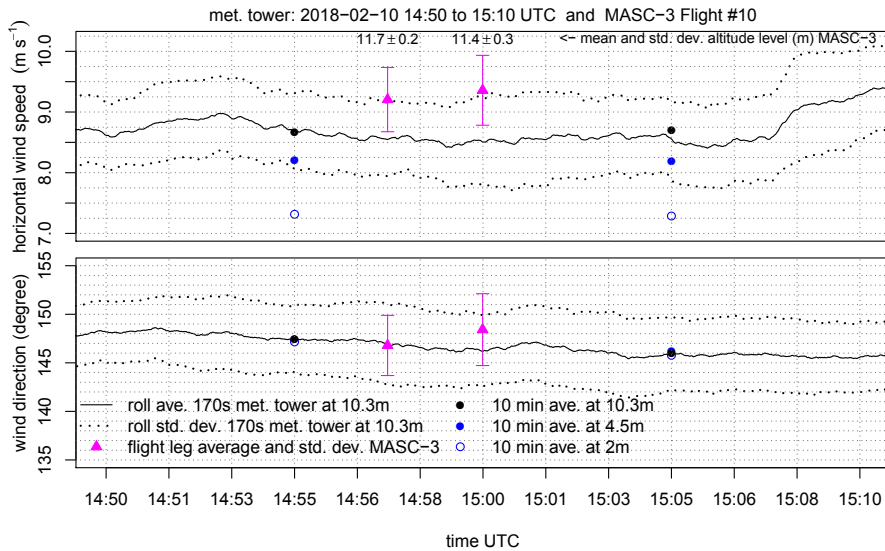
Figure 10. Time series of the tower with the corresponding leg averages and standard deviation of MASC-3 at the lowest flight levels for the horizontal wind v_h (**top**) and the wind direction ϕ (**bottom**). The mean altitude and standard deviation of the individual flight leg is given for the MASC-3 data points. The data of the tower at 10.3 m is plotted as rolling (moving) average with standard deviation and a window length of $\Delta t_{\text{tower}} = 170$ s corresponding to the fetch of the MASC-3 flight legs with an average duration of $\Delta t_{\text{UAS}} = 80$ s. Furthermore the neighboring ten minute averages of the tower at all height levels are given.

The variances of the horizontal wind speed Var_{v_h} and the vertical wind vector component Var_w are given in Figure 11. The first flight leg of MASC-3 shows, with ≈ 0.05 m^2 s^{-2}, a smaller value for Var_{v_h} than for the tower. The second flight leg has a deviation of ≈ 0.15 m^2 s^{-2}. The calculation of Var_{v_h} on the moving window shows a temporal increase during the second flight leg, concluding that the flow field is not stationary. The deviations can be partly explained by the strong gradient, as indicated with by the 10 min values of the tower ($\Delta \text{Var}_{v_h}/\Delta z$), as well as by the temporal and spatial variability. The data points of the variances of the vertical wind vector component Var_w agree very well with the tower measurements. This quantity is less subject to temporal change or the influence of gusts and transient motions on minute time-scales during the period of comparison, than Var_{v_h}. Although the 10 min values of the tower also indicate, with a changing offset between the height levels (gradients $\Delta \text{Var}_w/\Delta z$) between the first and the second group of values, that the state of the boundary layer changes.
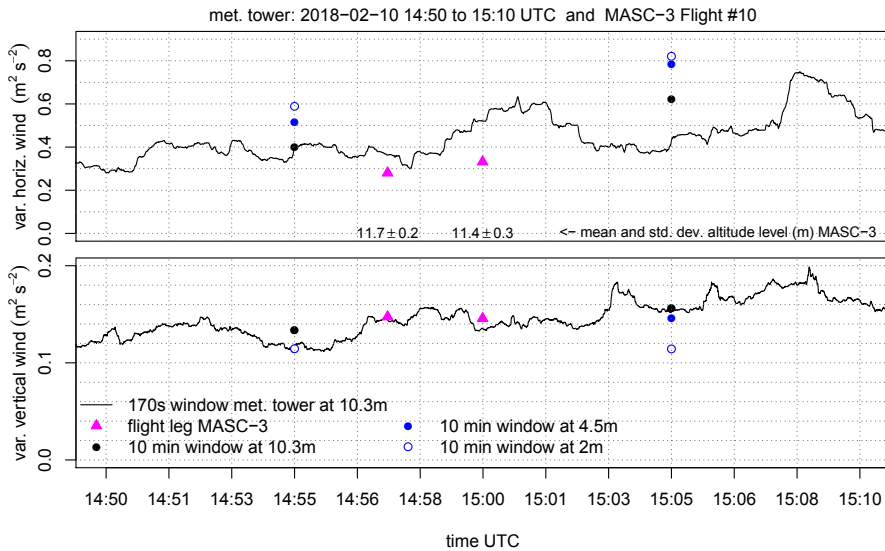
Figure 11. Time series of the tower with the corresponding leg averages of MASC-3 at the lowest flight levels for the variance of the horizontal wind Var_{v_h} (**top**) and the vertical wind component Var_w (**bottom**). The mean altitude and standard deviation of the individual flight leg is given for the MASC-3 data points. The data of the tower at 10.3 m is calculated on a moving window with a width of $\Delta t_{tower} = 170$ s corresponding to the fetch of the MASC-3 flight legs with an average duration of $\Delta t_{UAS} = 80$ s. Furthermore the neighboring ten minute averages of the tower at all height levels are given. The Var_w for the first ten minute interval of the tower at 10.3 m and 4.5 m lie on top of each other.

The turbulent kinetic energy TKE in Figure 12 also agrees very well between the measurement systems. The temporal evolution of the structure of the boundary layer is again visible in the gradients $\Delta TKE/\Delta z$ of the 10 min tower measurements. The importance of applying adapted window lengths is evident, since the slight increase of TKE during the period of comparison is well represented by both systems and could not be addressed by only applying flux converged 10 min windows. This is even more important for the covariances of the vertical and horizontal wind component $Cov_{wu_{rot}}$, since the variability is high. For both measurement systems, the coordinate systems was rotated into the mean wind direction so that the horizontal wind component u_h is aligned with the mean wind direction. The first flight leg does agree with the tower measurement for the moving window calculation and the 10 min value. The second leg has an offset of ≈ 0.02 m^2 s^{-2}. This correlates with the offset for Var_{v_h} in Figure 11 and can also be explained by the influence of gusts and transient motions on minute time-scales of the horizontal wind. Furthermore the spatial offset between the flight path and the measurement tower may cause these differences.
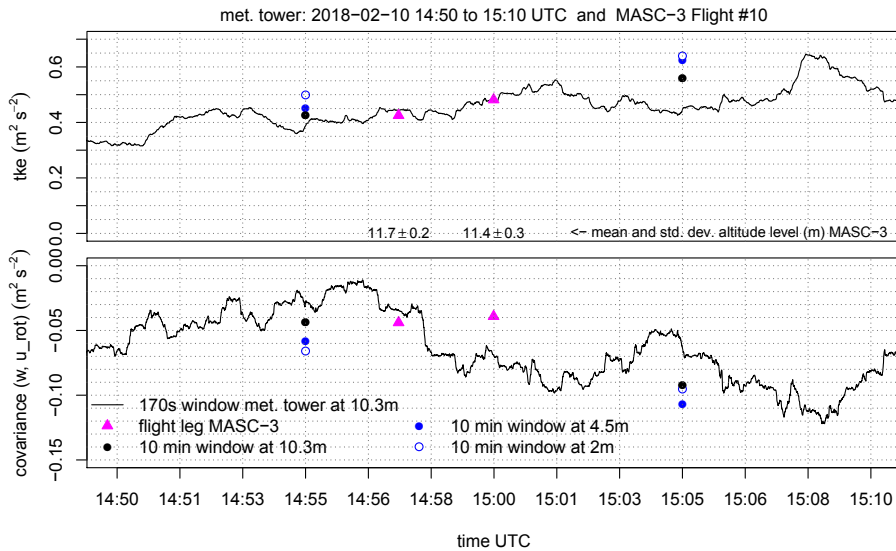
Figure 12. Time series of the tower with the corresponding leg averages of MASC-3 at the lowest flight levels for the turbulent kinetic energy (TKE) (**top**) and the covariance of the vertical and horizontal wind component $Cov_{wu_{rot}}$ (**bottom**). By 2D double rotation for the tower and by coordinate transformation with the mean wind direction of the individual MASC-3 flight legs, u_{rot} was aligned with the mean wind direction. The mean altitude and standard deviation of the individual flight leg is given for the MASC-3 data points. The data of the tower at 10.3 m is calculated on a moving window with the length of $\Delta t_{tower} = 170$ s corresponding to the fetch of the MASC-3 flight legs with an average duration of $\Delta t_{UAS} = 80$ s. Furthermore the neighboring ten minute averages of the tower at all height levels are given.

The integral length scale of the horizontal $L(v_h)$ and vertical wind component $L(w)$ is given in Figure 13. The integral length scale can be interpreted as the biggest scales or eddies that are inherited in the measurement [68]. For the first flight leg, both systems give $L(v_h) \approx 15$ m but for the second flight leg, the time series of MASC-3 yields again 15 m and the tower 20 m. This offset for the second flight leg does correlate with the offsets in Var_{v_h} and $Cov_{wu_{rot}}$ and leads back to previous explanation. It is remarkable, that the 10 min time series result in a negative gradient $\Delta L(v_h)/\Delta z$ for the first 10 min period and in a positive gradient for the second 10 min period, indicating again, that a temporal evolution of the boundary layer is present. Furthermore, the 10 min time series at the 10.3 m level do not agree with the smaller window of $\Delta t_{tower} = 170$ s, indicating that the shorter time periods do not include the same spectrum of eddies. The integral length scale of the vertical wind component $L(w)$ agrees well between the measurement systems. For the same reasons than mentioned previously, the variability is less than for $L(v_h)$. Also the deviation between the 10 min time series and the shorter time period of $\Delta t_{tower} = 170$ s of the tower measurements is smaller (1.5–2 m). Again, the comparison during the first leg agrees better than that of the second leg, where the evolution of $L(w)$ decreases before, during and after the comparison with the flight leg.
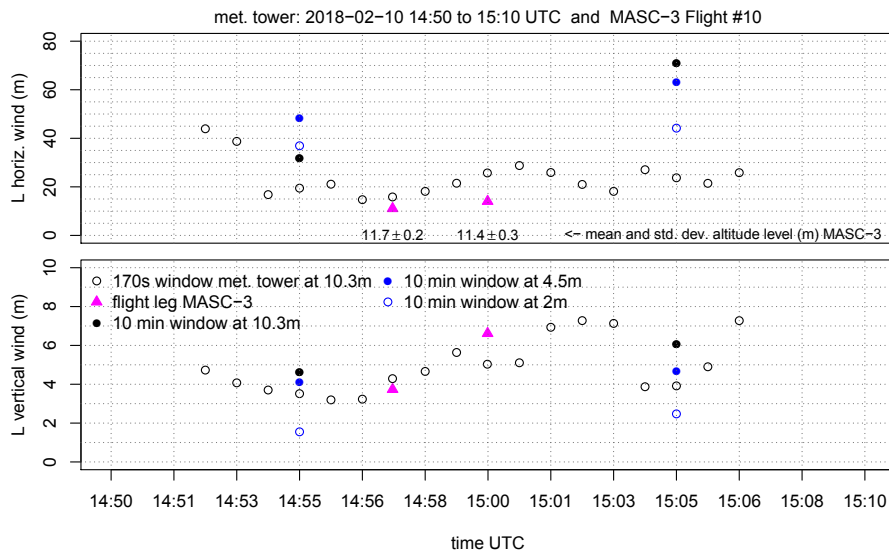
Figure 13. Integral length scales of the horizontal wind $L(v_h)$ (**top**) and the the vertical wind component $L(w)$ (**bottom**). For the tower at 10.3 m, several fractions of the time series with a duration of $\Delta t_{tower} = 170$ s, corresponding to the fetch of the MASC-3 flight legs with an average duration of $\Delta t_{UAS} = 80$ s, were used to plot the length scales alongside the values for the individual MASC-3 flight legs. The mean altitude and standard deviation of the individual flight legs are indicated. Furthermore, the integral length scales of the 10 min time series of the tower at all height levels are given.

It is concluded that the MASC-3 measurements of mean values and statistical moments of second order agree very well with the measurements of the meteorological tower. The comparison between the stationary tower and the moving UAS is best if the temporal fetch of both systems is considered. The structure functions and spectra in Figure 9 revealed, that the spatial and temporal resolution of MASC-3 is significantly higher than for the tower. This advantage is even more important if the mean wind speed is lower. In a stably stratified boundary layer, shorter averaging periods are applicable and may even be advantageous if the fast evolution of the boundary layer is of interest. Representative calculations of statistical moments of second order were given. Although the significance of only two legs is limited, the close analysis provides a first step towards validation of the 3D wind and turbulence measurements with MASC-3.

In order to summarize the persisting error sources and uncertainties for the presented comparison with the data of MASC-3 and to provide indications for future comparisons, the following list is given.

- The remaining spatial offset between the flight path and the tower, as well as differences of the footprint cause discrepancies.
- The temporal and spatial variability of the wind field and the questionable assumption of Taylor's hypothesis of frozen turbulence for the bigger scales of the wind field cause discrepancies.
- The measured quantities from MASC-3 do not represent the whole turbulence range and the measurements are influenced by a random error, which can be improved only by either having a larger ensemble of measurements or longer flight legs in horizontally homogeneous and stationary meteorological conditions.

- An error that is caused by the flight height persists. In sheared flow the changes in flight height and the associated changes of the turbulence regime may cause random error or bias. This depends on how the flight height changes during the flight leg and how strong the shear of the boundary layer is. If the flight height is constant on average but small variations in flight height are present, a random error must be expected. If there is a trend in flight height, or the flight height is clearly above the reference, a bias must be expected.
- Airspeed variations of MASC-3 and differences in the Reynolds number of the five hole probe's tip between the calibration in the wind tunnel and the measurement, influence the turbulence measurements [45].
- Airspeed variations of MASC-3 during the measurement cause an uneven sampling of the turbulent structures due to the acceleration and deceleration of the UAS, cf. References [69] and [37].
- The misalignment between the five-hole probe's orientation and MASC-3 requires three offset corrections. A forth correction factor for the norm of the true airspeed vector accounts for the differences between the airspeed of the calibration in the wind tunnel and during the measurements [45,47].
- The accuracy of the pressure and temperature sensors [47,59,60], as well as the accuracy of the INS, influence the results. The influence of the INS on the turbulence measurements with MASC-3 during dynamic motions of the UAS is especially very difficult to address and has not yet been analyzed sufficiently [45].

4.2. Profiles of the Atmospheric Boundary Layer with MASC-3

This section reverses the principle of the comparison and includes the temporally and spatially closest tower measurement periods into the height profiles of Flight #11. Figures 14 is also supplemented with the Sodar measurements and indicates the timestamps of the data of the three measurement systems. The Figures 14–16 inherit the tower measurements with the equivalent timestamps of the MASC-3 legs that are closest to the tower. MASC-3 ascended, descended and ascended for a second time during Flight #11. Two racetracks were conducted at every height level, resulting in two consecutive headwind legs at each height level. During the first ascent, the lowest flight level was approximately 14 m AGL and after descending and before ascending the second time, the lowest flight level was 25 m AGL. During these lowest flight legs, the corresponding time stamps for the tower data is used for calculating and plotting the data. With $\overline{v_h} = 6.3 \text{ ms}^{-1}$, $|\vec{u}_a| = 19.7 \text{ ms}^{-1}$ and $\Delta t_{\text{UAS}} = 55$ s for the first two legs of the first ascent, the duration of the considered time series of the tower is again $\Delta t_{\text{tower}} = 170$ s. For the second ascent, where the lowest flight level was 25 m AGL, the corresponding period of the tower was also set to $\Delta t_{\text{tower}} = 170$ s. The combined profiles of various quantities measured by the MASC-3 (triangles), the tower (circles), and Sodar (lines) are presented. Each profile took between 16 and 30 min to complete. The time difference between the first and the last triangle of a profile are summarized together with timestamp of the corresponding Sodar profile in Table 1. Each profile was flown with two racetracks, yielding two measurements per height. The first ascent started at 19:37 UTC, the descent at 20:09 UTC and the second ascent at 20:28 UTC.

Table 1. Timestamps (UTC) and duration of the profiles of MASC-3 and the corresponding timestamp of the Sodar measurement for Flight #11.

Flight #11	Start [hh:mm:ss]	End [hh:mm:ss]	Duration [mm:ss]	Sodar Profile [hh:mm]
ascent #1	19:37:05	20:07:04	29:59	19:45
descent #1	20:09:29	20:25:43	16:14	20:15
ascent #2	20:28:03	20:54:14	26:11	20:45 and 20:55

Figure 14 shows the averages of potential temperature, wind speed and wind direction. Potential temperature increases with height, that is, 1.2 K in the lower 50 m, indicating the presence of a weak surface-based inversion. The first two profiles, ascent #1 and descent #1, indicate that a stable stratification persists up to 140 m; whereas the third profile, ascent #2, indicates that the atmosphere has cooled and approaches neutral stratification above 50 m. Furthermore, in the lower 50 m all flight patterns show a decrease in wind speed with height of about 3 ms^{-1} together with a change in wind direction of about 40°. The first two MASC profiles agree well with the corresponding Sodar profiles of wind speed and direction at 19:45 UTC and 20:15 UTC, whereas ascent #2 reveals for the wind speed features of both the Sodar profiles taken at 20:45 UTC and 20:55 UTC. The MASC-3 data at levels below 80 m are closer to the Sodar profile from 20:45 UTC. Above this level data are in good agreement with the Sodar data profile from 20:55 UTC. This case indicates that what at first sight appears to be a jet like feature, observed during ascent #2, is in fact the result of a strong instationarity related to a decrease in wind speed during the time it took to complete the profile. The change in wind speed and wind direction occurred relatively sudden, which explains why the red triangles at 70 m are further apart from each other than at the other levels. The wind direction profiles of the Sodar measurements during ascent #2 deviate slightly more from the MASC-3 profiles than for ascent #1 and descent #1. Further, the turning of the wind direction measured by the tower and the lowest flight legs of MASC-3 between ascent #1 and ascent #2 was oppositely measured by the Sodar profiles above.
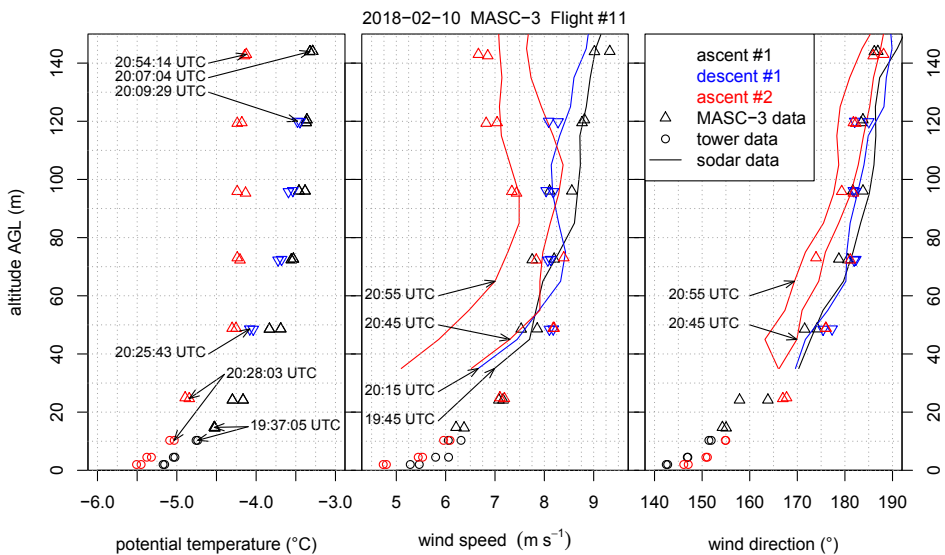

Figure 14. MASC-3 Flight #11 alongside the corresponding tower data and Sodar data as height profile for the potential temperature θ (**left**), the horizontal wind speed v_h (**middle**) and the wind direction ϕ (**right**). The time series of the tower data points have a duration of $\Delta t_{\text{tower}} = 170$ s, corresponding to the fetch of the MASC-3 flight legs at the lowest levels with an average duration of $\Delta t_{\text{UAS}} = 55$ s. The timestamps of the first measurement points of each profile and the timestamps of the Sodar profiles are given.

During the whole flight, a stable boundary layer was present, but surface observations reveal that turbulence conditions were not stationary. Around 18:30 UTC clouds enter the area. Long-wave

incoming radiation increases from 220 W m^{-2} to 280 W m^{-2} around 19:00 UTC, and recovers to its original values just after 20:00 UTC. At the same time, the sensible heat flux at 2 m height increases from -25 W m^{-2} at 18:00 UTC to 0 W m^{-2} at 19:00 UTC, and decreases to -20 W m^{-2} at 20:00 UTC. At 10 m height, the sensible heat flux also increased to 0 W m^{-2} at 18:00 UTC; but during the cloud free periods, the magnitude of the flux in 10 m height was about 5 W m^{-2} smaller than at 2 m height. Furthermore, stability at 2 m height was constant around 0.05 and, whereas at 10 m height values decreased from 0.4 at 18:00 UTC to 0.05 at 19:00 UTC, recovering to 0.4 at 20:00 UTC. Finally, the friction velocity, u_*, steadily decreased from 0.25 ms^{-1} to 0.16 ms^{-1} during this time period.

To get more insight in the atmospheric structure for this specific situation, the MASC-3 measurements allow to consider second-order moments as well. Figure 15 and 16 present variances of horizontal (Var$_{v_h}$) and vertical wind speed (Var$_w$), as well as turbulent kinetic energy (TKE) and the covariance of horizontal and vertical winds Cov$_{wu_{rot}}$. Note that also these variables represent time averages for the tower data of $\Delta t_{\text{tower}} = 170$ s. This is a rather short averaging interval for second-order moments but it contains 90% of the relevant information as shown by the Ogives in Figure 8 [70,71]. Furthermore, profile scaling functions of Var$_w$ and Cov$_{wu_{rot}}$ by Reference [72] are plotted . The scaling function for Cov$_{wu_{rot}}$ is given by

$$\text{Cov}_{wu_{rot}} = u_*^2 \left(1 - \frac{z}{h}\right)^{\frac{3}{2}} \tag{12}$$

and the scaling of the variance of the vertical wind vector component Var$_w$ is given by

$$\text{Var}_w = 1.96 \, u_*^2 \left(1 - \frac{z}{h}\right)^{\frac{3}{2}} \tag{13}$$

where h is the estimated height of the boundary layer. For this situation, we used $u_* = 0.16$ ms^{-1} based on the tower data at 2 m and $h = 50$ m. The main assumptions for this model are a stationary boundary layer with constant Richardson and Richardson flux numbers [72].

Figure 15 shows that Var$_{v_h}$ is 0.20–0.25 m^2 s^{-2} at the surface and decreases with height in the lower 60 m AGL. Above this level, the first two profiles show increasing Var$_{v_h}$, whereas the third profile remains constant with height. Also for Var$_w$ an apparent difference between the first and the last profile exist. The first profile shows an increase in height in the lower 60 m AGL, whereas the third profile shows a decrease Var$_w$ following the scaling function from Reference [72] presented in Equation (13). The profiles of TKE and Cov$_{wu_{rot}}$ as shown in Figure 16 are consistent with this picture. In the last profile TKE decreases in the lower 60 m AGL, whereas in the first profile TKE increases. The Cov$_{wu_{rot}}$, which is aligned in the mean wind and thus represents u_*, seems to follow the scaling profile of Nieuwstadt given in Equation (12) in all cases. Nevertheless, the first profile shows a greater spread between the two flight legs and suggests a maximum of Cov$_{wu_{rot}}$ at about 70 m AGL.

These data show that during the cloudy atmospheric conditions the boundary layer is not in balance with the surface, that is, conditions are non-stationary. Ascent #1 took place in the period when the clouds were leaving the area. The radiative cooling starts to enhance the magnitude from the surface fluxes, but at greater heights turbulence is still more active due to the previously existent neutral conditions. One may argue that this profile suggests the existance of a so-called upside-down boundary layer, that is, a boundary-layer containing an elevated shear layer. The profile of Var$_w$ shows a maximum at about 70 m [73] and TKE increases with height [52]. However, since conditions are non-stationary, we rather relate this elevated shear layer to the onset of radiative cooling at the surface than to an upside down boundary layer with an elevated source of turbulence cf. Reference [52,73].

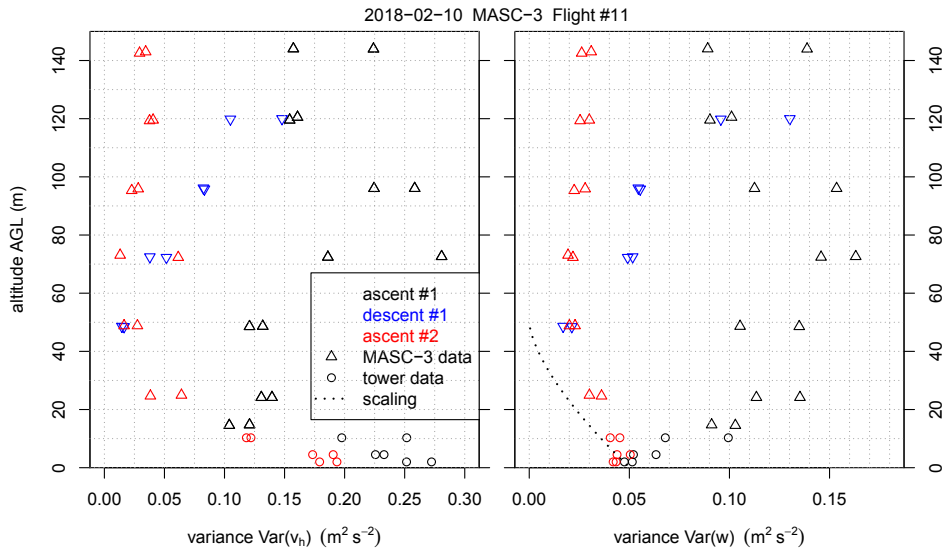Further scaling methods were not found to be applicable.

Figure 15. MASC-3 Flight #11 alongside the corresponding tower data as height profile for the variance of the horizontal wind speed Var_{v_h} (**left**) and the variance of the vertical wind speed Var_w (**right**). The time series of the tower data points have a duration of $\Delta t_{\text{tower}} = 170$ s, corresponding to the fetch of the MASC-3 flight legs at the lowest levels with an average duration of $\Delta t_{\text{UAS}} = 55$ s. The Var_w profile (**right**) inherits the scaling function.

After an hour without clouds, the situation has become more stationary and profiles suggest that turbulence is now mainly confined to the surface. The potential temperature approaches the neutral stratification at heights above 60 m [68]. Note that since the wind suddenly reduced during the measurements, there is no real jet, which explains why $\text{Cov}_{wu_{rot}}$ is not >0 above 60 m for ascent #2 cf. Reference [74]. Furthermore, turbulence parameters follow the scaling laws from Reference [72] and TKE and Var_w are largest close to the surface [52,73]. As such, the boundary layer classification, may be considered a weakly stable boundary layer in the transition regime, that is, no constant flux layer and stability >0.1 [75].

We conclude that the MASC-3 measurements agree well with measurements of the meteorological tower and the Sodar and the combination of these measurement systems captures the interactive nature of the stable boundary layer well. The relatively long sampling time for a full ABL profile, consisting of several straight and vertically stacked legs, may however cause misleading interpretations when sampled under conditions with strong instationarity. For such cases, additional boundary layer remote sensing systems such as Sodar are highly valuable.
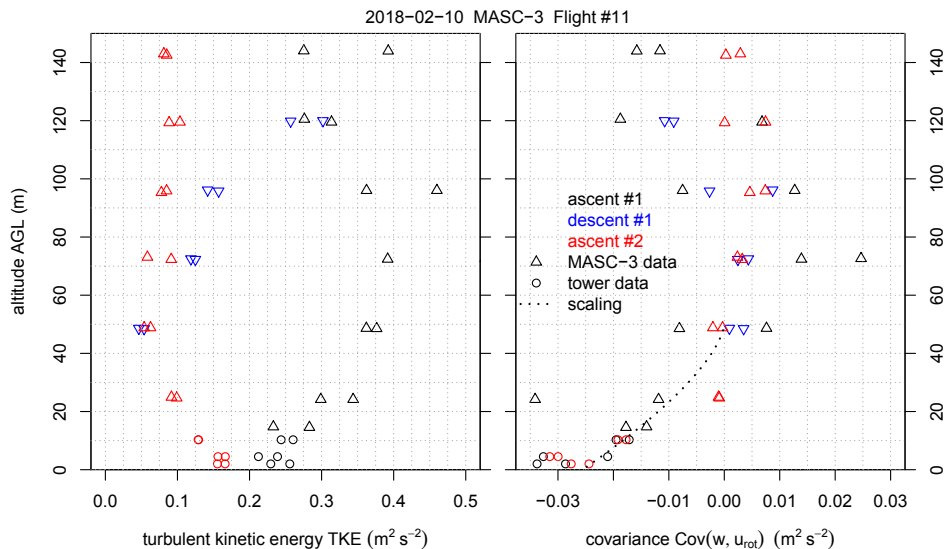
Figure 16. MASC-3 Flight #11 alongside the corresponding tower data as height profile for the TKE (**left**) and the covariance $\mathrm{Cov}_{wu_{rot}}$ (**right**) of the vertical wind w and the transformed vector component u_h which is aligned with the mean wind direction. The time series of the tower data points have a duration of $\Delta t_{\mathrm{tower}} = 170$ s, corresponding to the fetch of the MASC-3 flight legs at the lowest levels with an average duration of $\Delta t_{\mathrm{UAS}} = 55$ s. The $\mathrm{Cov}_{wu_{rot}}$ profile (**right**) inherits the scaling function.

5. Conclusions

The recent mark of the Multi-Purpose Airborne Sensor Carrier MASC-3 improved the turbulent 3D wind vector measurement and gained endurance, since the flight mechanical performance of the wing design with a high lift/drag ratio and the streamlined design is less susceptible to turbulence. The influence on the location of the sensors was minimized by locating the engine behind the tail unit. The fuselage and the installed sensor hat, as well as the modular software architecture of the data acquisition system, allow for different payloads and a variety of applications that can be supplemented to the turbulent 3D wind vector measurement. The autopilot system and the durable airframe can be deployed in polar conditions and provides manifold maneuverability including a multitude of flight patterns for different missions, as well as automatic landing. The precision and repeatability of the Pixhawk 2.1 autopilot ensures the quality of turbulence measurements in the atmospheric boundary layer. The telemetry of the autopilot and the sensor system, as well as the post-processing software MADA, provide insight of the prevailing conditions on sight and enable interactive and adjusted measurement campaigns. Two flight experiments in a SBL and a close comparison with a meteorological measurement tower, equipped with sonic anemometers, depicted the capabilities of MASC-3. Beside mean values, MASC-3 measurements allow second-order statistical moments, even suitable for estimating the turbulence regimes of SBL, where small differences distinguish between important characteristics of the SBL. The close comparison with the data of the measurement tower showed, that variances, covariances, turbulent kinetic energy and the integral length scale can be reliably estimated and agree well. With MASC-3 and its sensor system, the turbulent structure of the ABL can be sampled faster and with higher resolution than standard sonic anemometers mounted on a measurement tower. Considering the individual fetch of a stationary measurement system and a

moving UAS, the systems can be plotted together with continuous profiling systems, such as Sodar to depict fast evolving SBL. Due to the ability to transect the ABL, shorter averaging intervals for second-order moments are applicable when compared to stationary measurement systems, especially if the mean flow is weak and the advection over the stationary sensors is small. The temporal evolution and transition phases between turbulence regimes can be captured with higher resolution and thus, MASC-3 is a valuable addition to meteorological towers and Sodar measurements when investigating the interactive nature of the stable boundary layer.

References

1. Taylor, G.I. The spectrum of turbulence. *Proc. R. Soc. Lond. Ser. A Math. Phys. Sci.* **1938**, *164*, 476–490.
2. Lumley, J. Interpretation of time spectra measured in high-intensity shear flows. *Phys. Fluids* **1965**, *8*, 1056–1062.
3. Kaimal, J.C.; Finnigan, J.J. *Atmospheric Boundary Layer Flows: Their Structure and Measurement*; Oxford University Press: Oxford, UK, 1994.
4. Kolmogorov, A.N. The local structure of turbulence in incompressible viscous fluid for very large Reynolds numbers. *Dokl. Akad. Nauk SSSR* **1941**, *30*, 299–303.
5. Cheng, Y.; Sayde, C.; Li, Q.; Basara, J.; Selker, J.; Tanner, E.; Gentine, P. Failure of Taylor's hypothesis in the atmospheric surface layer and its correction for eddy-covariance measurements. *Geophys. Res. Lett.* **2017**, *44*, 4287–4295.
6. Wyngaard, J.; Clifford, S. Taylor's hypothesis and high–frequency turbulence spectra. *J. Atmos. Sci.* **1977**, *34*, 922–929.
7. Suomi, I.; Gryning, S.E.; O'Connor, E.J.; Vihma, T. Methodology for obtaining wind gusts using Doppler lidar. *Q. J. R. Meteorol. Soc.* **2017**, *143*, 2061–2072.
8. Samuelsson, P.; Tjernström, M. Airborne flux measurements in NOPEX: Comparison with footprint estimated surface heat fluxes. *Agric. For. Meteorol.* **1999**, *98*, 205–225.
9. Lenschow, D.H.; Mann, J.; Kristensen, L. How Long Is Long Enough When Measuring Fluxes and Other Turbulence Statistics. *J. Atmos. Ocean. Technol.* **1994**. *11*, 661–673.
10. Egger, J.; Bajrachaya, S.; Heinrich, R.; Kolb, P.; Lämmlein, S.; Mech, M.; Reuder, J.; Schäper, W.; Shakya, P.; Schween, J.; et al. Diurnal winds in the Himalayan Kali Gandaki valley. Part III: Remotely piloted aircraft soundings. *Mon. Weather Rev.* **2002**, *130*, 2042–2058.
11. Egger, J.; Blacutt, L.; Ghezzi, F.; Heinrich, R.; Kolb, P.; Lämmlein, S.; Leeb, M.; Mayer, S.; Palenque, E.; Reuder, J.; et al. Diurnal circulation of the Bolivian Altiplano. Part I: Observations. *Mon. Weather Rev.* **2005**, *133*, 911–924.

12. Spiess, T.; Bange, J.; Buschmann, M.; Vörsmann, P. First application of the meteorological Mini-UAV'M2AV'. *Meteorol. Z.* **2007**, *16*, 159–169.

13. Reuder, J.; Brisset, P.; Jonassen, M.; Müller, M.; Mayer, S. The Small Unmanned Meteorological Observer SUMO: A new tool for atmospheric boundary layer research. *Meteorol. Z.* **2009**, *18*, 141–147. doi:10.1127/0941-2948/2009/0363.

14. Reuder, J.; Jonassen, M.O.; Ólafsson, H. The Small Unmanned Meteorological Observer SUMO: Recent developments and applications of a micro-UAS for atmospheric boundary layer research. *Acta Geophys.* **2012**, *60*, 1454–1473. doi:10.2478/s11600-012-0042-8.

15. Chilson, P.B.; Gleason, A.; Zielke, B.; Nai, F.; Yeary, M.; Klein, P.; Shalamunec, W. SMARTSonde: A small UAS platform to support radar research. In Proceedings of the 34th Conference on radar meteorology, American Meteorological Society, Williamsburg, VI, USA, 5–9 October 2009; Volume 12.

16. Bonin, T.A.; Goines, D.C.; Scott, A.K.; Wainwright, C.E.; Gibbs, J.A.; Chilson, P.B. Measurements of the temperature structure-function parameters with a small unmanned aerial system compared with a sodar. *Bound.-Layer Meteorol.* **2015**, *155*, 417–434.

17. Thomas, R.; Lehmann, K.; Nguyen, H.; Jackson, D.; Wolfe, D.; Ramanathan, V. Measurement of turbulent water vapor fluxes using a lightweight unmanned aerial vehicle system. *Atmos. Meas. Tech.* **2012**, *5*, 243–257.

18. Wildmann, N.; Hofsäß, M.; Weimer, F.; Joos, A.; Bange, J. MASC—A small Remotely Piloted Aircraft (RPA) for wind energy research. *Adv. Sci. Res.* **2014**, *11*, 55–61. doi:10.5194/asr-11-55-2014.

19. Altstädter, B.; Platis, A.; Wehner, B.; Scholtz, A.; Wildmann, N.; Hermann, M.; Käthner, R.; Baars, H.; Bange, J.; Lampert, A. ALADINA—An unmanned research aircraft for observing vertical and horizontal distributions of ultrafine particles within the atmospheric boundary layer. *Atmos. Meas. Tech.* **2015**, *8*, 1627–1639.

20. Bärfuss, K.; Pätzold, F.; Altstädter, B.; Kathe, E.; Nowak, S.; Bretschneider, L.; Bestmann, U.; Lampert, A. New Setup of the UAS ALADINA for Measuring Boundary Layer Properties, Atmospheric Particles and Solar Radiation. *Atmosphere* **2018**, *9*, 28.

21. de Boer, G.; Palo, S.; Argrow, B.; LoDolce, G.; Mack, J.; Gao, R.S.; Telg, H.; Trussel, C.; Fromm, J.; Long, C.N.; et al. The Pilatus unmanned aircraft system for lower atmospheric research. *Atmos. Meas. Tech.* **2016**, *9*, doi:10.5194/amt-9-1845-2016.

22. Witte, B.M.; Singler, R.F.; Bailey, S.C. Development of an Unmanned Aerial Vehicle for the Measurement of Turbulence in the Atmospheric Boundary Layer. *Atmosphere* **2017**, *8*, 195.

23. Caltabiano, D.; Muscato, G.; Orlando, A.; Federico, C.; Giudice, G.; Guerrieri, S. Architecture of a UAV for volcanic gas sampling. In Proceedings of the 2005 IEEE Conference on Emerging Technologies and Factory Automation, Catania, Italy, 19–22 September 2005; Volume 1, p. 6.

24. Diaz, J.A.; Pieri, D.; Wright, K.; Sorensen, P.; Kline-Shoder, R.; Arkin, C.R.; Fladeland, M.; Bland, G.; Buongiorno, M.F.; Ramirez, C.; et al. Unmanned aerial mass spectrometer systems for in-situ volcanic plume analysis. *J. Am. Soc. Mass Spectrom.* **2015**, *26*, 292–304.

25. Platis, A.; Altstädter, B.; Wehner, B.; Wildmann, N.; Lampert, A.; Hermann, M.; Birmili, W.; Bange, J. An Observational Case Study on the Influence of Atmospheric Boundary-Layer Dynamics on New Particle Formation. *Bound.-Layer Meteorol.* **2016**, *158*, 67–92.

26. Schuyler, T.J.; Guzman, M.I. Unmanned Aerial Systems for Monitoring Trace Tropospheric Gases. *Atmosphere* **2017**, *8*, 206.

27. Hobbs, S.; Dyer, D.; Courault, D.; Olioso, A.; Lagouarde, J.P.; Kerr, Y.; Mcaneney, J.; Bonnefond, J. Surface layer profiles of air temperature and humidity measured from unmanned aircraft. *Agron. Sustain. Dev.* **2002**, *22*, 635–640.

28. Van den Kroonenberg, A.; Bange, J. Turbulent flux calculation in the polar stable boundary layer: Multiresolution flux decomposition and wavelet analysis. *J. Geophys. Res.* **2007**, *112*, 6112.

29. Martin, S.; Bange, J.; Beyrich, F. Meteorological Profiling the Lower Troposphere Using the Research UAV 'M²AV Carolo'. *Atmos. Meas. Tech.* **2011**. *4*, 705–716.

30. Van den Kroonenberg, A.; Martin, S.; Beyrich, F.; Bange, J. Spatially-averaged temperature structure parameter over a heterogeneous surface measured by an unmanned aerial vehicle. *Bound.-Layer Meteorol.* **2012**, *142*, 55–77.

31. Jonassen, M.O.; Ólafsson, H.; Ágústsson, H.; Rögnvaldsson, Ó.; Reuder, J. Improving high-resolution numerical weather simulations by assimilating data from an unmanned aerial system. *Mon. Weather Rev.* **2012**, *140*, 3734–3756.

32. Reuder, J.; Ablinger, M.; Agústsson, H.; Brisset, P.; Brynjólfsson, S.; Garhammer, M.; Jóhannesson, T.; Jonassen, M.O.; Kühnel, R.; Lämmlein, S.; et al. FLOHOF 2007: An overview of the mesoscale meteorological field campaign at Hofsjökull, Central Iceland. *Meteorol. Atmos. Phys.* **2012**, *116*, 1–13.

33. Bonin, T.; Chilson, P.; Zielke, B.; Fedorovich, E. Observations of the early evening boundary-layer transition using a small unmanned aerial system. *Bound.-Layer Meteorol.* **2013**, *146*, 119–132.

34. Martin, S.; Beyrich, F.; Bange, J. Observing Entrainment Processes Using a Small Unmanned Aerial Vehicle: A Feasibility Study. *Bound.-Layer Meteorol.* **2014**, *150*, 449–467. doi:10.1007/s10546-013-9880-4.

35. Wildmann, N.; Rau, G.A.; Bange, J. Observations of the Early Morning Boundary-Layer Transition with Small Remotely-Piloted Aircraft. *Bound.-Layer Meteorol.* **2015**, *157*, 345–373.

36. Wainwright, C.E.; Bonin, T.A.; Chilson, P.B.; Gibbs, J.A.; Fedorovich, E.; Palmer, R.D. Methods for evaluating the temperature structure-function parameter using unmanned aerial systems and large-eddy simulation. *Bound.-Layer Meteorol.* **2015**, *155*, 189–208.

37. Braam, M.; Beyrich, F.; Bange, J.; Platis, A.; Martin, S.; Maronga, B.; Moene, A.F. On the Discrepancy in Simultaneous Observations of the Structure Parameter of Temperature Using Scintillometers and Unmanned Aircraft. *Bound.-Layer Meteorol.* **2016**, *158*, 257–283. doi:10.1007/s10546-015-0086-9.

38. Kral, S.T.; Reuder, J.; Vihma, T.; Suomi, I.; O'Connor, E.; Kouznetsov, R.; Wrenger, B.; Rautenberg, A.; Urbancic, G.; Jonassen, M.O.; et al. Innovative Strategies for Observations in the Arctic Atmospheric Boundary Layer (ISOBAR)—The Hailuoto 2017 Campaign. *Atmosphere* **2018**, *9*, 268.

39. Båserud, L.; Flügge, M.; Bhandari, A.; Reuder, J. Characterization of the SUMO turbulence measurement system for wind turbine wake assessment. *Energy Procedia* **2014**, *53*, 173–183.

40. Subramanian, B.; Chokani, N.; Abhari, R.S. Drone-based experimental investigation of three-dimensional flow structure of a multi-megawatt wind turbine in complex terrain. *J. Sol. Energy Eng.* **2015**, *137*, 051007.

41. Wildmann, N.; Bernard, S.; Bange, J. Measuring the local wind field at an escarpment using small remotely-piloted aircraft. *Renew. Energy* **2017**, *103*, 613–619.

42. Neumann, P.P.; Bartholmai, M. Real-time wind estimation on a micro unmanned aerial vehicle using its inertial measurement unit. *Sens. Actuators A Phys.* **2015**, *235*, 300–310.

43. Brouwer, R.L.; De Schipper, M.A.; Rynne, P.F.; Graham, F.J.; Reniers, A.J.; MacMahan, J.H. Surfzone monitoring using rotary wing unmanned aerial vehicles. *J. Atmos. Ocean. Technol.* **2015**, *32*, 855–863.

44. Palomaki, R.T.; Rose, N.T.; van den Bossche, M.; Sherman, T.J.; De Wekker, S.F. Wind estimation in the lower atmosphere using multirotor aircraft. *J. Atmos. Ocean. Technol.* **2017**, *34*, 1183–1191.

45. Rautenberg, A.; Allgeier, J.; Jung, S.; Bange, J. Calibration Procedure and Accuracy of Wind and Turbulence Measurements with Five-Hole Probes on Fixed-Wing Unmanned Aircraft in the Atmospheric Boundary Layer and Wind Turbine Wakes. *Atmosphere* **2019**, *10*, 124. doi:10.3390/atmos10030124.

46. Lenschow, D.H. Aircraft Measurements in the Boundary Layer. In *Probing the Atmospheric Boundary Layer*; Lenschow, D.H., Ed.; American Meteorological Society: Boston, MA, USA, 1986; pp. 39–53.

47. Van den Kroonenberg, A.; Martin, T.; Buschmann, M.; Bange, J.; Vörsmann, P. Measuring the wind vector using the autonomous mini aerial vehicle M2AV. *J. Atmos. Ocean. Technol.* **2008**, *25*, 1969–1982.

48. Rautenberg, A.; Graf, M.; Wildmann, N.; Platis, A.; Bange, J. Reviewing Wind Measurement Approaches for Fixed-Wing Unmanned Aircraft. *Atmosphere* **2018**, *9*, 422.

49. Foken, T. 50 Years of the Monin–Obukhov Similarity Theory. *Bound.-Layer Meteorol.* **2006**, *119*, 431–447. doi:10.1007/s10546-006-9048-6.

50. Mahrt, L.; Vickers, D. Contrasting vertical structures of nocturnal boundary layers. *Bound.-Layer Meteorol.* **2002**, *105*, 351–363.

51. Banta, R.M.; Pichugina, Y.L.; Newsom, R.K. Relationship between low-level jet properties and turbulence kinetic energy in the nocturnal stable boundary layer. *J. Atmos. Sci.* **2003**, *60*, 2549–2555.

52. Banta, R.M.; Pichugina, Y.L.; Brewer, W.A. Turbulent velocity-variance profiles in the stable boundary layer generated by a nocturnal low-level jet. *J. Atmos. Sci.* **2006**, *63*, 2700–2719.

53. Mauritsen, T.; Svensson, G. Observations of stably stratified shear-driven atmospheric turbulence at low and high Richardson numbers. *J. Atmos. Sci.* **2007**, *64*, 645–655.

54. Tampieri, F.; Yagüe, C.; Viana, S. The vertical structure of second-order turbulence moments in the stable boundary layer from SABLES98 observations. *Bound.-Layer Meteorol.* **2015**, *157*, 45–59.

55. Mahrt, L. Nocturnal boundary-layer regimes. *Bound.-Layer Meteorol.* **1998**, *88*, 255–278.

56. Suomi, I.; Vihma, T. Wind gust measurement techniques—From traditional anemometry to new possibilities. *Sensors* **2018**, *18*, 1300.

57. Brown, N. Position error calibration of a pressure survey aircraft using a trailing cone. *NCAR Tech. Note NCAR/TN-313STR* **1988**, doi:0.5065/D6X34VF1.

58. Guinamard, A.; Ellipse, A.; Performance, I.H. *Miniature Inertial Sensors User Manual*; SBG Systems: Rueil-Malmaison, France, 2014.

59. Wildmann, N.; Ravi, S.; Bange, J. Towards higher accuracy and better frequency response with standard multi-hole probes in turbulence measurement with remotely piloted aircraft (RPA). *Atmos. Meas. Tech.* **2014**, *7*, 1027–1041. doi:10.5194/amt-7-1027-2014.

60. Wildmann, N.; Mauz, M.; Bange, J. Two fast temperature sensors for probing of the atmospheric boundary layer using small remotely piloted aircraft (RPA). *Atmos. Meas. Tech.* **2013**, *6*, 2101–2113. doi:10.5194/amt-6-2101-2013.

61. Platis, A. *Der Drohnenführerschein Kompakt. Das Grundwissen zum Kenntnisnachweis und Drohnenflug*; Motorbuch Verlag: Stuttgart, Germany, 2018; Volume 1.

62. Lenschow, D.H. *Probing the Atmospheric Boundary Layer*; American Meteorological Society: Boston, MA, USA, 1986; Volume 270.

63. Mahrt, L. Flux sampling errors for aircraft and towers. *J. Atmos. Ocean. Technol.* **1998**, *15*, 416–429.

64. Lenschow, D.H.; Stankov, B.B. Length Scales in the Convective Boundary Layer. *J. Atmos. Sci.* **1986**. *43*, 1198–1209.

65. Rotta, J. *Turbulente Strömungen: Eine Einführung in die Theorie und ihre Anwendung (Turbulent Flows: An Introduction to the Theory and Its Application)*; Teubner: Stuttgart, Germany, 1972.

66. Bange, J. *Airborne Measurement of Turbulent Energy Exchange Between the Earth Surface and the Atmosphere*; Sierke Verlag: Göttingen, Germany, 2009; ISBN 978-3-86844-221-2.

67. Foken, T.; Wimmer, F.; Mauder, M.; Thomas, C.; Liebethal, C. Some aspects of the energy balance closure problem. *Atmos. Chem. Phys.* **2006**, *6*, 4395–4402.

68. Stull, R.B. *An Introduction to Boundary Layer Meteorology*; Springer Science & Business Media: Berlin, Germany, 2012; Volume 13.

69. Martin, S.; Bange, J. The Influence of Aircraft Speed Variations on Sensible Heat-Flux Measurements by Different Airborne Systems. *Bound.-Layer Meteorol.* **2014**, *150*, 153–166. doi:10.1007/s10546-013-9853-7.

70. Hartogensis, O.; De Bruin, H.; Van de Wiel, B. Displaced-beam small aperture scintillometer test. Part II: CASES-99 stable boundary-layer experiment. *Bound.-Layer Meteorol.* **2002**, *105*, 149–176.

71. Foken, T.; Wichura, B.; Klemm, O.; Gerchau, J.; Winterhalter, M.; Weidinger, T. Micrometeorological measurements during the total solar eclipse of August 11, 1999. *Meteorol. Z.* **2001**, *10*, 171–178.

72. Nieuwstadt, F.T. The turbulent structure of the stable, nocturnal boundary layer. *J. Atmos. Sci.* **1984**, *41*, 2202–2216.

73. Mahrt, L. Stratified atmospheric boundary layers. *Bound.-Layer Meteorol.* **1999**, *90*, 375–396.

74. Grachev, A.A.; Leo, L.S.; Sabatino, S.D.; Fernando, H.J.S.; Pardyjak, E.R.; Fairall, C.W. Structure of Turbulence in Katabatic Flows Below and Above the Wind-Speed Maximum. *Bound.-Layer Meteorol.* **2016**, *159*, 469–494. doi:10.1007/s10546-015-0034-8.

75. Grachev, A.A.; Fairall, C.W.; Persson, P.O.G.; Andreas, E.L.; Guest, P.S. Stable Boundary-Layer Scaling Regimes: The Sheba Data. *Bound.-Layer Meteorol.* **2005**, *116*, 201–235. doi:10.1007/s10546-004-2729-0.

uib.no